A Thesis for the degree of Doctor of Philosophy

High-Fidelity Computational Modeling of In-Flight Ice Accretion on Aircraft and Rotorcraft Including Super-cooled Large Droplet

By

Prince Raj Lawrence Raj

Department of Mechanical and Aerospace Engineering

Graduate School

Gyeongsang National University

August, 2017

High-Fidelity Computational Modeling of In-Flight Ice Accretion on Aircraft and Rotorcraft Including Super-cooled Large Droplet

A dissertation submitted to the Faculty of the Graduate School of the Gyeongsang National University

By

Prince Raj Lawrence Raj

In partial fulfilment of the requirements for the degree of Doctor of Philosophy

August, 2017

Prof. Rho Shin Myong, Dissertation Supervisor

Approved by committees of the Graduate School of Gyeongsang National University in partial fulfilment of the requirements for the degree of Doctor of Philosophy

Dissertation Committee:

Prof. Dr. Jae Hyun Park

Chairman

Prof. Dr. Soo-Yong Cho

Prof. Dr. SungKi Jung 

Dr. Ji Hong Kim

Prof. Dr. Rho Shin Myong

Supervisor

Date: 2017.07

Department of Mechanical and Aerospace Engineering

Graduate School

Gyeongsang National University

Acknowledgement

First of all, I would like to express my deep gratitude to my adviser, Professor Rho Shin Myong, for all his support, patience and guidance. He never fails to challenge us to reach our highest potential, not only as a researcher but also as an individual. His expertise teaches me to work effectively as a part of a team and as an independent researcher.

I sincerely would like to thank Professors Jae Hyun Park and Soo-Yong Cho of Gyeongsang National University, South Korea; Professor Sungki Jung of Federal University of ABC, Brazil; and Dr. Ji Hong Kim of Korea Aerospace Industries, LTD for all their constructive criticism that help me enormously to finalize this manuscript.

I am grateful for my family – my parents and my brother, who constantly show their support, love, and concern. They are my source of encouragement and inspiration that continuously help me endure all the challenges I encounter.

I am also thankful for my friends, former Professors and spiritual family for all their support and teachings that took a great part in reaching my goals. I would like to thank my colleagues in ACML laboratory. I would like to acknowledge the support from the Brain Korea 21 PLUS program of the National Research Foundation of Korea (NRF).

Lastly and above all else, I am grateful and thankful to God Almighty, through His Son Jesus Christ, is my greatest reward. For without Him, every deed will be in vain.

An excerpt from *Tirukkural* by a famous Tamil poet *Tiruvalluvar*.

“பொருள்கருவி காலம் வினையிடனொடு ஐந்தும்
இருள்தீர எண்ணிச் செயல்.”

PRINCE RAJ LAWRENCE RAJ
July 15, 2017

Table of contents

List of figures

Abstract

High-Fidelity Computational Modeling of In-Flight Ice Accretion on Aircraft and Rotorcraft Including Super-cooled Large Droplet

Prince Raj Lawrence Raj

Department of Mechanical and Aerospace Engineering

Graduate School, Gyeongsang National University

Supervised by Prof. Rho Shin Myong

In-flight icing is a critical threat for the safety of an airplane flying inside clouds with supercooled droplets. Ice accumulations on aerodynamic surfaces of an aircraft significantly affect the performance of the aircraft. Hence, the design of proper ice protection system can be a feasible option to prevent the adverse effects of ice accretion. For a proper ice protection system design, the droplet impingement behavior, ice accretion behavior, and metrological parameters behavior need to be mastered.

In this study, an Eulerian-based droplet impingement code which provides the collection efficiency for air flows around any three-dimensional model containing water droplets is developed. A Finite Volume Method (FVM) is used to solve compressible Navier-Stokes equations, and shallow water based droplet equations. The supercooled large droplet (SLD) behaviors such as splashing, rebound, deformation are modeled and implemented in the FVM droplet solver without altering the governing equations. A unified grid technology is developed to use the same grid in both air and droplet solvers. A PDE-based ice accretion solver is also developed to predict the iced shape on the clean geometry. The ice accretion solver is able to handle all regimes of ice formation in which the water film flow is

automatically solved along with the mass of ice and equilibrium temperature. Further, the ice accretion solver is based on FVM in which the inputs can be easily given from the air and droplet solvers. An automatic grid regeneration method is then developed by using scripting on commercial grid generation software.

Further, several parameters critical in the ice accretion have been investigated. The effects of ice density, heat flux, surface roughness, turbulence model, and multi-shot approach are investigated using the present computational models. The numerical results were validated against the experimental and other numerical results. The validation study started with a two-dimensional airfoil and then extended to a three-dimensional engine intake under various metrological conditions. It was shown that the present air, droplet, and ice accretion solvers produce computational results in close agreement with the experimental results. The effects of SLD were also investigated in both two-dimensional and three-dimensional surfaces. After a rigorous validation study of each solver, various engineering problems were studied using the icing package solver.

The engineering problems such as a 2D multi-element airfoil, 3D rotorcraft engine intake, and a full-scale KC-100 aircraft are investigated under various ambient icing conditions. The new solvers are found capable of solving almost all the engineering problems. Moreover, an investigation of ice protection system was conducted for a wind turbine blade and the power requirements along with heater length are evaluated. Finally, to reduce the computation time of the solvers, parallelization techniques are implemented in air and droplet solvers. The air solver is parallelized using MPI library while the droplet solver is parallelized by Coarray Fortran. The performance of both solvers is measured and reported with relevant data. Overall, the developed ice package is a one step forward towards the accurate prediction of ice shapes.

Abstract in Korean

비행중 과냉각 액적은 항공기의 안전성을 위협하는 잠재적 요인이 된다. 특히 항공기의 공력 성능에 지배적인 영향을 미치는 부분에 발생된 결빙 증식은 항공기 성능에 매우 위협적이다. 따라서, 적절한 제빙 혹은 방빙 시스템의 설계가 결빙 증식으로 인한 역효과를 예방하기 위한 유용한 선택이 될수 있다. 적절한 제빙 혹은 방빙 시스템 설계를 위해 액적 충돌, 결빙 증식 및 기상학적 요소들에 대한 이해가 필수적이다.

본 연구에서, 액적이 포함된 삼차원 모델 주위의 공기흐름에 대한 축적율을 제공하는 오일러리안 기반 액적 충돌 코드를 개발하였다. 압축성 Navier-Stokes 방정식과 Shallow Water 기반의 액적 방정식을 계산하기 위해 유한체적법이 사용되었다. Splash, Rebound, Deformation과 같은 특징을 가지는 과냉각 대형 액적은 지배 방정식의 변경 없이 개발된 유한체적 기반 액적 Solver로 구현되었다. 본 계산에 사용된 격자는 공력 Solver와 액적 Solver에 동일하게 적용되었다. 결빙 형상을 예측하기 위하여 편미분 방정식 기반의 결빙 증식 Solver를 개발하였다. 개발된 결빙 증식 Solver는 모든 결빙 영역에서 얼음의 질량과 평형 온도에 따라 자동적으로 수막 유동을 계산할 수 있다. 또한, 전 단계인 공력 및 액적 Solver로부터 획득한 정보를 결빙 증식 Solver에 용이하게 적용하기 위해,결빙 증식 Solver는 유한체적법을 기반으로 개발하였다. 착빙에 따른 자동 격자 재생성 방법은 상용 격자 생성 프로그램의 Script를 이용하여 개발하였다.

본 연구의 한 부분으로써 착빙과 관련된 매개변수에 대한 조사를 수행하였고, 얼음의 밀도, 열 유량, 표면 거칠기, 난류 모델, Multi-shot 접근법의 중요성을 확인하였다. 계산 모델로 예측된 수치해석 결과는 실험 결과 등을 통해 검증되었으며, 이차원 익형에서부터 삼차원 엔진 유입구까지 다양한 조건에 대해 이루어졌다. 그 결과, 본 연구의 공력, 액적, 결빙 증식 Solver를 통한 수치해석 결과가 실험 결과와 매우 일치함을 확인 할

수 있었다. 이를 통해, 과냉각 대형 액적의 영향성은 이차원 및 삼차원 표면에서 확인되었으며, 개발된 Solver를 다양한 공학적 문제에 적용하였다.

고양력을 위한 이차원 다요소 익형, 삼차원 회전익기 엔진 흡입구, KC-100 전기체 형상과 같은 공학적 문제를 다양한 결빙 조건에서 해석하였다. 마지막으로, Solver의 계산 시간을 줄이기 위해 공력, 액적 Solver에 병렬 처리 기술을 적용하였고, 공력 Solver는 MPI 라이브러리, 액적 Solver는 새로운 병렬프로그래밍 기술인 Coarray 포트란을 이용하여 병렬화하였다.

Introduction

Objective

Atmospheric icing is a threat to the safety of aircraft flying inside the clouds surrounded by air-mixed super-cooled droplet and wind turbine blades operating in cold climates. In aircraft and wind turbine systems, this can result in degraded aerodynamic and propulsive performances and serious safety concerns. Hence, it is necessary to design proper ice protection systems to prevent any unnecessary risk to the safety of aircraft and to comply with airworthiness requirements. This work was motivated to elaborate the droplet impingement and ice accretion, especially in consideration of the behaviours of super-cooled large droplet (SLD) effects. The SLD effects considered in the present study are derived from well-reputed literature and the ice accretion model is based on Messinger thermodynamic model. The resulting non-linear partial differential equations are solved using advanced mathematical and computational methods.

Along with the aforementioned objective, the effect of different parameters such as ice density, heat transfer, surface roughness, turbulence models, evaporation, and multi-shot icing was studied. Moreover, the ice performance degradation on a multi-element airfoil under conventional and SLD icing conditions was investigated. The developed solvers are applied for various engineering problems such as rotorcraft engine inlet and KC-100 aircraft under conventional as well as SLD icing conditions. Finally, in order to reduce the computational time, parallelization of solvers is considered and different parallel programming methods are implemented for better performance.

Outlines

The remaining part of the thesis is organised into nine chapters. Chapter 1 addresses the basics of ice accretion. In Section 1.1, the physics of inflight- icing process is explained, and the general types of ice accretion are categorised in Section 1.2. The important factors which affect the atmospheric icing are discussed in section 1.3. Following that, the icing certification and methods of icing certification are explained in Section 1.4. The numerical modeling of ice accretion and ice accretion packages are discussed in Section 1.5. Finally, the previously available ice accretion models are discussed in Section 1.6.

Chapter 2 is divided into two parts: Shallow water based droplet equations and Navier-Stokes equations for air solution. This chapter starts with the introduction of one-way coupling formulation and its justification for the current problem. Followed by, in Section 2.1, the Shallow water based droplet equation is discussed along with the discretization methods, flux schemes, time step, and boundary conditions. Similarly, Navier-Stokes equations are discussed in Section 2.2 with all necessary sections.

In Chapter 3, special attention is given to supercooled large droplet modeling in Eulerian frame work. First two sections of this chapter discussed about the certification requirements and physical effects of SLD flight scenarios. A summary of available models for SLD effects such as drag, wall interaction, and breakup are discussed in further sections of this chapter. Finally, the implementation of SLD effects in current shallow water based droplet equations is discussed in Section 3.5.

The ice accretion model and its implementation in finite volume framework are discussed in Chapter 4. Furthermore, the necessary physical properties and its calculation are explained in the first few sections of this chapter. Following that, the flux calculations and numerical implementation are discussed. In Chapter 5, a parametric study on present ice

accretion solver is explained. Parameters such as ice density, turbulence model, surface roughness, evaporation, and multi-shot ice are discussed in detail with proper results.

Chapter 6 is deals with the validation and verification of present air, droplet, and ice accretion solvers. Various problems are solved and then their results are compared with experiments and other numerical solutions. Validation started with 2D airfoils and continued to 3D engine inlets, horizontal tail plane. Validation of droplet solver for various problems was conducted and discussed with proper results. Finally, the developed ice accretion solver is validated under various metrological conditions.

In Chapter 7, the developed computational model is applied for the investigation of atmospheric icing on various engineering problems such as a multi-element airfoil, KC-100 aircraft, and rotorcraft engine intake. Ice accretion investigation was done for given metrological conditions and the results are discussed in detail in the final section. The implementation of ice protection system is explained in Chapter 8. Moreover, Chapter 9 provides detailed information of parallelization of air and droplet solver using single program multi data (SPMD) parallel programming methods. The computational costs of both solvers using serial and parallel solvers are discussed under various conditions. Finally, in Chapter 10, outlook on further development in the line of the present study is discussed.

Chapter 1. Atmospheric Icing

In the Earth's atmosphere, two-phase flows of air and water droplets of various sizes [1-3] may exist in a cloud. Such flows can be found in the air-mixed super-cooled droplet fields around aircraft flying inside a cloud, wind turbine blades, boats, communication towers, and network cables operating in cold weather. Exposure to this condition for a considerable period may cause significant ice accretion on the surfaces of critical components like a wing [4, 5], blade, cables and engine inlet [6, 7]. This is called atmospheric icing in the field and remains a critical technological issue in the safety of aircraft [8] and performance of other structures.

1.1 In-flight icing

The study of atmospheric icing effects on aircraft is of critical importance due to significant degradation of aerodynamic performance [4, 9-12] and safety risks. Generally, ice accretion on aircraft surfaces is a result of a tendency for water drops in stratiform and

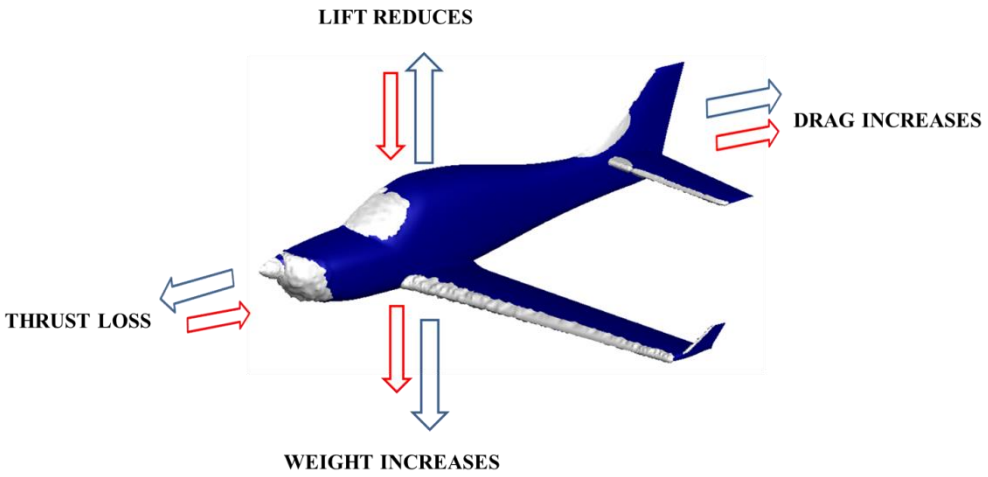

Figure 1-1 Ice accretion effect on a airplane

atmospheric clouds to stay in a liquid state (metastable state) even at temperatures as low as -40°C. These drops, called as supercooled drops [13-15], will crystallize in the presence of

ice crystal, snow flake, or dust and dirt. On the other hand, the water drops can remain in the liquid phase until they impinge on aircraft structure and begin to freeze forming an ice accretion. Accumulation of ice on the leading edge surfaces of aircraft will result in disruption of smooth flow, reduction of lift and increase of drag, stall at much higher speeds than normal, vibrations due to mass imbalance, blockage of pitot tube or other sensors and damage of aircraft components due to ice shedding [10, 16]. Figure 1-1 illustrates the effects of ice accretion on an aircraft.

1.2 Types of ice

In general, there are three types of possible ice accretion in aircraft, namely rime, glaze, and mixed ice [17, 18]. The type of ice on a surface depends on the metrological condition and exposed surface condition. Moreover, the temperature is an important parameter which controls the shape and type of ice.

When the temperature is very low, a highly rough ice formed by the instant freezing of super cooled droplets as they impact on the aircraft is known as rime ice. The presence of air pockets makes the rime ice to appear opaque, and brittle in nature. In general, low temperatures, lesser amounts of liquid water, low velocities, and small droplets are favorable for the formation of rime ice.

Next to rime, a transparent ice formed by the relatively higher temperature close to the freezing point is referred to as glaze ice. Generally, glaze ice is denser, harder, and sometimes more transparent than rime ice. With larger accretions, glaze ice may form “horns” due to the possibility of runback liquid film. Due to the formation of horn shapes or irregular shapes, glaze ice has worst characteristics on aerodynamic surfaces such as wings, tail planes, and wind turbine blades. Temperatures close to the freezing point, large amounts of liquid water, high aircraft velocities, and large droplets are favorable to the formation of clear ice.

Finally, mixed ice is a combination of glaze and rime ice which forms under slightly warm and not in very cold temperature. Due to combined behaviour of glaze and rime, it is difficult to predict this kind of ice formation. Furthermore, there is no doubt that the shape and roughness of mixed ice bring penalty in the performance of aerodynamic surfaces.

1.3 Factors affecting ice accretion

The amount of ice that forms on an exposed surface generally depends on the rate of water impingement and the amount of water that freezes on the given surface.

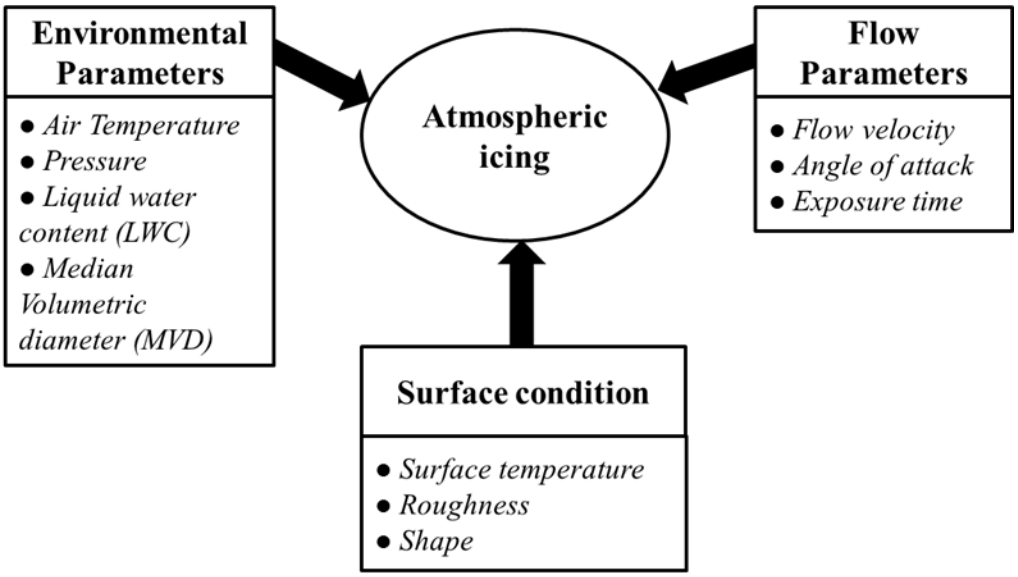

Figure 1-2 Parameters affecting ice accretion

The amount of water freezing is governed by various environmental, physical and surface properties. In general, as shown in Figure 1-2, environmental, flow, and surface parameters play a major role in the ice accretion.

1.3.1 Environmental parameters

Environmental or metrological parameters such as air temperature, pressure, Liquid water content (LWC), and Median volume diameter (MVD) have an important role in atmospheric icing.

1.3.1.1 Ambient air temperature

As discussed in section 1.2, ambient air temperature has an important contribution in determining the possibility and type of ice formation. The ambient air temperature is the critical parameter which controls the convective cooling of incoming droplets. At lower temperature, the convective cooling, as well as the amount of water that freezes is high. The latent heat of droplets is rapidly dissipated by the convection and evaporation at a lower temperature. Hence, the droplets freeze immediately upon impact on the aircraft surface and lead to rime ice accretion. On the other hand, the convective cooling is limited at high temperatures which result in low ice accretion and high liquid film flow. Therefore, at higher temperatures (close to freezing) glaze ice accretion is possible with "horns" due to the runback of the liquid film. The different possible ice formation at different temperatures is illustrated in Figure 1-3. Furthermore, the ambient air temperature has several effects on the liquid water content. As the temperature is reduced, the liquid water content of the cloud is also reduced.

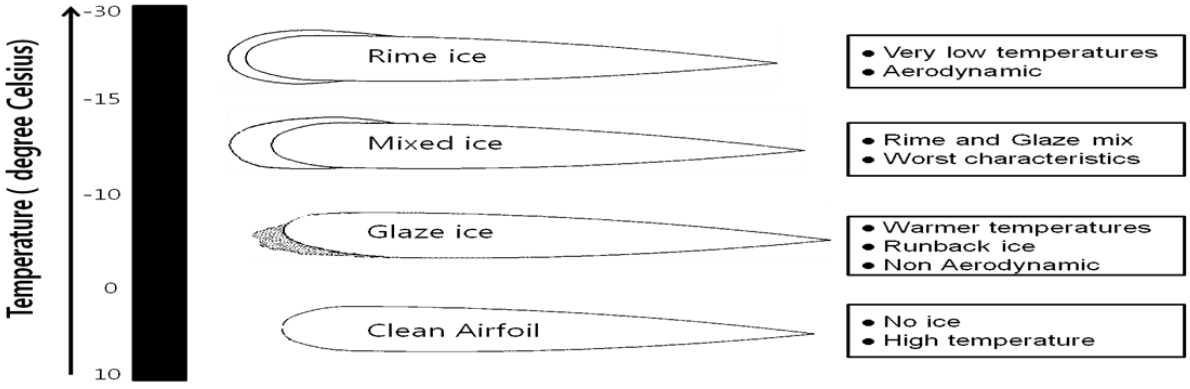

Figure 1-3 Temperature effects on ice accretion

1.3.1.2 Liquid water content

Liquid water content is the measure of the amount of liquid water available in a cloud in a specific amount of air. Liquid water content has a strong influence on the rate of ice accretion and type of ice formation. As the liquid water content increases, the latent heat to be

removed also increases, hence the higher possibility of glaze ice accretion. On the contrary, lower liquid water content has the tendency for rime ice growth due to the heat dissipation through evaporation and rapidly leads to free droplets. Generally, the liquid water content is expressed in g/m^3 and varies from cloud to cloud in the range of 0.1 to 2 g/m^3.

1.3.1.3 Droplet diameter

Droplet diameter is a very important parameter which affects the ice accretion due to its strong relation to the amount of water impingement. In clouds, the diameter of droplets varies from very small to large. Median volumetric diameter is a term used in the field of metrology and atmospheric icing community, defined as the droplet diameter which is the median value of the all the droplets available in the cloud.

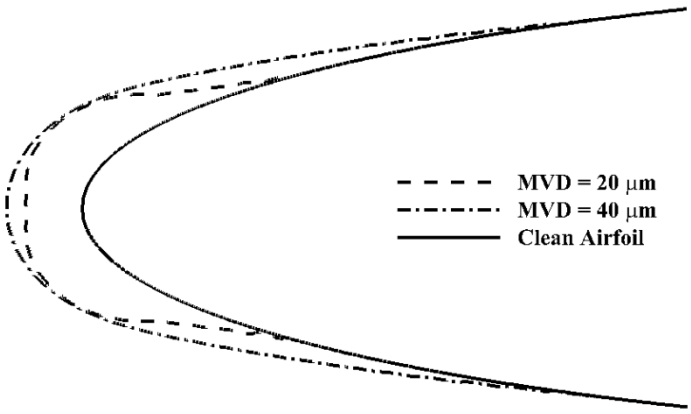

Figure 1-4 Droplet diameter effect on ice accretion

Generally, the median volumetric diameter is selected such that half of the total liquid water content is contained in droplets larger than the median and half in droplets smaller than the median. Furthermore, few numbers of larger droplets are generally a present and a large number of small droplets to have a mass balance of droplets. In aircraft icing, the conventional icing droplet range is from 10 μm to 50 μm, but in some weather conditions the droplets diameter can reach up to 600 μm or more. Once the droplet is more than 50 μm, it is referred as a supercooled large droplet (SLD).

1.3.2 Flow parameters

The air flow over the aircraft or wind turbines is different in nature due to the shape of the components. The flow parameters such as velocity, angle of attack, and exposure time have a strong effect on the ice accretion amount, shape, and location of the surface.

1.3.2.1 Flow velocity

Air flow velocity or airspeed has a strong influence on the amount of ice accretion due to its influence on the mass of water collected by the exposed surface. The mass of droplet impingement is given by the product of collection efficiency, liquid water content, and airspeed. Therefore, as the speed increases, the mass of water impingement increases, and consequently the amount of ice accretion may also increase.

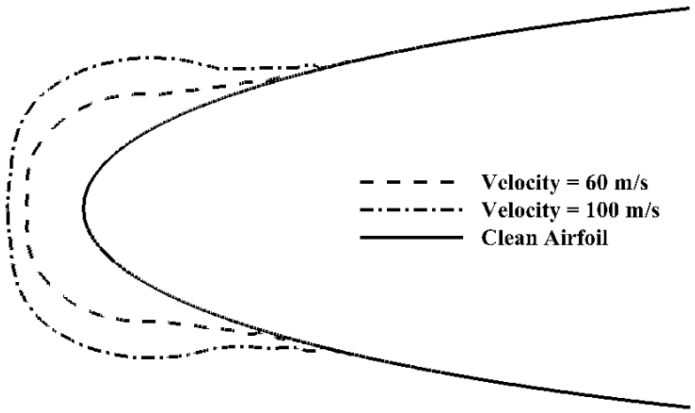

Figure 1-5 Airspeed effect on ice accretion

1.3.2.2 Angle of attack

The angle of attack is referred as the angle between relative wind direction and a reference line on the wing, airplane or blades. Generally, determination of the location of ice accretion is essential in the design of anti- or de-icing systems. The angle of attack has the capability to change the location of ice accretion. For the same object such as aerofoil, the location and impingement area of droplet vary for a different angle of attacks. In the case of

aerofoils, as the angle of attack increases, the pressure side receives more droplet strikes and more ice occurs at the lower side of the aerofoil.

1.3.2.3 Exposure time

Exposure time is an important parameter which affects the rate of ice accretion. As time increases ice accretion also increases for under constant impingement of droplets. Due to this factor, many of the small airplanes without ice protection system are advised to avoid flying through the clouds with droplets.

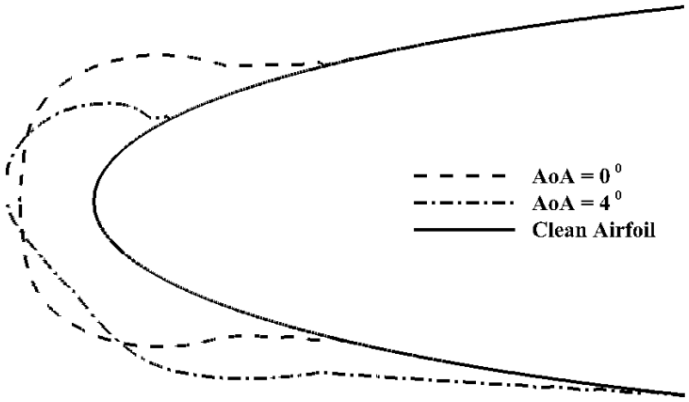

Figure 1-6 Angle of attack effect on ice accretion

1.3.3 Surface condition

Next, to the above two factors, the surface condition of an exposed body has its own behaviour in the amount of ice accretion. Surface temperature, roughness, and shape of the exposed object are the important surface parameters which affect the amount of ice accretion.

1.3.3.1 Surface temperature

The surface temperature of the exposed body has a strong influence on determining the possibility and shape of ice accretion. At high surface temperatures, the ice accretion amount is minimum, of which principle is used by most of the ice protection systems. Most of the ice protection systems help to increase the surface temperature of the exposed body and

consequently prevent ice accretion. Moreover, surface temperature affects the convective cooling and evaporation, which results in the ice accretion amount.

1.3.3.2 Surface roughness

Generally, the surface roughness of aircraft body is very low and it has a strong influence in the amount and shape of ice accretion. Surface roughness accounts for 0.3 percentage of the total airplane drag and strongly coupled with surface heat transfer. In most of the commercial airplanes, the skin roughness is typically maintained less than 400 micro inches to reduce the drag caused by friction. Therefore, the surface roughness enhances the heat transfer by increasing the skin friction coefficient.

1.3.3.3 Size of the exposed body

The size of the exposed body has an impact on the rate of ice accretion; ice accretion on small radius of the leading edge aerofoils is higher than big aerofoils. Hence, the rate of ice accretion on small aircraft wings is higher than the large inter-continental airliners under same metrological conditions. Due to this reason, many ice accretion based accidents are reported in small and short range airplanes.

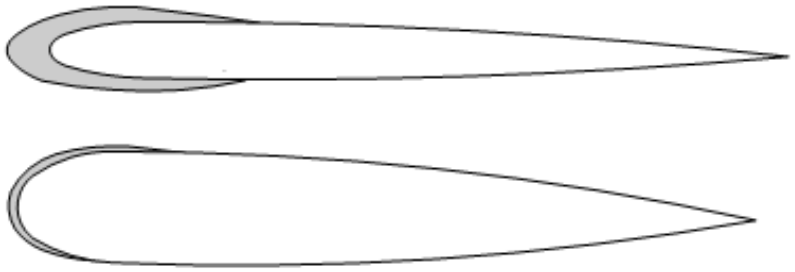

Figure 1-7 Size of the exposed body effect on ice accretion

1.4 Aircraft icing certification

As all other components and systems in an airplane, the ice protection systems also need to be certified by the civil aircraft certification authorities [19]. In order to certify an aircraft,

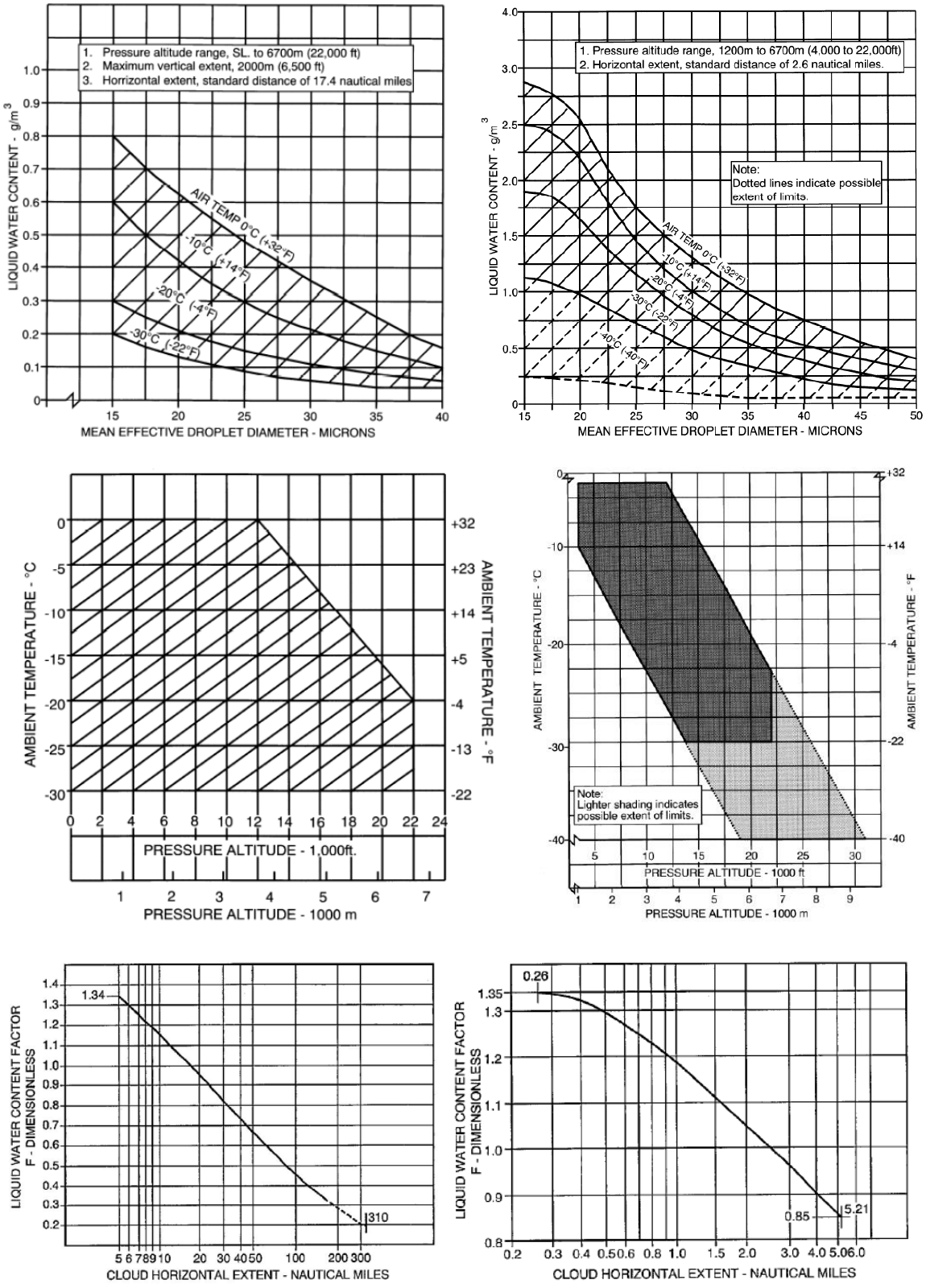

Figure 1-8 Appendix C cloud conditions at continuous maximum (left) and intermittent maximum (right) clouds [20]

it should pass the strict certification process to demonstrate its performance under various metrological condition dictated by civil aircraft certification authorities. The civil aircraft

certification authorities such as FAA (Federal Aviation Administration), EASA (European Aviation Safety Agency), TCCA (Transport Canada Civil Administration) and ANAC (Agência Nacional da Aviação Civil) are responsible for the certification of aircraft.

Based on the research of NACA (National Advisory Committee for Aeronautics), icing certification envelope is defined for demonstrating the aircraft safety in icing conditions. According to the current icing regulation, the analysis and design of ice protection system should show that no hazardous quantity of ice could form on the surfaces that are critical for safe operation of the aircraft when exposed to the icing conditions shown in Appendices C and O. The certification authorities are responsible to set realistic limits and ensure that the manufacturers have adequately tested and demonstrated these limits. Appendix C ice design envelopes for both stratiform and cumuliform clouds are shown in Figure 1-8. Appendix C defines the icing conditions in terms of LWC, MVD, horizontal cloud extent, altitude pressure and temperature. Appendix C envelopes in Figure 1-8 illustrates that the maximum LWC in supercooled droplets is a function of air temperature and respective droplet size of the clouds. On the other hand, the expected temperature range is a function of altitude.

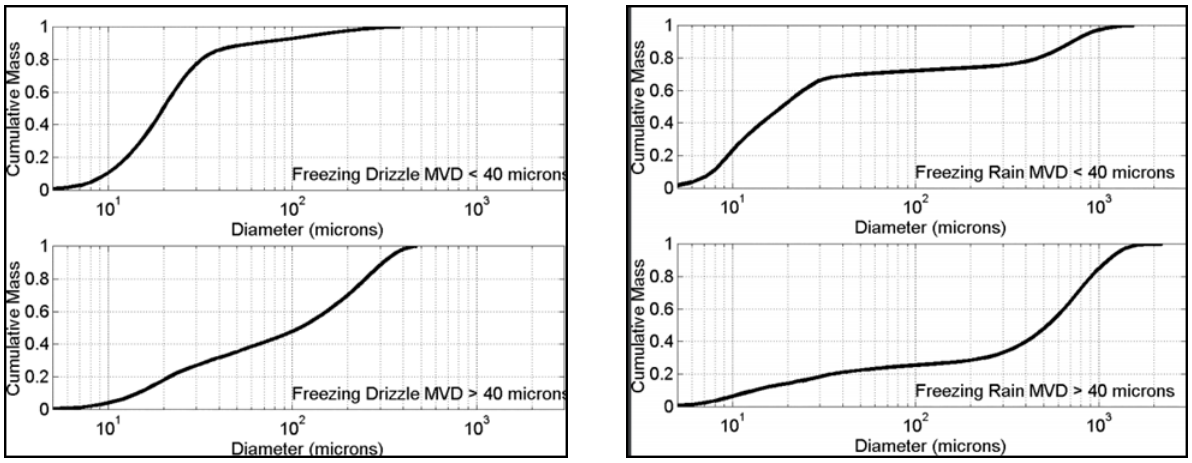

Figure 1-9 Appendix O cloud conditions for freezing drizzle and rain

As shown in Appendix C envelope, the mean effective diameter accounted for a maximum of 50 µm while in nature the MVD is far higher than 50 µm. Therefore, a new envelope appendix O introduced by FAA during the end of 2014 is shown in Figure 1-9. In Appendix

O, the droplets diameter bigger than 50 μm termed as the supercooled large droplet is taken into account along with freezing drizzle and freezing rain.

1.4.1 Accepted means of compliance

In order to demonstrate the safety of the aircraft under different icing envelopes and known icing conditions, different methods may be employed for icing certification, each of which has its own pros and cons. Generally, the following five methods are used in aircraft icing certification process which will be discussed in the next sections:

1. Experimental fluid dynamics
2. Computational fluid dynamics
3. Simulated ice tests
4. In-flight spray system (fly behind tanker)
5. Natural flight test

1.4.1.1 Experimental fluid dynamics

Experimental fluid dynamics is a traditional method used to study aerodynamics by means of wind tunnels. For studying ice accretion, an icing wind tunnel (IWT) can be used, which is one of the basic options available to perform icing analysis for certification requirements. Aircraft and component manufacturers can use IWT during the design and certification process. The natural icing environment is generated inside an IWT with the use of water-spray, refrigeration, and other necessary equipment. It is possible to control cloud LWC, drop diameter, temperature and airspeed.

Generally, IWTs are not capable of simulating full-scale aircraft due to limited test sections. Hence, a scaled model of a part of the model is tested to avoid test-section blockage limitations such as engine air intake, rotor blades, or ice detectors, which are tested separately for a better understanding of physics and to determine the ice shape. Moreover, IWT can simulate natural icing conditions under some limited ranges of airspeed, drop diameter, and

liquid water content. Hence, scaling method is often used to convert the scaled test conditions to the desired icing conditions. By using the reference conditions, i.e. model size and geometry, the scaled test conditions can be evaluated using a set of equations. While using the scaled test conditions, it is necessary to scale the relevant air flow field, droplet impingement, collection efficiency, and thermodynamic properties. Calibration of IWT is necessary before doing any experiment in order to characterize and acquire a stable icing cloud condition. Wind tunnel analysis is relatively cheaper than other experimental methods and it is risk-free. On the other hand, wind tunnel results show a lack of repeatability, scaling of the model is necessary, the start-up time of wind tunnel is high, and full-size models cannot fit in the test sections.

1.4.1.2 Computational methods

The computational simulations can be used to determine the ice accretion and the effect of ice protection system on an airplane under various metrological conditions. The computational analysis is also for pre-design of ice protection system and demonstration of metrological conditions not obtained by wind tunnel or natural flight test. The computational cost is far lower than the cost of wind tunnel and other flight tests. Moreover, it is possible to simulate all the metrological conditions which could not be obtained by other methods and permits the study of a wide range of metrological conditions. There is no restriction in size of the model, hence scaling is not necessary, which allows simulating the real model with full configurations. Real-time visualization of flow, time to time ice accretion study and performance degradation analysis is possible to perform by using computational methods. The determination of impingement limit, surface water mass flux, and catch efficiency can be determined by the computational simulations. The determination of impingement limits can be used to identify the position of ice detectors and the preliminary design of ice protection systems. Complex ice phenomena such as lobster tails, ice breaking, ice shedding, and dynamics of ice after shedding are not yet fully understood by computational models.

Moreover, icing microphysics such as surface roughness and ice density are not well understood and simulations of the transient behavior of aircraft are not possible. Although computational methods have grown enough in last few decades, it is necessary to confirm the accuracy of the computed results by validating against the experimental results obtained from the wind tunnel, in-flight spray system or natural flight test.

1.4.1.3 Simulated ice test

Simulated ice tests are dry air tests on the iced aerodynamic surfaces or the whole models under wind tunnel or in-flight. Generally, the ice shapes predicted by wind tunnels or computational methods are used in the simulated ice test to study the performance degradation of aerodynamic surfaces. The aerodynamic properties such as lift, drag, and the flow behaviour over the engine inlet are investigated using this method. The predicted ice shape castings are attached to the leading edge of the aerodynamic surfaces to do performance degradation analysis under wind tunnels or real test flights. Moreover, this method can be used to study the change in flow behaviours of ice accretion effect on engine inlet, probes, and external kits.

1.4.1.4 In-flight spray system

Next to simulated ice tests, flying behind icing tanker is a method to simulate the ice accretion. In this method, the flight test is conducted by flying behind tanker aircraft which carry water. The in-flight spray system is difficult and quite expensive to develop and calibrate for a specific project. Generally, the in-flight spray systems are used to develop ice protection system, preliminary evaluation of aircraft handling under icing environments, preliminary evaluation of performance degradation, evaluate the ice accretion on the whole aircraft with all equipment such as antennas, probes, sensors, etc., determination of the type of ice formation, and evaluation of ice shedding. Moreover, in-flight spray test methods are safe real flight test before a natural test, hence the failure of systems can be studied safely. In spite of a lot of advantages, few points should be considered before the start of an in-flight

spray test. In nature, supercooled droplets are formed out of the pure water but the tanker water is not pure due to the micro or nano-sized particles. Due to the impurities, supercooling of the droplets formed by tanker water is not possible and results in more runback ice. Finally, the cost of fly behind tanker method is very high and all spectrums of metrological conditions are not possible to achieve. The horizontal extend of the cloud is limited, hence the entire aircraft could not immerse in the developed cloud. The tanker and test aircraft have to fly close enough for this in-flight test which is a high-risk activity that requires very experienced crew. Moreover, the close formation of aircraft makes the test aircraft fly in the wake created by the tanker aircraft. These wakes affect the droplet impingement locations considerably.

1.4.1.5 Natural flight test

Next to in-flight spray system, natural flight icing test is an option to do icing test on a full-scale airplane. It is essential to demonstrate the icing condition effectiveness of the ice protection system and its components by flight tests. The main objective of these natural flight tests is to show that the aircraft is safely operational in the known icing conditions provided by the certification authorities. Generally, natural in-flight tests under measured atmospheric icing conditions are necessary to obtain certification of aircraft. During natural flight tests, the aircraft is equipped with necessary instruments and systems to demonstrate the aircraft's system effectiveness under given icing conditions. Hence, natural ice test can be used to evaluate the system functions, the effectiveness of ice detection system, the effectiveness of ice protection system, and performance characteristics. Ice accretion and ice shedding are continuously monitored by using video cameras focused on the entire critical aerodynamic surface such as a wing, propeller, tailplanes, the nose of the aircraft, etc. Using the onboard instruments and equipment, the cloud data and ice accretion data are recorded carefully for further investigations. These gathered data can be useful for the final determination of the position of ice detectors and air data probes, ice shedding damage investigation, engine performance studies under icing conditions, stability analysis, and

handling qualities. However, this method is limited by the availability of all metrological conditions guided by Appendix C. Furthermore, season and risk of crew and aircraft are the important limitations which make this method more complicated. Moreover, the flight test cost is very high and quantitative measurement of ice is not possible by this method.

As a result of the limitations of each method, application of a combination of methods can be used to demonstrate aircraft safety under various icing envelopes. Computational fluid dynamics and Experimental fluid dynamics are widely used in icing certification, and the former can be applied under all given metrological conditions. The predicted ice shape castings are attached to the leading edge of the aerodynamic surfaces to do performance degradation analysis under wind tunnels or even real test flights. Nowadays, very few set of fly behind icing tanker and natural icing test methods are used for icing certification of aircraft. Since computational methods take a significant part of the icing certification, it is necessary to do an accurate and efficient numerical ice accretion modeling.

1.4.2 Icing certification of helicopters

Similar with airplanes, helicopters also undergo rigorous certification processes for icing certification. However, the maximum altitude of helicopters operations is limited (10,000 to 12,000 feet) due to power reduction and density changes at high altitudes. The experimental results show that the helicopters suffer from unbalance and torque problems at high altitudes (more than 10000 feet). Hence, Appendix C icing envelope is not appropriate [21, 22] for icing certification process for rotorcrafts, which are certified under "Altitude- Limited icing envelopes" in accordance with AC 29.1419. The helicopter tailored envelope is used for the certification of helicopters as shown in Figure 1-10 and Figure 1-11.

The methods used for rotorcraft certification is same as for aircraft as explained in section 1.4.1. However, simulated ice tests are not widely used in helicopter icing

certification owing to the difficulties in installing the ice shapes on the main and tail rotor

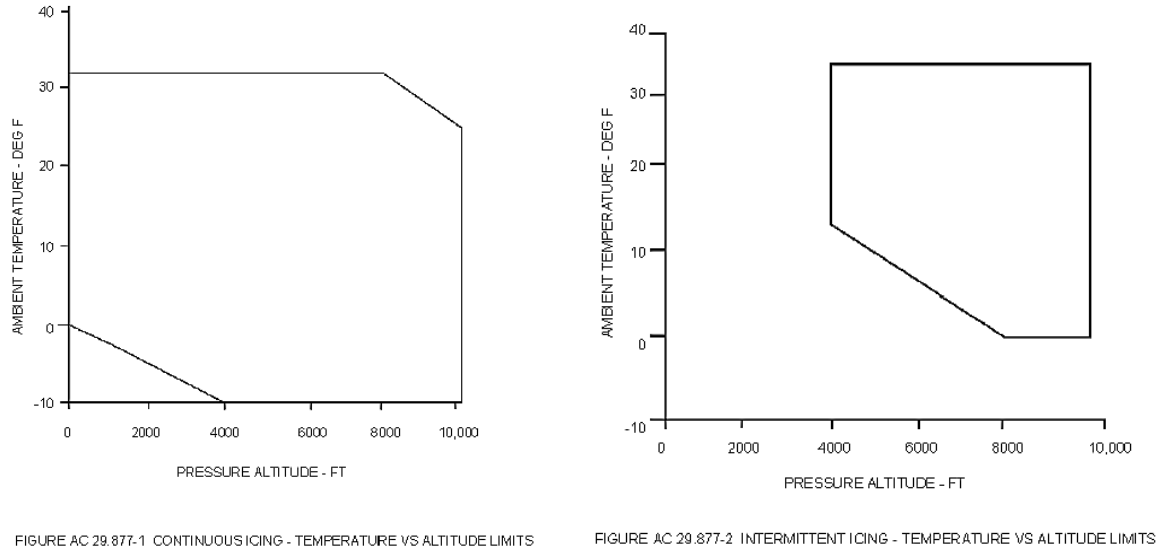

Figure 1-10 AC29.1419 envelop for continuous (left) and intermittent (right) icing temperature profile [23]

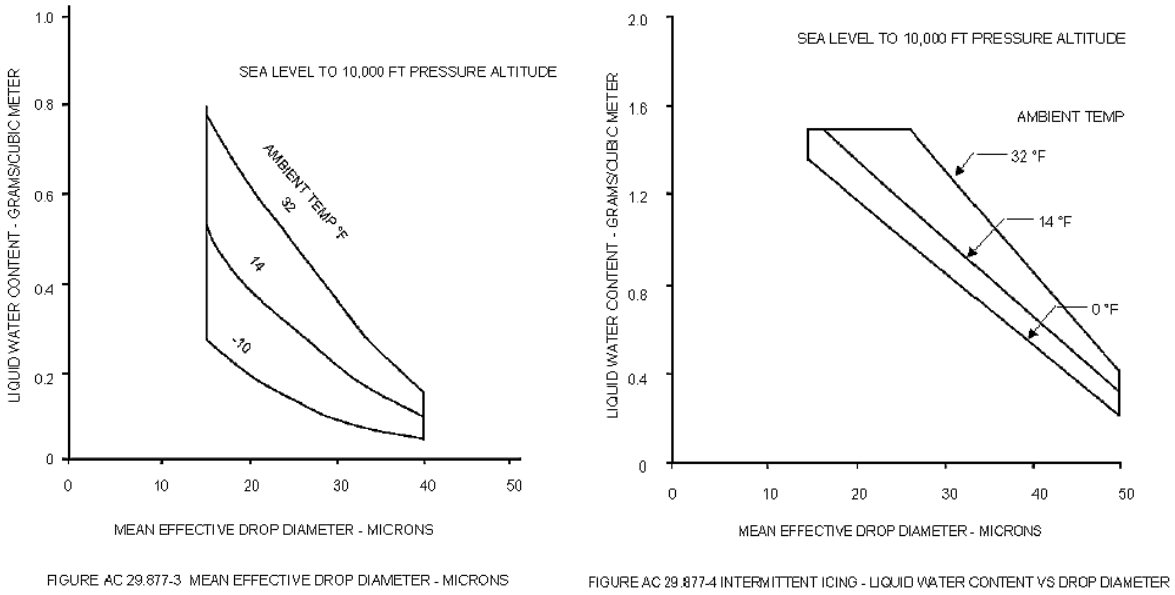

Figure 1-11 AC29.1419 envelop for mean effective drop diameter (left) and intermittent droplet diameter (right) with LWC [23]

blades. Furthermore, simulated ice flight tests are dangerous in operation although can be used for the investigation of engine flow behaviours and other components in helicopters. In

addition to normal flight conditions, ice accretion effects on autorotation characteristics, stability, and ground resonance are needed to be investigated.

1.5 Ice accretion modeling

Numerical ice accretion modeling requires deep knowledge of entire icing physics, efficient mathematical techniques, and sufficient computation power. Generally, the ice accretion modeling starts with the prediction of the flow field around the model and continued by a droplet model which predicts the droplet impingement on the surface. Finally, a thermodynamic model is necessary for predicting the ice accretion and surface water flow.

a. Airflow field prediction

The prediction of accurate airflow field around the model is necessary to predict the possible location of ice accretions. The metrological condition as boundary conditions and mesh over the given model geometry is the input for airflow field solver. Generally, the computational fluid dynamics (CFD) can be employed to obtain the accurate flow field around the model. It should be mentioned that the mesh around the geometry has a significant effect on the solution produced by the CFD methods. The output from airflow field solution may be used as the input for the droplet model and ice accretion model.

b. Droplet model

Droplet impingement distribution on the given surface is predicted by the droplet model using metrological conditions, air flow field solution, and mesh over the given model geometry as the input. Droplet impingement can be predicted by both Lagrangian and Eulerian methods, of which the former follows the trajectory of each individual droplet and the latter describes the property of the flow field as the functions of space and time. The droplet wall interactions and other physical behaviors should be modeled properly using necessary expressions. The predicted droplet impingement solution can be used as input for the ice accretion model.

c. Ice accretion model

The ice accretion model uses the air solution over the surface, and the droplet impingement distribution as input to predict the ice accretion on the given surface. The ice accretion model solves a mass and energy balance along the surface to predict the amount of water freeze. The unfreeze water is taken into account as a runbackwater and the height of the water film is evaluated on the surface. Once the mass of ice accretion is evaluated, other necessary outputs such as ice thickness and volume can be evaluated. Finally, the iced surface geometry is predicted using ice thickness results.

1.6 Previous numerical methods

Nowadays, several research groups all over the world study and develop numerical schemes to predict ice growth methodology. Since the revision of all techniques, methods, and approaches is an extensive process, very few important approaches are focused in this chapter. The approach developed by NASA the LEWICE [24, 25], French aerospace lab's ONERA [26, 27], and McGill University's FENSAP-ICE [28-30] are discussed in this chapter. Few other codes such as TRAJICE2, ICECREMO [31], MULTI-ICE [32], and CANICE [33] often use the same approach used by LEWICE and ONERA with minor refinements. Generally, in all ice accretion solver packages the basic steps to be same like explained in section 1.5. However, each solver follows different approaches in solving the flow field, droplet filed, surface properties, and ice shape.

1.6.1 LEWICE

The well-established ice solver package LEWICE [25] was developed by the NASA Lewis Research Center for two-dimensional flows. The basic version of LEWICE used panel method to solve the airflow field assuming air as inviscid, incompressible, and irrotational. The subsonic flows are dealt by the implementation of compressibility corrections such as the

Prandtl-Glauert. To account the air viscosity effects, a boundary layer code based on experimental correlations are solver to determine the convective heat transfer coefficient in the laminar and turbulent regions.

Hess and Smith in the 1960's pioneered the panel method, which is the simplest model to solve an inviscid flow field. Incompressible, inviscid, irrotational flow can be solved by panel methods that utilize superposition of fundamental solutions of the linear Laplace equation. The equation is based on one or more singularities types that include sources, sinks, doublets, and vortices. Initially, the method discretizes a body by a finite number of panels (segments in 2D) over each of which acts an unknown singularity value or a distribution, and all singularities induce local potential calculated at n control points on the surface with the no-penetration condition used to balance this against the potential induced by the free stream resulting in a n x n full matrix which is then solved for the unknown strengths of the singularities needed to achieve the no-penetration condition. When the system is large, solution costs become prohibitive, hence special techniques are necessary such as the addition of compressibility corrections up to Mach 0.5 to the classical panel method. An example of compressibility corrections is the Prandtl-Glauert. LEWICE was initially based on 2D panel method [25] although several modified versions are currently in use such as three-dimensional [34] version of the panel method (LEWICE3D) where the flow prediction is 3D while icing calculations are performed in 2D along straight cuts provided by the 3D solution. However, in reality, this can only be called a 2.5D solution since ice accretion does not account for the spanwise effects. On the other hand, another version is also in use where viscous-inviscid interaction [35] methods solve the pseudo-viscous field.

To account the air viscosity effects, a boundary layer code based on experimental correlations are solver to determine the convective heat transfer coefficient in the laminar and turbulent regions. The convective heat transfer coefficient in the laminar and turbulent

regions is determined and the transition from laminar to turbulent flow is detected which requires the application of the boundary layer method in LEWICE. The turbulent skin friction coefficient definition includes the equivalent sand-grain roughness while the convective heat transfer coefficient is retrieved by using the Reynolds analogy.

In consideration that the flow is laminar until the boundary layer transition, calculation starts at the stagnation point and the criterion for the transition over a rough surface is defined by Von Doenhoff [36], presuming that the flow becomes turbulent when the local roughness Reynolds number is greater than 600:

$$\mathrm{Re}_k = \frac{u_k k_s}{\nu} \geq 600, \tag{1.1}$$

where k_s and u_k are the equivalent sand-grain roughness height and the velocity at $y = k_s$, respectively. The latter is defined using the formula:

$$\frac{u_k}{u_e} = \frac{2k_s}{\delta} - 2\left(\frac{k_s}{\delta}\right)^3 + \left(\frac{k_s}{\delta}\right)^4 + \frac{1}{6}\frac{\delta^2}{\nu}\frac{du_e}{ds}\frac{k_s}{\delta}\left(1-\frac{k_s}{\delta}\right)^3, \tag{1.2}$$

where δ is the boundary layer thickness which is related to the laminar momentum thickness as shown by:

$$\delta \approx 8.5\theta_l.$$

The Thwaites formula [37] as shown below can be used to evaluate the laminar momentum thickness:

$$\theta_l^2 = \frac{0.45}{u_e^6}\int_0^5 u_e^5 ds, \tag{1.3}$$

assuming that the velocity at the edge of the boundary layer, u_e, is the surface velocity that is calculated by the potential flow or the Euler equations.

The convective heat transfer coefficient is obtained by Smith and Spalding [37] considering that the boundary layer is still laminar at a surface distances from the stagnation point. The relation is as follows:

$$h_c = 0.296\frac{\lambda}{\sqrt{v}}\left[u^{-2.88}\int_0^s u_e^{1.88}ds\right], \tag{1.4}$$

where the thermal conductivity of air is designated as λ. Given that the boundary layer is turbulent at a surface distances from the stagnation point, the convective heat transfer coefficient can be obtained using the Stanton number as:

$$h_c = St\rho u_e c_p, \tag{1.5}$$

$$St = \frac{c_f/2}{P_{rt} + \sqrt{c_f/2\left(1/St_k\right)}}, \tag{1.6}$$

where the turbulent Prandtl number is given by P_{rt} = 0.9 and the roughness Stanton number [38] is given by St_k defined as:

$$St_k = 1.156\left[\frac{u_\tau k_s}{v}\right]^{-0.2}, \tag{1.7}$$

where shear velocity is given as:

$$u_\tau = u_e\sqrt{c_f/2}, \tag{1.8}$$

and skin friction coefficient is given as:

$$c_f/2 = \frac{0.168}{\left[\ln\left(864\frac{\theta_t}{k_s}\right)\right]^2}, \tag{1.9}$$

Using the formula below, the turbulent momentum thickness can be evaluated:

$$\theta_t = \left[\theta\frac{0.0156}{u_e^{4.11}}\int_{s_{tran}}^{s} u_e^{3.86}ds\right]^{0.8} + \theta_l\left(s_{tran}\right). \tag{1.10}$$

Here, $\theta_l\left(s_{tran}\right)$ given by equation (1.3) must be added since initially, the laminar boundary layer exists, the turbulent boundary layer begins at the transition point, $s = s_{tran}$, and the laminar momentum thickness is already existing.

The second step in the ice simulation process is computing impingement which is required to predict the amount (total collection efficiency, β_{TOT}), the distribution (local collection efficiency, β) and the limits (impingement limits) of the water that impacts the aerodynamic body. The ratio of the actual mass of impinging water to the maximum value that would occur if the droplets followed straight-line trajectories, as seen in Figure 1-12, defines the total collection efficiency.

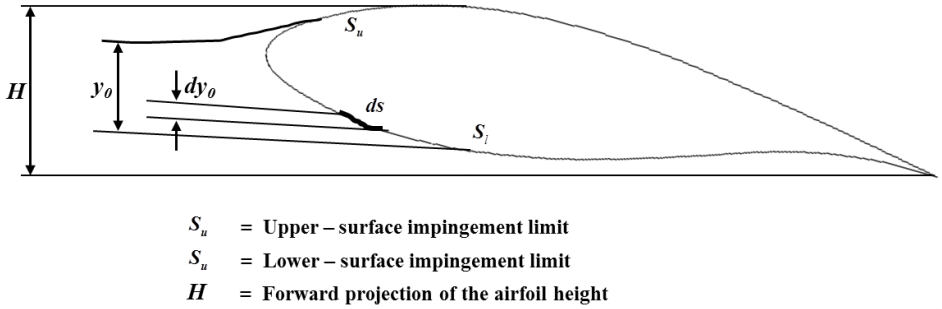

S_u = Upper – surface impingement limit
S_u = Lower – surface impingement limit
H = Forward projection of the airfoil height

Figure 1-12 Total and local droplet collection efficiency definition by LEWICE

The equation for the total collection efficiency is as follow:

$$\beta_{TOT} = \frac{y_0}{H}. \tag{1.11}$$

In the given equation above, y_o is the vertical distance between the droplet release points of the upper and lower surface tangent trajectories. On the other hand, the local collection efficiency β can be written as:

$$\beta = \frac{dy_0}{ds}. \tag{1.12}$$

The previous equation is related to the total collection efficiency, which can be given as:

$$\beta_{TOT} = \frac{1}{H}\int_{S_l}^{S_u} \beta ds. \tag{1.13}$$

where s_u and s_l are the upper and the lower surface impingement limits, respectively. The solution of a partial differential equation representing the force balance on the droplet is the droplet trajectory, where the forces involved are inertia, drag, buoyancy and gravitational

forces. Analysis of the motion of a particle as a point mass particle is acted on by the flow field. The fundamental assumptions for all methods are:

- The influence of water droplets on the flow field can be disregarded;
- There is no grazing collisions, bouncing, splashing, coalescence, breakup, and droplet eccentricity.

The droplet size and the liquid water content of the cloud are important factors in which the former could influence the balance between inertia and drag forces. Droplets that are small will mostly follow the flow streamlines until impact while those that are large are less affected by the flow field and most likely follow their own inertia before impact.

The thermodynamic model proposed by Messinger [39] which satisfies the first law of thermodynamics is usually used in ice accretion models. Generally, a control volume approach is used, in which the control volume extends from the surface of the body to the water film /air interface.

The mass and energy equations can be described as follows,

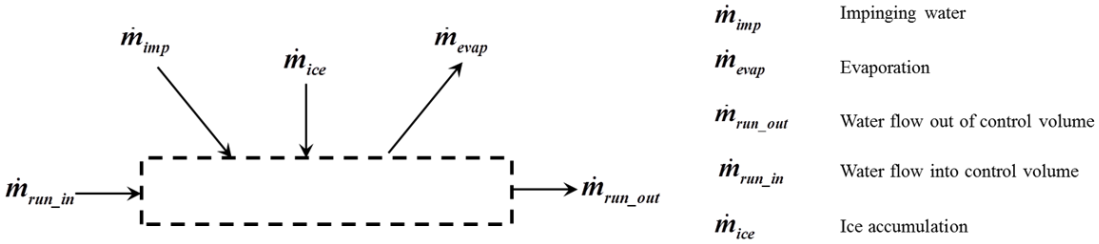

Figure 1-13 Mass balance for a control volume

Figure 1-13 shows all masses entering and leaving a control volume, which can be written as,

$$\dot{m}_{imp} + \dot{m}_{run\_in} - \dot{m}_{evap} - \dot{m}_{run\_out} = \dot{m}_{ice}. \tag{1.14}$$

In this method, it is assumed that there will be no water inflow $\left(\dot{m}_{run\_in} = 0.0\right)$ at stagnation point. Hence, the calculations start at the stagnation point of the surface and in the case of a 3D surface, stagnation line (or strip) is used. By using the known mass variables, an unknown term named as freezing fraction *f* is evaluated. The freezing fraction is a term which

defines the fraction of impinging liquid freezes in the given control volume. The total fraction of water freezes in a control volume can be written as,

$$f = \frac{\dot{m}_{ice}}{\dot{m}_{imp} + \dot{m}_{run\_in}}. \tag{1.15}$$

The value of freezing fraction varies from 0 to 1, the value of *f* set to be zero for no water freezes, and unity can be set for all water freezes. By substituting equation (1.15) into equation (1.14), the mass balance is as follows,

$$\dot{m}_{run\_out} = (1-f)\left(\dot{m}_{imp} + \dot{m}_{run\_in}\right) - \dot{m}_{evap}. \tag{1.16}$$

Next to the mass balance, it is necessary to solve energy balance which is based on the first law of thermodynamics. The same control volume approach as shown in Figure 1-14 is applicable for the energy balance which can be expressed as,

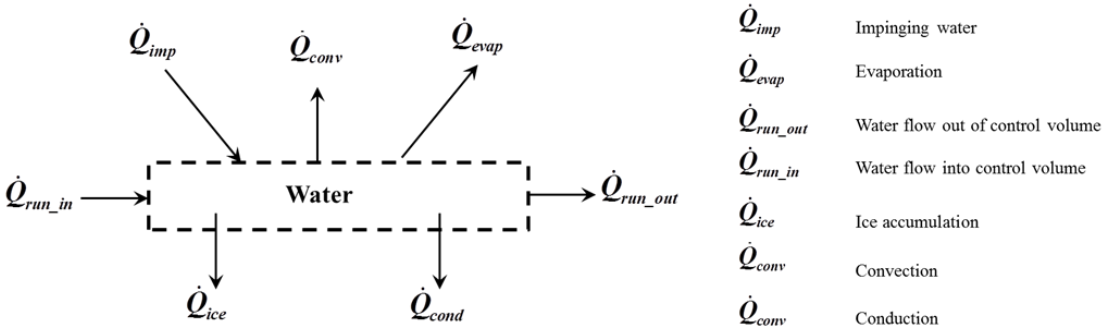

Figure 1-14 Energy balance for a control volume

$$\dot{Q}_{imp} + \dot{Q}_{run\_in} = \dot{Q}_{evap} + \dot{Q}_{run\_out} + \dot{Q}_{ice} + \dot{Q}_{conv} + \dot{Q}_{cond}. \tag{1.17}$$

Each term in the energy equation can be evaluated based on different methods, which results in the following equation:

$$\begin{aligned}
&\dot{m}_{imp}\left[C_{p,w}\left(T_{sur} - 273.15\right) + \frac{u_\infty^2}{2}\right] + \dot{m}_{run_in}\left[C_{p,w}\left(T_{sur(i-1)} - 273.15\right)\right] + \dot{Q}_{cond} = \\
&\dot{m}_{evap}\left[C_{p,w}\left(T_{sur} - 273.15\right) + L_v\right] + \left[(1-f)\left(\dot{m}_{imp} + \dot{m}_{run_in}\right) - \dot{m}_{evap}\right]C_{p,w}\left(T_{sur} - 273.15\right) \\
&+ f\left(\dot{m}_{imp} + \dot{m}_{run_in}\right)\left[C_{p,ice}\left(T_{sur} - 273.15\right) + L_f\right] + h_c\left[T_{sur} - T_e - \frac{r_c u_\infty^2}{2C_{p,a}}\right]\Delta S.
\end{aligned} \tag{1.18}$$

Where $C_{p,w}, C_{p,ice}$, and $C_{p,a}$ are the specific heat capacities of water, ice and air, respectively; h_c is the convective heat transfer coefficient, T_s, T_{sur}, T_e are the droplet, surface, and boundary layer temperatures, respectively; L_v, L_f are the latent heat of vaporization and the latent heat of fusion, respectively; r_c, u_e, u_∞ are the recovery factor, velocity at the edge of boundary layer and the free stream velocity, respectively.

1.6.2 ONERA

The linear potential flow equation or the Euler equations can be used to model inviscid air flow field in the ONERA [26] code which requires the creation of a volumetric C-grid. The former model uses a 3D panel method code (ECOPAN) with compressibility corrections up to Mach 0.5 (Prandtl-Glauert) while the latter model uses a 3D finite element method. Artificial viscosity and a multi-grid method are used to obtain stabilization and convergence acceleration, respectively.

The three-dimensional layer equations are calculated using a finite volume code in the ONERA code [26]. A finer grid is built, which is called the aerodynamic grid, to improve the boundary layer calculations where it was found that the "geometric" grid on which the inviscid flow calculations have been performed was too coarse and ONERA made the grid denser close to the flow singularities – the stagnation lines. With the same transition criterion as LEWICE given by equation (1.1), the local roughness Reynolds number detects the transition caused by roughness. However, the roughness model is different with LEWICE but uses the Van Driest formulation. The increase of the convective heat transfer is modeled by an increase of the smooth wall turbulent shear stress, which is expressed using the mixing length formulation:

$$\tau_t = \rho F^2 l_m^2 \left[\left(\frac{\partial u}{\partial y} \right)^2 + \left(\frac{\partial w}{\partial y} \right)^2 \right], \tag{1.19}$$

where the mixing length is defined by Michael et al. as:

$$l_m = \delta k_r \tanh\left(\frac{ky}{k_r \delta}\right), \tag{1.20}$$

with k_r and k equal to 0.085 and 0.41, respectively. Near a smooth wall, the turbulent damping factor, F, is:

$$F = 1 - \exp\left(\frac{l_m \sqrt{\tau\rho}}{26k\mu}\right). \tag{1.21}$$

By modifying F, the roughness effect can be simulated to reduce its damping effect and increase the turbulent shear stress. Below is the modification given by Van Driest roughness model,

$$F = 1 - \exp\left(\frac{l_m \sqrt{\tau\rho}}{26k\mu}\right) + \exp\left(\frac{60y}{26k_s}\right), \tag{1.22}$$

where the sand-grain roughness height is the same, given as k_s. The thermal structure of the boundary layer is obtained using the abovementioned roughness model and the convective heat transfer coefficient is defined as:

$$h_c = k\left(\frac{\partial T}{\partial y}\right)_{y=0} \Big/ \left(T_w - T_r\right), \tag{1.23}$$

where k is the thermal conductivity of air.

The ONERA code also built based on Lagrangian particle tracking method for droplets which is similar to LEWICE [25] approach. The only difference between LEWICE and ONERA in droplet impingement calculations is their force balance equation. Moreover, the LEWICE and the ONERA codes use similar approaches and equations to solve the ice accretion phenomenon but the differences can be observed in the evaporation model and the way these codes handle three-dimensional calculations.

Inside ONERA code [26], Jakob's formulation is used to define the evaporation term assuming that the saturation vapor pressure at the edge of the boundary layer is the same as at freestream:

$$\dot{m}_{evap} = \left(\frac{1}{Le}\right)^{2/3} \frac{h_c}{c_{p,a}} \frac{M_{m(water)}}{M_{m(air)}} \frac{T_\infty}{T} \frac{P_{v,p} - P_{v,\infty}}{P_\infty}, \tag{1.24}$$

where the mean temperature is equivalent to $\bar{T} = (T_{sur} + T_\infty)/2$.

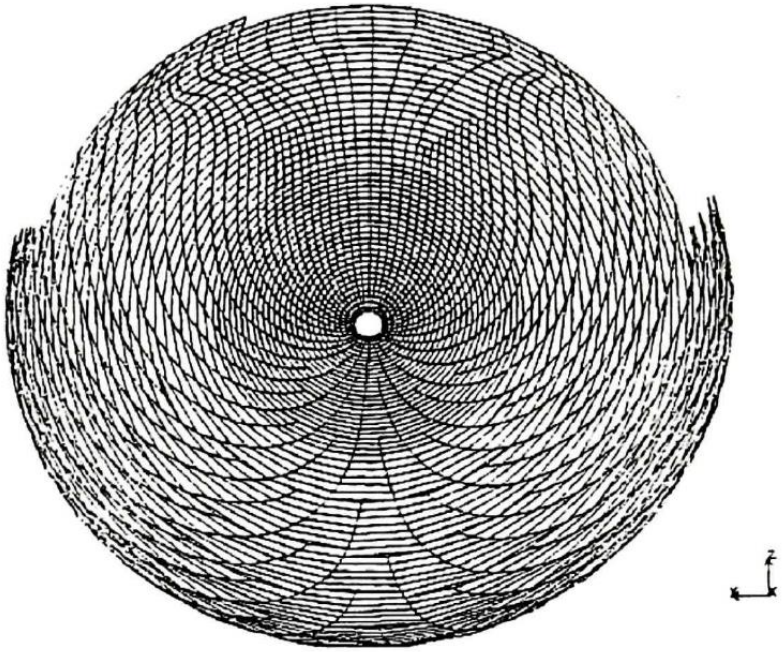

Figure 1-15 ONERA thermodynamic grid along the runback paths [26]

ONERA [26] generates a new body grid to simplify the thermodynamic balance along the runback paths. This grid is called the thermodynamic grid (Figure 1-15) built on the complete geometry. Since runback water occurs on surfaces in a three-dimensional icing model, calculation of runback paths is necessary to determine the location where the water will freeze. A study on an order of magnitude by Hedde et al. [26] revealed that the runback water closely follows the wall air streamlines for the usual speed of aircraft. The thermodynamic balance on the thermodynamic grid is nearly the same as that of a two-dimensional model. No runback across lateral grid edges occur in this new grid and the only

difference with a classical 2D ice accretion code is that one or more runback lines may disappear or appear to keep the cell size within a given range as seen in Figure 1-15.

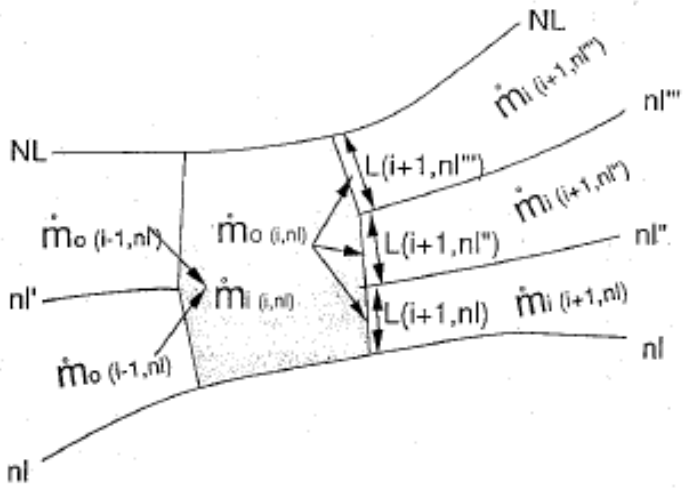

Figure 1-16 To maintain a quasiconstant cell width runback paths lines may disappear or appear in ONERA [26], running back water is mixed or split

The flow from two or more cells is mixed into one cell conserving heat and mass in case of the disappearance of one or more lines while the flow from one cell is split between the children cells in case of the appearance of one or more lines, where each child cell receives a flow proportional to the length of the edge common with the parent cell.

In both LEWICE and ONERA two kind of mesh is required, one is for body surface for panel methods, and a volumetric grid for Euler approach. Although the 2D panel methods are very fast and efficient for 2D, the CPU time increases considerably in 3D panel methods. Furthermore, the global compressibility corrections can be implemented until 0.5 Mach number while it is not possible to implement the local compressibility effects owing to the growth of ice horns. The viscous effects are considered indirectly into the model which may give an inaccurate representation in separated flows. These separations can modify the flow pattern considerably which may affect the convective heat transfer, and impingement calculations. The boundary layer codes used for evaluation of convective heat transfer have

difficulty in predicting the accurate convective heat transfer for high Reynolds numbers. Moreover, in ONERA code, another grid “aerodynamic grid” is necessary for the calculation of streamlines.

Further, the Lagrangian method used for the prediction of droplet impingement encounter major difficulties in solving complex geometries. The computation cost of particle tracking methods rapidly increases while applied for 3D droplet impingement. Finally, the ice accretion models used in LEWICE and ONERA are very efficient in 2D ice shape prediction. On the other hand, the 3D calculations are not really 3D, it is basically the 2D version of code applied on the streamlines of 3D geometry. Hence, the runback ice direction is predefined which may not consider the lateral runback mass flux.

1.6.3 FENSAP

The FENSAP [28, 40] approach is based on partial differential equations for the airflow, water droplet, and ice accretion. FENSAP air solver is a Finite Element based Navier-Stokes solver which can handle an inviscid and viscous, steady and unsteady, compressible airflow. This code is capable of solving both Low-Mach number and compressible flows within the same framework. An implicit weak-Galerkin finite element method and a Newton linearization of primate variable are used to solve the conservation equations and Spalart-Allmaras model. A segregated formulation which couples mass and momentum together, and then the energy and turbulence equations are solved to reduce the size of the linear system. A local time –stepping approach is used for steady calculation to improve the convergence while a second-order Gear scheme is used to evolve the flow in time for an unsteady calculation. An iterative approach, the Generalized Minimum Residual method (GMRES) with a diagonal preconditioner is used to solve the linear systems.

In order to account the wall roughness effects, a modified Spalart-Allmaras turbulence model is used. The roughness height is computed from the equations provide by LEWICE.

Moreover, minimum wall distance used in the Spallart-Allmaras is increased to account the surface roughness effect. This can be given as,

$$d = d_{\min} + 0.03K_s. \tag{1.25}$$

Here d_{min} is the minimum distance to the wall from the cell center (or node). A non-zero wall boundary condition is necessary for this extension. A second-order accurate method is employed to obtain wall convective heat fluxes. Since the ice accretion strongly depends on wall convective fluxes, these second order method is a better option.

Next, to the air solver, a droplet solver named as DROP3D is used by FENSAP. A Eulerian approach is used for solving the droplets in three-dimensional space. General droplet physical assumptions are used to model mass and momentum conservation equations. Source terms such as gravity, buoyancy, and droplet drag were considered in modeling. The discretization of droplet equations also follows the same approach as in FENSAP. Finally, the ice shape is determined by ICE3D solver which is based on shallow water icing model (SWIM). This ice solver model is PDE based Messinger model which represents mass and energy balance within the thin film of water. More details of FENSAP solvers are explained in Chapter 8.

Chapter 2. Eulerian-based Droplet Modeling

The computational method based on Lagrangian [24, 41, 42] or Eulerian [1, 43, 44] method is usually used for the droplet impingement prediction. Lagrangian droplet tracking method has some limitations, especially for cases in which complex geometries are involved. This method encounters difficulty in solving multi-element airfoils, non-axisymmetric models, and systems involving both external and internal flows. Furthermore, the computation of Lagrangian method is extremely expensive and complex for three-dimensional models. On the other hand, the Eulerian method is a wonderful option to overcome all these issues.

In Eulerian droplet method, a single pressure is shared by all phases, dispersed phase is considered as continuum, continuity and momentum equations are solved to predict the droplet distributions. Since the mass loading ratio of the bulk density of the droplets over the bulk density of air is in the order of 10^{-3} in air-droplet flows, the two-phase flow can be simulated using a weakly coupled (one-way coupling) algorithm. The air flow data should then be provided to the droplet solver through the source terms in case of the Eulerian droplet equations [44].

Generally, the droplet codes are built on the following assumptions:

- The droplets are spherical without deformation or breaking
- There is no collision, coalescence or splashing of droplets
- There is no heat and mass exchange between the droplets and the surrounding air
- The only forces acting on the droplets are due to air drag, gravity, and buoyancy

2.1 Shallow water-type droplet equations

A Eulerian based shallow water-type droplet equations (SWDE) [43, 45] are employed for the droplet solver. The conservative form of SWDE can be written as,

$$\boldsymbol{U}_t + \boldsymbol{F}_X + \boldsymbol{G}_Y + \boldsymbol{H}_Z = \boldsymbol{S}_D + \boldsymbol{S}_G + \boldsymbol{S}_S, \tag{2.1}$$

where,

$$\mathbf{U} = \begin{bmatrix} \rho \\ \rho u \\ \rho v \\ \rho w \end{bmatrix}, \mathbf{F} = \begin{bmatrix} \rho u \\ \rho u^2 + \rho g d \\ \rho u v \\ \rho u w \end{bmatrix}, \mathbf{G} = \begin{bmatrix} \rho v \\ \rho u v \\ \rho v^2 + \rho g d \\ \rho u w \end{bmatrix}, \mathbf{H} = \begin{bmatrix} \rho w \\ \rho u w \\ \rho v w \\ \rho w^2 + \rho g d \end{bmatrix}, \tag{2.2}$$

$$\mathbf{S}_D = \begin{bmatrix} 0 \\ A_u(u_g - u) \\ A_v(v_g - v) \\ A_w(w_g - w) \end{bmatrix}, \mathbf{S}_G = \rho g \begin{bmatrix} 0 \\ 0 \\ 0 \\ 1 - \rho_g / \rho_w \end{bmatrix}, \mathbf{S}_S = \begin{bmatrix} 0 \\ (\rho g d)_x \\ (\rho g d)_y \\ (\rho g d)_z \end{bmatrix}. \tag{2.3}$$

Here, ρ is the density of droplets in terms of liquid water content (LWC). Also u, v and w are the velocity components of x, y and z directions respectively. $\boldsymbol{S}_D$, $\boldsymbol{S}_G$ and $\boldsymbol{S}_S$ are the aerodynamic drag, gravity and buoyancy forces acting on the droplets, and added source terms, respectively. The $A_u(u_g\text{-}u)$, $A_v(v_g\text{-}v)$, and $A_w(w_g\text{-}w)$ denote the drag on droplets caused by the airflow, the term $1-\rho_g/\rho_w$ denotes the resultant force of the gravity and buoyancy of droplets. The density of air and water is given by ρ_g and ρ_w respectively. u_g, v_g and w_g are the velocities of gas in each direction, respectively; and g is the acceleration due to gravity. The coefficients $\boldsymbol{A}_{u,v,w}$ can be expressed as,

$$A_{u,v,w} = A_{\mathbf{u}} = 0.75\rho C_{D_{\mathbf{u}}} \operatorname{Re}_{\mathbf{u}} \mu / \rho_w d^2, \ \operatorname{Re}_{\mathbf{u}} = \rho_g . d . \left| \boldsymbol{u}_g - \boldsymbol{u} \right| / \mu, \tag{2.4}$$

where $Re_{\boldsymbol{u}}$ is the Reynolds number of droplets, μ is the dynamic viscosity of the gas, and C_D is the drag coefficients of the spherical droplets. The drag coefficient [46] can be derived as follows,

$$\mathrm{C}_{\mathrm{D}_{\mathbf{u}}} = \begin{cases} \dfrac{24}{\mathrm{Re}_{\mathbf{u}}}\left(1 + 0.0197\,\mathrm{Re}_{\mathbf{u}}^{0.63} + 2.6\mathrm{e}^{-4} \cdot \mathrm{Re}_{\mathbf{u}}^{1.38}\right) & \text{if} \quad \mathrm{Re}_{\mathbf{u}} < 1000, \\ 0.4 & \text{if} \quad \mathrm{Re}_{\mathbf{u}} \geq 1000. \end{cases} \tag{2.5}$$

2.1.1 Spatial discretization of SWDE

There are various numerical methods that are possible to use for solving shallow water based droplet equation. However, very few methods show positivity in preserving behavior around the shadow region where the density of droplets is very low. The HLLC approximate Riemann solver has shown good behavior in satisfying the positivity preservation. Therefore, HLLC approximate Riemann solver was adopted to solve the shallow water based droplet equation. The HLLC solver is a modification of the basic Harten-Lax-vanLeer scheme [47, 48], in which an intermediate wave is introduced with two distinct fluxes in star region. The structure of the HLLC scheme can be derived for a one-dimensional SWDE. The governing equations can be expressed as follows,

$$U=\begin{bmatrix}\rho\\ \rho u\\ \rho\psi\\ \rho\gamma\end{bmatrix}, A=\begin{bmatrix}\rho u\\ \rho u^2+\rho gd\\ \rho u\psi\\ \rho u\gamma\end{bmatrix}, Q=\begin{bmatrix}0\\ (\rho gd)_x\\ 0\\ 0\end{bmatrix}. \tag{2.6}$$

In equation (2.6), the x-split case with $\psi = v$ and $\gamma = w$ is included, which is the tangential velocity component; here $\psi(x,t)$ and $\gamma(x,t)$ represents the concentration of a pollutant or some other passive scalars. A middle Eigenvalue, $\lambda_2 = u$ is introduced by the quantity ψ and γ. The HLLC flux at the interface of left and right cells are expressed by equation (2.7),

$$\mathbf{A}_{i+\frac{1}{2}}=\begin{cases}\mathbf{A}_L & \text{if} \quad 0\le S_L \quad ,\\ \mathbf{A}_{*L} & \text{if} \quad S_L\le 0\le S_* \quad ,\\ \mathbf{A}_{*R} & \text{if} \quad S_*\le 0\le S_R \quad ,\\ \mathbf{A}_R & \text{if} \quad 0\ge S_R \quad ,\end{cases} \tag{2.7}$$

where,

$$\begin{aligned}\mathbf{A}_{*L}&=\mathbf{A}_L+S_L\left(\mathbf{U}_{*L}-\mathbf{U}_L\right),\\ \mathbf{A}_{*R}&=\mathbf{A}_R+S_R\left(\mathbf{U}_{*R}-\mathbf{U}_R\right).\end{aligned} \tag{2.8}$$

The states, U_{*L}, U_{*R} and the wave speeds S_L and S_R are expressed as,

$$\mathbf{U}_{*K} = \rho_k \left(\frac{S_K - u_K}{S_K - S_*} \right) \left[1, S_*, \psi_K, \gamma_K \right]^T , \tag{2.9}$$

where,

$$\begin{aligned} S_L &= u_L - a_L q_L , \\ S_R &= u_R + a_R q_R . \end{aligned} \tag{2.10}$$

Where $a_L = \sqrt{2\rho_L}$, $a_R = \sqrt{2\rho_R}$. To evaluate the middle wave speed, S_*, numerous methods were found in literature and an efficient way is considered in this study of which the expression is as follows,

$$S_* = \frac{S_L \rho_R \left(u_R - S_R \right) - S_R \rho_L \left(u_L - S_L \right)}{\rho_R \left(u_R - S_R \right) - \rho_L \left(u_L - S_L \right)}, \tag{2.11}$$

This wave speed estimation for S_* has the remarkable property of being exact when one of the data states is a dry bed state q_K is given as,

$$q_K = \begin{cases} \sqrt{\dfrac{0.5\left(\rho_* + \rho_K \right) \rho_*}{\rho_K^2}} & \text{if} \quad \rho_* > \rho_K , \\ 1 & \text{if} \quad \rho_* \le \rho_K , \end{cases} \tag{2.12}$$

where ρ_* is an estimate of the exact solution for ρ in the star region. The depth and particle velocity in the star region, ρ_* and u_* are derived as,

$$\begin{aligned} \rho_* &= \frac{1}{2}\left(\rho_L + \rho_R \right) - \frac{1}{4}\left(u_R - u_L \right) \frac{\rho_L + \rho_R}{a_L + a_R} , \\ u_* &= \frac{1}{2}\left(u_L + u_R \right) - \frac{1}{4}\left(\rho_R - \rho_L \right) \frac{a_L + a_R}{\rho_L + \rho_R} , \end{aligned} \tag{2.13}$$

The third component of the flux can be expressed in terms of the first component and the variable ψ, that is $\mathbf{A}^3 = \mathbf{A}^1 \psi$, where $\mathbf{A}^3$ is defined as follows,

$$\mathbf{A}^3_{i+\frac{1}{2}} = \begin{cases} \mathbf{A}^1_{i+\frac{1}{2}} \psi_L & \text{if} \quad u_* \ge 0, \\ \mathbf{A}^1_{i+\frac{1}{2}} \psi_R & \text{if} \quad u_* \le 0. \end{cases} \tag{2.14}$$

2.1.2 High order solution reconstruction

The piecewise linear reconstruction is employed to enhance the accuracy of the developed solver. The solution is assumed to be piecewise linearly distributed over the control volume. For a cell-centered scheme [49, 50], the left and right state can be found as follows,

$$\begin{aligned} U_R &= U_J + \Psi_I \left(\nabla U_I . \vec{r}_L\right), \\ U_L &= U_I + \Psi_J \left(\nabla U_J . \vec{r}_R\right), \end{aligned} \tag{2.15}$$

where Ψ denotes a limiter function and ∇U_I is the gradient of the conservative variable at U at the cell center **I**. The vector $\vec{r}$ point from the cell centroid to the face-midpoints is shown in Figure 2-1.

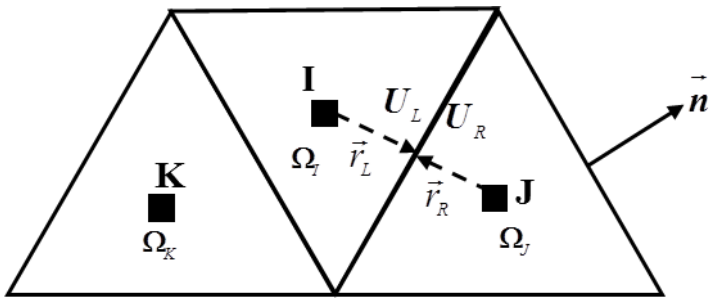

Figure 2-1 Cell-Centered scheme: Linear reconstruction

The gradient ∇U can be evaluated by the Green-Gauss approach, which approximates the gradient of scalars as the surface integral of the product of U with an outward pointing unit normal vector over some control volume Ω.

$$\nabla U \approx \frac{1}{\Omega} \int_{\partial\Omega} U . \vec{n} dS. \tag{2.16}$$

The integral form of the equation (2.16) can be expressed as,

$$\nabla U \approx \frac{1}{\Omega} \sum_{J=1}^{N_f} \frac{1}{2} \left(U_I + U_J\right) . \vec{n}_{IJ} \Delta S_{IJ}. \tag{2.17}$$

Here, N_f is the number of faces of the cell, ΔS_{IJ} is the total face area, and $\vec{n}_{IJ}$ is the average unit normal vector. The limiter function described by Venkatakrishna's limiter [51] is,

$$\Psi_I = \min_J \begin{cases} \dfrac{1}{\Delta_2}\left[\dfrac{\left(\Delta_{1,\max}^2 + \varepsilon^2\right)\Delta_2 + 2\Delta_2^2\Delta_{1,\max}}{\Delta_{1,\max}^2 + 2\Delta_2^2 + \Delta_{1,\max}\Delta_2 + \varepsilon^2}\right] & \text{if } \Delta_2 > 0, \\ \dfrac{1}{\Delta_2}\left[\dfrac{\left(\Delta_{1,\min}^2 + \varepsilon^2\right)\Delta_2 + 2\Delta_2^2\Delta_{1,\min}}{\Delta_{1,\min}^2 + 2\Delta_2^2 + \Delta_{1,\min}\Delta_2 + \varepsilon^2}\right] & \text{if } \Delta_2 < 0, \\ 1 & \text{if } \Delta_2 = 0, \end{cases} \tag{2.18}$$

where

$$\begin{aligned} \Delta_{1,\max} &= U_{\max} - U_I, \\ \Delta_{1,\min} &= U_{\min} - U_I. \end{aligned} \tag{2.19}$$

Here, U_{max} and U_{min} denotes the maximum/minimum values of all surrounding cells **J** and including the cell **I** itself. The limiting control parameter ε is given as,

$$\varepsilon^2 = \left(K\Delta h\right)^3. \tag{2.20}$$

Where K is a constant and Δh is the cube root of the volume of the control volume.

2.1.3 Finite volume formulation

In finite volume method, the numerical scheme applied to the integral form of the equations is utilized. In the preprocessing stage, the domain of solution is divided into small volumes named as grid cells. The grid generation is done such that, the whole domain is filled by the grid, there should be no free space between the grids, and there should be no overlapping between the grids. In finite volume method, both structured and unstructured grids can be easily formulated. The resulting grid is described by the coordinates x, y, z of the nodes and the cell indexes are essential for an unstructured grid. Unlike structured grids, the unstructured grid needs a very strong algorithm and data structure for easy access to the cell neighbors. The control volumes are defined to evaluate the integrals of the convective flux and the source term. It should be mentioned that the control volumes are based on the grids generated in preprocessing step. The complete set of the three-dimensional Eulerian droplet equations with the source terms can be written as,

$$\frac{\partial}{\partial t}\int_{\Omega}\mathbf{U}d\Omega+\oint_{\partial\Omega}\mathbf{F}dS=\int_{\Omega}(\mathbf{S}_D+\mathbf{S}_G+\mathbf{S}_S)d\Omega. \tag{2.21}$$

After applying the time derivatives for the conservative variables, we can write the equation (2.21) as follows,

$$\frac{\partial\mathbf{U}}{\partial t}=-\frac{1}{\Omega}\left[\oint_{\partial\Omega}\mathbf{F}dS-\int_{\Omega}(\mathbf{S}_D+\mathbf{S}_G+\mathbf{S}_S)d\Omega\right]. \tag{2.22}$$

The surface integral on the right-hand side of equation (2.22) is approximated by a sum of the fluxes crossing the faces of the control volume. In finite volume method, it is assumed that the flux is constant along the individual face of a cell and it is evaluated at the midpoint of the face. On the other hand, the source terms are assumed to be constant inside a control volume. Now the discretized form of the equation (2.22) can be written as,

$$\frac{d\mathbf{U}}{dt}=-\frac{1}{\Omega}\left[\sum_{k=1}^{N_f}\mathbf{F}_k\Delta S_k-(\mathbf{S}_D+\mathbf{S}_G)\Omega-gd\sum_{k=1}^{N_f}\rho_k\begin{pmatrix}0\\ \mathbf{n}_k\end{pmatrix}\Delta S_k\right]. \tag{2.23}$$

In order to solve the above discretized equation (2.23) numerically, the cell-centered scheme is employed including the location of the flow variables with respect to the computational grid. In equation (2.23), the left side is solved by HLLC approximation as explained in section 2.1.1 and the source terms at the right side of the equation (2.23) are calculated by the equations explained in section 2.1.

2.1.4 Temporal discretization of SWDE

In the present work, a method of lines is employed to discretize the governing equations separately for spatial and temporal. Since the Shallow water droplet equations are time dependent, an explicit multistage Runge-Kutta scheme [52] was employed for temporal discretization. In order to accelerate the steady-state solution, local time stepping scheme was used,

$$\mathbf{U}_I^{n+1}=\mathbf{U}_I^{(m)}=\mathbf{U}_I^{(0)}-\alpha_i\frac{\Delta t_I}{\Omega_I}\mathbf{R}_I^{(i-1)}. \tag{2.24}$$

In equation (2.24), α_i denotes the stage coefficients, $\mathbf{R}_I^i$ represents the residual evaluated with the solution $\mathbf{U}_I^n$ from the *i*-th stage. The time step Δt can be determined for a control volume Ω from the approximate relation,

$$\Delta t = \sigma \frac{\Omega}{(\Lambda)}, \tag{2.25}$$

Where,

$$\Lambda = \sum_{i=1}^{N_f} \left(|\vec{v}_i . \vec{n}_i| + c_i \right) \Delta S_i . \tag{2.26}$$

The CFL number and the coefficients for the five stages of the second-order upwind spatial discretization were followed as prescribed by the literature [49, 52].

2.1.5 Boundary condition for droplet solver

The boundary condition plays a very important role in the accuracy and convergence of any numerical simulations. In the case of SWDEs, special attention is necessary to impose the solid wall boundary condition. Generally, droplet solvers provide droplet distribution around the given geometry and it is necessary to know the collection efficiency. The collection efficiency is a non-dimensional to measure the potential of ice accretion, which is based on droplet volume fraction (α), the velocity, and the normal vector on the solid surface. It can be expressed as,

$$\beta = -\alpha \mathbf{u} \cdot \mathbf{n}. \tag{2.27}$$

Therefore, the setting of the solid surface condition is an important factor in the solution of droplet flow fields. In the present work, a permeable wall boundary condition [53, 54] is employed for the droplet impingement. This boundary condition works such that the droplets would collide once the projection of a normal vector on a solid surface and the droplet velocity in an adjacent cell on the solid surface is negative as shown in Figure 2-2.

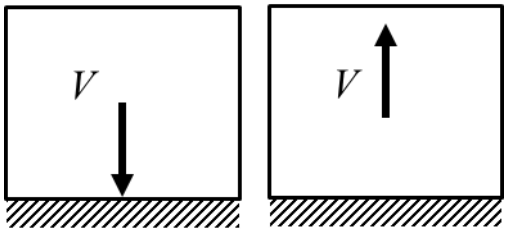

Figure 2-2 Wall boundary condition for droplet impingement

This behavior of droplets at the wall boundary can be implemented numerically as follows,

$$\begin{aligned} \vec{U}_{wall} &= \vec{U} \ \text{ if } \ V \cdot \vec{n} \le 0, \\ \vec{U}_{wall} &= 0 \ \text{ if } \ V \cdot \vec{n} \ge 0. \end{aligned} \tag{2.28}$$

2.2 Compressible Navier-Stokes air solver

The current computational methodology is based on one-way coupling model in which the air flow field data are needed to input into the droplet solver through the source terms. For this purpose, a well-known compressible Navier-Stokes equation is employed as,

$$\frac{\partial}{\partial t}\begin{bmatrix} \rho_g \\ \rho_g \boldsymbol{u}_g \\ E \end{bmatrix} + \nabla . \begin{bmatrix} \rho_g \boldsymbol{u}_g \\ \rho_g \boldsymbol{u}_g \boldsymbol{u}_g + p\boldsymbol{I} \\ (E+p)\boldsymbol{u}_g \end{bmatrix} = \nabla . \begin{bmatrix} 0 \\ \boldsymbol{\tau} \\ \boldsymbol{\tau} . \boldsymbol{u}_g + \boldsymbol{Q} \end{bmatrix}, \tag{2.29}$$

where,

$$\boldsymbol{\tau} = 2\mu \left[\nabla \mathbf{u}_g \right]^{(2)}, \ \mathbf{Q} = k \nabla T. \tag{2.30}$$

Here ρ_g, $\boldsymbol{u}_g$, p, and E represent the density, the velocity, the pressure, and the total energy of the air, respectively. The non-conserved variables $\boldsymbol{\tau}$ and $\boldsymbol{Q}$ denote the viscous shear stress tensor and the heat flux, respectively. The symbol $[\mathbf{A}]^{(2)}$ in the shear stress tensor stands for the traceless symmetric part of the tensor $\mathbf{A}$. The μ and k are the viscosity and thermal conductivity, respectively, and are dependent on the air temperature. For the air flow, the ideal equation of state $p = \rho g R T$ is used. The specific gas constant R can be written as,

$$R = c_p - c_v,$$

where

$$c_p = \frac{\gamma R}{\gamma - 1}, c_v = \frac{R}{\gamma - 1},$$

Now the ratio of specific heats γ can be define as,

$$\gamma = \frac{c_p}{c_v}.$$

It is necessary to include the effect of turbulence in ice accretion calculations. Hence, Reynolds Average Navier-Stokes equations are employed to determine the dynamic viscosity coefficient μ and the thermal conductivity coefficient k in equation (2.29) as,

$$\mu = \mu_L + \mu_T, \tag{2.31}$$

and,

$$k = k_L + K_T = c_p \left(\frac{\mu_L}{\mathrm{Pr}_L} + \frac{\mu_T}{\mathrm{Pr}_T} \right). \tag{2.32}$$

Where Pr_L and Pr_T is the laminar and turbulent Prandtl number, respectively. Generally, the Prandtl number is assumed to be constant over the flow field (Pr_T = 0.9 for air). Here, the turbulent eddy viscosity μ_T is unknown in equations (2.31) and (2.32). In order to predict the turbulent eddy viscosity, Spalart-Allmaras [55] one-equation model was employed. In this model, a transport equation is employed for an eddy-viscosity variable $\tilde{\nu}$. This model requires moderate grid resolution near the wall, fast convergence, and robust. Moreover, this method is compact and easily applicable in both structured and unstructured grids. The Spalart-Allmaras turbulence model can be written as,

$$\begin{aligned} \frac{\partial \tilde{\nu}}{\partial t} + \frac{\partial}{\partial x_j}\left(\tilde{\nu} \nu_j\right) &= C_{b1}\left(1 - f_{t2}\right)\tilde{S}\tilde{\nu} \\ &+ \frac{1}{\sigma}\left\{ \frac{\partial}{\partial x_j}\left[\left(\nu_L + \tilde{\nu}\right)\frac{\partial \tilde{\nu}}{\partial x_j} \right] + C_{b2}\frac{\partial \tilde{\nu}}{\partial x_j}\frac{\partial \tilde{\nu}}{\partial x_j} \right\} - \left(C_{w1} f_w\right), \end{aligned} \tag{2.33}$$

By solving equation (2.33), $\tilde{\nu}$ can be predicted and the turbulent eddy viscosity can be obtained as follows,

$$\mu_T = f_{v1}\rho\tilde{\nu}. \tag{2.34}$$

The production terms in equation (2.33) can be calculated as follows,

$$\begin{aligned} \tilde{S} &= f_{v3}S + \frac{\tilde{\nu}}{k^2 d^2} f_{v2}, \\ f_{v1} &= \frac{\chi^3}{\chi^3 + C_{v1}^3}, \; f_{v2} = \left(1 + \frac{\chi}{C_{v2}}\right)^{-3}, \\ f_{v3} &= \frac{\left(1 + \chi f_{v2}\right)}{\max\left(\chi, 0.001\right)}, \chi = \frac{\tilde{\nu}}{\nu_L}. \end{aligned} \tag{2.35}$$

Here *S* denoted the magnitude of the mean rotation rate,

$$S = \sqrt{2\Omega_{ij}\Omega_{ij}},$$

where Ω_{ij}, the rotation-rate tensor can be given as,

$$\Omega_{ij} = \frac{1}{2}\left(\partial v_i \partial x_j + \frac{\partial v_j}{\partial x_i}\right).$$

The destruction of eddy viscosity terms in equation (3.33) can be calculated as follows,

$$\begin{aligned} f_w &= g\left(\frac{1 + C_{w3}^6}{g^6 + C_{w3}^6}\right)^{\frac{1}{6}}, \\ g &= r + C_{w2}\left(r^6 - r\right), \\ r &= \frac{\tilde{\nu}}{\tilde{S}k^2 d^2}. \end{aligned} \tag{2.36}$$

Finally, the constants used in all the above equations are as follows,

$$\begin{aligned} &C_{b1} = 0.1355, C_{b2} = 0.622, \\ &C_{v1} = 7.1, C_{v2} = 5, \sigma = 2/3, k = 0.41, \\ &C_{w1} = C_{b1}/k^2 + \left(1 + C_{b2}\right)/\sigma, C_{w2} = 0.3, C_{w3} = 2, \\ &C_{t1} = 1, C_{t2} = 2, C_{t3} = 1.3, C_{t4} = 0.5. \end{aligned} \tag{2.37}$$

Furthermore, other turbulence models such as *K*-ε and *K*-ω SST two equation model was used in order to evaluate the heat flux and incorporate the roughness of the wall.

2.2.1 Discretization for convective flux

The numerical scheme is based on cell-centred finite volume method with Roe's flux-difference splitting method. Roe's approximate solver [56] has the capability to work in both cell-centered and dual control volume scheme framework. The flux across each face *c* of a control volume face can be expressed as,

$$F_c = \frac{1}{2}\left[F\left(U_R\right) + F\left(U_L\right) - \left|\overline{A}_{Roe}\right|\left(U_R - U_L\right)\right]. \tag{2.38}$$

In equation (2.38) U_R and U_L are the dependent variable vectors evaluated at the left and right state of face c, respectively, $F\left(U_R\right)$ and $F\left(U_L\right)$ are the flux vectors evaluated using the dependent variable vectors is depicted in Figure 2-1. The matrix $\overline{A}_{Roe}$ can be constructed from the flux Jacobian and it can be expressed as,

$$\left|\overline{A}_{Roe}\right| = \overline{R}\overline{\Lambda}\overline{L}. \tag{2.39}$$

In equation $\overline{R}$ and $\overline{L}$ are the right and left eigenvector matrices, respectively and $\overline{\Lambda}$ is a diagonal matrix with the absolute values of the Eigenvalues. In equation (2.38), the product of $\overline{A}_{Roe}$ and the difference between right and left state can be expressed as,

$$\left|\overline{A}_{Roe}\right|\left(W_R - W_L\right) = \left|\Delta F_1\right| + \left|\Delta F_{1,2,3}\right| + \left|\Delta F_5\right|. \tag{2.40}$$

Here, $\left|\Delta F_1\right|$, $\left|\Delta F_{1,2,3}\right|$, and $\left|\Delta F_5\right|$ are the flux components of governing equations. By using the Roe averaged variable, the jump condition can be evaluated.

2.2.2 Discretization for viscous flux

Generally, the diffusive flux is evaluated from the flow quantities and its first derivatives at the face of the control volume. The control volume is chosen to be same in both convective and diffusive flux to obtain a consistent spatial discretization. The viscous fluxes are elliptic in nature, which requires a simple average of quantities at the face of control volume. For a cell-centered scheme, the values at the face of the control volume can be given as,

$$U_{IJ} = \frac{1}{2}\left(U_I + U_J\right), \tag{2.41}$$

here, U is the flow variables, and the first derivatives essential for the prediction of viscous flux is calculated by Green's theorem at the cell center. The Green-Gauss approach approximates the gradient of some scalar function U as the surface integral of the product of U with an outward pointing unit normal vector over some control volume, which can be written as follows,

$$\nabla U \approx \frac{1}{\Omega}\int_{\partial\Omega} U\vec{n}dS, \tag{2.42}$$

For a cell-centered scheme, the Green-Gauss method can be written as,

$$\nabla U_I \approx \frac{1}{\Omega}\sum_{J=1}^{N_f}\frac{1}{2}\left(U_I + U_J\right)\vec{n}_{IJ}\Delta S_{IJ}, \tag{2.43}$$

Finally, the gradients also average to predict the quantity at the face of the control volume. The simple average may bring unbalanced weights due to the unstructured nature of the grid. Hence, a modified average is used in the current simulations, which can be written as,

$$\nabla U_{IJ} = \overline{\nabla U}_{IJ} - \left[\overline{\nabla U}_{IJ}.\vec{t}_{IJ} - \left(\frac{\partial U}{\partial \ell}\right)_{IJ}\right]\vec{t}_{IJ}, \tag{2.44}$$

where,

$$\left(\frac{\partial U}{\partial l}\right)_{IJ} \approx U_J - U_I \ell_{IJ}, \qquad \vec{t}_{IJ} = \frac{\vec{r}_{IJ}}{\ell_{IJ}}.$$

Here, ℓ_{IJ} denotes the distance between the cell-centroids of the cell I and J as shown in Figure 2-3 and the unit vector along the line connecting I and J is given by $\vec{t}_{IJ}$. Finally, the average gradient $\overline{\nabla U}_{IJ}$ at the face of control volume is given as,

$$\overline{\nabla U}_{IJ} = \frac{1}{2}\left[\nabla U_I + \nabla U_J\right]. \tag{2.45}$$

The modified equation (2.44) leads to strongly coupled stencils on unstructured grids.

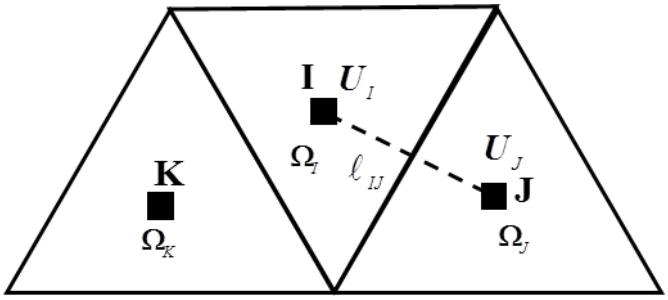

Figure 2-3 Stencil for the gradient computation for cell-centered scheme

2.2.3 Temporal discretization of Navier-Stokes equations

Similar to droplet solver, the air solver governing equations are also solved through the method of lines. As the compressible Navier-Stokes equations are time-dependent, an explicit multi-stage Runge-Kutta scheme [49] was employed. In order to accelerate the steady-state solution, local time stepping scheme was used,

$$\mathbf{U}_I^{n+1} = \mathbf{U}_I^{(m)} = \mathbf{U}_I^{(0)} - \alpha_i \frac{\Delta t_I}{\Omega_I} \mathbf{R}_I^{(i-1)}. \tag{2.46}$$

In equation (2.46), α_i denotes the stage coefficients, $\mathbf{R}_I^i$ represents the residual evaluated with the solution $\mathbf{U}_I^n$ from the *i*-th stage. The time step Δt can be determined for a control volume Ω from the approximate relation,

$$\Delta t = \sigma \frac{\Omega}{\left(\Lambda_c + C\Lambda_v\right)}, \tag{2.47}$$

where Λ_c and Λ_v are the spectral radii of convective and viscous flux respectively. The constant C is usually set as $1 \le C \ge 4$ for cell-centered schemes.

$$\Lambda_c = \sum_{i=1}^{N_f} \left(\left| \vec{v}_i . \vec{n}_i \right| + c_i \right) \Delta S_i,$$

$$\Lambda_v = \max\left(\frac{4}{3\rho}, \frac{\gamma}{\rho} \right) \left(\frac{\mu_L}{\mathrm{Pr}_L} + \frac{\mu_T}{\mathrm{Pr}_T} \right) \frac{\left(\Delta S\right)^2}{\Omega}.$$

2.2.4 Boundary conditions for air solver

In any numerical simulations, boundary condition has its effect in convergence, stability, and accuracy of the solution. Hence modeling boundary is very important and slightly complicated due to the truncation of the real physical domain. The boundary conditions applied for the current Navier-Stokes equations are as follows,

2.2.4.1 Solid surface

In the present work, the no-slip boundary condition is applied to the solid surfaces, in which the relative velocity between the surface and the fluid directly at the surface is assumed to be zero. The velocity components can be given as,

$$u = v = w = 0. \tag{2.48}$$

In order to implement the no-slip boundary condition, dummy cells can be utilized for simplification purpose. Dummy cells are often used in numerical boundary implementations to simplify the computations of fluxes, gradients, etc. The dummy cells can be implemented by extending the stencil of the spatial discretization scheme beyond the physical boundaries as shown in Figure 2-4.

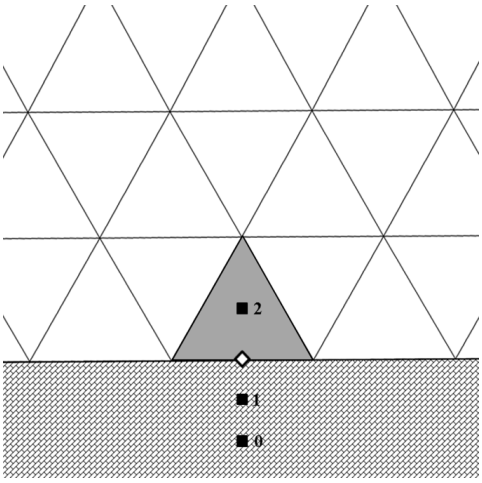

Figure 2-4 Solid surface boundary condition for cell-centered scheme. Dummy cells are denoted as 0 and 1. The diamond symbol shows the location where convective fluxes are evaluated.

In case of an adiabatic wall, primitive variables can be set as follows,

$$\begin{aligned} &\rho_1 = \rho_2, \quad E_1 = E_2, \\ &u_1 = -u_2, \quad v_1 = -v_2, \quad w_1 = -w_2. \end{aligned} \tag{2.49}$$

In the same way, the cells 0 and 3 are implemented. The properties such as total energy and density are evaluated by extrapolation. Moreover, this method can be applied to both structured and unstructured grids.

2.2.4.2 Far-field

In many of the ice accretion predictions, the numerical simulations on external flow over models such as a wing, aircraft, and other configurations have to be conducted within a bounded domain. In order to implement an accurate and efficient far-field, attention should be given such that the truncated domain should not affect the flow solution and the outgoing disturbance must not reflect back to the flow.

Generally, two flow situations are possible at the far-field boundary of which the flow can either leave or enter the domain, as shown in Figure 2-5. Moreover, since the flow classification depends on Mach number, four different kinds of far-field boundary conditions are possible: supersonic inflow, supersonic outflow, subsonic inflow, and subsonic outflow.

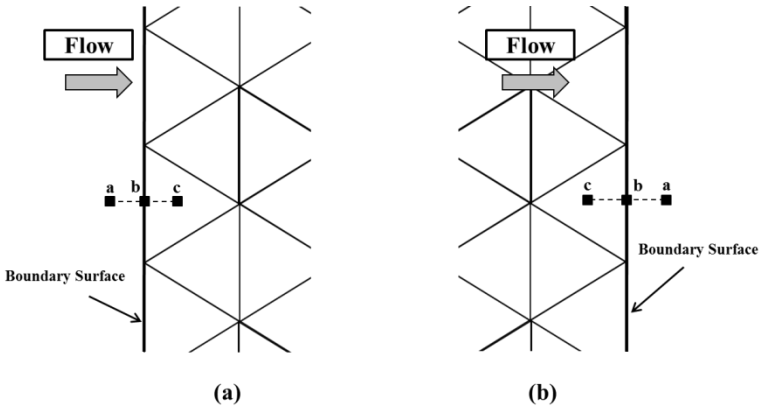

Figure 2-5 Far-field boundary for inflow (a) and outflow (b) situations. Position a, b, and c denotes the outside, boundary, and inside (interior) of the domain.

a. Supersonic inflow

In the case of supersonic flows, all the Eigenvalues have the same sign. Hence, in supersonic inflow implementation, the free stream values are used to compute the conservative variable on the boundary. Thus,

$$\boldsymbol{U}_b = \boldsymbol{U}_a. \tag{2.50}$$

b. Supersonic outflow

For supersonic outflow, all the Eigenvalues also have the same sign. Since the flow is leaving the physical domain, the conservative variables at the boundary are evaluated from the solution inside the domain. This can be written as,

$$\boldsymbol{U}_b = \boldsymbol{U}_c. \tag{2.51}$$

Generally, extrapolation methods are used to determine the boundary conservative values and care should be taken in choosing the extrapolation methods as they could affect the stability of the solution scheme.

c. Subsonic inflow

The characteristics of subsonic flow are different, in which four characteristics enter and one leaves the physical domain. Hence, one characteristic variable can be extrapolated from the inside of the domain and other four have to be evaluated from free-stream values. Accordingly, the boundary condition can be written as,

$$\begin{aligned}
p_b &= \frac{1}{2}\left\{ p_a + p_c - \rho_0 c_0 \left[n_x \left(u_a - u_c \right) + n_y \left(v_a - v_c \right) + n_z \left(w_a - w_c \right) \right] \right\}, \\
\rho_b &= \rho_a + \left(p_b + p_a \right) / c_0^2 , \\
u_b &= u_a - n_x \left(p_a - p_b \right) / \left(\rho_0 c_0 \right), \\
v_b &= v_a - n_y \left(p_a - p_b \right) / \left(\rho_0 c_0 \right), \\
w_b &= w_a - n_z \left(p_a - p_b \right) / \left(\rho_0 c_0 \right).
\end{aligned} \tag{2.52}$$

In equation (2.52), ρ_0 and c_0 denote the reference properties which can be set equal to the state at the interior point adjacent to the boundary.

d. Subsonic outflow

In contrast to subsonic inflow, four flow variables have to be extrapolated from the interior of the domain in case of subsonic outflow. Finally, one variable must be specified from outside of the physical domain. In general, the density and three velocity components are extrapolated from the interior and the static pressure is given externally. The boundary condition variables can be evaluated as follows,

$$\begin{aligned} p_b &= p_a, \\ \rho_b &= \rho_c + \left(p_c + p_d\right)/c_0^2, \\ u_b &= u_c + n_x\left(p_c - p_b\right)/\left(\rho_0 c_0\right), \\ v_b &= v_c + n_y\left(p_c - p_b\right)/\left(\rho_0 c_0\right), \\ w_b &= w_c + n_z\left(p_c - p_b\right)/\left(\rho_0 c_0\right). \end{aligned} \tag{2.53}$$

The necessary properties of the dummy cells can be extrapolated from the interior of the domain.

2.2.4.3 Symmetry

Symmetry is an essential boundary condition in order to reduce the computation time in case of the flow which is symmetrical with respect to a line or a plane. The numerical implementation must guarantee that there is no flux across the boundary. Further, the gradient of scalar quantity normal to the boundary, gradient of the tangential velocity normal to the boundary, and gradient of the normal velocity along the boundary should be eliminated. These conditions can be written as,

$$\begin{aligned} \vec{n}.\vec{\nabla}U &= 0, \\ \vec{n}.\vec{\nabla}\left(\vec{v}.\vec{t}\right) &= 0, \\ \vec{t}.\vec{\nabla}\left(\vec{v}.\vec{n}\right) &= 0, \end{aligned} \tag{2.54}$$

where, U denotes scalar variable, and $\vec{t}$ denotes the vector tangential to the symmetry line or plane.

Chapter 3. Supercooled Large Droplet Modeling

In atmospheric conditions, the droplet size may be 40 to 600 micrometers or more, which is known as a supercooled large droplet (SLD) [54, 57-59] Their large size leads to faster ice accretion, decreased performance due to reduction in lift, changes in stall angle of attack, and increases in drag dramatically [4, 5]. Numerical simulation results of droplet impingement intensity including and excluding SLD effects are mostly different for same flow properties and median volume diameter (MVD). Since the subsequent assumptions are no longer valid for SLD condition: the droplets are spherical without deformation or breaking; there is no collision, coalescence or splashing of droplets; there is no heat and mass exchange between the droplets and the surrounding air; the turbulence effects on the droplets are negligible; and the only forces acting on the droplets are due to air drag, gravity, and buoyancy. After the fatal crash of an ATR-72 commuter aircraft near Roselawn, Indiana in 1994, SLD were recognized as extremely hazardous. In recent years, appendix O is added in icing certification regulations in order to make sure that the aircraft is safe under SLD atmospheric icing conditions.

For instance, Cliff et al. [60] proposed a semi-empirical method to describe the physics of a liquid drop surrounded by air. Several studies based on the Eulerian approach have also been proposed to model the SLD effects. Honsek et al. [61] proposed a Eulerian model by considering SLD effects such as droplet deformation and breakup, and droplet wall interactions. Iuliano et al. [62] developed another Eulerian model for an aircraft icing simulation by considering three types of splash and rebound mechanism for droplet-wall interactions. In order to estimate the splashing mass loss, Sabri et al. [63] also proposed a splash parameter for the impingement efficiency factor. Further, Rendall and Allen [64] developed an implicit method for air-mixed droplet flow with finite-volume representation in a Lagrangian icing simulation.

The Appendix O consists of two parts: the first part defines a description of supercooled large drop icing conditions in which the drop MVD is less than or greater than 40 μm, the maximum mean effective drop diameter (MED) of Appendix C of this part continuous maximum (stratiform clouds) icing conditions. In this Appendix, supercooled large drop icing conditions consist of freezing drizzle and freezing rain occurring in and/or below stratiform clouds; while the second part defines ice accretions used to show compliance with the airplane performance and handling qualities requirements.

3.1 SLD effects on droplets

Due to large MVDs, the behavior of the droplets is different in SLD conditions. The first important SLD effect is the droplet deformation, the droplet deforms due to the aerodynamic shear force around the droplet. The deformed droplet is not a sphere in shape anymore and the droplet drag needs to be evaluated by considering this deformation. Next, to droplet deformation, droplet wall interaction is an important SLD effect. Since the droplet is large, the droplet might splash, rebound, spread or stick as a result of its impact on the surface [60]. Unless conventional droplets, more wall interactions are possible in large droplets which need to be included in the modeling. Droplet breaking is also possible in case of large droplets along with the terminal velocity effects. Droplet breaking is a result of a large shear force acting on the droplet and the terminal velocity is the effect in large droplets due to its high mass. Due to the terminal velocity effects, the droplets take their own path rather than following the air flow field as conventional droplets do.

3.2 Droplet wall interaction

Droplet wall interaction is a significant SLD effect which alters the impingement limit and ice accretion location. Wall interactions [65] such as splashing, rebound, stick, and

spread are considered in the present work. Figure 3-1 shows the pictorial explanation of the possible droplet wall interactions.

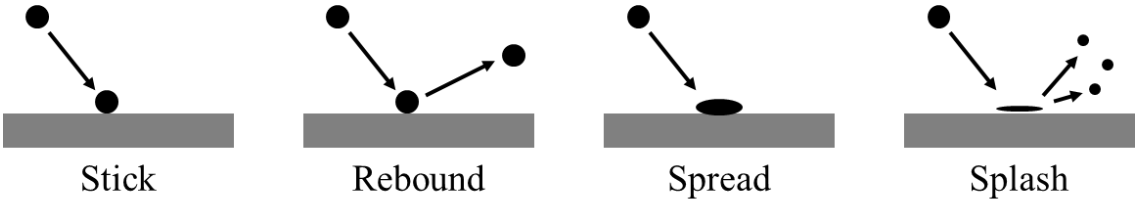

Figure 3-1 Droplet wall interactions

Among the four types of wall interactions, stick and spread are easy to model and special numerical implementations are not necessary. On the other hand, the other two types of wall interactions need special attention and in the following sections, most appropriate models available for these two types are described.

3.2.1 Splashing

The splashing effect is the most important effect specific for SLD's which usually parameterized by the Weber number (*We*) and Reynold's number (*Re*), or by a combination of both – the Ohnesorge number (*Oh*), that is similar to the Laplace number (*La*) defined as:

$$We = \rho_g . V^2 . MVD / \sigma , \; La = Re^2 / We,$$
$$Oh \equiv \frac{1}{La} \equiv \frac{We}{\mathrm{Re}} \equiv \frac{\mu_g}{\sqrt{\rho_g \sigma MVD}}, \tag{3.1}$$

Splashing is usually characterized by a combination of Weber and Ohnesorge and the two widely used combinations are the Cossali splashing parameter defined as [66],

$$K = Oh^{2/5} We. \tag{3.2}$$

Yarin and Weiss [67] splashing parameter which is similar to the former parameter,

$$K_y = \Lambda^{-3/8} \left(Oh^{2/5} We \right)^{5/16},$$
$$= \left[\frac{3}{2} \left(\frac{LWC}{\rho_w} \right)^{1/3} \right]^{-3/8} \left(Oh^{2/5} We \right)^{5/16}, \tag{3.3}$$

where Λ is the droplet frequency used to measure film thickness. In both combinations, a larger diameter increases the parameter leading to a higher probability of a splashing event as seen with SLD. Furthermore, both determined a critical value of splashing parameter and higher value than this critical level leads to a splashing event. The critical value of the former parameter is determined as a function of film thickness which is mostly unknown in a numerical simulation while the latter parameter is found to be a constant as shown below

$$K_{y,crit} = 17. \tag{3.4}$$

3.2.1.1 Trujillo model

A complete model for the numerical simulation of splashing events requires not only the critical values for splashing but also the number, size, direction, and velocity of the secondary droplets. Trujillo et al. [68] was one of the first papers that attempted to model these parameters which were intended for fuel injection sprays and statistically analyzed several impingement experiments.

Trujillo et al. [68] used the splashing parameter from the work of Cossali, equation (3.2) of which an empirical relation for its critical value was determined from the data by Stow and Hadfield [69] and Mundo et al. [70] The impinging droplet will splash when the splashing parameter *K* exceeds this critical value which is only valid for dry surface conditions and this relation is a function of surface roughness *Rs*:

$$K_{c,dry} = 180\left(Rs/MVD\right)^{-0.35}. \tag{3.5}$$

$K_{c,spray}$ is estimated by the data from Yarin and Weiss in order to account the wetting of the surface from previous droplet impacts assuming that the ratio *K* remains constant for varying surface *Rs*:

$$\frac{K_{c,spray}}{K_{c,dry}} = k \approx 3.0. \tag{3.6}$$

A linear correlation between the kinetic energy and the number of secondary droplets was reported by Stow and Stainer [71] which is extended using the experimental data from Trujillo et al. and obtained a relation between the Cossali splashing parameter K and the number of secondary droplets. The parameter $K_{c,dry}$ contains any influence from surface roughness:

$$N = \frac{1}{22}\left[0.0437\left(K\left(\frac{|\boldsymbol{V}_0|}{\boldsymbol{V}_0 \bullet \boldsymbol{n}}\right)^2 - K_{c,dry}\right) - 44.92\right]. \tag{3.7}$$

Here $\boldsymbol{V}_0$ is the velocity vector of the incoming droplet and $\boldsymbol{n}$ is the normal vector. In addition, the number of secondary droplets is dependent on the incident angle of the incoming droplet:

$$\theta_0 = \arcsin\left(\frac{\boldsymbol{V}_0 \bullet \boldsymbol{n}}{|\boldsymbol{V}_0|}\right). \tag{3.8}$$

A linear relation of the number of secondary droplets with the splashing parameter is attained if the incident angle is constant. A relation for the mean tangential velocity and mean normal velocity can be obtained with the application of a Gaussian distribution to the data from Mundo et al.:

$$\begin{aligned} u_{t,s} &= u_{t,0}\left(0.85 + 0.0025\theta_0\right), \\ u_{n,s} &= -u_{n,0}\left(0.12 + 0.0020\theta_0\right). \end{aligned} \tag{3.9}$$

Here $u_{t,s}$ $u_{n,s}$ are tangential and normal velocity components of post-impact velocities, respectively and $u_{n,0}$ $u_{t,0}$ are normal and tangential velocity component of impact velocity of droplets, respectively. θ_0 is the angle of incidence of the droplet. In equation (3.9), the angle of incidence is restricted between 4 and 65 degrees.

A relation for the amount of splashed mass is determined from the work of Yarin and Weiss which is expressed as the mass loss ratio $f_m = m_s / m_0$ and the splashing parameters are converted to Cossali's splashing parameter for convenience:

$$f_m = \frac{m_s}{m_0} = 0.8\left\{1-\exp\left[-0.85\left(K_y - K_{y,crit}\right)\right]\right\} \\ = 0.8\left\{1-\exp\left[-0.85\left(\Lambda^{-3/8}K^{5/16} - \Lambda^{-3/8}K_{c,spray}^{5/16}\right)\right]\right\}. \quad (3.10)$$

The local catching efficiency for the amount of water that moves away from the surface resulting from splashing can be corrected using the mass loss coefficient. The trajectory of the secondary droplets can be calculated using the velocity of the secondary droplets. It should be mention that the mass loss increases very rapidly to an asymptote of 0.8 in Trujillo model.

3.2.1.2 Habashi model

The over-prediction of mass loss is addressed by Honsek et al. [61] which is commonly known as the Habashi model by calibrating Trujillo's mass loss function to SLD conditions. This results in an equation very similar to equation (3.10) which replaces the constant 0.8 by $3.8/\sqrt{K_y}$:

$$f_m = \frac{m_s}{m_0} = \left(\frac{3.8}{\sqrt{K_y}}\right)\left\{1-\exp\left[-0.85\left(K_y - K_{y,crit}\right)\right]\right\}, \\ = 3.8\Lambda^{3/16}K^{-5/32}\left\{1-\exp\left[-0.85\Lambda^{-3/8}\left(K^{5/16} - K_c^{5/16}\right)\right]\right\}. \quad (3.11)$$

Here, $\sqrt{K_y}$ ensures that for increasing splashing parameter K_y, the mass loss decreases from 0.8 asymptotes. Taking in consideration that for $K_y > 23$, the mass loss equation can estimate within 1 per cent by:

$$f_m = \frac{m_s}{m_0} \approx \left(\frac{3.8}{\sqrt{K_y}}\right) = 3.8\Lambda^{3/16}K^{-5/32} : K_y > 23. \quad (3.12)$$

3.2.3 Rebound

Next, to splashing, rebound is an SLD effect strongly related to splashing which resulted in a single secondary droplet moving away from the surface without depositing mass and takes place mostly near the impingement limits with the effect of moving the impingement limits further upstream that reduces the impingement area.

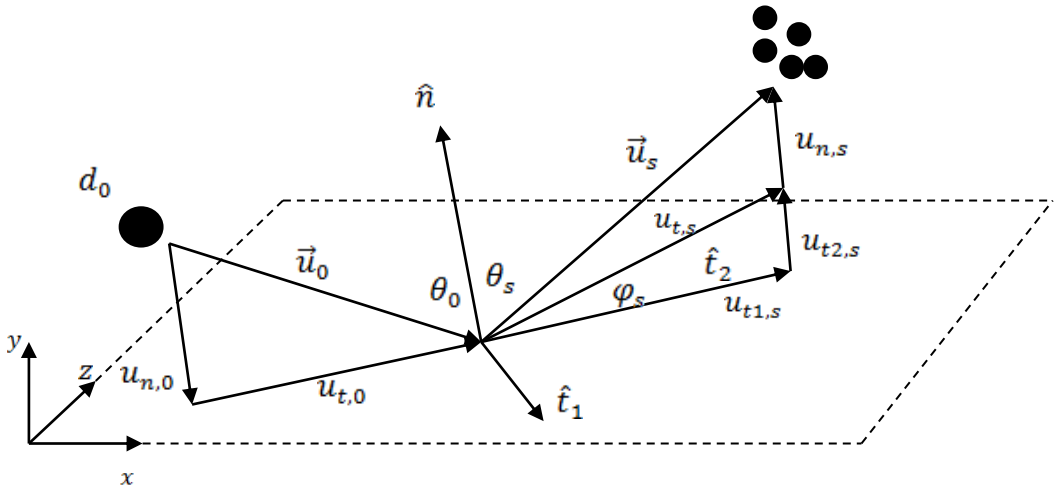

Figure 3-2 Droplet splashing and rebound velocity components

3.2.3.1 Bai and Gosman model

The model by Bai and Gosman [72] was used to derive the rebound model which is taken from the implementation of Honsek et al. [61] Weber number is used to define a splashing threshold. A minimum and maximum value was determined from experiments where the maximum value depends on the Laplace- or Ohnesorge- number:

$$10 \le We \le 1320 La^{-0.18} = 1320 Oh^{0.36}. \tag{3.13}$$

The relations for the secondary velocity were also determined by Bai and Gosman similar to relations for the velocities of a splashing droplet described in equation (3.9) taking into account that the tangential velocity does not depend on the incidence angle:

$$u_{t,s} = \frac{5}{7} u_{t,0}, \tag{3.14}$$

$$u_{n,s} = -u_{n,0}\left[0.9930 - 0.0307\left(90^0 - \theta^0\right) + 0.0272\left(90^0 - \theta^0\right)^2 - 0.0086\left(90^0 - \theta^0\right)^3\right].$$

The diameter for a rebound event remains unchanged where a single droplet rebound from the surface leads to all mass being lost which leads to f_m is set to be zero. The splashing and rebound velocity components are shown in Figure 3-2.

3.3 Droplet deformation

Droplet deformation is one of the noticeable effects for larger droplets caused by larger shear forces, hence disqualifies the validity of the assumption that a droplet behaves as a solid sphere [73]. Droplet breakup can result from droplet deformation; hence similar relations apply to both.

3.3.1 Deformation models

3.3.1.1 FEO model

Feo and Jarillo [74] attempted to improve the trajectory calculations due to droplet deformation in which the droplet drag coefficient is determined from droplet velocity while moving towards an airfoil. The droplet sizes and motion were captured using a high-speed camera with double exposure and then the drag coefficients were compared to the drag coefficients for spheres, hence a linear approximation of the drag coefficient as a function of the local Reynolds number is proposed. The data suggest that the spherical model is valid for low droplet Reynolds number but the spherical droplet drag coefficient is modified for a droplet Reynolds number larger than $\mathrm{Re}_d > 345$. However, data is not available for $\mathrm{Re}_d > 720$, hence the linear relations were followed:

$$\frac{C_D \,\mathrm{Re}_d}{24} = \begin{cases} -0.00355\,\mathrm{Re}_d + 3760: & if \;\; 345\,\mathrm{Re}_d \le 385, \\ -0.00517\,\mathrm{Re}_d + 4782: & if \;\; 385\,\mathrm{Re}_d \le 442, \\ -0.00255\,\mathrm{Re}_d + 3425: & if \;\; 442\,\mathrm{Re}_d \le 475, \\ -0.0318\,\mathrm{Re}_d - 12903: & if \;\; 475\,\mathrm{Re}_d \le 518, \\ -0.00333\,\mathrm{Re}_d - 0313: & if \;\; 518\,\mathrm{Re}_d \le 630, \\ -0.00325\,\mathrm{Re}_d + 2221: & if \;\; 630\,\mathrm{Re}_d \le 720. \end{cases} \tag{3.15}$$

There is no direct time dependence in this relation and deformation such as breakup is very much a time-dependent process. Also, no droplet properties were included in this model and valid only for water droplets.

3.3.1.2 TAB-Model

The Taylor analogy breakup (TAB) model is a breakup model that uses droplet deformation to estimate when a droplet will breakup and can be used to modify the droplet drag coefficient, such as one model according to Tan et al. [57] used in FLUENT which uses the droplet deformation described in the TAB breakup model (equation **(**3.23)).

$$C_D = C_{D,Sphere}\left(1 + 2632y\right), \tag{3.16}$$

where *y* is the non-dimensional deformation of a droplet.

In the present work, by interpolating a sphere and the oblate disk drag coefficient depending on the value of eccentricity *e*, the effective drag coefficient of the droplet is evaluated. The expression is as follows[60],

$$C_{D_{droplet}} = C_{D_{Sphere}} + e\left(C_{D_{Disk}} - C_{D_{Sphere}}\right), \tag{3.17}$$

where, $e = 1 - \left(1 + 0.07\left(We\right)^{0.5}\right)^{-6}$. The droplet behaves as a sphere at low Weber numbers and at higher Weber numbers, the aerodynamic drag is closer to an oblate disk. The drag coefficients for the sphere and disk depend on Reynolds number can be summarized as,

$$C_{D_{Disk}} = \begin{cases} \left(64/\pi\,\mathrm{Re}\right)\left[1+\left(\mathrm{Re}/2\pi\right)\right] & \text{if} \quad \mathrm{Re} \le 1.0\text{e-}02, \\ \left(64/\pi\,\mathrm{Re}\right)\left[1+10^{x}\right] & \text{if} \quad 1.0\text{e-}02 < \mathrm{Re} \le 1.5\text{e+}00, \\ \left(64/\pi\,\mathrm{Re}\right)\left[1+0.138\,\mathrm{Re}^{0.792}\right] & \text{if} \quad 1.5\text{e+}00 < \mathrm{Re} \le 1.33\text{e+}02, \\ 1.17 & \text{if} \quad 1.33\text{e+}02 \le \mathrm{Re}, \end{cases} \tag{3.18}$$

$$C_{D_{Sphere}} = \begin{cases} 24/\mathrm{Re} + 0.1875 & \text{if} \quad \mathrm{Re} < 1.0\text{e-}02, \\ 24\left(1+0.1315\,\mathrm{Re}^{(0.82-0.05w)}\right)/\mathrm{Re} & \text{if} \quad 1.0\text{e-}02 < \mathrm{Re} \le 2.0\text{e+}01, \\ 24\left(1+0.1935\,\mathrm{Re}^{0.6305}\right)/\mathrm{Re} & \text{if} \quad 2.0\text{e+}01 \le \mathrm{Re} \le 2.6\text{e+}02, \\ 10^{\left(1.6435-1.1242w+0.1558w^2\right)} & \text{if} \quad 2.6\text{e+}02 \le \mathrm{Re} \le 1.5\text{e}+03, \\ 10^{\left(-2.4571+2.5558w-0.9295w^2+0.1049w^3\right)} & \text{if} \quad 1.5\text{e}+03 \le \mathrm{Re} \le 1.2\text{e}+04, \\ 10^{\left(-1.9181+0.6370w-0.0636w^2\right)} & \text{if} \quad 1.2\text{e}+04 < \mathrm{Re} \le 4.4\text{e}+04, \\ 10^{\left(-4.3390+1.5809w-0.1546w^2\right)} & \text{if} \quad 4.4\text{e}+04 < \mathrm{Re} \le 3.38\text{e}+05, \\ 29.78-5.3w & \text{if} \quad 3.38\text{e}+05 < \mathrm{Re} \le 4.0\text{e}+05, \\ 0.1w-0.49 & \text{if} \quad 4.0\text{e}+05 < \mathrm{Re} \le 1.0\text{e}+06, \\ 0.19-8\text{e+}04/\mathrm{Re} & \text{if} \quad 1.0\text{e}+06 < \mathrm{Re}, \end{cases} \tag{3.19}$$

in these equations, $x = -0.883+0.906\log_{10}Re-0.025(\log_{10}Re)^2$ and $w = \log_{10}Re$.

3.4 Droplet breakup

The droplet might breakup into smaller droplets brought by the large stresses or the long persistence of deformation enough to deform a droplet. The breakup will continue until a certain critical diameter is reached and become stable when the diameter of the droplets is smaller than this critical diameter [75, 76]. The relative Weber number mostly determines the stresses on a droplet.

3.4.1 Droplet breakup models

According to Honsek et al. [61] and Pilch and Erdman [77] the critical Weber number for the breakup is usually for cases neglecting droplet viscosity. Multiple types of a breakup can

be identified by most models such as identified by Pilch and Erdman [77] which include vibrational breakup, bag breakup, bag-and-stamen breakup, sheet stripping, and wave crest stripping (followed by catastrophic breakup) as illustrated in Figure 3-3. A model based on the experiments is described in the succeeding section.

3.4.1.1 Pilch and Erdman model

Pilch and Erdman [77] use the critical Weber number, the stable diameter, and the critical resident time to predict droplet breakup. Each of the five breakup models uses a separate resident time and to this end, a dimensionless time is defined as

$$T = t\frac{\left|\boldsymbol{u}_g - \boldsymbol{u}\right|\sqrt{\frac{\rho_a}{\rho_w}}}{MVD}. \tag{3.20}$$

Using the equation below, the stable diameter can be estimated

$$d_{stab} = We_c \frac{\sigma_a}{\rho_a \left|\boldsymbol{u}_g - \boldsymbol{u}\right|^2}. \tag{3.21}$$

The resident times are shown below for the five breakup models to reach total breakup where the drop $MVD > d_{stab}$.

$$T = \begin{bmatrix} 6\left(We-12\right)^{-0.25}: & if\ 12 \le We \le 18 \\ 245\left(We-12\right)^{-0.25}: & if\ 18 \le We \le 45 \\ 141\left(We-12\right)^{-0.25}: & if\ 45 \le We \le 351 \\ 0766\left(We-12\right)^{-0.25}: & if\ 351 \le We \le 2670 \\ 5.5: & if\ We \ge 2670 \end{bmatrix}. \tag{3.22}$$

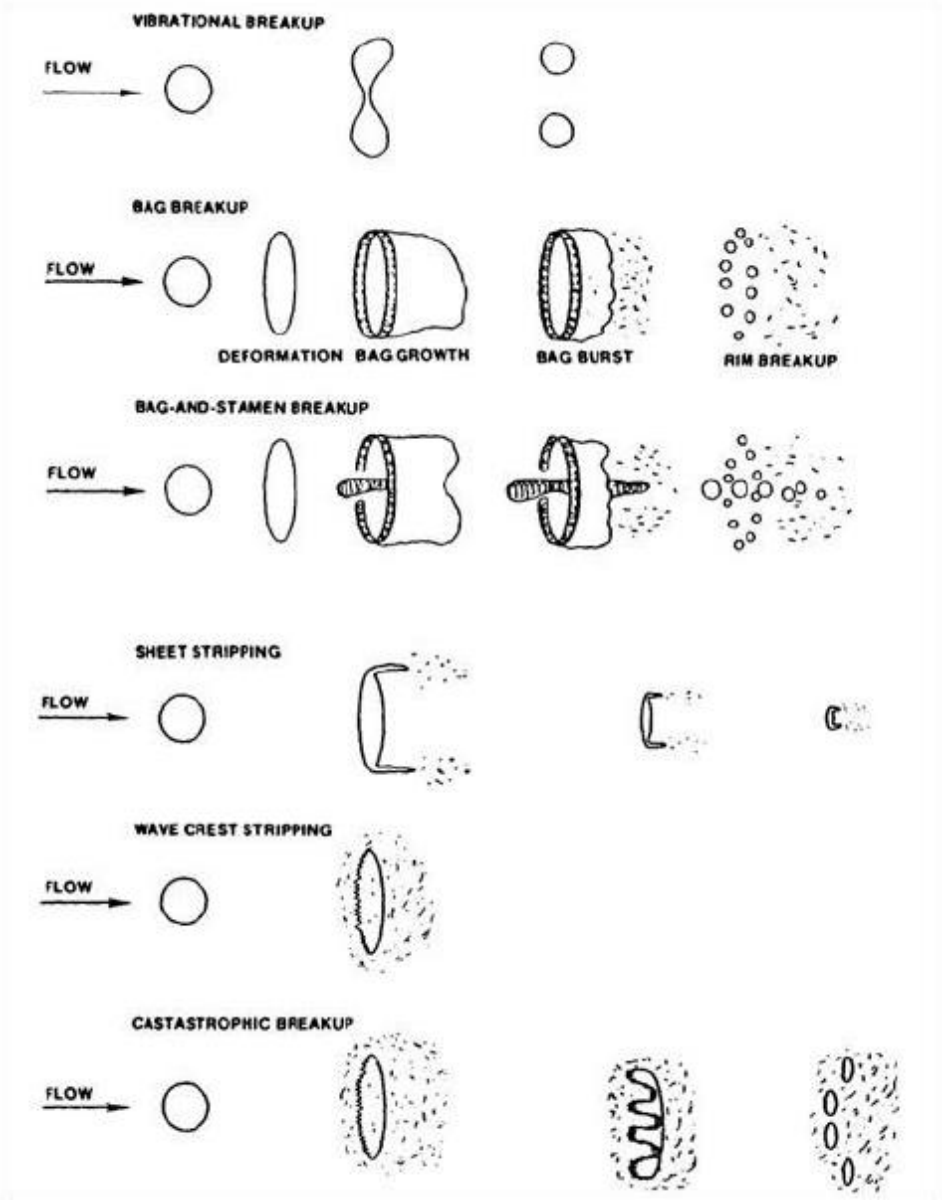

Figure 3-3 Breakup map proposed by Pilch and Erdman [77]

3.4.1.2 Tab-method

A widely used breakup model is the TAB model from O'Rourke and Amsden [78] where the breakup is assumed to occur from the internal vibration of a droplet that is governed by the equation shown below:

$$F - kx - d\frac{dx}{dt} = m\frac{d^2x}{dt^2}, \tag{3.23}$$

where d is the damping coefficient and x is the relative displacement of the droplet equator. The coefficients given by Taylor's analogy are as follow:

$$\frac{F}{m} = C_f \frac{\rho_a \left| \boldsymbol{u}_g - \boldsymbol{u} \right|^2}{\rho_w r},$$

$$\frac{k}{m} = C_k \frac{\sigma_w}{r^3}, \tag{3.24}$$

$$\frac{d}{m} = C_d \frac{\mu_w}{\rho_w r^2},$$

where r is the droplet radius and in order to match the experimental data, C_f, C_k and C_d are chosen. According to this model, droplet breakup takes place when the droplet distortion is larger than the critical ratio C_b of the droplet radius, that is

$$x > C_b r. \tag{3.25}$$

Here, C_b = 0.5 is the most common assumption for the critical ratio which means that breakup occurs when a droplet vibrates with a magnitude where north and south poles meet at the middle of a droplet. Using $x/C_b r$ for non-dimensionalisation and substituting equation (3.24) into equation (3.23), the equation acquired is:

$$\frac{d^2 y}{dt^2} = \frac{C_f}{C_b} \frac{\rho_a \left| \boldsymbol{u}_g - \boldsymbol{u} \right|^2}{\rho_w r} - C_k \frac{\sigma_w}{\rho_w r^3} y - C_d \frac{\mu_w}{\rho_w r^2} \frac{dy}{dt}. \tag{3.26}$$

The breakup will now occur for a non-dimensional droplet deformation $y > 1$ and solving y is possible assuming that the relative velocity is constant:

$$y(t) = We_m + e^{-t/t_d} \left[-\left(y_0 - We_m \right) \cos\left(\omega t \right) + \frac{1}{\omega} \left(\frac{dy_0}{dt} + \frac{y_0 + We_m}{t_d} \right) \sin\left(\omega t \right) \right], \tag{3.27}$$

given that the modified Weber number We_m as,

$$We_m \equiv \frac{C_f}{C_f - kC_d} We. \tag{3.28}$$

The damping frequency can be given as,

$$\frac{1}{t_d} = \frac{C_d}{2}\frac{\mu_w}{\rho_w r^2}, \tag{3.29}$$

and the oscillation frequency as

$$\omega^2 = C_k \frac{\sigma_w}{\rho_w r^3} - \frac{1}{t_d^2}. \tag{3.30}$$

The energy conservation determines the diameter of the secondary droplets after the breakup of which the Sauter mean radius of the secondary droplets using the vibrational energy of the droplet is shown below:

$$r_{32} = \frac{r}{1 + \frac{9Ky^2}{20} + \frac{\rho_w r^2 \left(dy/dt\right)^2}{\sigma}\frac{6K-5}{120}}, \tag{3.31}$$

where K is the ratio of the total energy in distortion and oscillation in the fundamental mode of the order $K = 0.33$.

3.5 Implementation of SLD effects

In the case of SLD particle evaluation, additional effects due to large droplet dynamics have to be taken into account and should be modeled properly. Wright and Potapczuk [79] proposed a ranking system for SLD effects: first-order effects are due to the droplet splashing/rebound mechanism, on the other hand, the second-order effects are due to droplet deformation and breakup. In the present work, droplet splashing, bouncing and drop deformation drag are considered by introducing suitable semi-empirical formulations. Generally, the empirical formulations of wall interactions are in a Lagrangian plane and it is necessary to convert into the Eulerian form. In other words, the SLD empirical functions are in local impingement coordinate system and it is necessary to convert it into the global coordinate system [61]. In splashing/bouncing phenomena, there is a possibility of some indirect effects along with the direct effects: when the droplet splash or rebound, part of the incoming mass remaining on the surface or merged with the water film on the surface which

is clearly depicted in Figure 3-4. Usually the part ejected away from the surface or film have the mass less than the incoming mass and there is a chance of re-impingement of ejected mass on the downstream of the surface. Although the mass deposit and loss can be modeled in this present work, the re-impingement is not considered. The original mathematical shallow water droplet should be extended by including the SLD effect and droplet deformation on the right-hand side of the equations (2.2) and (2.3). Also, the droplet-wall interactions are considered as the numerical boundary condition on the solid surface without altering the governing equation.

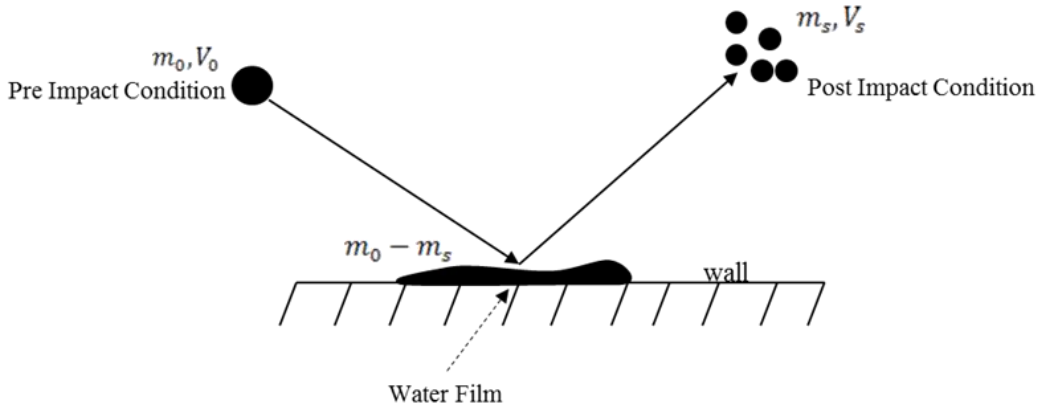

Figure 3-4 Velocity and water mass by SLD effect

To implement the SLD effects in SWDE, the conventional droplet drag model is replaced by Cliff model [60] as explained in section 3.3.1.2. Further, the implementation of droplet wall interactions is not very straight forward. Among the four types of droplet wall interactions, splashing and rebound need to be modeled very carefully. In order to implement droplet wall interactions, the boundary conditions given in equation (2.28) are not sufficient. Since the droplet splashing and rebound change the mass and velocity of the droplet, the boundary condition can be written as,

$$\rho_{wall} = (1 - f_m)\rho_{in},\ u_{wall} = \boldsymbol{V}_S, \quad if \quad \mathbf{V}\cdot\mathbf{n} \le 0. \tag{3.32}$$

Here $f_m = m_s / m_0$ is the ratio between the ejected mass and initial mass of the droplet, which accounts for the mass loss at the wall due to droplet splashing or bouncing by altering the

density in mass conservation equation. V_S is the secondary velocity of droplet or post-impact velocity, which can be calculated from $f_u = V_S / V_0$, which is the ratio between ejected droplet velocity and incoming droplet velocity, ρ_{in} is the volume fraction at an adjacent point of the wall. The impact mass loss and momentum change of droplets are directly implemented in the wall therefore, modification in governing equation is not necessary. The terms f_m and f_u for splashing are provided by the semi-empirical correlations proposed by Trujillo [68] as explained in section 3.2.1.1. On the other hand, for rebound, the mass loss f_m will be zero and f_u can be evaluated by Bai and Gosman [72] model as explained in 3.2.3.1. The empirical formulations provided by Trujillo et al [68] and Bai et al [72] for post impact velocities are in the local impingement coordinate system and it is necessary to transform the coordinate into global in the Eulerian formulation. In the case of Lagrangian formulation, this transformation is not necessary and the correlations can be directly used. Since the present formulations are based on Eulerian form, the transformation from local reference frame into global Cartesian reference frame has been done with appropriate formulations.

Chapter 4. Ice Accretion Modeling

The ice accretion model was developed by considering the mass and heat transfer at the surface of the body. The rate and amount of ice accretion on a body surface have to be evaluated by the ice accretion model. General, an ice accretion model should have the capability to solve all regimes of ice. The convective heat transfer has a very big influence on the ice accretion, which should be calculated carefully from the air solver. The thermodynamic model proposed by Messinger [39] which satisfies the first law of thermodynamics is usually used in ice accretion models. Generally, a control volume approach is used, in which the control volume extends from the surface of the body to the water film /air interface.

4.1 PDE-based ice accretion model

A PDE-based [28] ice accretion model was introduced by using the mass balance and energy equation mentioned in equations (1.14) and (1.17). These equations are called as shallow water model which assumes a linear velocity profile in relation to liquid film on the

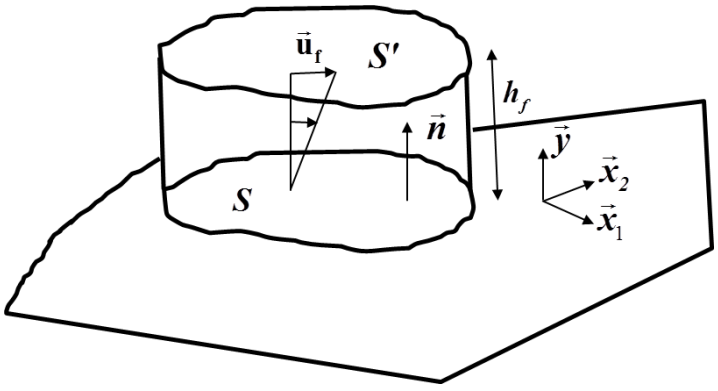

Figure 4-1 Shallow water icing model control volume

surface. Figure 4-1 shows the control volume, where *S* denotes the iced wall surface and *S'* is the thin water film surface. The height of the water film (h_f) is the distance between the two surfaces *S* and *S'*. The equations (1.14) and (1.17) can be written as,

$$\dot{m}_v + \dot{m}_{run} = \dot{m}_{imp} - \dot{m}_{evap} - \dot{m}_{ice}. \tag{4.1}$$

$$\dot{Q}_v + \dot{Q}_{run} = \dot{Q}_{imp} + \dot{Q}_{ice} - \dot{Q}_{evap} - \dot{Q}_{conv} - \dot{Q}_{rad}. \tag{4.2}$$

In above equations, $\dot{m}_v$ is the rate of change of mass in time of liquid water and $\dot{m}_{run}$ is the runback mass flux of water $\left(\dot{m}_{run\_out} - \dot{m}_{run\_in}\right)$ that passes through the control volume. The mass balance equation is expressed in Kg/s and the energy balance equation is expressed in J/s. In energy equation, $\dot{Q}_v$ denotes the rate of change of energy in time of the liquid water, $\dot{Q}_{run}$ is the runback energy flux of water $\left(\dot{Q}_{run\_out} - \dot{Q}_{run\_in}\right)$ that passes through the control volume, $\dot{Q}_{rad}$ is the heat flux due to heat flux, and $\dot{Q}_{cond}$ denotes the heat flux due to convection. The pictorial view of equations (1.14) and (1.17) is shown in Figure 4-2.

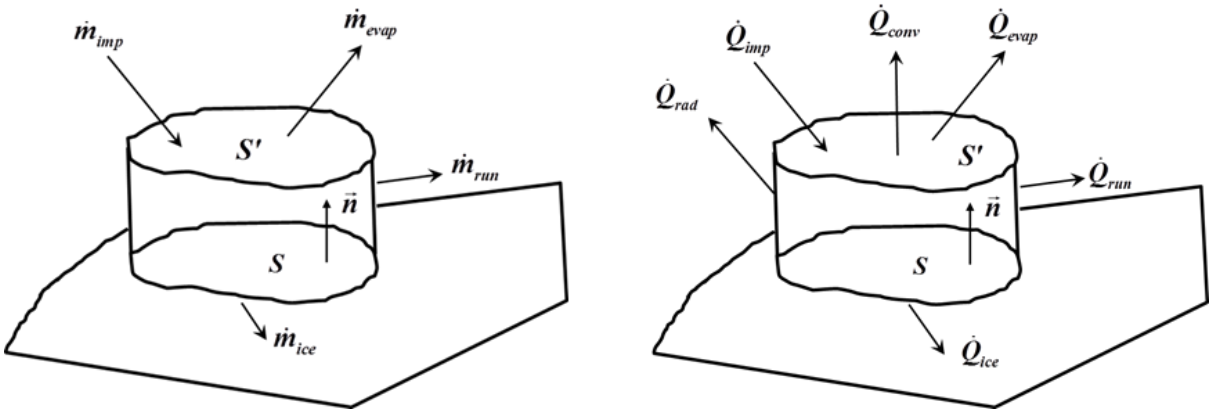

Figure 4-2 Mass (left) and energy (right) balance

General, the film thickness is very small [80] and it is possible to assume that the temperature across the water film is constant in a control volume. Moreover, it is assumed that all the physical and thermodynamic variables are constant within a control volume. The mean water film velocity can be expressed as,

$$\bar{u}_f = \frac{1}{h_f}\int_0^{h_f} u_f dy = \frac{h_f}{2\mu_w}\vec{\tau}_{wall}. \tag{4.3}$$

Now, the terms in equations (4.1) and (4.2) can be expressed as follows,

a. Rate of change of liquid water mass

General, the liquid water on the surface of the body flows due to the shear stress on the surface and the rate of change of liquid water in a control volume can be given as,

$$\dot{m}_v = \frac{\partial}{\partial t}\int_0^{h_f}\int_S \rho_w d\vec{x}dy = \rho_w \frac{\partial}{\partial t}\int_S\int_0^{h_f} dyd\vec{x}. \tag{4.4}$$

b. Water runback water mass

The water passing through one control volume to another need to be considered, this can be given as,

$$\dot{m}_{run} = \int_{\partial S}\int_0^{h_f} \rho_w \vec{u}_f \cdot \vec{n}dydS = \int_S \vec{\nabla}\cdot\left(\rho_w \overline{u}_f h_f\right)d\vec{x}. \tag{4.5}$$

c. Impinging water droplets mass

The droplet impingement adds mass to the control volume or it is the mass entering the control volume. The impinging water is assumed to be uniformly distributed on the surface of the control volume. It can be expressed as,

$$\dot{m}_{imp} = U_\infty LWC_\infty \int_{S'} \beta d\vec{x} \approx U_\infty LWC_\infty \int_S \beta d\vec{x}. \tag{4.6}$$

d. Evaporation mass loss

The evaporation mass loss on a given control volume can be given as,

$$\dot{m}_{evap} = -\int_{S'} \dot{m}''_{evap} d\vec{x} \approx -\int_S \dot{m}''_{evap} d\vec{x}. \tag{4.7}$$

Here $\dot{m}''_{evap}$ is the mass of water lost by evaporation which can be evaluated from parametric model expressions explained in the succeeding section.

e. Ice accumulation mass loss

General, it is assumed that the control volume remains on the surface of the body and the ice accumulates outside the control volume. Hence, the mass rate of water freezing is considered as leaving the control volume. It can be expressed as follows,

$$\dot{m}_{ice} = -\int_S \dot{m}''_{ice} d\vec{x}. \tag{4.8}$$

f. Energy flow due to water flow

The water flow from one control volume to another brings changes in the energy along with the mass. The surface temperature in a control volume at time *t* can be given as $\tilde{T}$. It should be mention that a tilde over any temperature indicates the temperature specified in degrees Celsius otherwise in Kelvin. By using the specific heat capacity $C_{p,w}$, the enthalpy of the water can be given as $C_{p,w}\tilde{T}$. Now, using this enthalpy, the energy term for the liquid water flow can be given as,

$$\dot{Q}_v = \frac{\partial}{\partial t}\int_S \left(\int_0^{h_f} \rho_w C_{p,w} \tilde{T}_{equi} dy \right) d\vec{x} = \int_S \frac{\partial}{\partial t}\left[\rho_w C_{p,w} h_f \tilde{T}_{equi} \right] d\vec{x}. \tag{4.9}$$

Now, by using equation (4.3), we can express the energy due to water runback as,

$$\dot{Q}_{run} = \int_{\partial S} \left(\int_0^{h_f} \rho_w C_{p,w} \tilde{T}_{equi} \vec{u}_f \cdot \vec{n} dy \right) d\vec{x} = \int_S \vec{\nabla} \cdot \left(\rho_w \bar{u}_f h_f C_{p,w} \tilde{T}_{equi} \right) d\vec{x}. \tag{4.10}$$

g. Energy by the water impingement

Once the droplet strikes the surface and brought to rest, some kinetic energy dissipates into the body and by using stagnation enthalpy, it can be evaluated. The equilibrium temperature is considered as the reference for zero enthalpy. Hence, the energy flow rate due to impinged droplets can be expressed as,

$$\dot{Q}_{imp} = \int_S U_\infty LWC_\infty \beta \left[C_{p,w} \left(T_{d,\infty} - T_{equi} \right) + \frac{\left\| \vec{u}_d \right\|^2}{2} \right] d\vec{x}. \tag{4.11}$$

Here $\tilde{T}_{d,\infty}$ is the ambient droplet temperature and $\left\| \vec{u}_d \right\|^2$ is the square norm of the droplet impact velocity.

h. Evaporation energy loss

The rate of energy loss due to evaporation can be given as,

$$\dot{Q}_{evap} = -\int_S L_{evap}\dot{m}_{evap}d\vec{x}. \tag{4.12}$$

Here L_{evap} is the latent heat of evaporation.

i. Ice accumulation energy release

When the water in a control volume freezes, the phase changes of water from liquid to solid releases some energy into the control volume. This energy can be called as latent heat of solidification. The rate of energy release by a control volume for ice accumulation can be given as,

$$\dot{Q}_{ice} = \int_S \dot{m}_{ice}\left[L_{fus} - C_{p,ice}\tilde{T}_{equi}\right]d\vec{x}. \tag{4.13}$$

Here L_{fus}, and $C_{p,ice}$ is the latent heat of fusion and specific heat capacity of ice respectively.

j. Convective heat loss

The airflow over the given surface produces convective heat transfer, which can be given by Newton's cooling law. General, convective heat transfer is given by the airflow solver as input to the ice accretion solver. Since the convective heat transfer has a strong influence on the ice shape evaluation, it is necessary to model the air solver for better accuracy.

Before starting the ice accretion calculations, the heat transfer coefficient is evaluated from the convective heat flus input as follows,

$$h_c = \frac{\dot{Q}_{conv\_air}}{T_{sur} - T_\infty}. \tag{4.14}$$

Here $\dot{Q}_{conv\_air}$ is the convective heat transfer provided by the air solver, and T_{sur} is the initial surface temperature of the body. The initial surface temperature effect in the heat transfer coefficient calculation is minor. Hence, the ice accretion solver uses a fixed value of heat transfer coefficient to evaluate the convective heat flux which can change with the equilibrium temperature.

$$\dot{Q}_{conv} = h_c\left(\tilde{T}_{equi} - \tilde{T}_{\infty}\right). \tag{4.15}$$

k. Radiation heat loss

The radiation heat loss is the result of electromagnetic waves brought by the difference between the ambient and the surface temperatures. This can be expressed as,

$$\dot{Q}_{rad} = \int_S \sigma\varepsilon\left[\tilde{T}_{equi}^4 - \tilde{T}_{\infty}^4\right]d\vec{x}. \tag{4.16}$$

Where σ and ε are the Boltzmann constant and solid's emissivity, respectively. General, heat loss due to radiation is low under unheated surfaces with a range of 1 percent.

Finally, by using equations (4.4) to (4.8), a partial differential equation for mass and energy conservation for a surface (volume) can be written as,

$$\int_S\left(\rho_w\left[\frac{\partial h_f}{\partial t} + \vec{\nabla}\cdot\left(\bar{u}_f h_f\right)\right]\right)d\vec{x} = \int_S\left(U_{\infty}LWC_{\infty}\beta - \dot{m}_{evap} - \dot{m}_{ice}\right)d\vec{x}, \tag{4.17}$$

$$\begin{aligned}\int_S \rho_w\left[\frac{\partial h_f C_{p,w}\tilde{T}_{equi}}{\partial t} + \vec{\nabla}\cdot\left(\bar{u}_f h_f C_{p,w}\tilde{T}_{equi}\right)\right]d\vec{x} = \int_S\Bigg\{&\left[C_{p,w}\tilde{T}_{d,\infty} + \frac{\left\|\vec{u}_d\right\|^2}{2}\right]\times U_{\infty}LWC_{\infty}\beta \\ &+\dot{m}_{ice}\left[L_{fus} - C_{p,ice}\tilde{T}_{equi}\right] - L_{evap}\dot{m}_{evap} + h_c\left(\tilde{T}_{equi} - \tilde{T}_{\infty}\right) + \sigma\varepsilon\left[\tilde{T}_{equi}^4 - \tilde{T}_{\infty}^4\right]\Bigg\}d\vec{x}.\end{aligned} \tag{4.18}$$

The conservative form of equation (4.17) and (4.17) can be written as,

$$\rho_w\left[\frac{\partial h_f}{\partial t} + \vec{\nabla}\cdot\left(\bar{u}_f h_f\right)\right] = U_{\infty}LWC_{\infty}\beta - \dot{m}_{evap} - \dot{m}_{ice}, \tag{4.19}$$

$$\begin{aligned}\rho_w\left[\frac{\partial h_f C_{p,w}\tilde{T}_{equi}}{\partial t} + \vec{\nabla}\cdot\left(\bar{u}_f h_f C_{p,w}\tilde{T}_{equi}\right)\right] = &\left[C_{p,w}\tilde{T}_{d,\infty} + \frac{\left\|\vec{u}_d\right\|^2}{2}\right]\times U_{\infty}LWC_{\infty}\beta - L_{evap}\dot{m}_{evap} \\ &+\dot{m}_{ice}\left[L_{fus} - C_{p,ice}\tilde{T}_{equi}\right] + h_c\left(\tilde{T}_{equi} - \tilde{T}_{\infty}\right) + \sigma\varepsilon\left[\tilde{T}_{equi}^4 - \tilde{T}_{\infty}^4\right].\end{aligned} \tag{4.20}$$

Here, all the physical properties of water, air, and droplets parameters are specified by the user. The air solver provides the shear stress and convective heat flux. The droplet solver provides the collection efficiency and droplet impact velocity. The evaporation mass flux

need to be evaluated separately. General, mass evaporation is derived from convective heat flux by using some parametric models.

In the present work, the mass loss by evaporation [81] is defined as a function of the mass transfer coefficient by diffusion. Primarily, only a small fraction of liquid water covering the surface evaporates in the air. The mass lost by evaporation can be given as,

$$\dot{m}_{evap} = h_{dif}\left(\rho_{vs} - \rho_{ve}\right)A. \tag{4.21}$$

Here, h_{dif} is the mass transfer coefficient, ρ_{vs} is the saturated water vapor density at the surface temperature, ρ_{ve} is the water vapor density at the temperature at the edge of the boundary layer, and A is the area of the surface. By perfect gas law, saturated water vapor density can be given as

$$\rho_{vs} = \frac{P_{vs}(T_s)}{R_v T_s}. \tag{4.22}$$

Similarly, the water vapor density at the edge of the boundary layer can be given as,

$$\rho_{ve} = \frac{P_v(T_e)}{R_v T_e}, \tag{4.23}$$

here, saturated water vapor density and water vapor density at the edge of the boundary layer are dependent on the water vapor pressure for respective temperatures. The term R_v is water vapor constant. The air vapor pressure $\left(P_v\right)$ can be derived from relative humidity. This can be written as,

$$\phi = \frac{P_v(T_e)}{P_{vs}(T_e)}. \tag{4.24}$$

Now, the saturated vapor pressure can be expressed as,

$$P_{vs} = 610.8e^{\frac{L_{evap}}{R_v}\left(\frac{1}{T_f}-\frac{1}{T}\right)}, \tag{4.25}$$

By using the analogy developed by Chilton- Colburn, the mass diffusion coefficient of vapor in air can be written as,

$$h_{dif} = \frac{h_c}{\rho_a C_{p,a} Le^{2/3}}, \tag{4.26}$$

here, Le is the Lewis number defined as the ratio of the Schmidt number over the Prandtl number. Lewis number is a non-dimensional number which is usually given by the ratio of thermal and mass diffusivity. This can be written as follows,

$$Le = \frac{k_a}{\rho_a C_{p,a} D_{va}}. \tag{4.27}$$

Here, k_a is the air thermal conductivity and D_{va} is the water vapor diffusion coefficient in the air.

In equation (4.20), the terms in the left-hand side are derived with temperature given in Celsius and the right-hand side terms are in Kelvin. Therefore, the enthalpy calculation brings dissimilar units in both sides of the equations. In order to avoid this situation, the enthalpy of the water film is evaluated using Kelvin. The left-hand side of the equation (4.20) does not give the same quantity of energy, if the temperature unit is simply expressed in Kelvin. Therefore, the equation (4.20) is needed to be recalibrated. The left-hand side of the equation can be changed as,

$$\begin{aligned} \rho_w \left[\frac{\partial h_f C_{p,w} \tilde{T}_{equi}}{\partial t} + \vec{\nabla} \cdot \left(\bar{u}_f h_f C_{p,w} \tilde{T}_{equi} \right) \right] = \rho_w C_{p,w} \left[\frac{\partial h_f T_{equi}}{\partial t} + \vec{\nabla} \cdot \left(\bar{u}_f h_f T_{equi} \right) \right] \\ - \rho_w C_{p,w} T_c \left[\frac{\partial h_f}{\partial t} + \vec{\nabla} \cdot \left(\bar{u}_f h_f \right) \right]. \end{aligned} \tag{4.28}$$

In equation (4.28), the second term on the right-hand side can be replaced by the mass transfer. Now, the recalibrated equation can be written as,

$$\begin{aligned} \rho_w C_{p,w} \left[\frac{\partial h_f T_{equi}}{\partial t} + \vec{\nabla} \cdot \left(\bar{u}_f h_f T_{equi} \right) \right] = \left[C_{p,w} \tilde{T}_{d,\infty} + \frac{\left\| \vec{u}_d \right\|^2}{2} \right] \times U_\infty LWC_\infty \beta - L_{evap} \dot{m}_{evap} \\ + \dot{m}_{ice} \left[L_{fus} - C_{p,ice} T_{equi} \right] + h_c \left(T_{equi} - T_\infty \right) + \sigma \varepsilon \left[T_{equi}^4 - T_\infty^4 \right] \\ + C_{p,w} T_c \left(U_\infty LWC_\infty \beta - \dot{m}_{evap} - \dot{m}_{ice} \right). \end{aligned} \tag{4.29}$$

Here, T_c is the critical temperature (T_c = 273.15K). In the present work, these recalibrated equations are used after all the necessary equations are derived using the (4.19) and (4.29).

4.1.1 Compatibility relations

In equations (4.19) and (4.29), there are 3 unknowns to be computed: water film thickness h_f, equilibrium temperature T_{equi}, and the mass accumulation $\dot{m}_{ice}$. Since there are only two governing equations available, compatibility relations are necessary to close the system. The compatibility equations can be given as,

$$\begin{aligned} &h_f \geq 0, \\ &\dot{m}_{ice} \geq 0, \\ &h_f T_{equi} \geq h_f T_C, \\ &\dot{m}_{ice} T_{equi} \leq \dot{m}_{ice} T_C. \end{aligned} \tag{4.30}$$

Based on the physical behavior, the above compatibility relations are derived. The first compatibility relation makes sure that the film thickness remains positive. The second compatibility relation prevents the melting of accreted ice. The third compatibility relation makes sure that the water film only can exist for equilibrium temperature above freezing point. Finally, the fourth compatibility equation stipulates that the ice cannot form for equilibrium temperatures above freezing point.

The above four compatibility equations can be represented into three for the three different regimes of ice accretion. The first regime corresponds to a running wet with no ice accretion which is basically above the freezing point. Hence this regime can be described as, $h_f \geq 0$, $T_{equi} \geq T_c$, $\dot{m}_{ice} = 0$. The second regime corresponds to glaze ice growth which happens when the water film and ice are present simultaneously. The equilibrium temperature is assumed to be freezing temperature of water, hence this regime can be expressed as $h_f \geq 0$, $T_{equi} = T_c$, $\dot{m}_{ice} \geq 0$. The final regime which corresponds to rime ice cases where the liquid

film flows are not available and only dry ice accumulation is possible. This regime can be described as $h_f = 0$, $T_{equi} \leq Tc$, $\dot{m}_{ice} \geq 0$.

4.1.2 System of equations to solve

The system of equations to be solved can be expressed by using equation (4.3) in equations (4.19) and (4.29) along with the compatibility relations as,

$$\begin{cases} \rho_w \left[\dfrac{\partial h_f}{\partial t} + \vec{\nabla} \cdot \left(\vec{\tau}_{wall} \dfrac{h_f^2}{2\mu_w} \right) \right] = U_\infty LWC_\infty \beta - \dot{m}_{evap} - \dot{m}_{ice}, \\ \rho_w C_{p,w} \left[\dfrac{\partial h_f T_{equi}}{\partial t} + \vec{\nabla} \cdot \left(\vec{\tau}_{wall} \dfrac{h_f^2 T_{equi}}{2\mu_w} \right) \right] = \left[C_{p,w} \tilde{T}_{d,\infty} + \dfrac{\|\vec{u}_d\|^2}{2} \right] \times U_\infty LWC_\infty \beta - L_{evap} \dot{m}_{evap} \\ \qquad + \dot{m}_{ice} \left[L_{fus} - C_{p,ice} T_{equi} \right] + h_c \left(T_{equi} - T_\infty \right) + \sigma \varepsilon \left[T_{equi}^4 - T_\infty^4 \right] \\ \qquad + C_{p,w} T_c \left(U_\infty LWC_\infty \beta - \dot{m}_{evap} - \dot{m}_{ice} \right), \\ h_f \geq 0, \\ \dot{m}_{ice} \geq 0, \\ h_f T_{equi} \geq h_f T_C, \\ \dot{m}_{ice} T_{equi} \leq \dot{m}_{ice} T_C. \end{cases} \tag{4.31}$$

4.2 Finite volume formulation

The governing equations expressed in equation (4.31) for the water film on the surface of the body. The computation elements are spread over the surface of the body and need to be solved using some numerical technique. After some investigations, a cell center based finite volume method is chosen for solving these governing equations. The conservative mass and energy equations can be written as,

$$\frac{\partial h_f}{\partial t} + \vec{\nabla} \cdot \left(\vec{\tau}_{wall} \frac{h_f^2}{2\mu_w} \right) = \frac{S_M}{\rho_w}, \tag{4.32}$$

Where,

$S_M = U_\infty LWC_\infty \beta - \dot{m}_{evap} - \dot{m}_{ice}$.

$$\frac{\partial h_f T_{equi}}{\partial t}+\vec{\nabla}\cdot\left(\vec{\tau}_{wall}\frac{h_f^2 T_{equi}}{2\mu_w}\right)=\frac{S_E}{\rho_w C_{p,w}}+\frac{T_c S_M}{\rho_w},$$

where,

$$S_E=\left[C_{p,w}\tilde{T}_{d,\infty}+\frac{\left\|\vec{u}_d\right\|^2}{2}\right]\times U_\infty LWC_\infty\beta-L_{evap}\dot{m}_{evap}$$
$$+\dot{m}_{ice}\left[L_{fus}-C_{p,ice}T_{equi}\right]+h_c\left(T_{equi}-T_\infty\right)+\sigma\varepsilon\left[T_{equi}^4-T_\infty{}^4\right]. \tag{4.33}$$

The conservative form of the system of equations can be written as,

$$\frac{\partial U}{\partial t}+\vec{\nabla}\cdot\vec{F}\left(U\right)=S, \tag{4.34}$$

equation (4.34) can be written as,

$$U=\begin{bmatrix}h_f\\ h_f T_{equi}\end{bmatrix};\ \vec{F}\left(U\right)=\begin{bmatrix}\frac{h_f^2}{2\mu_w}\vec{\tau}_{wall}\\ \frac{h_f^2 T_{equi}}{2\mu_w}\vec{\tau}_{wall}\end{bmatrix};\ S=\begin{bmatrix}\frac{S_M}{\rho_w}\\ \frac{S_E}{\rho_w C_{p,w}}+\frac{T_c S_M}{\rho_w}\end{bmatrix}. \tag{4.35}$$

A first order Godunov Roe scheme [56] is used to discretize the divergence terms in the governing equations. For a vector of unknowns U_i and U_j of two cells, as shown in Figure 2-1, we can express as,

$$Vol\left(C_i\right)\frac{\partial U_i}{\partial t}+\sum_{j=1}^{N_f}\int_{\partial C_{ij}}\Phi^{Roe}\left(U_i,U_j,\vec{n}\right)ds=Vol\left(C_i\right)S_i, \tag{4.36}$$

where,

$$\Phi^{Roe}\left(U_i,U_j,\vec{n}\right)=\frac{1}{2}\left(\vec{F}\left(U_i\right)+\vec{F}\left(U_j\right)\right)\cdot\vec{n}-\frac{1}{2}\left|\vec{J}\left(U_{i+1/2}\right)\cdot\vec{n}\right|\left(U_j-U_i\right),$$
$$\vec{J}\left(U_{i+1/2}\right)=\vec{J}\left(\frac{U_i-U_j}{2}\right). \tag{4.37}$$

The Jacobian matrix of the current system of equations can be written as,

$$\vec{J}\left(U\right).\vec{n}=\left(\vec{\tau}_{wall}\cdot\vec{n}\right)\begin{bmatrix}\frac{h_f}{\mu_w} & 0\\ \frac{h_f T_{equi}}{2\mu_w} & \frac{h_f}{2\mu_w}\end{bmatrix}. \tag{4.38}$$

Finally, cell *i* can be solved using the equation (4.39) and for convenience, h_f is specified as *h* and T_{equi} is specified as *T* in equation (4.39).

$$\begin{aligned} Vol(C_i)\left(\rho_w \frac{\partial h_i}{\partial t} - S_{M_i}\right) + \sum_{\text{j neighbour of i}} R_{ij}^M = 0, \\ Vol(C_i)\left(\rho_w c_{p,w} \frac{\partial h_i T_i}{\partial t} - S_{E_i}\right) + \sum_{\text{j neighbour of i}} R_{ij}^E = 0. \end{aligned} \tag{4.39}$$

Using equation (4.40), the flux R_{ij}^M and R_{ij}^E can be written as,

$$\begin{aligned} R_{ij}^M &= \frac{1}{2}\rho_w\left[h_i^2 - h_j^2\right]\vec{u}_{ij}.\vec{n}_{ij} - \rho_w\left|\vec{u}_{ij}.\vec{n}_{ij}\right| h_{ij}\left[h_j - h_i\right], \\ R_{ij}^E &= \frac{c_{p,w}}{2}\rho_w\left[h_i^2 T_i + h_j^2 T_j\right]\vec{u}_{ij}.\vec{n}_{ij} - \rho_w\left|\vec{u}_{ij}.\vec{n}_{ij}\right| \cdot \\ &\qquad \frac{c_{p,w}}{2}\left[\frac{\left(h_i T_i + h_j T_j\right)}{2}\left(h_j - h_i\right) + h_{ij}\left(h_j T_j - h_i T_i\right)\right]. \end{aligned} \tag{4.40}$$

and

$$\vec{u} = \frac{\vec{\tau}_{wall}}{2\mu_w}, \quad h_{ij} = \frac{h_i + h_j}{2}, \quad \vec{u}_{ij} = \frac{\vec{u}_i + \vec{u}_j}{2}, \quad \vec{n}_{ij} = \frac{\vec{n}_i + \vec{n}_j}{2}. \tag{4.41}$$

In the system of equations, $\dot{m}_{ice}$ is also an unknown property. Therefore, the discretized equation can be written as,

$$\begin{aligned} Vol(C_i)\left[\rho_w \frac{\partial h_i}{\partial t} + \dot{m}_{ice}^{n+1} - S_{M_i}^{'}\right] + \sum_{j=1}^{N_f} R_{ij}^M = 0, \\ Vol(C_i)\left[\rho_w c_{p,w} \frac{\partial h_i T_i}{\partial t} - \dot{m}_{ice}^{n+1}\left(L_{fus}\left(T_c\right) - C_{p,ice}\left(T_{equi} - T_c\right) - C_{p,w} T_c\right) - S_{E_i}^{'}\right] \\ + \sum_{j=1}^{N_f} R_{ij}^E = 0. \end{aligned} \tag{4.42}$$

Here, $S_M^{'}$ and $S_E^{'}$ are the source terms of mass and energy equations without $\dot{m}_{ice}$ term as shown in equation (4.43).

$$S_{M_i}^{'} = U_\infty LWC_\infty \beta - \dot{m}_{evap},$$

$$S_{E_i}^{'} = U_\infty LWC_\infty \beta \left[C_{p,w}\left(T_{d,\infty} - T_c\right) + \frac{\left\|\vec{u}_d\right\|^2}{2} \right] - L_{evap}\dot{m}_{evap} + h_c\left(T_{equi} - T_\infty\right) + \sigma\varepsilon\left[T_{equi}^4 - T_\infty{}^4\right] + U_\infty LWC_\infty \beta C_{p,w} T_c - \dot{m}_{evap} C_{p,w} T_c. \quad (4.43)$$

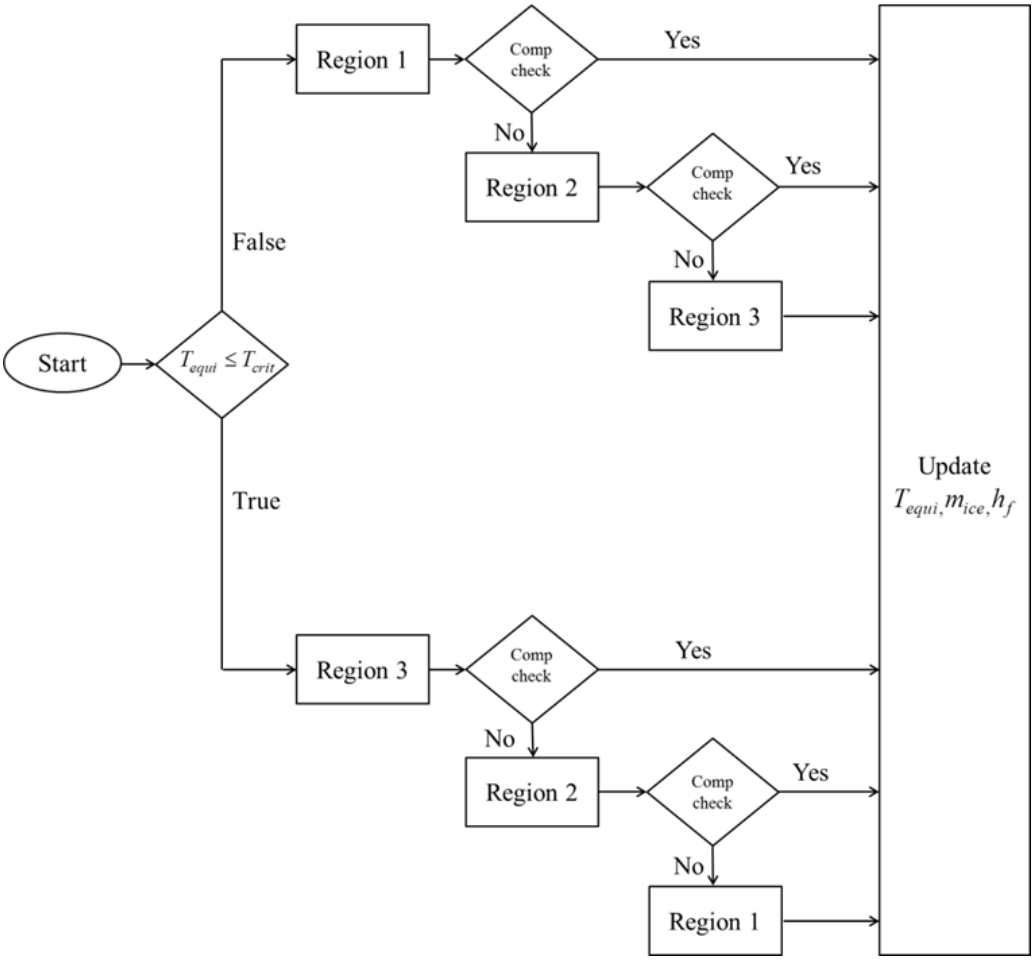

Figure 4-3 Flow chart of ice accretion solver

Now the equation to solve can be written as,

$$\left[\rho_w \frac{h_i^{n+1} - h_i^n}{\Delta t} + \dot{m}_{ice}^{n+1} - S_{M_i}^{'} \right] \cdot V_i + \sum_{j=1}^{N_f} R_{ij}^M = 0,$$

$$\left[\rho_w c_{p,w} \frac{h_i^{n+1} T_i^{n+1} - h_i^n T_i^n}{\Delta t} - \dot{m}_{ice}^{n+1}\left(L_{fus}\left(T_c\right) - C_{p,ice}\left(T_{equi} - T_c\right) - C_{p,w} T_c\right) - S_{E_i}^{'} \right] \cdot V_i + \sum_{j=1}^{N_f} R_{ij}^E = 0. \quad (4.44)$$

An explicit time marching scheme is used to solve the equation (4.44) for all icing regions, where the previous time step n solution is used to evaluate the next time step (n+1). By using the compatibility equations, each cell of the domain is solved as illustrated in Figure 4-3. Detailed formulations for each regime of icing are explained in Appendix A.

4.3 Pure rime ice model

At very low ambient temperatures, the droplets freeze immediately upon impact on solid surface. Since there is no water runback, all the incoming mass through the droplets turn into ice. The mass flux at each time step can be calculated as follows,

$$\dot{m}_{ice} = U_{\infty} LWC_{\infty} \beta. \tag{4.45}$$

4.4 Ice growth and node displacement

The rate of ice accretion for a given control volume is provided by the ice accretion solvers (glaze and rime). It is necessary to convert the rate of ice accretion to ice thickness, later which can be used to evaluate the nodal displacement. Basically, the nodal displacements are determined under an assumption that the displacement must be in normal to the wall. The ice density can be constant $\left(\rho_{ice} = 917 kg/m^3\right)$ or variable, according to makkonen and Stallabrass [82] formula,

$$\rho_{ice} = \begin{cases} 40.73 & if\ R_M \le 0.2, \\ 378 + 425\log_{10}\left(R_M\right) - 82.3\left(\log_{10}\left(R_M\right)\right)^2 & if\ \ 0.2 \le R_M \le 170, \\ 917 & if\ R_M \ge 170. \end{cases} \tag{4.46}$$

where,

$$R_M = -\frac{MVD\left\|\vec{u}_d \cdot \vec{n}\right\|}{2\bar{T}_{wall}}, \tag{4.47}$$

For a given time span Δt the volume of ice accretion can be expressed as,

$$V_{ice} = \int_0^{\Delta t} \int_S \frac{\dot{m}_{ice}}{\rho_{ice}} ds dt, \tag{4.48}$$

For a single surface *ds(t)*, the ice thickness can be given as,

$$D_{ice} = \frac{\dot{m}_{ice}}{\rho_{ice}}. \tag{4.49}$$

The ice thickness determined by equation (4.49) is added to each successive time steps to find the total thickness of ice accretion. Finally, this ice thickness is used to find the node displacement and for re-meshing/grid movement.

Chapter 5. Parametric Study on Ice Solver

Several parameters from previous chapters involved in the numerical ice accretion modeling have their own behavior in shape, location, and amount of ice accretion. Parameters such as velocity, ambient temperature, surface temperature, droplet diameter, and liquid water content have been thoroughly studied. Hence, in this chapter, other parameters such as ice density, surface roughness, and evaporation model along with turbulence models effects on heat transfer and their influence on ice shapes are discussed. Finally, multi-shot ice accretion behavior is also discussed with relevant algorithms and examples.

5.1 Density of ice

Ice density plays an essential role in the ice shape and amount of ice accumulation as clearly illustrated in equation (4.49). Generally, ice density assumed to be constant with a value of 917 Kg/m^3 for glaze ice and 800 Kg/m^3 for rime ice. However, previous researchers notified that the ice density might not be constant under all ambient conditions and that it also has an effect on the ice accretion. Many literatures investigated the relation between metrological conditions and ice density and proposed several semi-empirical models. After a thorough investigation of these literature, the semi-empirical formulations proposed by Jones [83] and by Macklin [84] are used for illustrating the effect of ice density in ice accretion. The equations (4.46) and (5.1) proposed by Macklin [84] and Jones [83] respectively, are used for ice density calculations.

$$\rho_{ice} = \begin{cases} 210R_M & if\ R_M \le 10, \\ R_M / (115R_M + 294) & if\ 10 \le R_M \le 60, \\ 840 & if\ R_M \ge 60. \end{cases} \tag{5.1}$$

Here, the value of R_M is evaluated by equation (4.47). In these two models, the surface temperature, droplet diameter, and droplet impact velocity are taken into account. The ice density distribution over an airfoil given by various ice density models is shown in Figure 5-1.

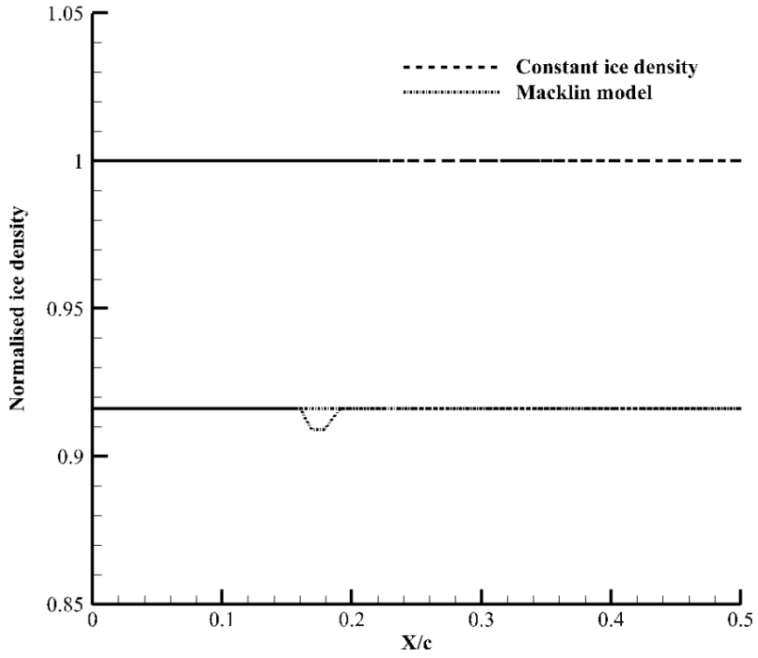

Figure 5-1 Ice density over an airfoil

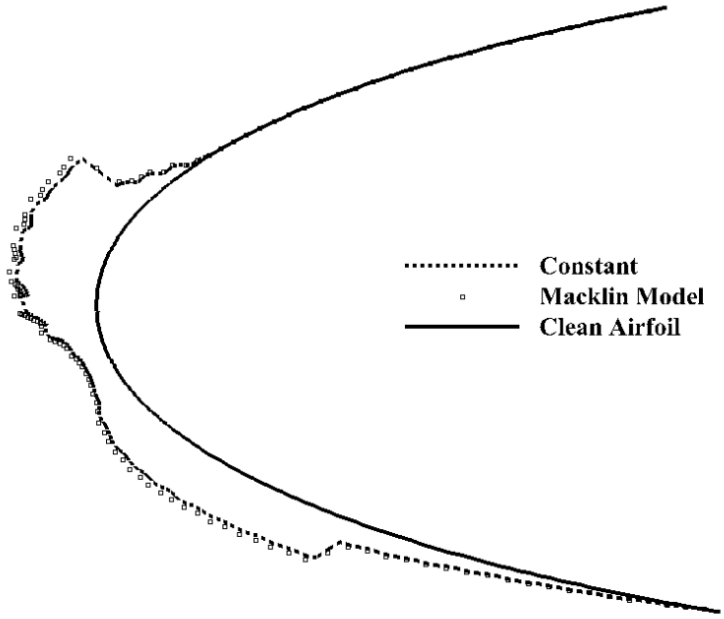

Figure 5-2 Ice density effect on ice accretion

As seen here, the density varies depending on the ice density models used and Figure 5-2 illustrates the different ice shapes obtained by the different ice density models for a same metrological condition. In the present ambient condition, Macklin model ice density results

are different than the constant and the amount of ice accretion. Hereafter, all the ice accretions simulations the model proposed by Macklin is used.

5.2 Effect of heat transfer

Heat transfer coefficient is an eminent variable which can alter the ice shape and the amount of ice accretion on any surface. As the heat transfer coefficient is involved in the convective and evaporative cooling, the influence of this parameter is easily observed in ice accretion modeling. Since this parameter affects the convective and evaporative cooling, this parameter directly affects the freezing of water. Thus, the freezing of ice can be reduced by decreasing the heat transfer coefficient.

In flow physics, the heat transfer coefficient is significantly affected by the surface roughness and the temperature difference between the flow and the surface. Furthermore, in numerical simulations, the turbulence model has its effect in the computation of heat transfer coefficient and the surface roughness treatment. Before doing any simulation for ice accretion, it is essential to find the appropriate surface roughness calculation and turbulence model.

5.2.1 Surface roughness

Generally, surfaces are considered as smooth in aerodynamic simulations, however surface roughness increases in ice accreted condition [85], hence it is essential to include roughness effect in the simulations. The increase of surface roughness also increases the chance of the flow transition into turbulence. Therefore, the surface roughness increases the surface heat transfer due to the increase in effective area on the surface, caused by skin friction increment. Many researches in the field of surface roughness and heat transfer coefficient revealed the strong connection between them.

Poinsatte [86] conducted experiments on smooth and roughed airfoils to investigate the heat transfer coefficient behavior under different roughness conditions. The airfoils are

investigated under a variety of roughness patterns and angle of attacks. The experiments revealed that the increase of roughness increases the heat transfer under all test conditions and at a higher angle of attacks, the heat transfer increases sharply at the leading edge of the airfoil. For a rough airfoil at zero angles of attack, the heat transfer increases approximately two times while for a 4 degree angle of attack, the heat transfer increases dramatically up to four times than a smooth airfoil.

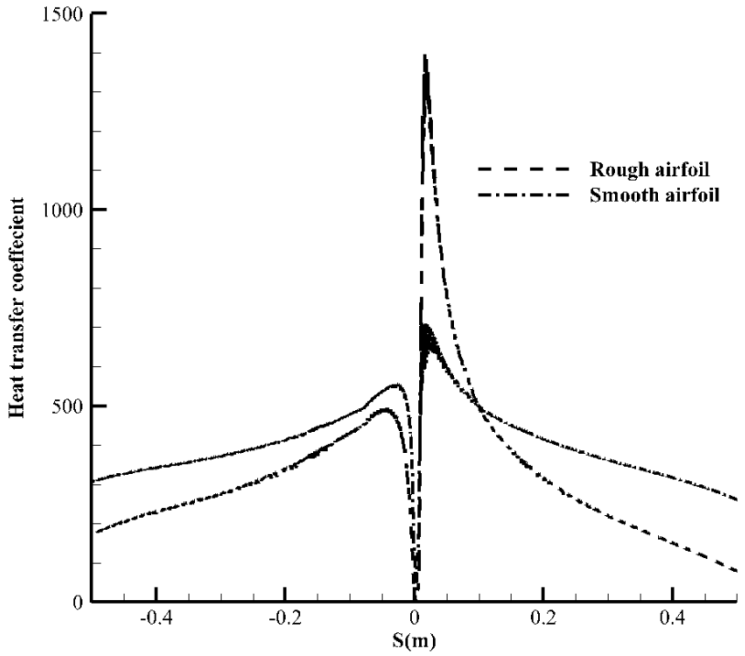

Figure 5-3 Heat transfer coefficient for smooth and rough airfoil

Figure 5-3 shows the computed heat transfer for both smooth and rough surfaces under the same ambient condition. A similar effect of the experiment can also be noticed in computed results. The heat transfer coefficient increased drastically at a point and the difference between upper and lower side of the airfoil is also quite different, which might lead to different ice shape at lower and upper side of the airfoil. Once the heat transfer decreases, the freezing of water also decreases and the water flows on the surface.

Figure 5-4 shows the ice accretion on an airfoil under smooth and rough surfaces, which clearly depicts the effects of heat transfer coefficient. Due to the heat transfer effect, the ice thickness at the stagnation is slightly reduced while the water flows on the surface and

freezes at the aft. Figure 5-3 and Figure 5-4 shows the strong relationship between the heat transfer and the ice shape while Figure 5-3 illustrates the roughness effect. Therefore, it is essential to model the roughness by considering the metrological condition and type of ice for better ice accretion modeling.

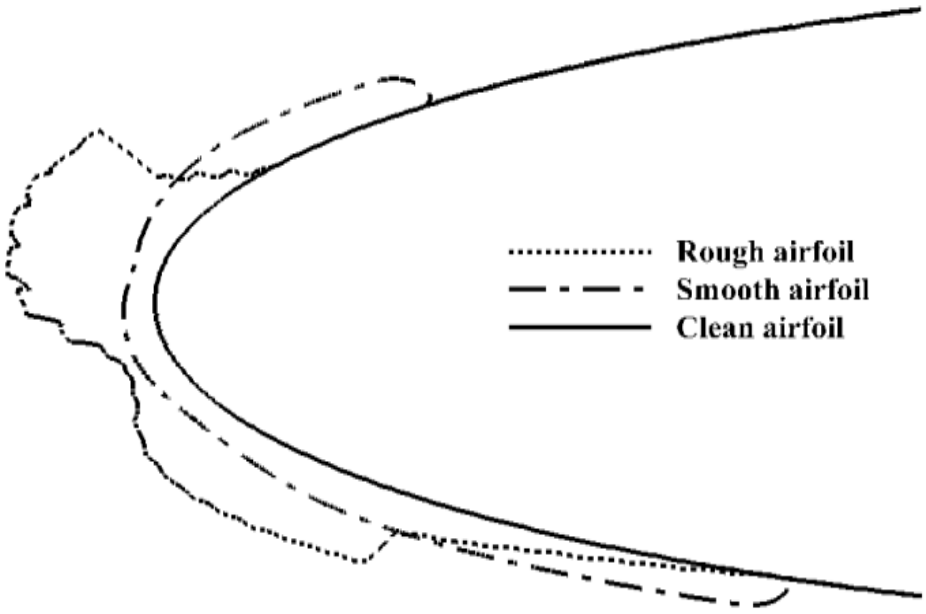

Figure 5-4 Roughness effect on ice shape

The lack of detailed information on the microphysics of roughness distribution on ice surface leads to the development of empirical correlation in order to compute the equivalent sand grain roughness. These correlations are derived from the experimental results rather than considering the physics of ice accretion or actual condition of the iced surface.

The correlation developed by LEWICE [25] which relates the metrological condition with equivalent sand grain roughness as shown in equation (5.2) is used in the present study.

$$
\begin{aligned}
k_s &= k_{s,V_\infty} k_{s,LWC} k_{s,T}\, 0.00117C, \\
k_{s,V_\infty} &= 0.4286 + 0.0044139V_\infty, \\
k_{s,LWC} &= 0.5714 + 0.2457LWC + 1.2571LWC^2, \\
k_{s,T} &= 46.8384\left(\frac{T_\infty}{1000}\right) - 11.2037.
\end{aligned}
\tag{5.2}
$$

The three parameters included in equation (5.2) have a significant influence on the type of ice growth. However, other external parameters are missing in these correlations would bring some limitations in the calculation of surface roughness. Generally, the roughness may be updated at each update of airflow solution to account the roughness effects properly.

5.2.2 Turbulence model

The heat transfer coefficient is strongly influenced by the turbulence model used in the numerical simulations.

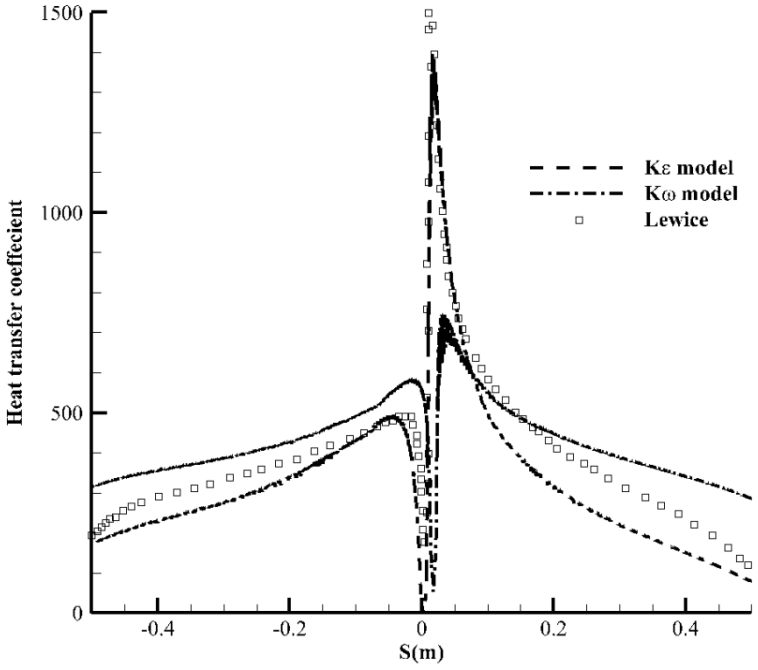

Figure 5-5 Heat transfer coefficient by different turbulence model

Therefore it is necessary to carefully model the turbulence effect using relevant turbulence model. In order to check the effect of turbulence model, the heat transfer coefficient provided by different turbulence model under same metrological and surface roughness is shown in Figure 5-5. Furthermore, the present simulated results are compared with reliable sources in Figure 5-5.

The turbulence model Spalart Allmaras [55] is not capable of invoking the surface roughness effect in the model. However, there is a variety of modified version of Spalart

Allmaras model to invoke the surface roughness can be employed in the current simulations. In Figure 5-5 shows the heat transfer coefficient results provided by *K-ω SST* model and *K-ε* turbulence model. The comparison shows that the maximum heat transfer given by *K-ω SST* is far lower than the *K-ε* turbulence model results. Furthermore, the comparison reveals that the *K-ε* turbulence model results well agreed with the other computation models. As the heat transfer coefficient decreases, the ice accretion also decreases as explained in section 5.2.1. Therefore, in this current work, *K-ε* turbulence model is used for the simulations. The ice shapes formed by two different turbulence models are shown in Figure 5-6.

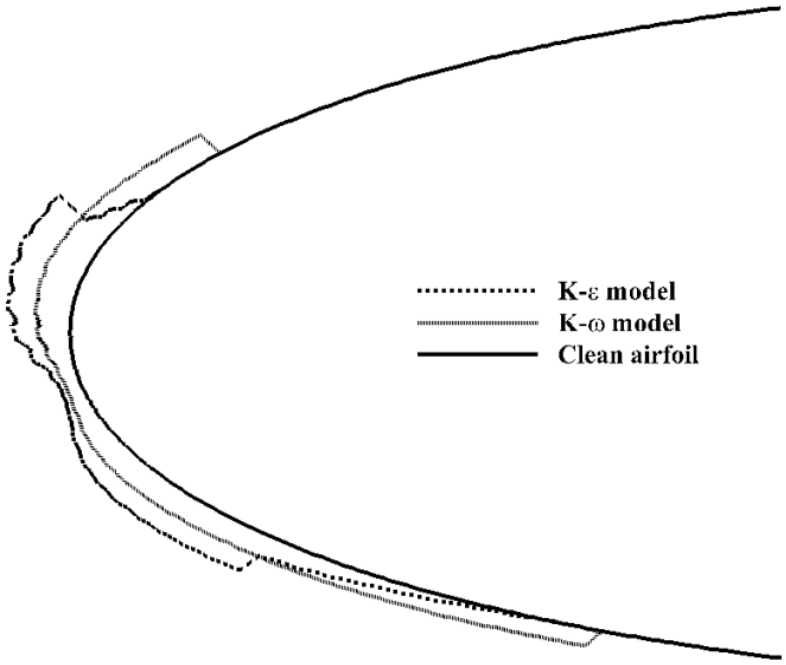

Figure 5-6 Turbulence model effect on ice shape

5.3 Evaporation model

Evaporative heat transfer is one of the major cooling parameters next to convective cooling which affects the ice accretion shape. As explained in section 4.1, the evaporative heat transfer is evaluated from convective heat transfer coefficient using Chilton and Colburn [87]. In order to show the effect of evaporative cooling in ice accretion modeling, an attempt

was made to simulate an ice accretion on an airfoil surface with and without evaporative cooling effect. In Figure 5-7, ice accretion on an airfoil under same metrological conditions with and without evaporative cooling is shown. The only difference in these two simulations is the inclusion of the evaporative heat transfer which modified the ice shape.

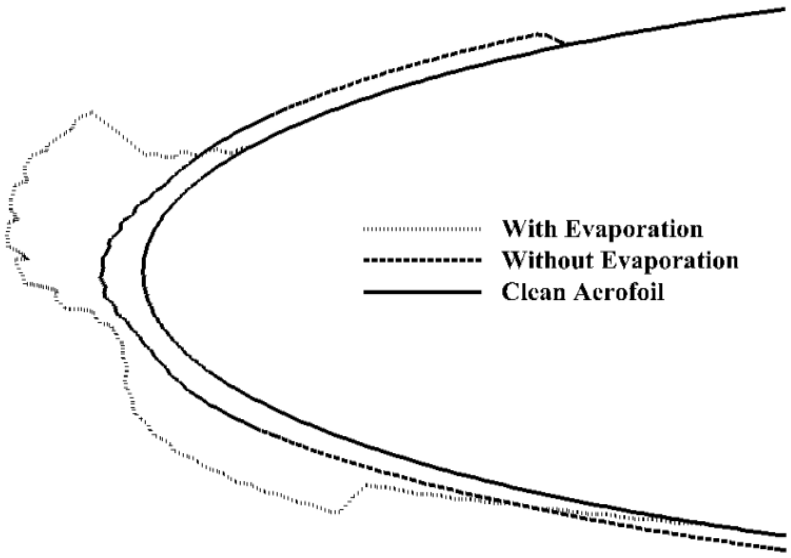

Figure 5-7 Evaporation model effect on ice shape

Although this is a short time simulation, the ice shapes are quite different and we can expect more significant for longer ice accretion time steps. It is evident that the evaporative cooling affects the freezing rate such that more water flows than freezes in evaporation-deactivated case. Therefore, it is critical to predicting the evaporation mass and proper models to be incorporated in ice accretion models.

5.4 Multi-shot ice model

In ice accretion modeling, two kinds of calculations are basically used to determine the ice shape with respect to time. The single-shot ice accretion is the simplest one and less time-consuming method in which the ice shape is computed using only the original air flow field and droplet solutions. On the other hand, in multi-shot ice accretion method, the airflow field and droplet solutions are updated after a certain number of ice accretion time steps. Both

methods are illustrated pictorially in Figure 5-8. In multi-shot ice accretion approach, geometric deformation of the surface due to ice accretion should be taken into account for each airflow field and droplet calculation. This multi-shot ice accretion approach can be termed as quasi-steady approach and the true time-accurate unsteady approach was not in use due to the enormous requirement of computation power. A true unsteady ice accretion model can be illustrated as seen in Figure 5-9. In addition to high computation cost, another complexity in multi-shot ice accretion approach is the grid deformation to account the ice growth in between each time step. Grid deformation requires a strong algorithm to solve the input given by ice accretion solver. However, there is an option to regenerate the grid using the deformed ice shape which is feasible and can be done manually.

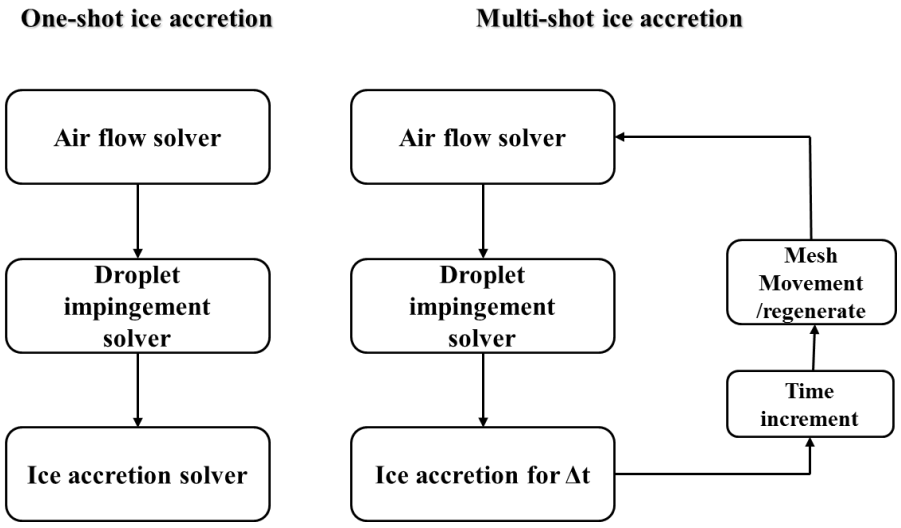

Figure 5-8 Single-shot and multi-shot ice accretion approach

In the present work, an automatic grid regeneration methodology is implemented using script program for conventional grid generation software. The algorithms were built such that independent on the shape, the number of cells, and nodes in a deformed surface, the automation will be incorporated in the ice accretion package. Hence, at the end of each ice accretion calculation, the script to be run in the grid generation software is updated with respect to the ice results.

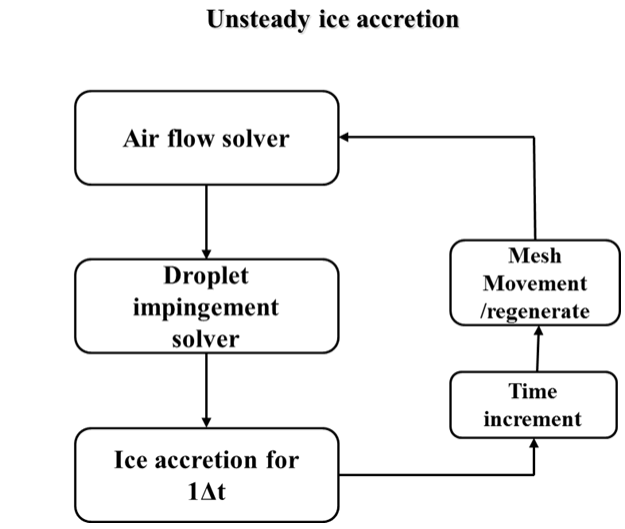

Figure 5-9 Fully unsteady ice accretion approach

The ice shape generated by both single and multi-shot ice accretion solvers are illustrated in Figure 5-10. It can be observed that the final ice accretion for a given metrological conditions under single and multi-shot ice accretion simulations are different. The implementation of multi-shot approach increases the accuracy of the ice accretion result, however, no proper guide exists on the number of shots to be used to improve accuracy. Therefore, depending on each test case, the accuracy and the required number of shots are different, and the computation requirement is increasing the number of shots increases.

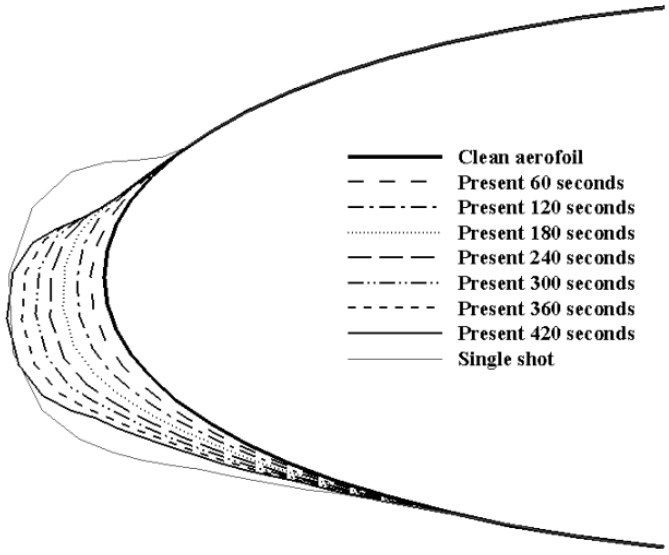

Figure 5-10 Multi-shot effect on ice shape

Chapter 6. Validation

The physical models described in previous chapters were implemented into the numerical method and the results generated by these models validated with the available experimental results are explained in this chapter. Data from several experiments are used in this chapter to validate the developed computational model starting from air solution and followed by droplet solution and ice accretion results.

6.1 Validation of droplet solvers

The developed droplet solvers are based on SWDE as explained in previous chapters. Before the droplet solver validation, it is necessary to first validate the air solver, as an accurate air solution is essential for the accurate prediction of droplet solution. Hence, in every droplet validation case, air solution validation is also conducted.

6.1.1 Two-dimensional droplet solver

The validation started with two single element airfoils. The first one is GLC305 which was experimentally analyzed [88] by NASA in icing research tunnel (IRT). The Mach and Reynolds number are 0.23 and 4.9×10^6, respectively. Figure 6-1 shows the grid and pressure distributions around the GLC305 airfoil under a given boundary condition. The grid is clustered near the airfoil for better capturing of physics near the wall surface. The pressure coefficient and collection efficiency around the GLC305 airfoil under given metrological condition are compared with the experimental result as shown in Figure 6-2, which was simulated with a liquid water content of 0.05 g/m^3 and a droplet diameter of 21μm. Here, the collection efficiency is a non-dimensional number which measures the potential of ice accretion. Generally, the collection efficiency is based on droplet volume fraction, velocity and normal vector on the solid surface as shown in equation (2.27).

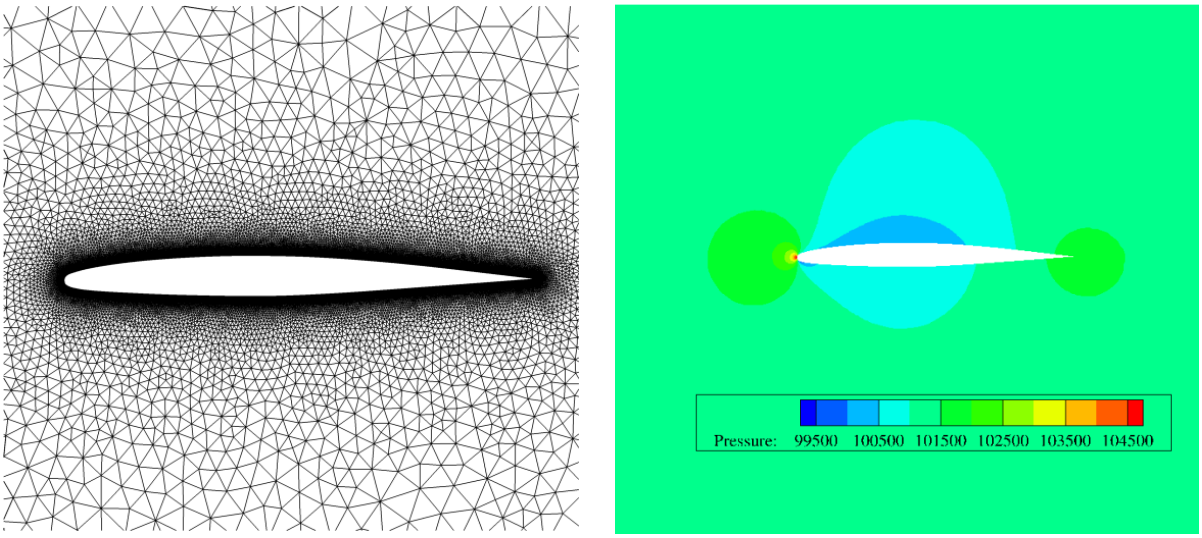

Figure 6-1 Grid (left) and pressure (right) distribution around GLC305 airfoil

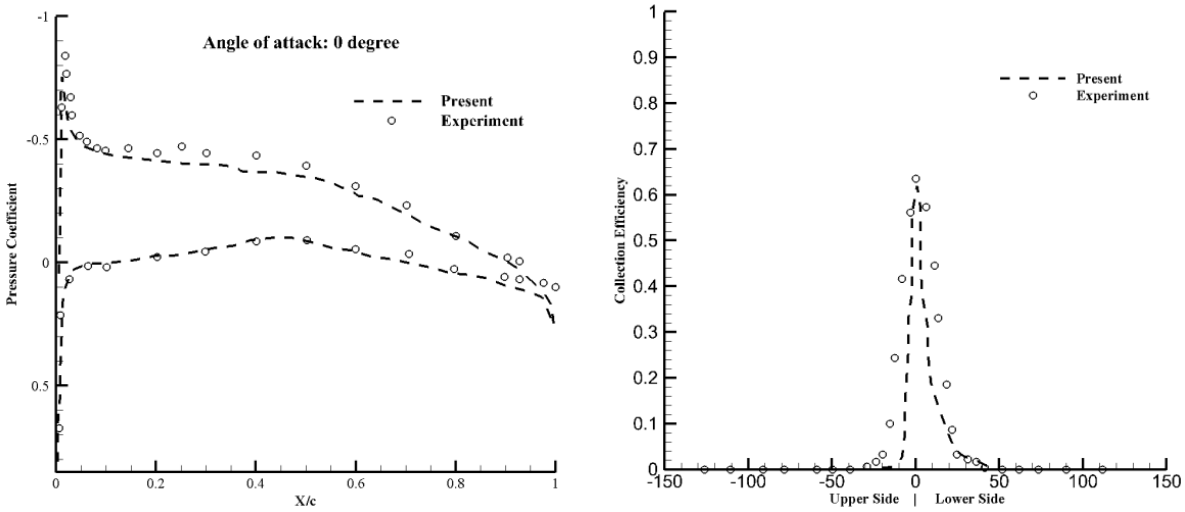

Figure 6-2 Pressure coefficient (left) and collection efficiency (right) on GLC305 airfoil at M = 0.23, Re = 4.9×10^6, LWC = 0.05 g/m^3, and MVD = 21µm

Next, to the GLC305 airfoil, a thick airfoil NACA65$_2$415 was simulated with 8 degree angle of attack. The ambient condition used for the simulation of NACA65$_2$415 is given by NASA IRT experiments. The Mach, Reynolds number, LWC, and MVD are 0.23, 4.9×10^6, 0.19 g/m^3, and 21µm, respectively. The computed pressure distribution and pressure coefficient are shown in Figure 6-3. The computed LWC distribution and collection efficiency comparison is shown in Figure 6-4. The comparisons showed that the current computational results are in well agreement with the experimental results under given metrological conditions. Hence, this present computational model can be used for further

investigation of air and drop solutions. The presented two results are for conventional icing and it is also necessary to validate the developed SLD droplet solver. Therefore, the new second- order positivity-preserving unstructured finite volume upwind scheme for droplet impingement in SLD conditions was validated for NACA 23012 airfoil, which was tested for

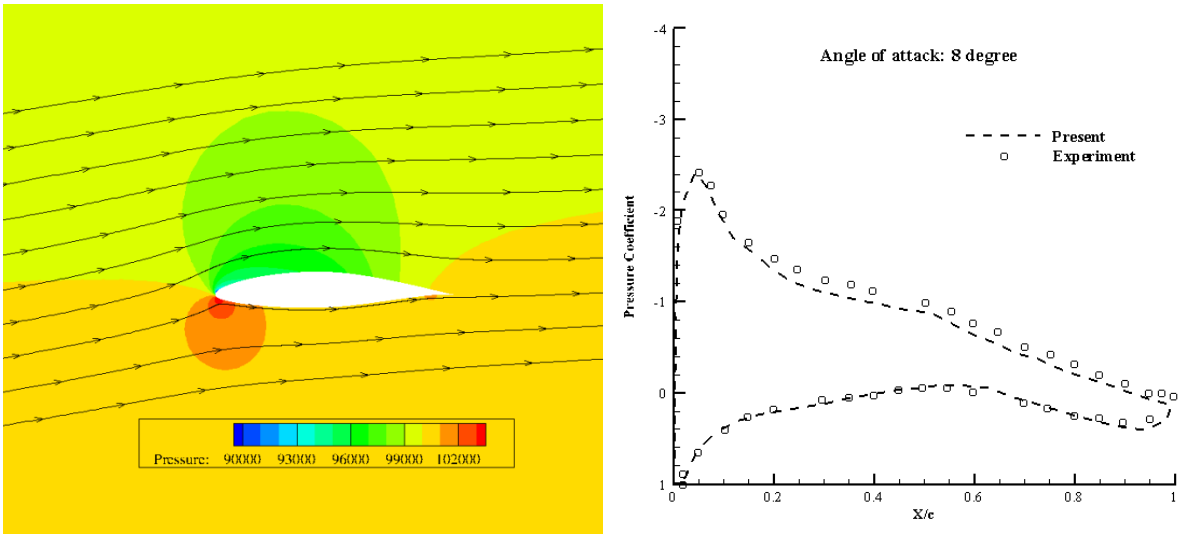

Figure 6-3 Pressure distribution (left) and coefficient (right) around NACA65$_2$415 airfoil at M = 0.23, Re = 4.9x10^6

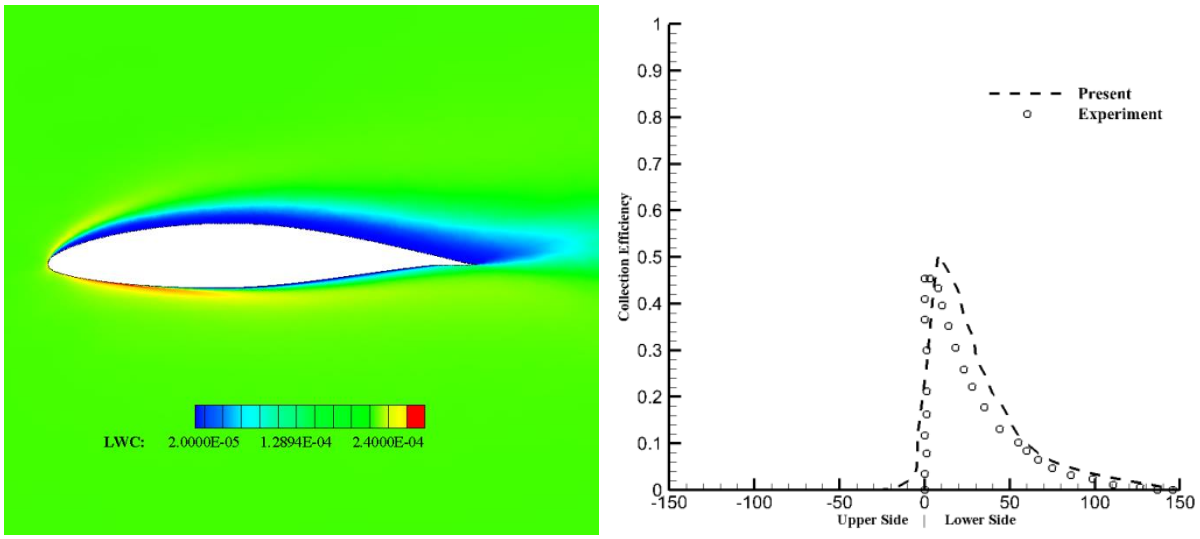

Figure 6-4 LWC distribution and collection efficiency around NACA65$_2$415 airfoil at LWC = 0.19 g/m^3, and MVD = 21µm

air flow and droplet impingement in NASA Langley Low Turbulence Pressure Tunnel, and NASA's Glenn's Icing Research Tunnel (IRT), respectively [89]. The free-stream Mach and Reynolds numbers are 0.23 and 4.6x10^6, respectively. SLD cases with monodisperse droplet

diameters of 111 μm (LWC of 0.73 g/m^3) and 154 μm (LWC of 1.44 g/m^3) were considered in the present study.

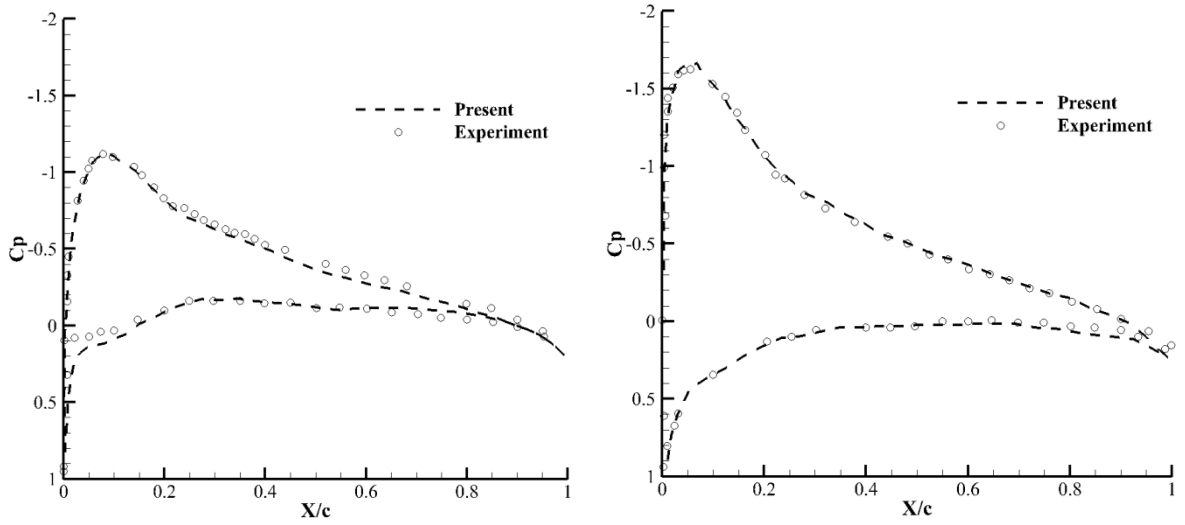

Figure 6-5 Pressure coefficient on NACA 23012 airfoil at AoA = 2.5 degrees (left) and AoA = 5 degrees (right)

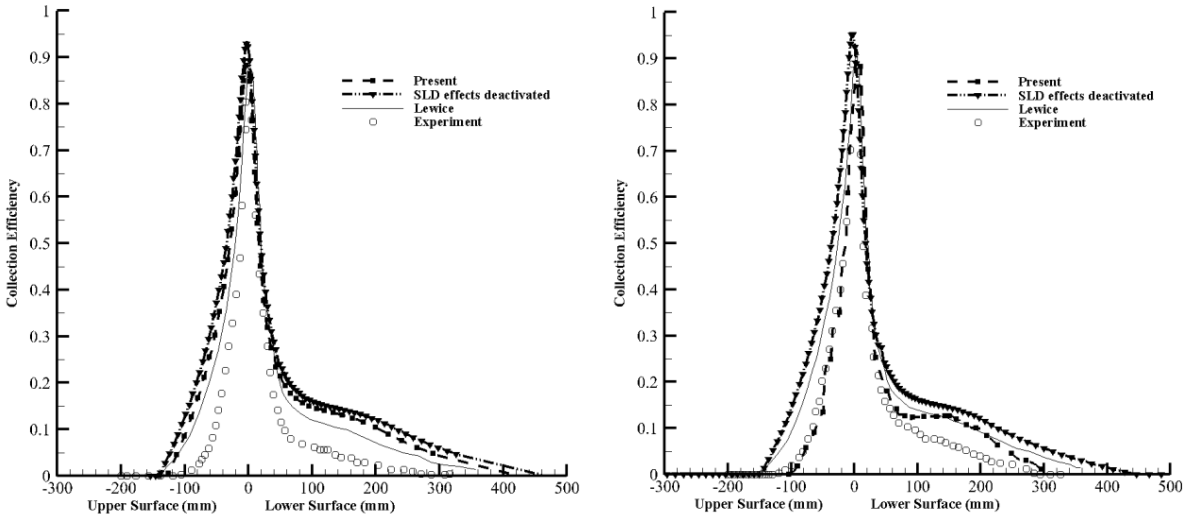

Figure 6-6 Collection efficiency around on NACA 23012 airfoil at MVD = 111 μm (left) and 154 μm (right)

Figure 6-5 shows the pressure coefficient around the NACA23012 airfoil for angles of attack at 2.5 and 5 degrees, respectively. In these clean air flows, a good agreement was found for pressure coefficients between the computational and experimental results, demonstrating that the present unstructured Navier-Stokes-Fourier code is capable of producing clean air information for droplet impingement.

Figure 6-6 shows the comparison of the computational and experimental results for the local collection efficiency. Further, Figure 6-6 clearly shows that the collection efficiency and impingement area of SLD-deactivated cases are relatively higher than those of SLD-activated cases. The computational results are in fairly good agreement with the experimental data, and in particular, the maximum value of the droplet impingement intensity and the impingement area. Nonetheless, the collection efficiency on the lower side of the airfoil is slightly over-predicted in comparison to the experiment. This gap may be due to the difference of droplet distribution -- it was mono-disperse in the computation versus 27 bins of the spray cloud drop distributions in the experiment.

The next airfoil used for validation is a multi-element airfoil case. Multi-element airfoils are used in a variety of aerodynamic devices from airplanes to cars depending on the lift or drag requirements. These airfoils are typically closely coupled airfoil consisting of two or more elements as shown in Figure 6-7.

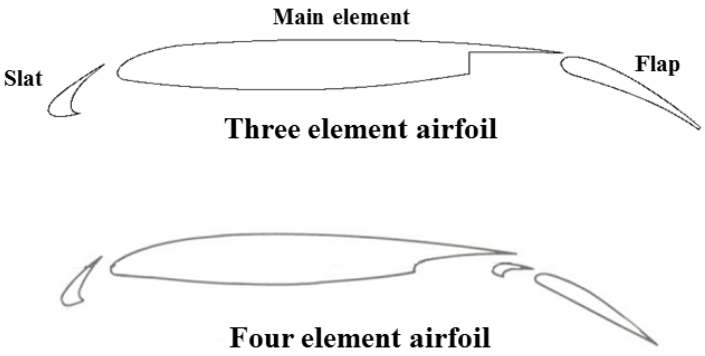

Figure 6-7 Multi-element airfoil

Generally, multi-element airfoils are often used to satisfy the need for high lift as they have the capability to produce more lift at low speeds and high angle of attacks. The component slat located ahead of the main element delays the flow separation which makes these airfoils operable at very high angle of attacks without any great performance penalties. Due to the maintenance and manufacturing complexities, most of the commercial aircraft are using three element airfoils rather than four or more elements.

The multi-element wing system with small gaps complicates generation of mesh and capture of flow features also complicated. The boundary layer transition, flow separation, and interaction of wakes bring difficulties in the simulation of multi-element airfoils. In order to show the complexity of the flow pattern over a multi-element, an NHLPL1T2 three element airfoil is simulated as shown in Figure 6-8.

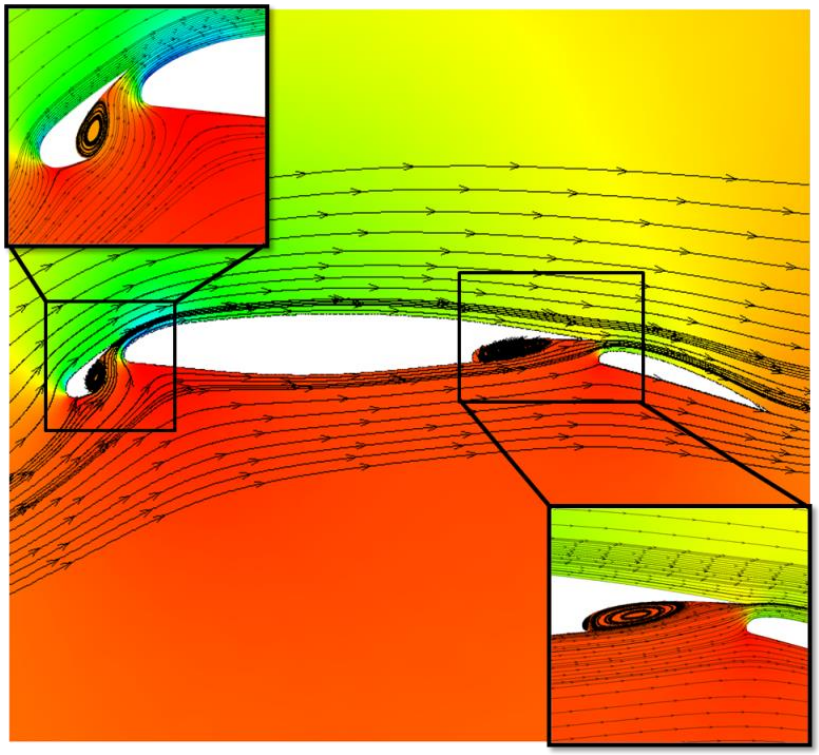

Figure 6-8 Flow over an NHLP L1T2 three element airfoil

Generally, multi-element wings are in action during the take-off and landing to increase the lift in the former and to lower the stall speed in the latter. An ice accretion during take-off would collapse the lift and might affect the landing performance of an airplane. Due to the location and angle of deflection, flaps acquire more ice accretion at the lower surface that could affect the performance. Therefore, ice accretion on a multi-element is a significant threat during take-off and landing. An attempt was made to investigate the performance loss of a multi-element airfoil under conventional and SLD icing conditions. The selection of an appropriate multi-element airfoil to investigate the ice accretion effects is initiated. For this current investigation, a multi-element airfoil experimentally studied by NASA is considered.

Since the experimental results are available, the current numerical results are compared with the experimental results before proceeding to the performance degradation.

The experimental collection efficiency data pertaining to the specified droplet impingement has originated from a study performed by Papadakis et al. [90] at NASA Glenn's IRT. The landing configuration of a three-element airfoil with slat deflection of 30^0 and flap deflection of 30^0 is used for the icing study. The numerical simulations of ice accretion are performed under geometric, aerodynamic, and meteorological conditions shown in Table 6-1.

	Case 1	Case 2	Case 3	Case 4
Velocity (m/s)	76.0	76.0	76.0	76.0
Temperature (K)	276.2	276.2	276.2	276.2
LWC (g/m^3)	0.15	0.15	0.19	0.19
MVD (μm)	21.0	21.0	92.0	92.0
AoA (deg)	0	4	0	4

Table 6-1 Metrological conditions for multi-element airfoil

Figure 6-9 shows the unstructured mesh distribution with approximately 55,000 nodes and 95,000 triangular elements around the three-element airfoil. For clean air, a non-slip condition for the wall and the Riemann invariant for far-field boundary condition are employed. In weakly coupled droplet solvers, the accuracy of droplet solution mostly depends on the airflow solution, hence it is important to validate the airflow solution. Figure 6-9 shows the pressure coefficient on a three-element airfoil for 0 degree angle of attack. The collection efficiency comparison on the multi-element airfoil slat and flap for case 1 is shown in Figure 6-10. Further, collection efficiency and LWC distribution on the main element for case 2 metrological conditions are shown in Figure 6-11. Near the upper side, cove region of slat, and cove region of the main element, a shadow region area appears signifying a very low density of LWC. The larger shadow area around the upper side of the model is due to the effect of the free-stream angle of attack. The shadow regions indicate that the droplets impingement does not occur on the surface except specified area of the model. Generally, at

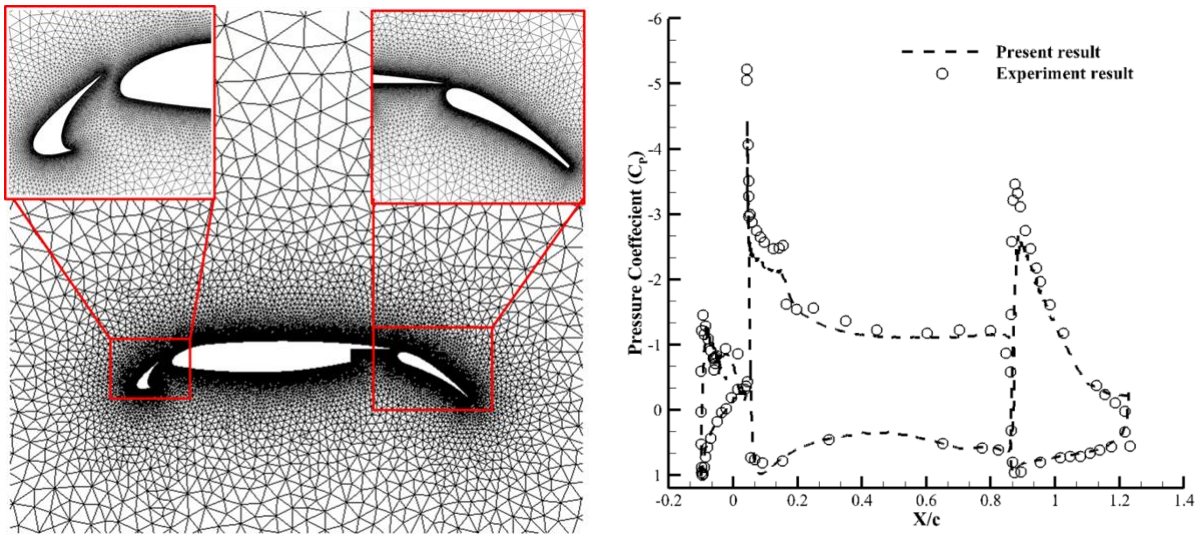

Figure 6-9 Grid distribution (left) and pressure coefficient (right) at α = 0, M = 0.23, Re = 4.9 million on the muli-element airfoil

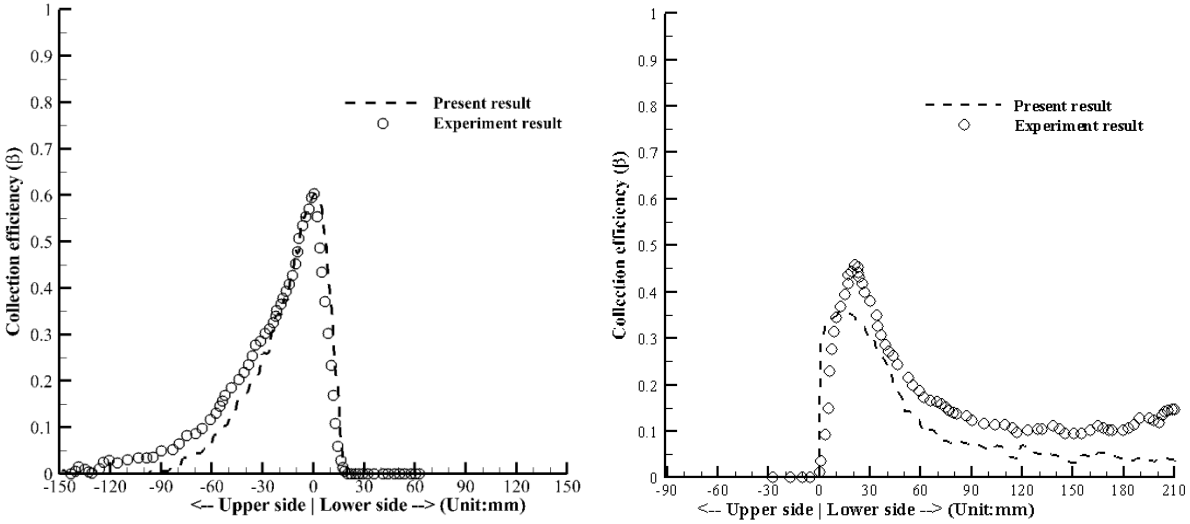

Figure 6-10 Collection efficiency comparison on slat (left) and flap (right) for case 1

zero degrees angle of attack, the impingements of droplets are higher on the leading edge of slat followed by the lower side of the flap. Due to the position of leading edge slat, the main element acquires no significant impingements at zero degree angle of attack (cases 1 and 3). Figure 6-12 illustrates the collection efficiency distributions on the slat for cases 3 and 4. As seen in Figure 6-13, the collection efficiency is increasing with droplet diameter. Furthermore, the impingement area is higher in case 4 which indicates that the droplets diameter is directly

affecting the impingement area. These properties have to be taken into account during the design of ice protection systems. Overall, the present computational results show good agreement with the experimental results.

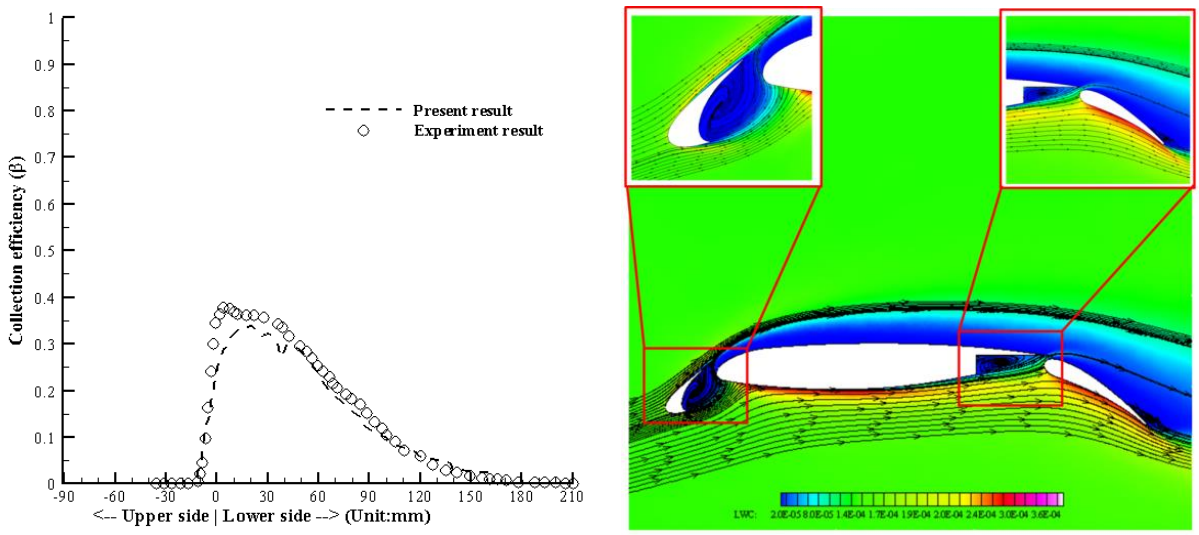

Figure 6-11 Collection efficiency comparison on main element (left) and LWC contour (right) for case 2

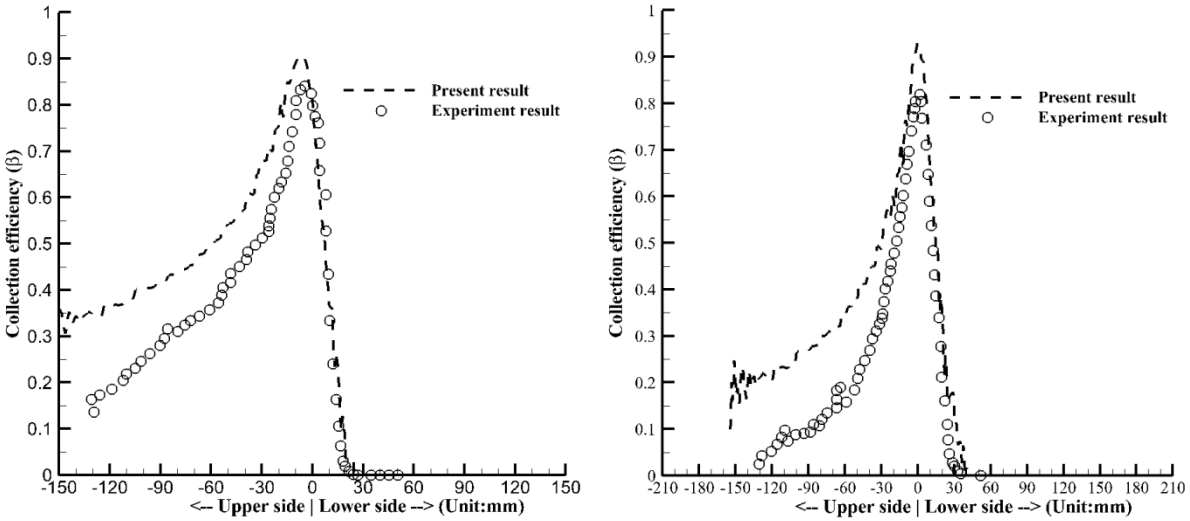

Figure 6-12 Collection efficiency comparison on slat element for case 3 (left) and case 4 (right)

However, there are some discrepancies which are easily notable in the impingement area. These gaps may be due to the mono-dispersed assumption of the current computational model which can be minimized by using multi-dispersed droplet distribution. In SLD cases, the collection efficiency is generally over-predicted, which renders a room for improvement in the SLD modeling.

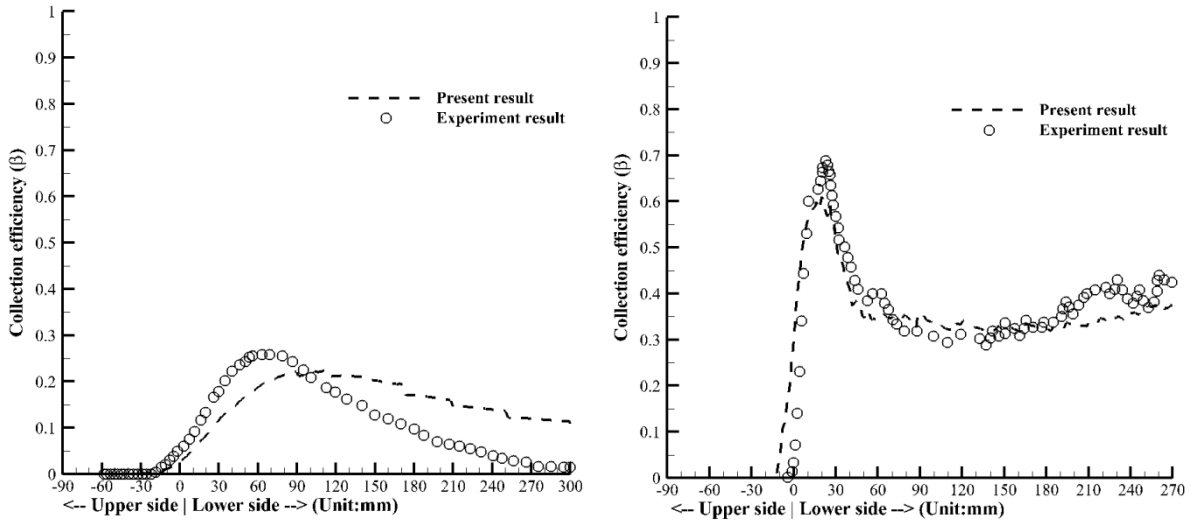

Figure 6-13 Collection efficiency comparison on main element (left) and flap (right) element for case 4

6.1.2 Three-dimensional droplet solver

In order to validate the three-dimensional formulation on tetrahedral grids of the new scheme, a sphere of 0.1504 meters in diameter was considered. This case was experimentally tested in NASA IRT [91]. The unstructured mesh as shown in Figure 6-14 with approximately one hundred thousand cells around the sphere was used in the computations. The free-stream Mach and Reynolds numbers are 0.2236 and 7.9×10^6, respectively.

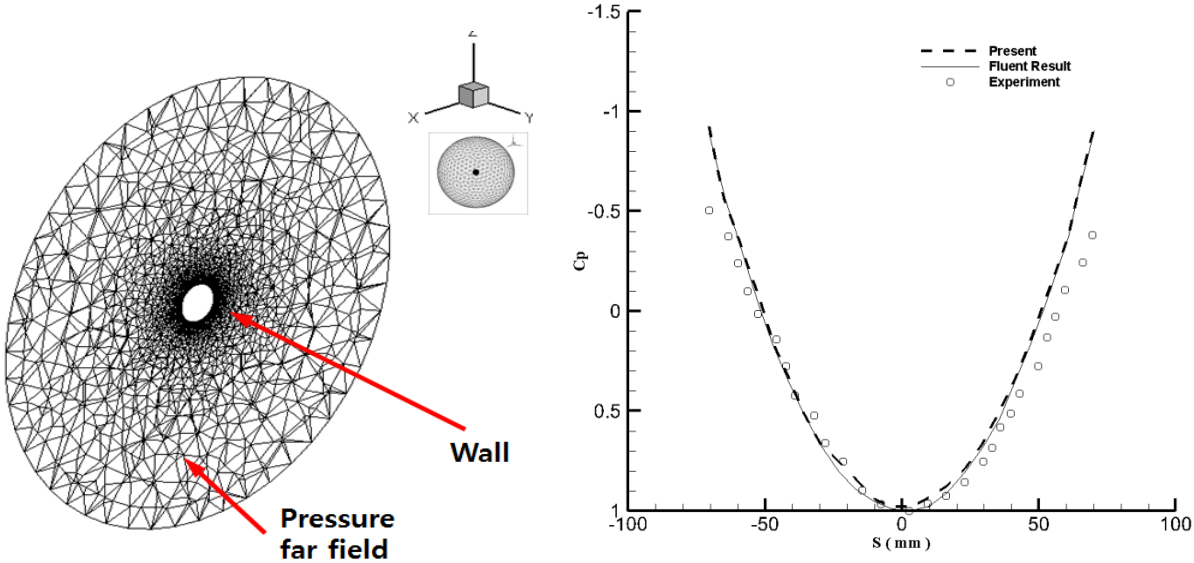

Figure 6-14 Grid (left) and pressure (right) distribution around sphere (M = 0.2236, Re = 7.9×10^6)

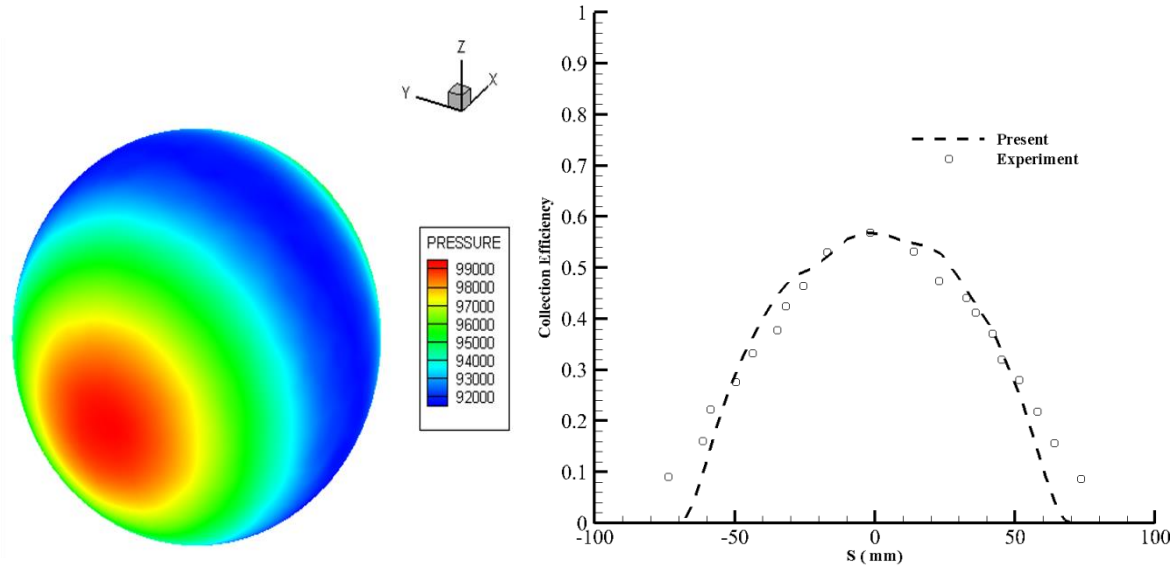

Figure 6-15 Pressure distribution (left) and collection efficiency (right) around sphere at LWC = 0.2 g/m^3, and MVD = 18.7 μm

A non-SLD case with the monodisperse droplet diameter of 18.7 μm (LWC of 0.2 g/m^3) was considered. The pressure coefficient comparison at the central section of the sphere is also shown in Figure 6-15. The Figure 6-15 shows the pressure distribution around the sphere and the comparison between the collection efficiency at the central section of the sphere and the experimental data. The present computational results seem to accurately predict the maximum value of droplet impingement intensity near the stagnation region and the droplet impingement area.

Next to this, the droplet solver is validated on an axisymmetric engine inlet nacelle which was experimentally studied by Papadakis et.al [92]. The geometry of external cowl lines are defined through a super ellipse analytical expression provided by NASA as,

$$\left(\frac{x}{a}\right)^n + \left(\frac{x}{b}\right)^m = 1, \tag{6.1}$$

with $n = 1.0;\ a = 0.2234$ m

$m = 1.96;\ b = 0.05448$ m

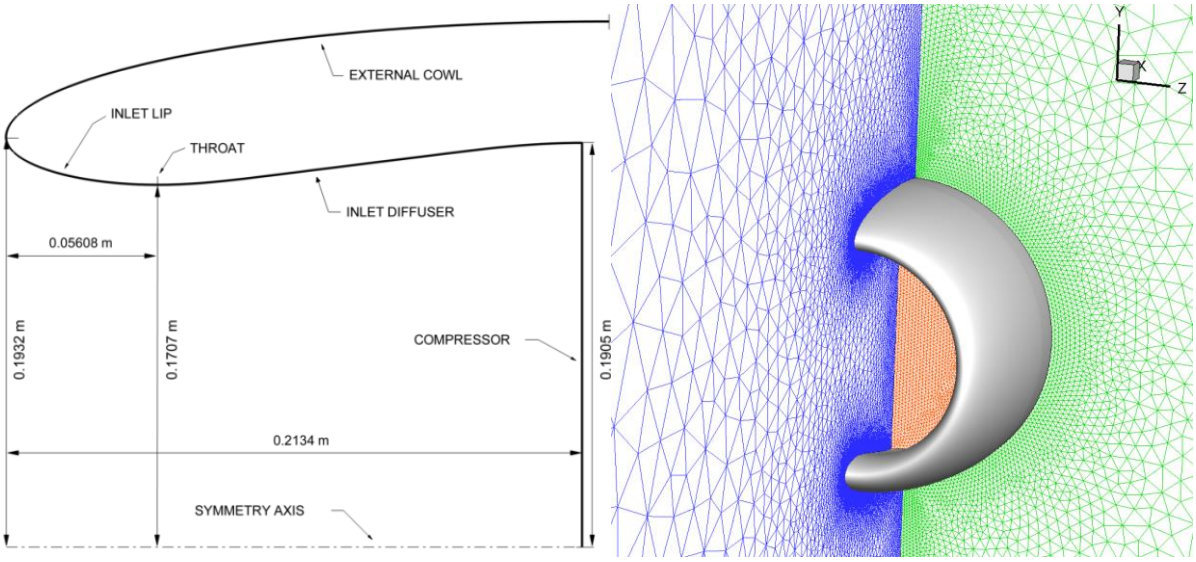

Figure 6-16 Nacelle geometry (left) and mesh (right) around the nacelle

The inlet lip line is described by an ellipse analytical expression as follows,

$$\left(\frac{x}{a}\right)^{2.0}+\left(\frac{x}{b}\right)^{2.0}=1 \tag{6.2}$$

with, $a = 0.05608$ m

$b = 0.2243$ m

The solution of the airflow has been determined by solving Navier-Stokes-Fourier equations with appropriate metrological conditions as shown in Figure 6-17. The θ station on engine inlet nacelle for comparing the experimental results can be seen in Figure 6-17. In Figure 6-18, the air solution obtained is reported as pressure contour and Mach number contour around the engine inlet nacelle under a various angle of attack and mass flow rate. As seen in Figure 6-18, the angle of attack and the mass flow rate have a substantial influence on the stagnation point. Hence, we can expect the same effects in both droplet and ice accretion.

Figure 6-19 and Figure 6-20 show the Mach number variation comparison over the engine inlet nacelle under various metrological conditions. A good comparison is found with the experimental results and it is possible to use this air solution for the evaluation of droplet solution.

Flow conditions	
Mach	0.234
Temperature (K)	280K
LWC (g/m^3)	0.55
MVD (μm)	20.36
AoA (deg)	0 / 15
Mass flow (Kg/s)	7.9 / 10.2

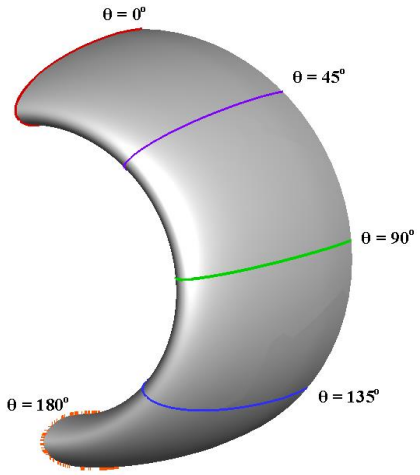

Figure 6-17 Metrological conditions (left) and θ station on engine nacelle (right)

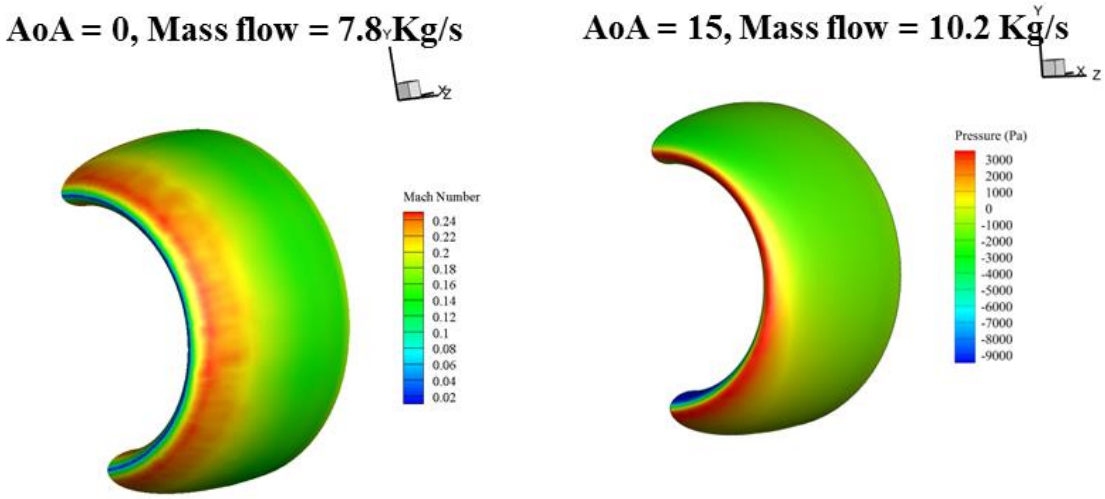

Figure 6-18 Mach number (left) and pressure contour (right)

Next to the air solver, the droplet solver is applied to determine the droplet impingement on the engine inlet nacelle. The collection efficiency is compared with the experimental results and revealed a good agreement as shown in Figure 6-21 and Figure 6-22. The collection efficiency contours at various metrological conditions are illustrated in Figure 6-23 where the effect of angle of attack and mass flow rate can be observed.

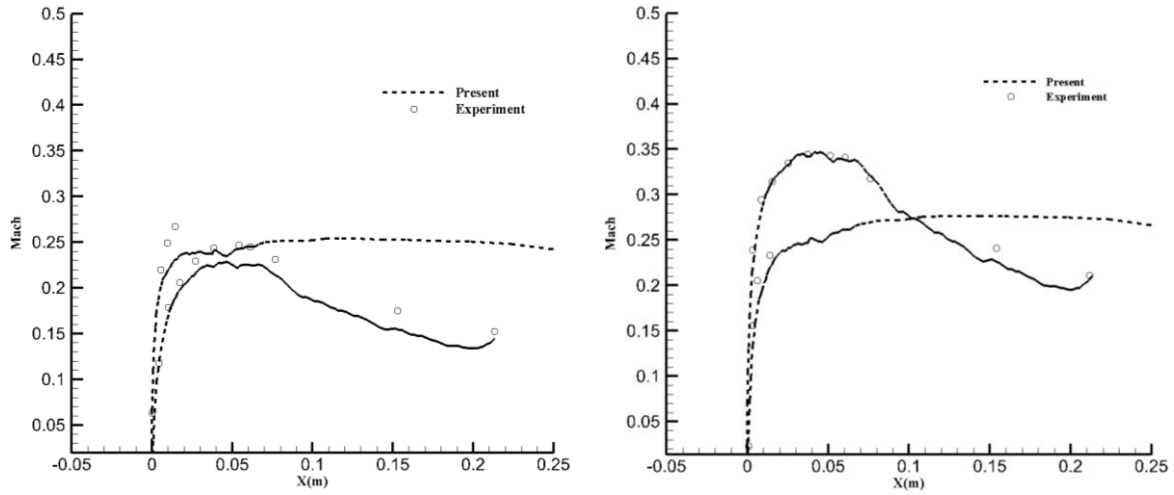

Figure 6-19 Mach number on the surface of the engine inlet mass flow = 7.8 Kg/s (left) and 10.42 Kg/s (right) at 0 degrees AoA

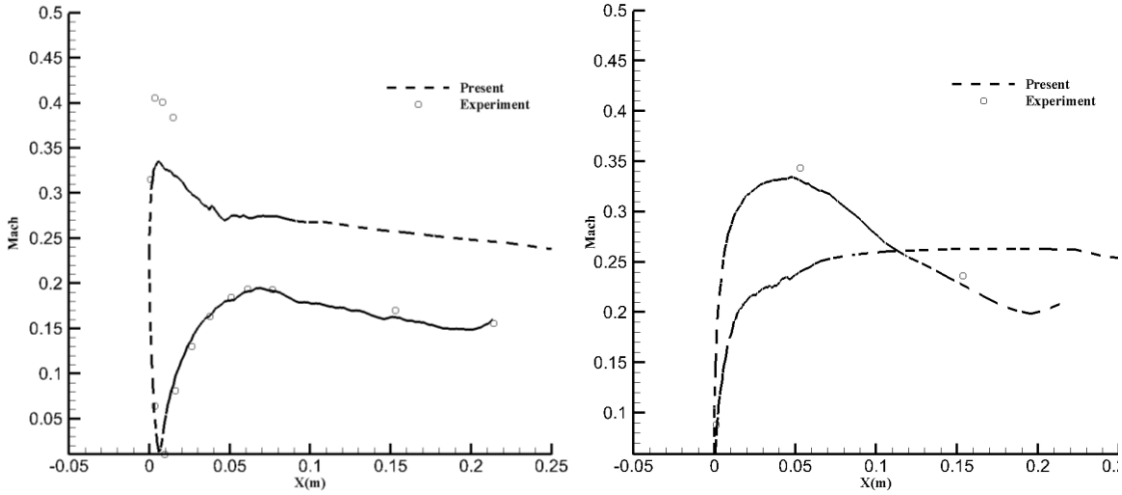

Figure 6-20 Mach number on the surface of the engine inlet at AoA = 0^o, θ = 0, mass flow = 7.8 Kg/s (left) and AoA = 15^o, θ = 90, mass flow = 10.42 Kg/s (right)

Moreover, in the last case, a significant underestimation of the outer impingement limit is found and similar discrepancies are also reported by several researchers using their own codes in the computation of numerical impingement. Since all the trends and some details of the collection curves seem to be well represented in the present study, further studies and provision of updated wind tunnel database on this axisymmetric or similar case and to extend the validation phase of the three-dimensional impingement method to other geometries of interest.

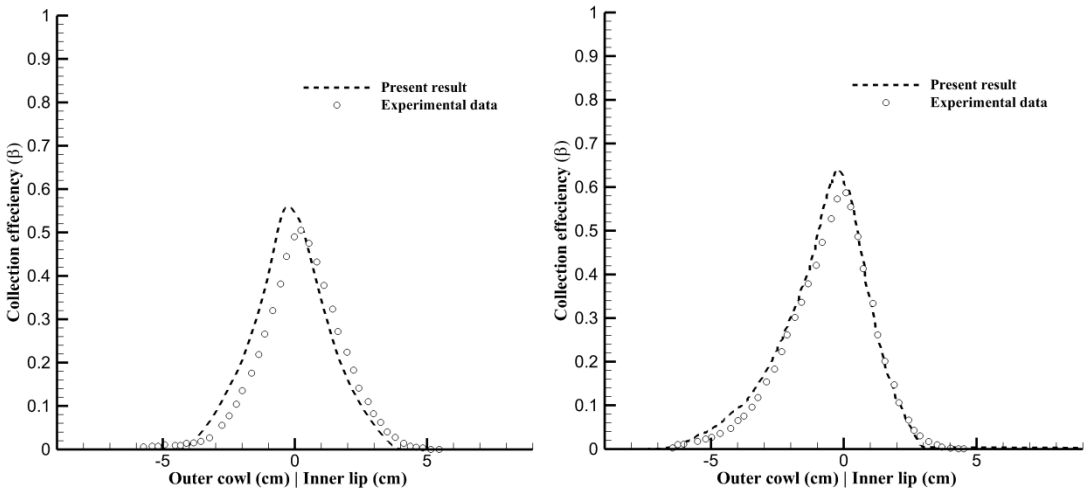

Figure 6-21 Collection efficiency on the surface of the engine inlet AoA = 0^o, θ = 0^o, mass flow = 7.8 Kg/s, MVD = 20.36 μm (left) and AoA = 0^o, θ = 90^o, mass flow = 10.2 Kg/s, MVD = 20.36 μm (right)

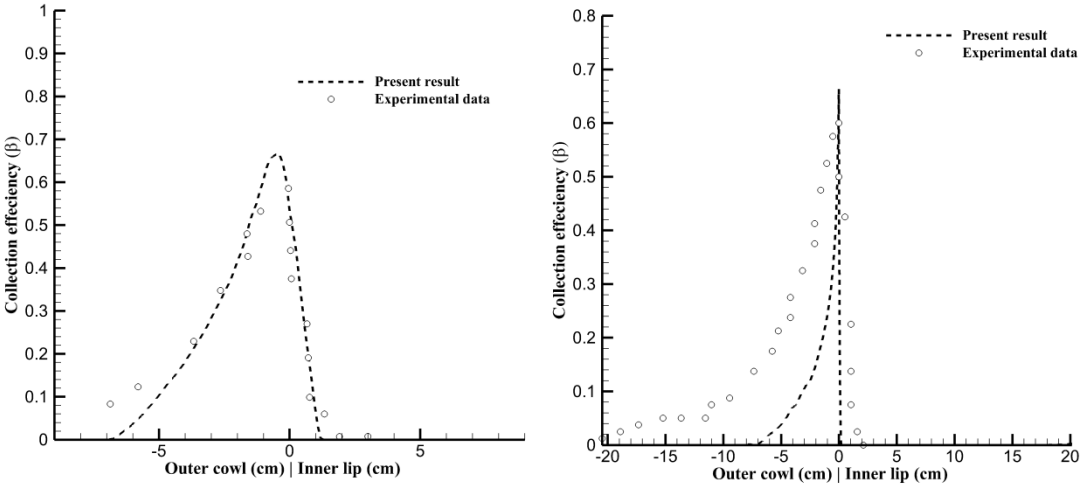

Figure 6-22 Collection efficiency on the surface of the engine inlet AoA = 15^o, θ = 90^o, mass flow = 7.8 Kg/s, MVD = 20.36 μm (left) and AoA = 15^o, θ = 180^o, mass flow = 10.2 Kg/s, MVD = 20.36 μm (right)

Finally, in order to validate the new three-dimensional unstructured finite volume upwind scheme for droplet impingement in SLD conditions, a swept horizontal tail wing was considered. The tail wing, with a sectional airfoil NACA64A008, a span of 121.92 cm, a leading edge swept angle of 29.1 degrees, a root chord of 116.21 cm, and the taper ratio of 0.62, was experimentally tested in NASA IRT by Bidwell and Papadakis [92]. Figure 6-24 shows the geometry of the tailplane and the unstructured mesh with approximately two hundred thousand cells.

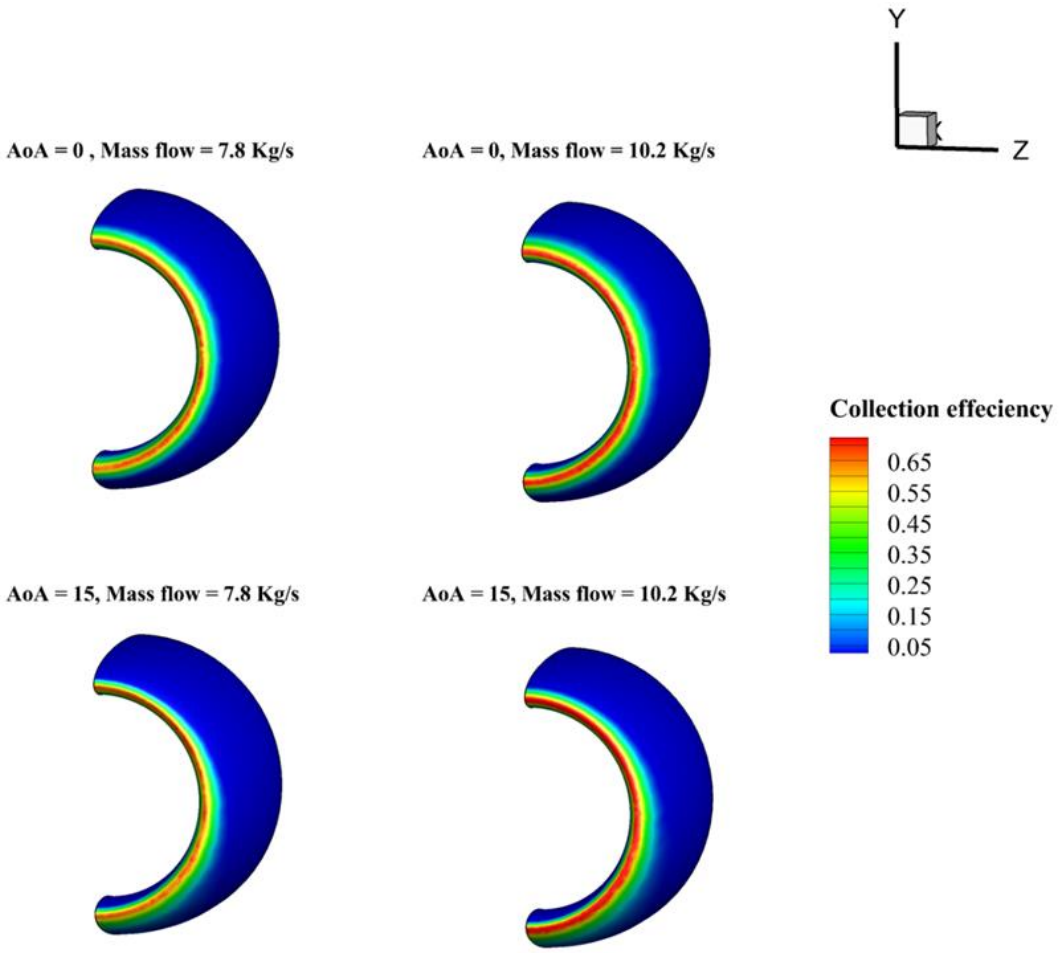

Figure 6-23 Collection efficiency contour on the surface of the inlet

The Navier-Stokes code for the clean air flow was first validated with the experimental data with free-stream conditions of Mach number 0.2236, pressure 95,840 Pa, and temperature 280 K. The pressure coefficients at two sections of the horizontal tail are shown in Figure 6-25. It can be seen that the present computational results are in qualitative agreement with the experimental data. To confirm the capability of the present droplet solver to handle both the simple non-SLD and complicated SLD cases, monodisperse droplet diameters of 21 and 92 μm (LWC of 0.2 g/m3) were considered. Figure 6-26 shows the collection efficiency distributions of the wing at a section of 92 percent of span. Generally, the maximum value near the stagnation region and the impingement area essential in the study of ice accretion and IPS design are well captured in both cases, in comparison with other computational results (LEWICE 3D based on the panel method) and the experimental

data. In addition, the increase of the maximum value in collection efficiency due to the large droplets is clearly illustrated. However, the collection efficiency in the rear of the stagnation region is slightly over-predicted in comparison to the experimental data.

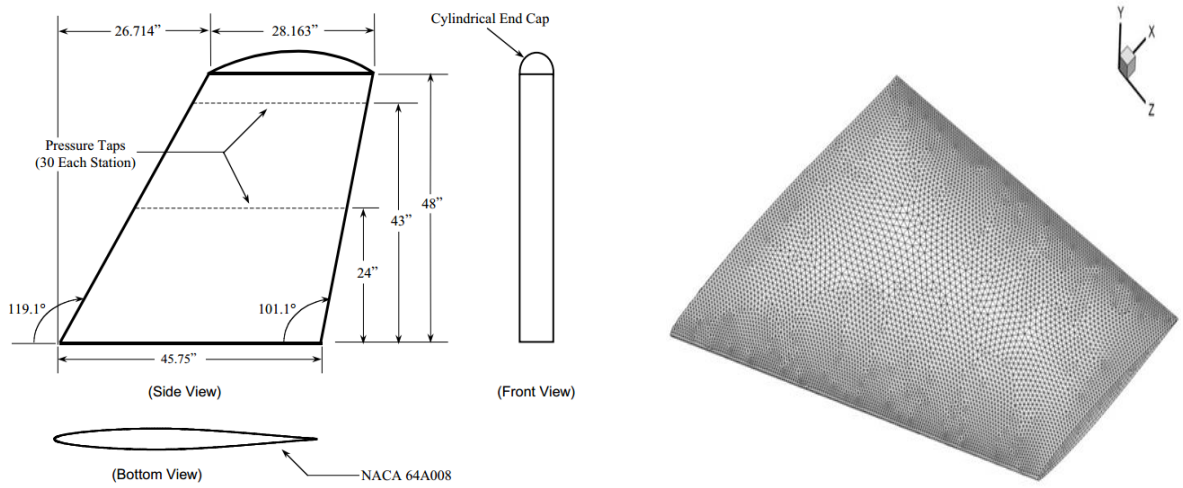

Figure 6-24 Swept tail geometry (left) and mesh topology (right) of NACA64A008 swept wing

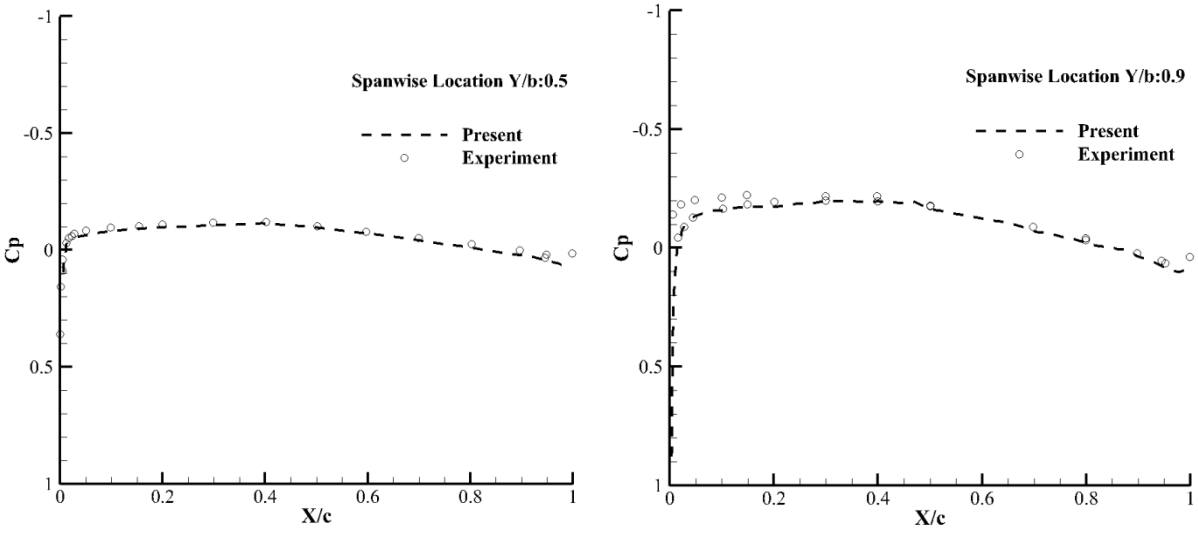

Figure 6-25 Pressure coefficient comparison at y/b = 0.50 (left) and y/b = 0.9 (right) for swept wing NACA64A008 at M = 0.226 and T = 280 K

Furthermore, a non-zero angle of attack case with six degrees as shown in Figure 6-27 was considered. The generic features in the collection efficiency are highly similar with the two-dimensional SLD case as depicted in Figure 6-6 where an abrupt increase near the stagnation point and the gradual decrease on the lower side of the sectional airfoil can be observed. The collection efficiency and impingement area are also found to be higher in

SLD-deactivated cases, highlighting the importance of SLD effects. In the non-SLD case, the agreement between computational predictions and experimental data is excellent. However, similar to previous SLD cases, the new scheme, including LEWICE 3D, over-predicts the

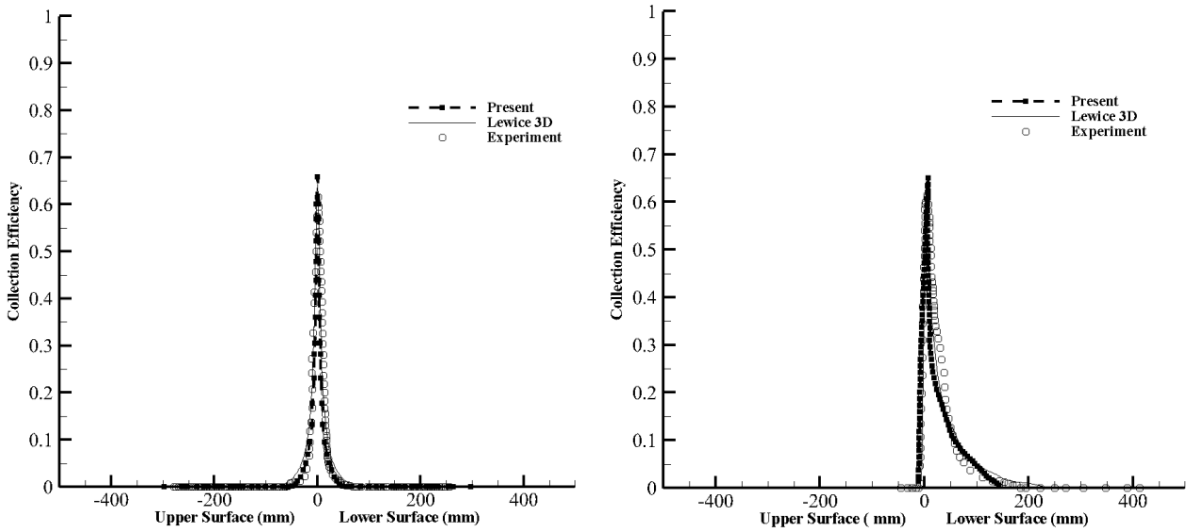

Figure 6-26 Collection efficiency comparison at a section of 92 % of span of swept wing NACA64A008 at AoA = 0 (left) and AoA = 6 (right) for 21μm

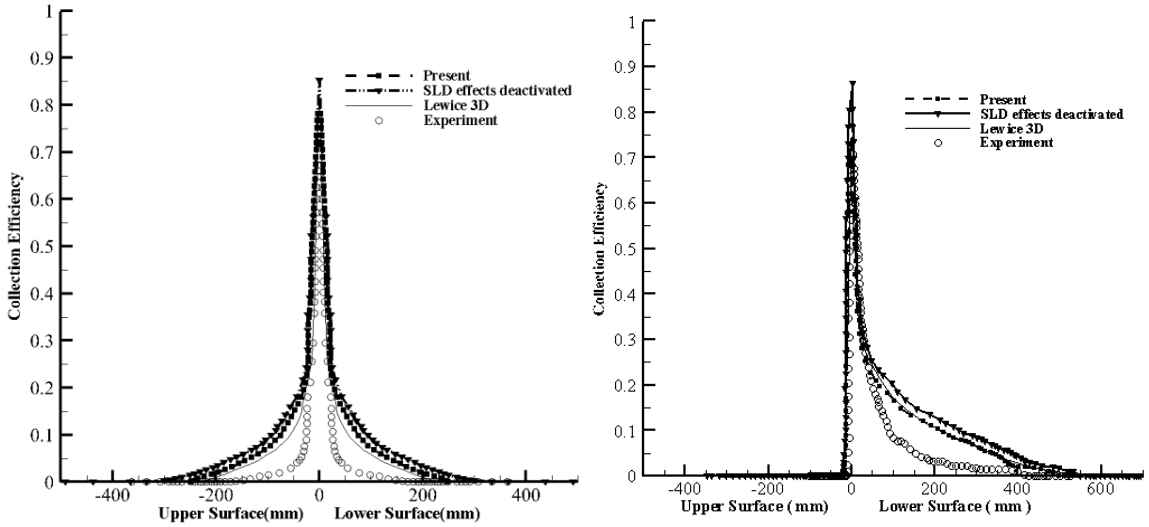

Figure 6-27 Collection efficiency comparison at a section of 92 % of span of swept wing NACA64A008 at AoA = 0 (left) and AoA = 6 (right) for 92μm

collection efficiency on the lower side of the sectional airfoil. This gap may again be due to the difference of droplet distribution; mono-disperse in the computation versus multiple bins of the spray cloud drop distributions in the experiment. However, a definitive explanation for this discrepancy is not yet available and further study seems to be needed to resolve it.

6.2 Validation of ice accretion solver

The ice accretion models described in Chapter 5 have been implemented in the numerical method. Several ice accretion experimental results are used to validate the present ice accretion numerical data.

6.2.1 Two-dimensional ice accretion solver

NACA0012 is considered in order to validate the developed 2D ice accretion solver ice shapes on a symmetric airfoil. The results from current numerical methods are compared with the experimental results obtained by NASA IRT [93]. As the ice type changes from rime to glaze depending on the ambient temperature, validation of ice accretion also starts with rime ice case. The metrological condition for the first test case is as follows,

Temperature	243.78 K	MVD	51.04 μm
Pressure	100 kPa	LWC	2.58 g/m^3
Velocity	57.43 m/s	Mach	0.18
AoA	0^o	Exposure time	246 Sec

Table 6-2 Metrological conditions for test case1

As explained by ice physics concerning ice, the runback water reduces and almost all the droplets freeze upon impact on the surface when the temperature reduces to -20^0C. In the first test case, the ambient temperature is 243.78 K which is much lower than -20^0C. Therefore, rime ice with very less runback water can be expected under this metrological condition. The ice shape predicted by the present numerical method is shown along with experimental results in Figure 6-28. The ice shapes obtained by various options were shown where the ice shape predicted by full rime option is much closer to the experimental results. Runback ice occurs in case of glaze ice model activated, hence ice thickness is high at the upper and lower part of the airfoil.

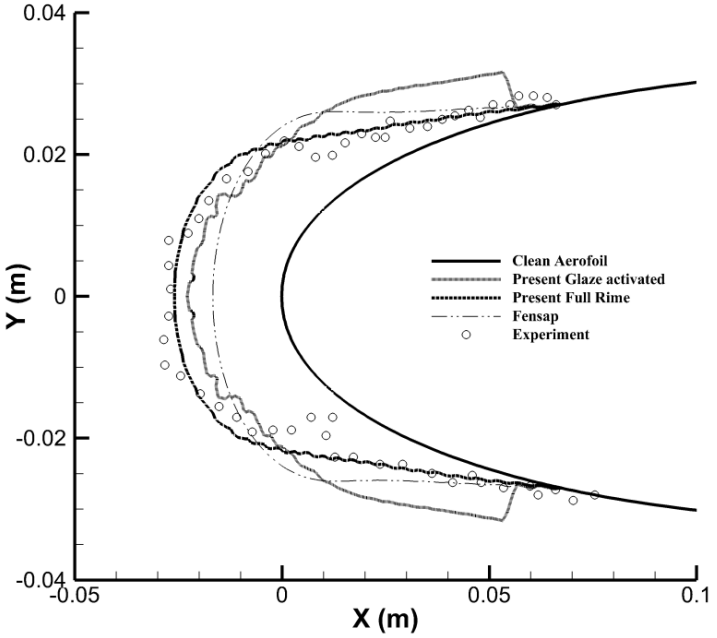

Figure 6-28 Ice shape for test case 1

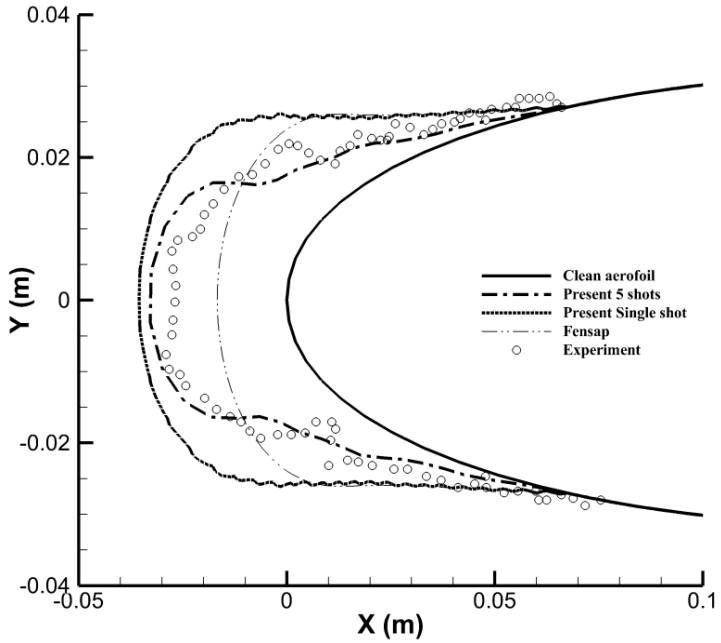

Figure 6-29 Ice shape with multi-shot approach for test case 1

In Figure 6-29, the ice shape obtained by multi-shot ice approach is presented along with the single shot ice accretion. As expected, the ice shape obtained by multi-shot approach is much closer to the experimental results.

Next to this, another one case with non-zero angle of attack is simulated to predict the ice shape. The metrological condition for this test case is as follows,

Temperature	241.49 K	MVD	20 μm
Pressure	100 kPa	LWC	0.55 g/m^3
Velocity	102.8 m/s	Mach	0.33
AoA	3.8^o	Exposure time	420 Sec

Table 6-3 Metrological conditions for test case 2

In test case 2, the ambient temperature is under rime ice region. However, the velocity is high which can affect the ice shape as shown in Figure 6-30.

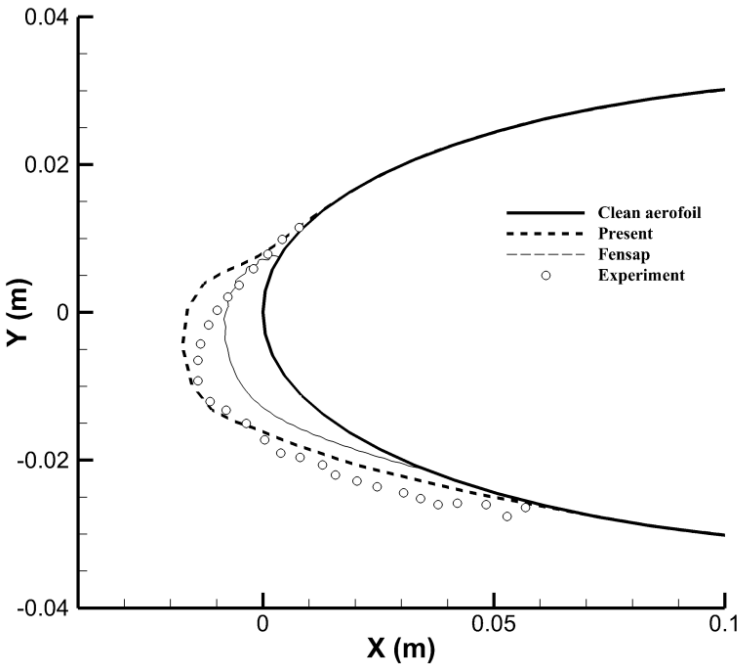

Figure 6-30 Ice shape for test case 2

The present numerical results are almost matched with the experimental results under the given metrological condition. Moreover, the maximum thickness of the ice is clearly predicted by the present numerical model. In Figure 6-31, the experimental results are

compared with the multi-shot approach, which shows that the multi-shot approach results improved the accuracy of the ice shape prediction.

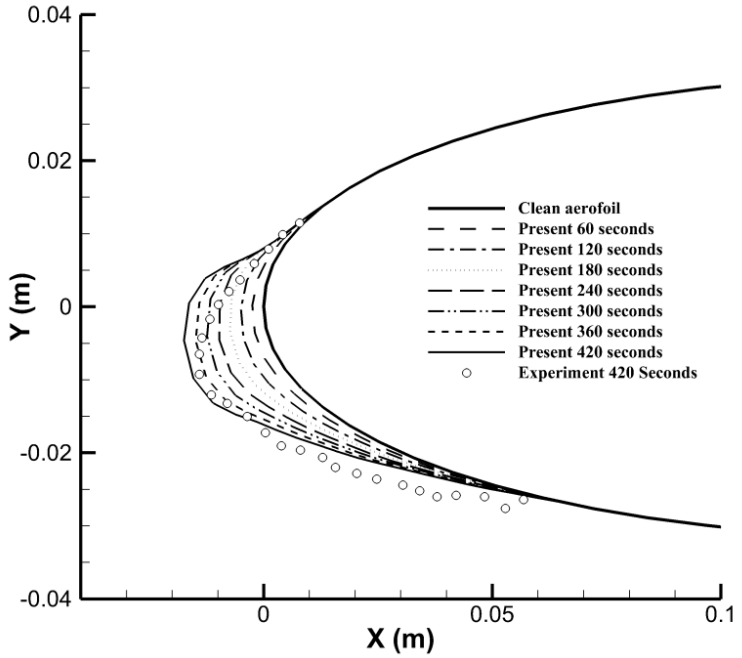

Figure 6-31 Ice shape with multi-shot approach for test case 2

An investigation on a glaze ice test case is conducted with the present numerical model. The metrological condition for the glaze ice test case is as follows,

Temperature	262.04 K	MVD	20 μm
Pressure	100 kPa	LWC	1.0 g/m^3
Velocity	102.8 m/s	Mach	0.32
AoA	3.8^o	Exposure time	231 Sec

Table 6-4 Metrological conditions for test case 3

As the temperature increases, the runback water also increases and horn-shaped ice accretion is possible to occur. Higher temperature has a dramatic effect on the final ice formation because the amount of heating on the airfoil impedes the formation of distinctive horns; in these conditions, the water film mostly affects the extent of the iced surface, which compared to previous runs has increased on both the upper and lower surface. A significant

amount of ice is still forming on the airfoil, but the maximum thickness is less than in previous cases.

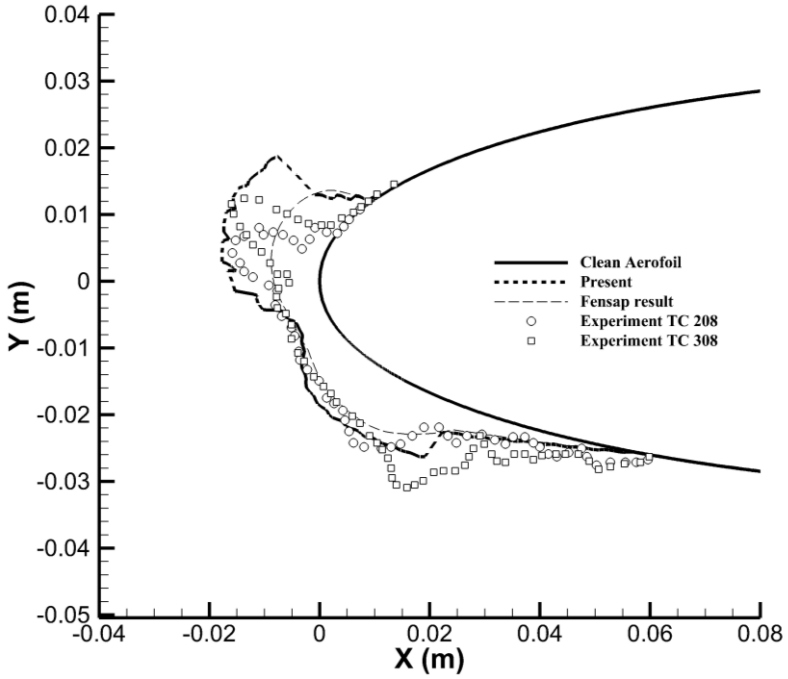

Figure 6-32 Ice shape for test case 3

The maximum ice thickness is predicted almost accurately in test case 3. However, the amount of ice accreted on the leading edge of the airfoil is higher than the experimental results. Although the ice shapes are bit irregular and over predicted, the overall ice shape is under acceptable limit.

Temperature	268.4 K	MVD	20 μm
Pressure	100 kPa	LWC	1.0 g/m^3
Velocity	67.1 m/s	Mach	0.2
AoA	4^o	Exposure time	360 Sec

Table 6-5 Metrological conditions for test case 4

Finally, a glaze ice case with a temperature near to freezing point is validated in test case 4. The metrological condition for test case 4 is shown in Table 6-5. In this case, the higher temperature shows a drastic effect on the ice thickness and ice accretion limit on the surface as shown in Figure 6-33. The increase of ambient heat increases the runback water and

reduces the horn thickness when compared with test case 3. Moreover, the icing limit increased owing to the runback water.

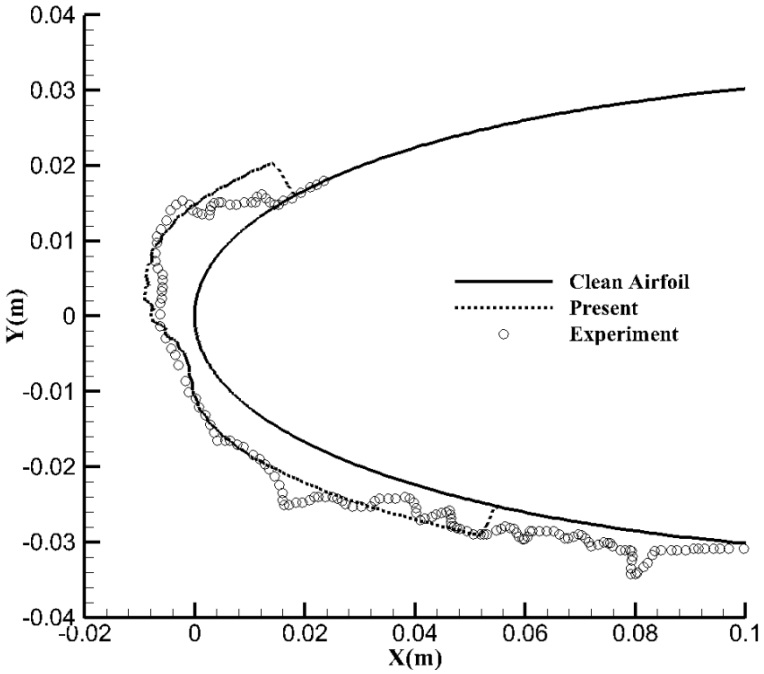

Figure 6-33 Ice shape for test case 4

Although the ice thickness is marginally underestimated, the shape of the ice and the icing limit are well predicted. Moreover, the direction and angle of the horn are predicted properly in all cases.

Next to the single element airfoil, a multi-element airfoil case is used to validate the developed code. The given multi-element airfoil is simulated to predict the ice shape and the results are validated with the experimental results for the metrological condition provided in

Temperature	264.2 K	MVD	20 μm
Pressure	100 kPa	LWC	0.66 g/m^3
Velocity	67.5 m/s	Mach	0.269
AoA	8^o	Exposure time	360 Sec

Table 6-6 Ambient conditions for multi-element ice validation

Table 6-6. The heat transfer coefficient and the ice accretion comparison on the slat for the given ambient condition is shown is Figure 6-34.

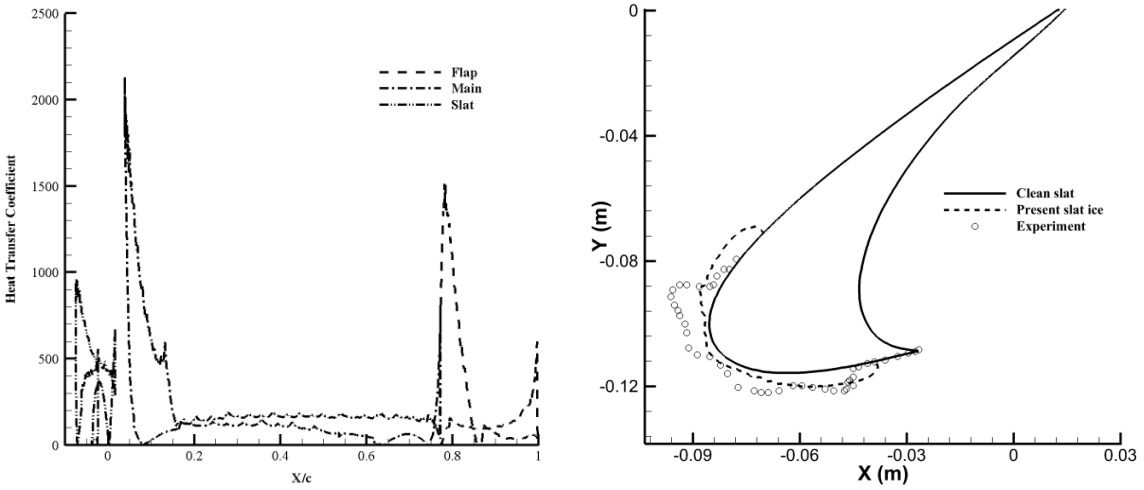

Figure 6-34 Heat transfer coefficient on multi-element airfoil (left) and ice shape comparison on slat (right)

Similarly, the ice accretion shape on the main element and flap element under given metrological condition is shown in Figure 6-35.

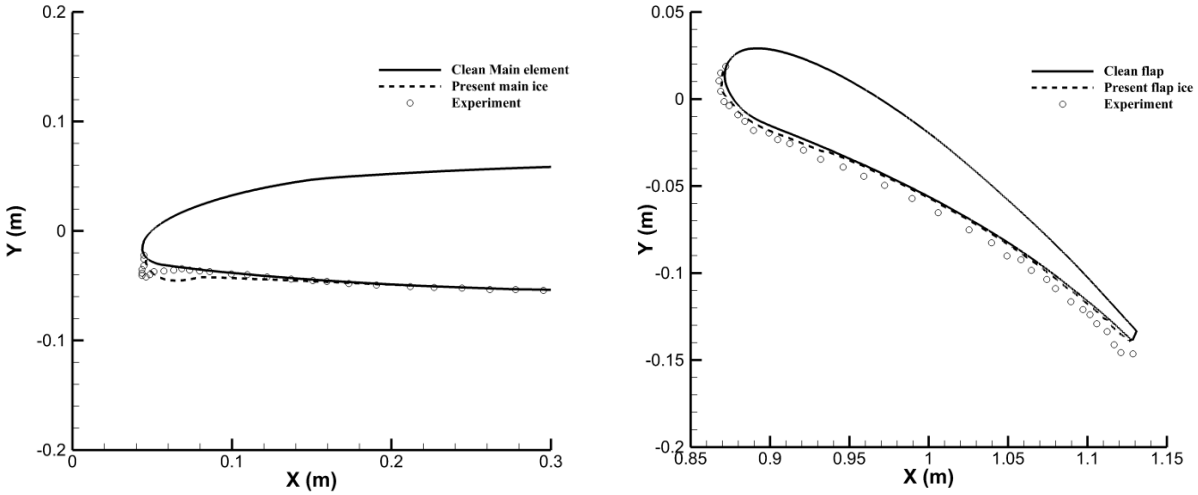

Figure 6-35 Ice shape comparison on main (left) and flap (right) element

Overall, the developed numerical method is capable of solving all the regimes of ice and it is possible to extend the same methodology to three-dimensional planes.

6.2.2 Three-dimensional ice accretion solver

In continuation to 2D ice accretion solver, the 3D ice accretion solver is also validated in this section using an experimental case studied by NASA IRT on GLC-305 [94] and MS-317 [95] swept wing.

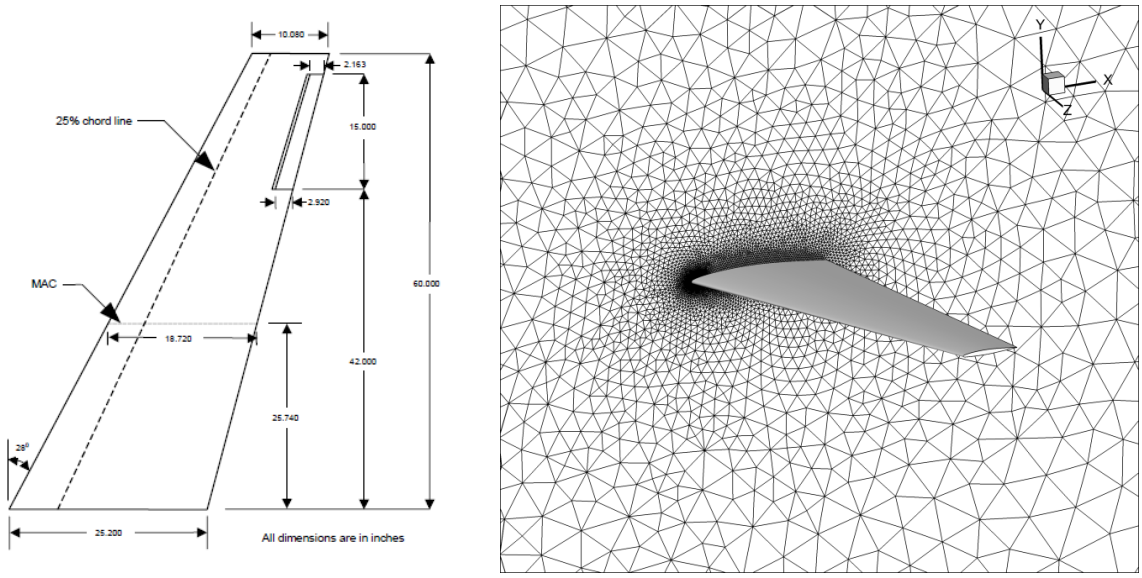

Figure 6-36 GLC-305 wing geometry (left) and grid distribution (right)

In Figure 6-36, the geometry of GLC-305 wing is shown along with the grid generated for the current numerical simulation. The grid near the wing is clustered to predict accurate wall fluxes such as heat flux and shear stress. The Y+ value near the wall is maintained according to the turbulence model requirements. The metrological condition used for the current validation is shown as follows,

Temperature	269 K	MVD	20 µm
Pressure	100 kPa	LWC	$0.68 g/m^3$
Velocity	111.25 m/s	Mach	0.24
AoA	4^o	Exposure time	300 Sec

Table 6-7 Metrological conditions for GLC-305 wing ice validation

After successful prediction of air flow field and droplet distribution around the wing, the results are used as the input for the ice accretion solver.

The computed results are compared with the experimental results at three sections of the wing geometry. The first section is at the root, the second at the 25-inch span from the root and the final section is at 50-inch span from the root. The pictorial view of the sections and the ice accretion comparison at root is shown in Figure 6-37. The ice shapes at 25-inch and 50-inch sections are shown in Figure 6-38.

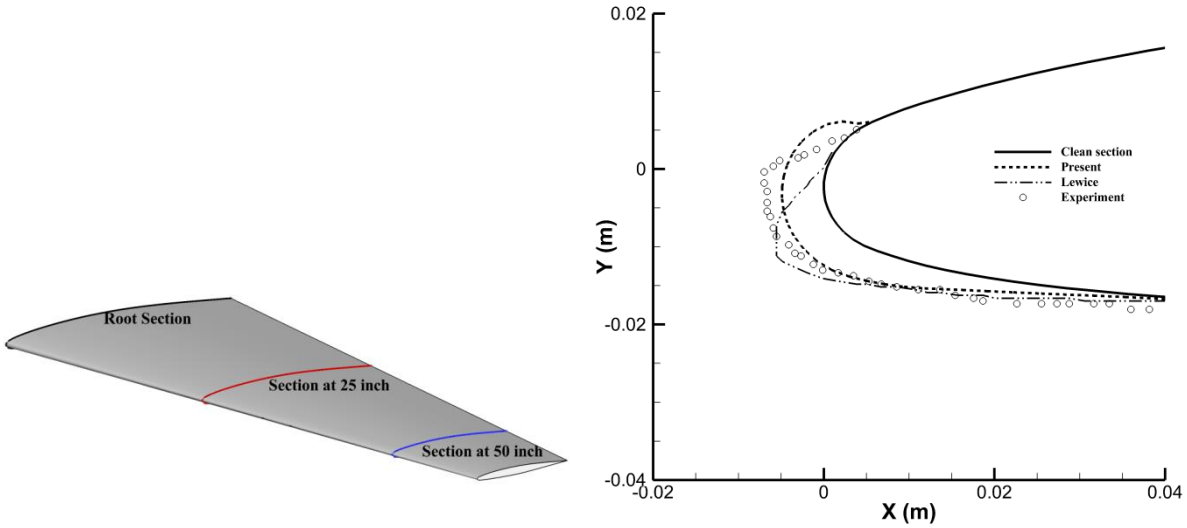

Figure 6-37 GLC-305 wing cut sections (left) and validation at root (right)

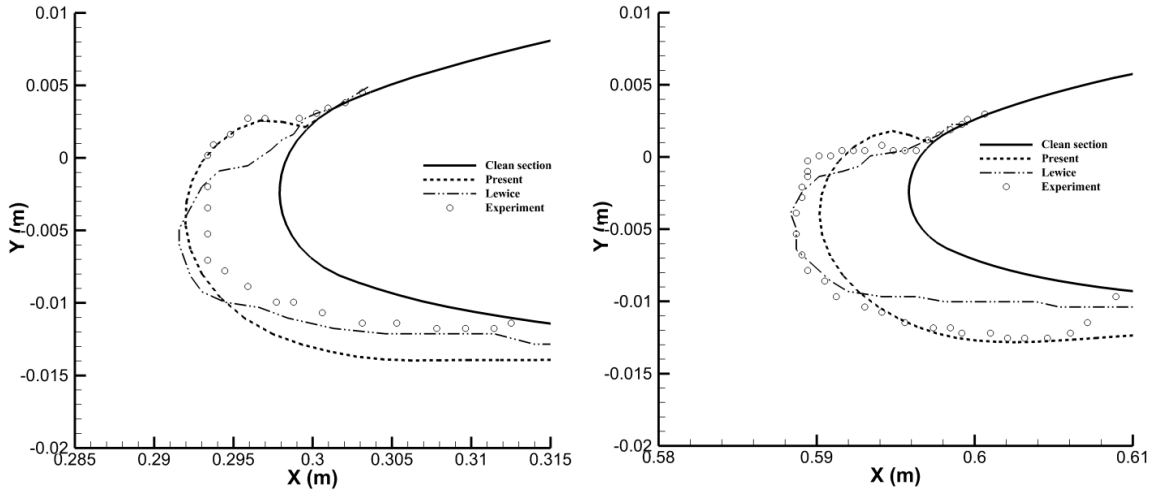

Figure 6-38 GLC-305 validation at 25 (left) and 50 (right) inches cut sections

The ice shape is overpredicted at the upper surface of the wing by the current numerical method at root section. However, the upper surface ice shape is correctly predicted at the section of 25-inch and the same having some discrepancies at the 50-inch section. At the 50 inch, the ice limit is not correctly predicted at the lower surface of the wing, which might be

due to more runback water. Another validation is important to better understand of the developed code. Hence, another validation study was conducted on the MS-317 wing.

The MS-317 wing with a chord of 0.9144 m is experimentally studied in NASA IRT under various metrological conditions. The ambient conditions used for the present validation is shown in Table 6-8.

Temperature	255 K	MVD	20 μm
Pressure	100 kPa	LWC	$1.03 g/m^3$
Velocity	67.5 m/s	Mach	0.24
AoA	8^o	Exposure time (Case 9 / 10)	390 / 1164 Sec

Table 6-8 Metrological conditions for MS-317 wing

The geometry used in IRT and the grid used for the present simulations are shown in Figure 6-39.

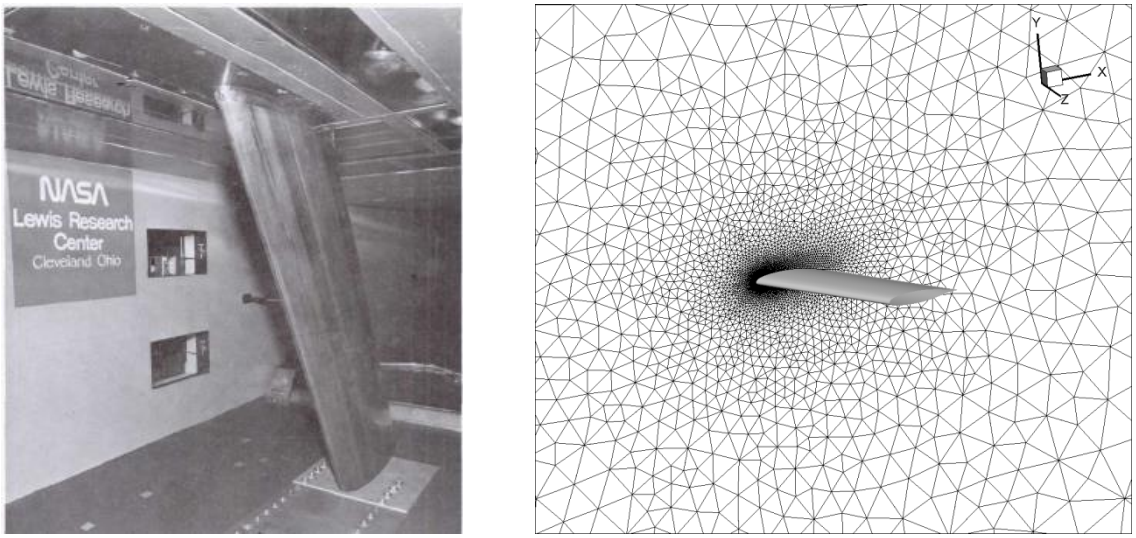

Figure 6-39 MS-317 wing in IRT (left) and grid distribution (right)

For the purpose of current validation, case 9 and case 10 were used. Both cases are using the same metrological condition with different exposure time 390s and 1164s for case 9 and 10, respectively. In Figure 6-40, the predicted ice shape is compared with the experimental ice shape given by case 9 and 10. In both cases, the ice accretion direction is accurately

matching with the experiment and the ice thickness slightly under predicted. Taken together, the overall ice shape prediction is under the acceptable limit and this model can be used for engineering applications.

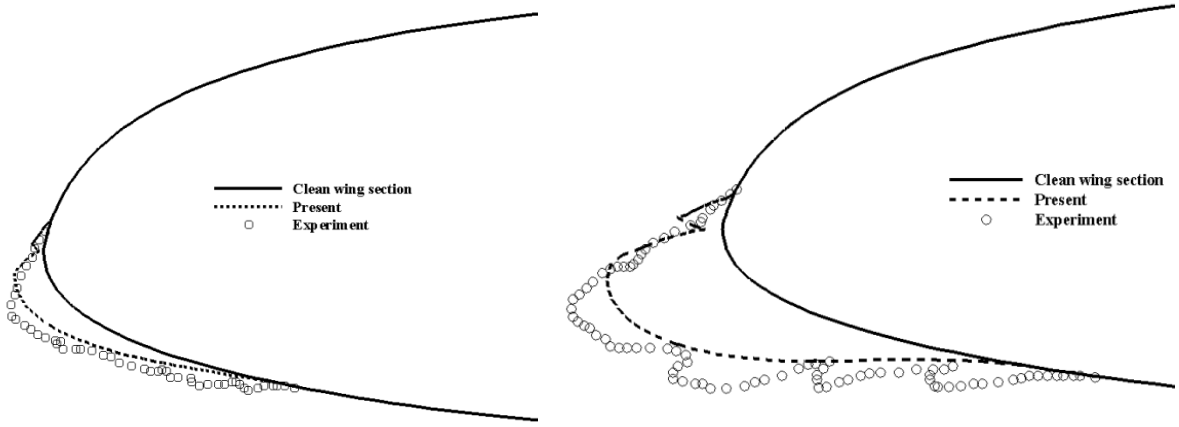

Figure 6-40 MS-317 ice shape validation case 9 (left) and case 10 (right)

Finally, the ice shape over an engine inlet is predicted by the current numerical method and the results are compared with Bidwell and Mohler [92] theoretical results. Two cases were studied – the first one is rime and the second one is glaze ice accretion condition. The metrological conditions can be given as,

	Velocity (m/s)	AoA (Degree)	Pressure (Pa)	Temperature (K)	LWC (g/m^3)	MVD (μm)	Time (Min)
Case 1	75.2	0	100 kPa	243.25	20.36	0.2	30
Case 2	75.2	0	100 kPa	263.85	20.36	0.695	30

Table 6-9 Metrological conditions for engine intake nacelle

The ice shape comparison is shown in Figure 6-41, which illustrates some discrepancies with the previous theoretical results. However, it was observed that other researchers also face the same problem in obtaining the specific result. The ice shape contour is shown in Figure 6-42 for case 2 under 0 and 15 degrees of angle of attack for an exposure time of 30 minutes.

The overall validation of air, droplet, and ice accretion solvers shows that the developed ice package software can be applied to various engineering problems. Although some discrepancies were found under some test cases, the overall predictions of physical quantities are under the allowable limit.

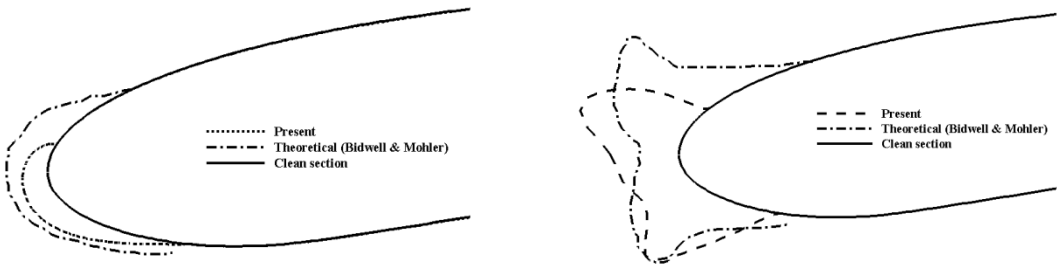

Figure 6-41 Ice shapes on the air intake at mass flow = 7.9 Kg/s for case 1 (left) and case 2 (right)

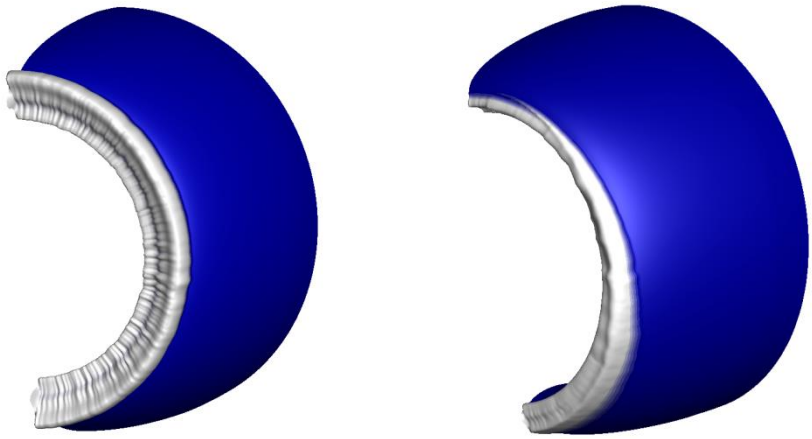

Figure 6-42 Ice shapes contour on air intake at mass flow = 7.9 Kg/s for case 2 at AoA 0 (left) and 15 degrees (right)

Chapter 7. Application of Ice Solver

The development of any numerical tool or solver is used to help the industry in the relevant field for further investigation or to find new physics. In the case of ice accretion, numerical tools are applicable in a vast area of atmospheric icing. In this chapter, few engineering problems are studied by using the developed numerical tools.

7.1 Performance study of iced multi-element airfoil

Multi-element wing systems are often used in the aircraft as high lift devices for take-off, climb, and landing. Ice accretion on these multi-elements can reduce the aerodynamic characteristics of the wing. Hence, a proper design of ice protection system is necessary to avoid unnecessary performance degradation due to ice on multi-elements. Moreover, the increase in droplet diameter changes the ice accretion amount and icing limit on any surface. Although several numerical studies based on the Eulerian approach have also been proposed to model the SLD effects, there are an only limited set of investigations are conducted on multi-element airfoil under SLD icing conditions. Tan [96] has investigated the droplet trajectory over the multi-element airfoil including SLD effects and focused on the droplet splashing effects. Petrosino [97] has studied the effect of Euler and RANS solvers in the context of ice accretion on multi-element airfoils. However, Tan [96] has not studied the ice accretion and Petrosino [97] studies are limited far below the SLD drop sizes. Bidwell [98] has studied the heat transfer and collection efficiency over multi-element airfoil using CFD++ for air solution and particle tracking method such as Monte Carlo for droplet trajectories. Zhang [99] has studied the aerodynamic characteristics of an iced multi-element airfoil with a Lagrangian based solver for droplets trajectories and an analytical based method for ice accretion. In this current work, an attempt is made to study the performance degradation on an iced multi-element airfoil under various metrological conditions ranging

from conventional to SLD MVDs using the developed ice analysis package. The metrological conditions used for the performance study of the multi-element airfoil are shown in Table 7-1.

	Velocity (m/s)	AoA (Degree)	Temperature (K)	LWC (g/m^3)	MVD (μm)	Time (Sec)
Case 1	88.4	0,4,8,12,16	270.3	0.6	30	900
Case 2	88.4	0,4,8,12,16	270.3	0.19	92	900
Case 3	88.4	0,4,8,12,16	270.3	1.44	154	900

Table 7-1 Ambient conditions for multi-element ice accretion

The performance study of the multi-element airfoil starts with the validation of lift coefficient on clean airfoil under case 1 metrological conditions. The validation result is shown in Figure 7-1, illustrating a good agreement with the experimental results for an angle of attack of 8^0 in case 1 metrological conditions.

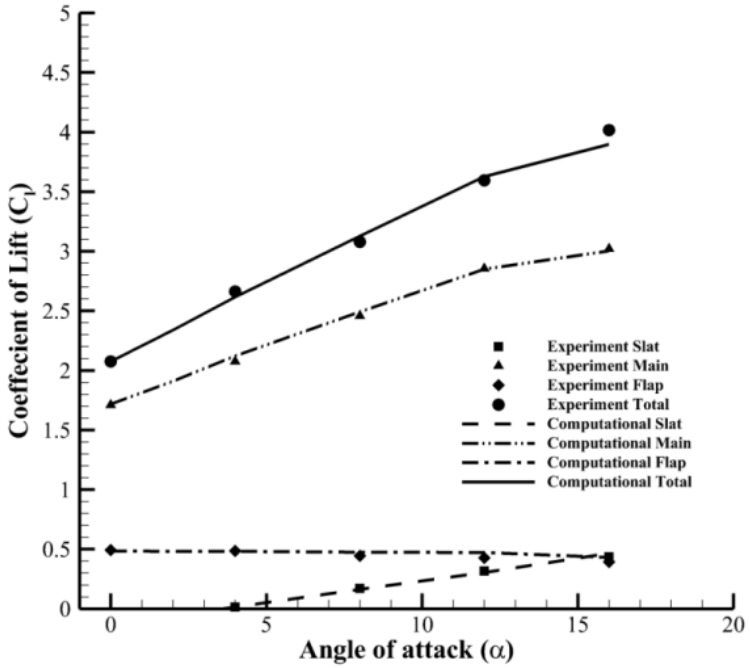

Figure 7-1 Lift coefficient for case 1 at AoA=8 degrees

The validated clean airfoil lift coefficient can be used to analyse the performance degradation of the iced multi-element airfoils. By using the developed numerical solvers as explained in previous chapters, the multi-element airfoil is simulated under various

metrological conditions as shown in Table 7-1. The ice accretion and lift coefficient results under various metrological conditions are shown in Figure 7-2 to Figure 7-7.

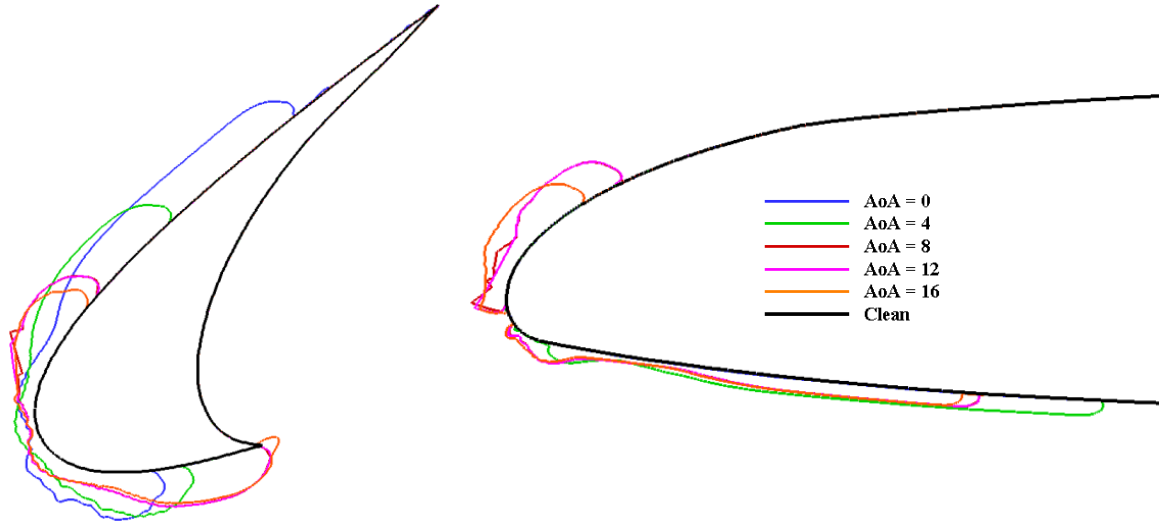

Figure 7-2 Predicted ice shape over a slat (left) and main element (right) at case 1 metrological conditions

Figure 7-2 shows the ice accretion over the slat and main element in case 1 metrological condition under various angles of attacks. The increase of angle of attack shows its effects in both slat and main element. The ice accretion limit of the slat element varies tremendously

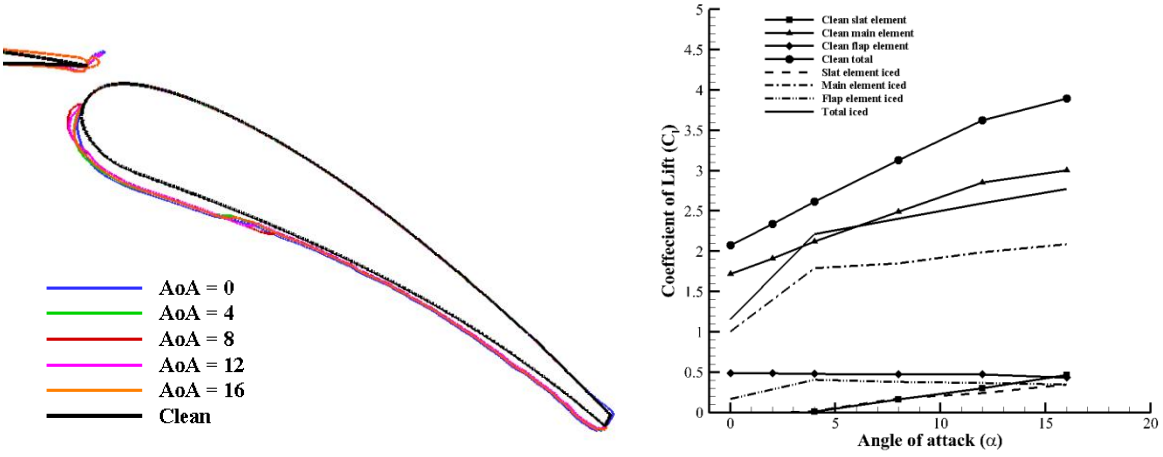

Figure 7-3 Predicted ice shape over a flap element (left) and lift coefficient comparison (right) at case 1 metrological conditions

with respect to the angle of attack. At low angle of attack, more water flows towards the upper side of the stagnation point while the icing limit is reduced on the upper side of

stagnation region at a high angle of attacks. The ice accretion on the main element is negligible at a low angle of attacks and more runback ice is formed at a high angle of attack.

The ice accretion on flap element and the lift coefficient comparison at case 1 metrological conditions are shown in Figure 7-3. The ice accretion varies depending on the angle of attack due to the droplet impingement and shear flow over the element. Unlike the other two elements, the whole lower side of the flap element is contaminated with ice which might reduce its performance. Additionally, the lift coefficient comparison shows the drop of

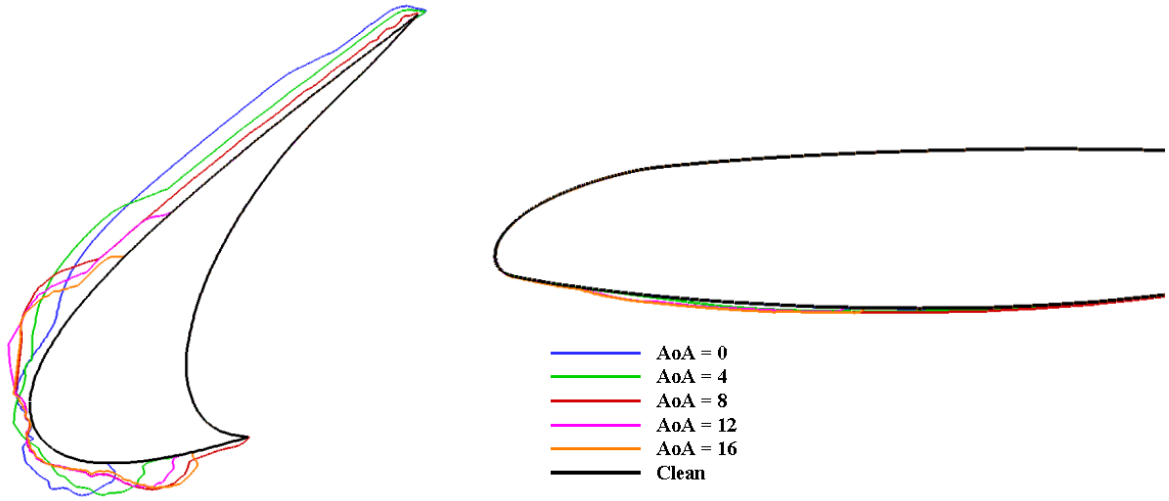

Figure 7-4 Predicted ice shape over a slat (left) and main (right) element at case 2 metrological condition

lift under all angles of attacks. In Figure 7-4, the ice shape on slat and the main element at case 2 is shown. The icing limit on the slat element is increased when compared with case 1 which might be due to the bigger droplet diameter. Furthermore, the icing limit of the main element is changed which leads to a clear leading edge of the main element. The runback ice accretion is more in this case which extends more than half of the main element. Since there is no horn or no formation of the irregular shape of ice on the main element, the performance degradation might not be very high. Figure 7-5 shows the ice shape on the flap at various angles of attacks and the lift degradation for case 2 metrological conditions. The increase in angle of attack increased the icing limit on the slat element as observed in Figure 7-5. At

higher angles of attacks, more ice are accumulated which can block the gap between the main element and the flap. Finally, another case with bigger droplets was simulated and the results are presented in Figure 7-6 and Figure 7-7.

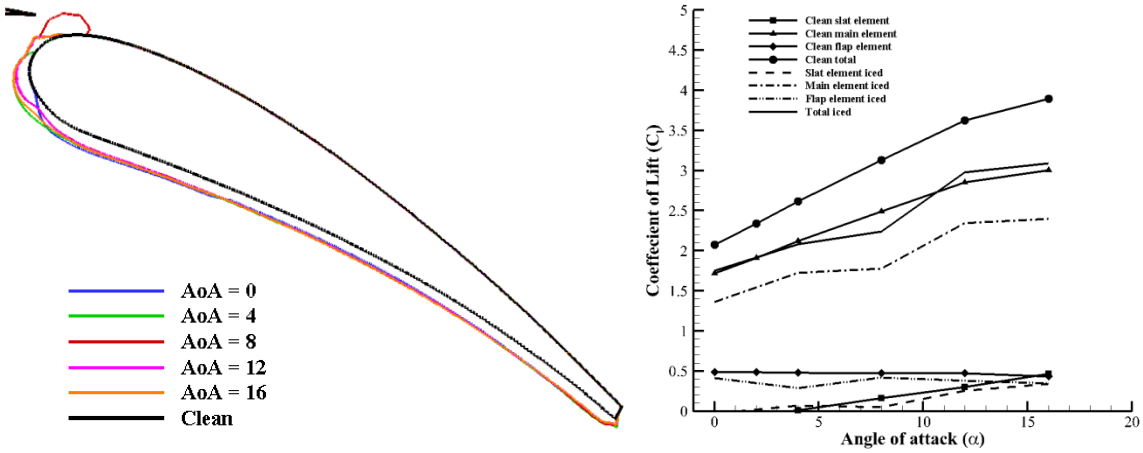

Figure 7-5 Predicted ice shape over a flap element (left) and lift coefficient comparison (right) at case 2 metrological conditions

The amount of accumulated ice revealed that the size of the droplet is bigger than the other two cases while the ice accretion on the main element did not change much other than more runback ice formation. The runback ice on the lower side of the main element extends to the flap well cove while the whole front side of slat is covered with ice. The higher LWC can also be a reason for the higher ice accumulation and icing limit on the slat as well as in the main element. Furthermore, the flap element ice accumulation is also higher for this metrological condition and runback is very high at a high angle of attack. The gap between the main element and the flap is almost filled with ice accumulated on the flap element. The increase of angle of attack also increases the icing limit on the flap, in which most of the upper surface is also covered with ice. The contaminated multi-element airfoils are simulated with proper metrological conditions to predict the performance degradation.

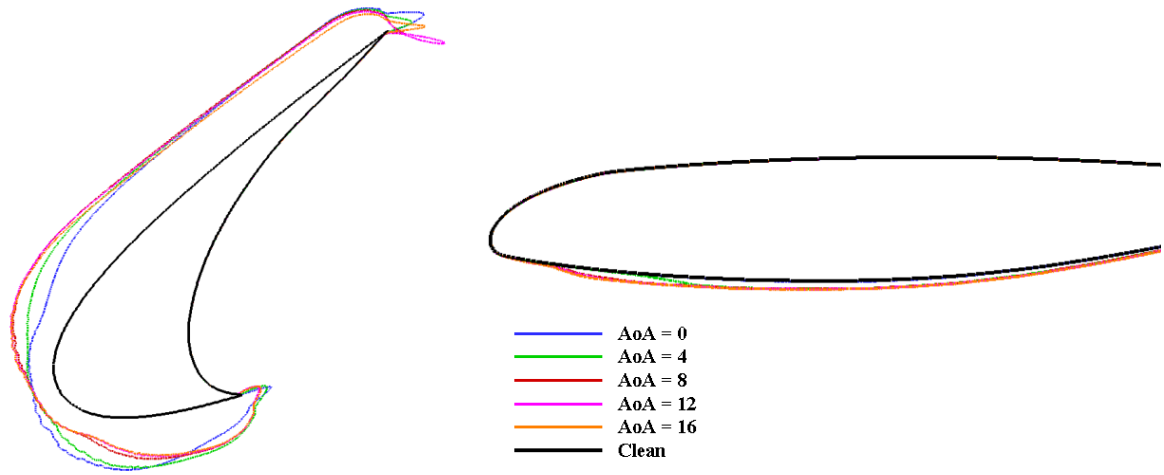

Figure 7-6 Predicted ice shape over a slat (left) and main element (right) at case 3 metrological condition

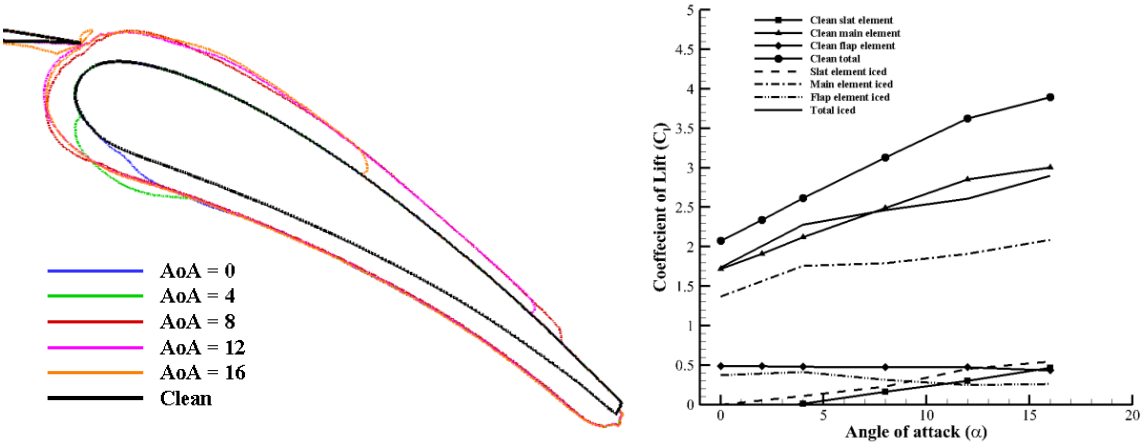

Figure 7-7 Predicted ice shape over a flap element (left) and lift coefficient comparison (right) at case 3 metrological conditions

The velocity magnitude contour of clean and contaminated airfoil simulations are shown in Figure 7-8 to Figure 7-9. For the same angle of attack and metrological conditions, at each MVD, the velocity magnitude is different due to the ice accretion. The increase of wake region is observed at the upper surface of flap for MVD 20 case as shown in Figure 7-8. In Figure 7-9, the contour shows velocity magnitude around the iced airfoil for MVD 92 and 154 µm droplet case at 16 degrees of angle of attack. Owing to the accumulated ice, the gap between main element and flap element is blocked this increased the wake region in case of MVD 154 µm. Moreover, the flow field is changed in all the cases which may lead to the degradation of airfoil performance.

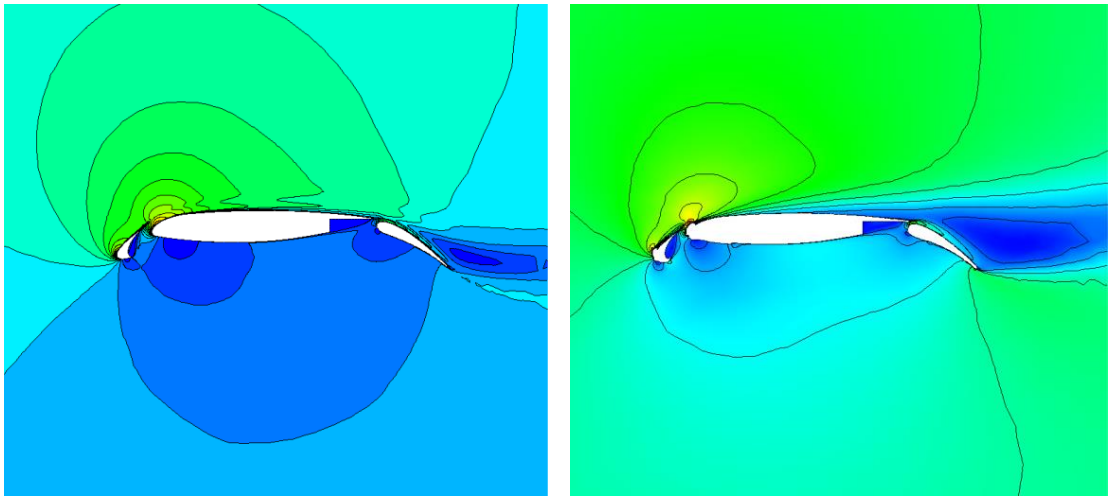

Figure 7-8 Velocity magnitude over clean (left) and iced at 20 MVD (right) multi-element airfoil

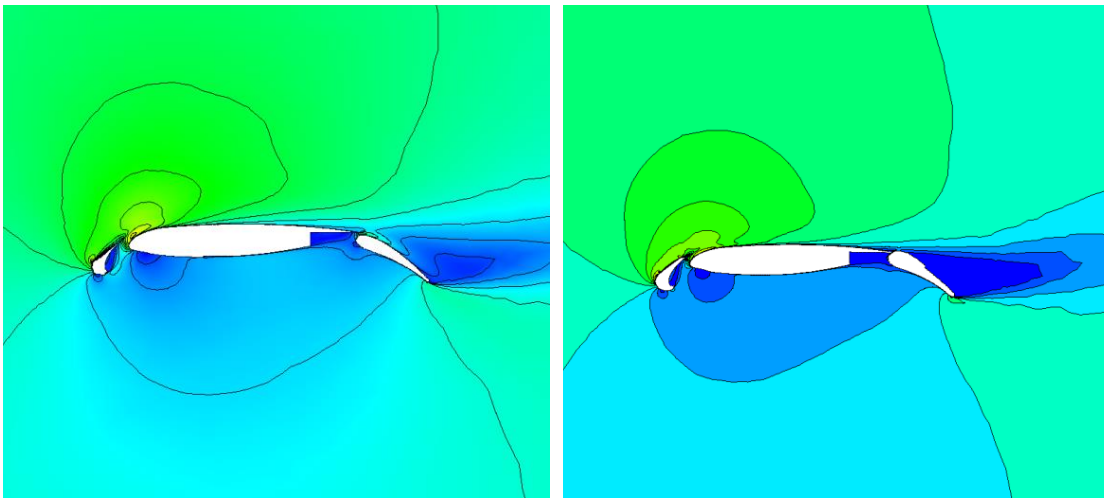

Figure 7-9 Velocity magnitude over iced multi-element airfoil at 92 MVD (left) and 160 MVD (right)

The lift coefficient degradation for all the given metrological conditions at a various angle of attacks are shown in Figure 7-10. The overall lift coefficient on the iced multi-element airfoil shows that the performance of the multi-element wing drops dramatically under all the icing conditions. Additionally, the performance of case 1 iced airfoil is less than the other two metrological conditions (case 2 and case 3). The performance degradation of case 1 iced airfoil may be due to the bigger loss of performance in the main element. Moreover, the lift contribution of the main element is higher which was distorted by the ice accumulation that could lead to loss of performance.

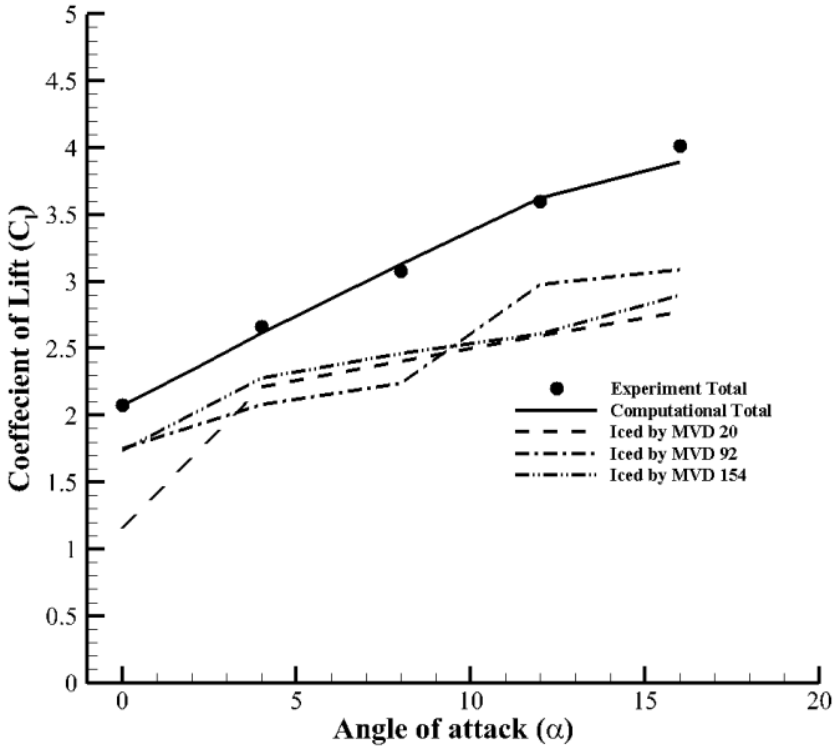

Figure 7-10 Lift coefficient after ice accretion under various metrological conditions

7.2 Ice accretion on KC-100 aircraft

The KC-100 is a South Korean four seat aircraft developed by Korean Aerospace Industries (KAI) that first flew during July 2011 [100]. This lightweight aircraft is configured with a low-wing and single engine at the nose of the fuselage [101]. The aircraft body is built with carbon fiber and featured with gull-wing doors. A fixed tricycle landing gear system is equipped in this airplane. Moreover, this aircraft is powered by a single IO-550-K engine, manufactured by Teledyne Continental Motors. The aircraft can fly with a maximum speed of 398km/h for a range of 1,852 km. The wing span is 11.37 m, length is 8.5 m, empty and gross weights are 1089 kg and 1633 kg, respectively.

Figure 7-11 KC-100 aircraft

The grid distribution around KC-100 aircraft as shown in Figure 7-11 is illustrated in Figure 7-12. Two simulations were conducted on KC-100 aircraft, the first one is under conventional icing while the second one is under SLD icing. The ambient temperature in conventional and SLD icing conditions are considered to be same while the LWC and MVD are different. Moreover, the flight speed of SLD case is relatively lower than the conventional metrological conditions. The metrological conditions used for the present simulations are shown in Table 7-2

	Velocity (m/s)	AoA (Degree)	Pressure (Pa)	Temperature (K)	LWC (g/m^3)	MVD (μm)	Time (Min)
Conventional	76.5	4	98420	253.15	0.09	35	15
SLD	52.0	4	98420	253.15	1.5	160	15

Table 7-2 Metrological conditions for KC-100 aircraft ice accretion

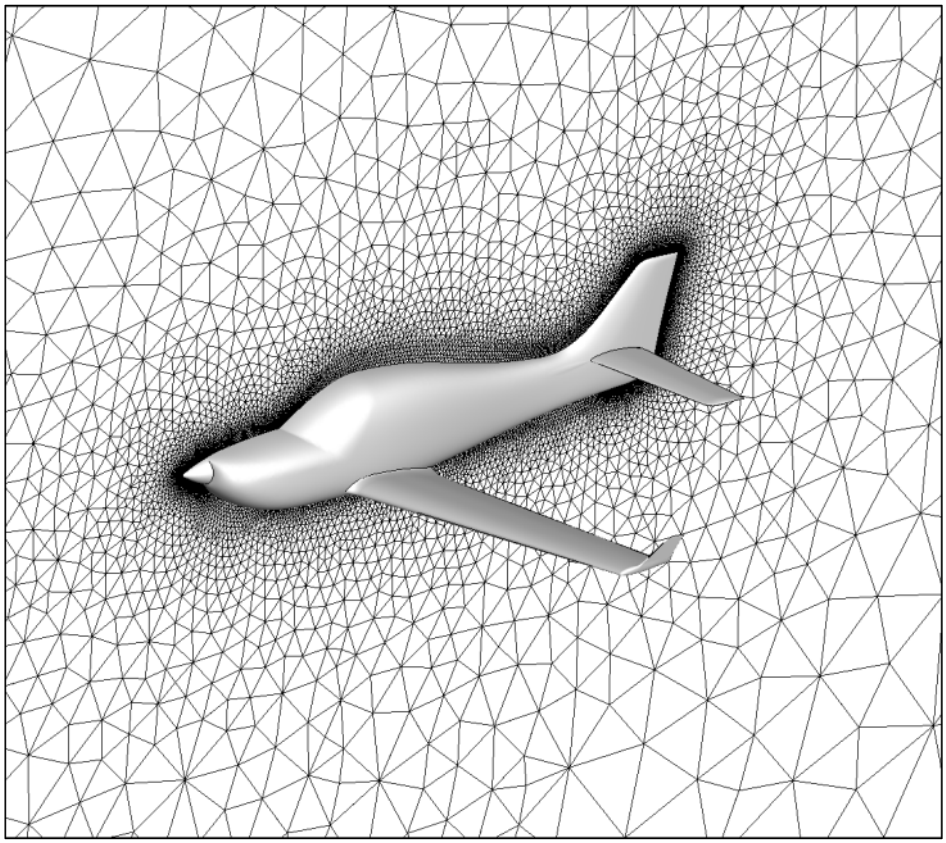

Figure 7-12 Grid distribution around KC-100 aircraft

7.2.1 Collection efficiency

The developed 3D droplet solver is used to simulate the droplet impingement around the KC-100 aircraft. In order to reduce the computational requirement, symmetry boundary condition is used at the symmetry plane of the aircraft. Before using the droplet solver, the model was solved for air flow field using Navier-Stokes Fourier solver including relevant turbulence model to account the turbulence effect. The pressure distribution and the collection efficiency around the aircraft for the conventional metrological condition are shown in Figure 7-13 and Figure 7-14, respectively. As seen here, the collection efficiency is significant at the leading edge of the wing, empennage, and the nose of the aircraft. Followed by this, the same model is used for simulation under SLD icing condition which is shown in Figure 7-15.

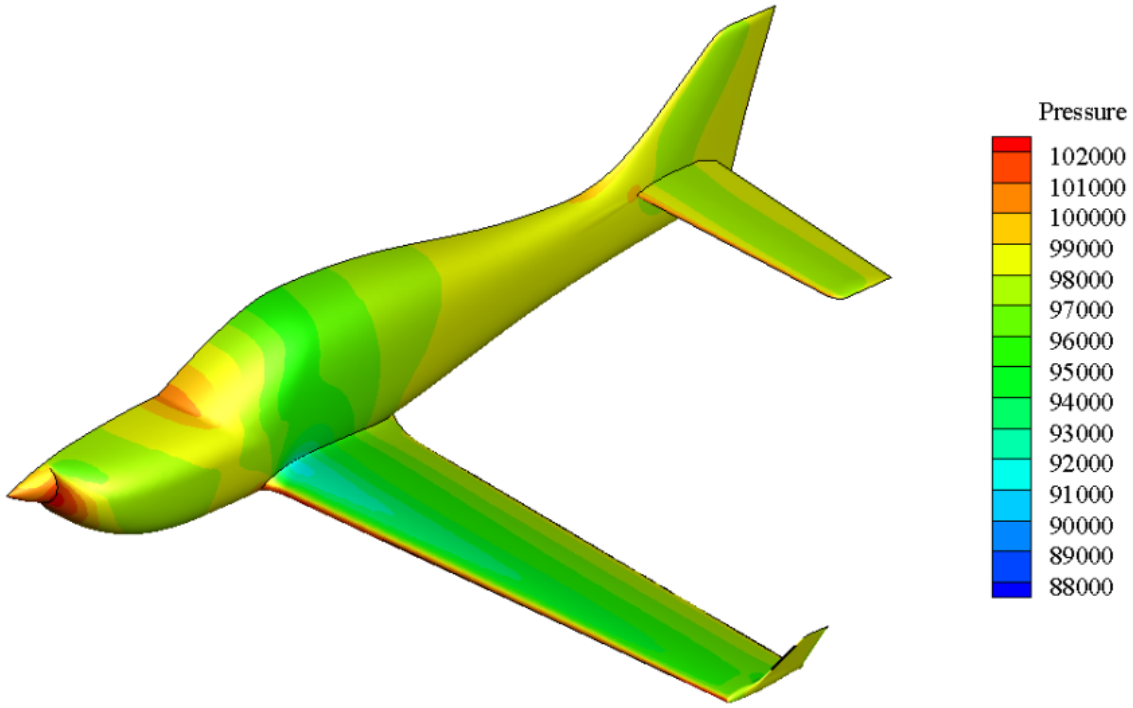

Figure 7-13 Pressure distribution around KC-100 aircraft

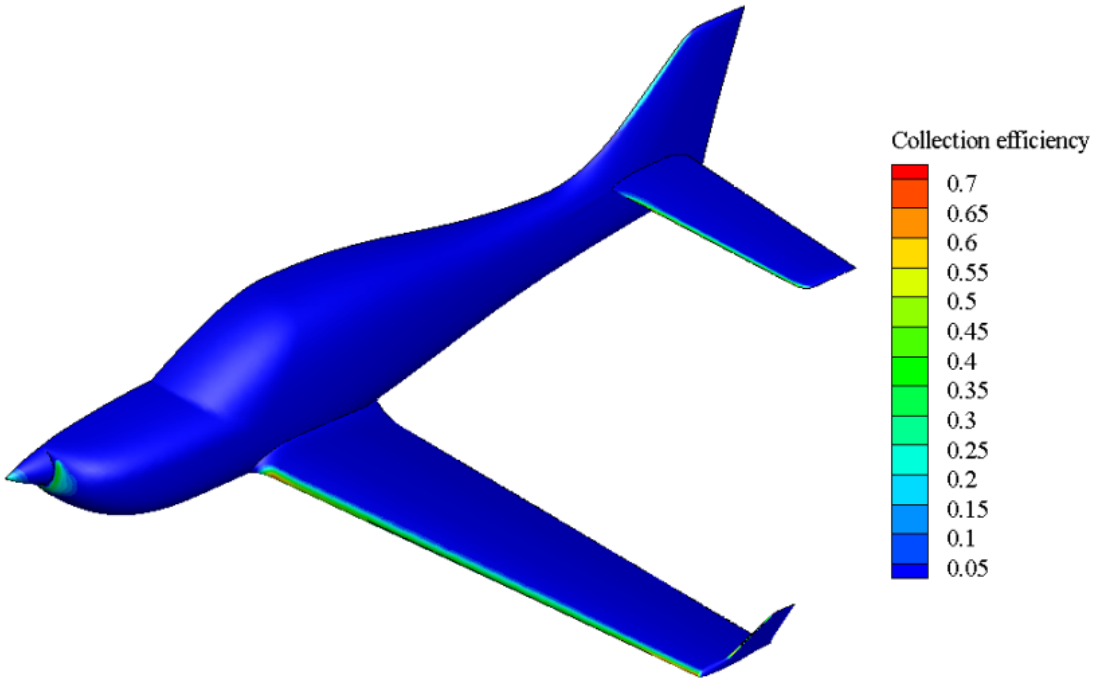

Figure 7-14 Collection efficiency on KC-100 aircraft at conventional icing conditions

From Figure 7-15 it is easily understandable that the icing potential is very high under SLD conditions. Figure 7-16 shows the comparison of collection efficiency at a section of the

KC-100 aircraft wing. The magnitude of collection efficiency is increased almost double under SLD condition and we can also expect the same effect in ice accretion.

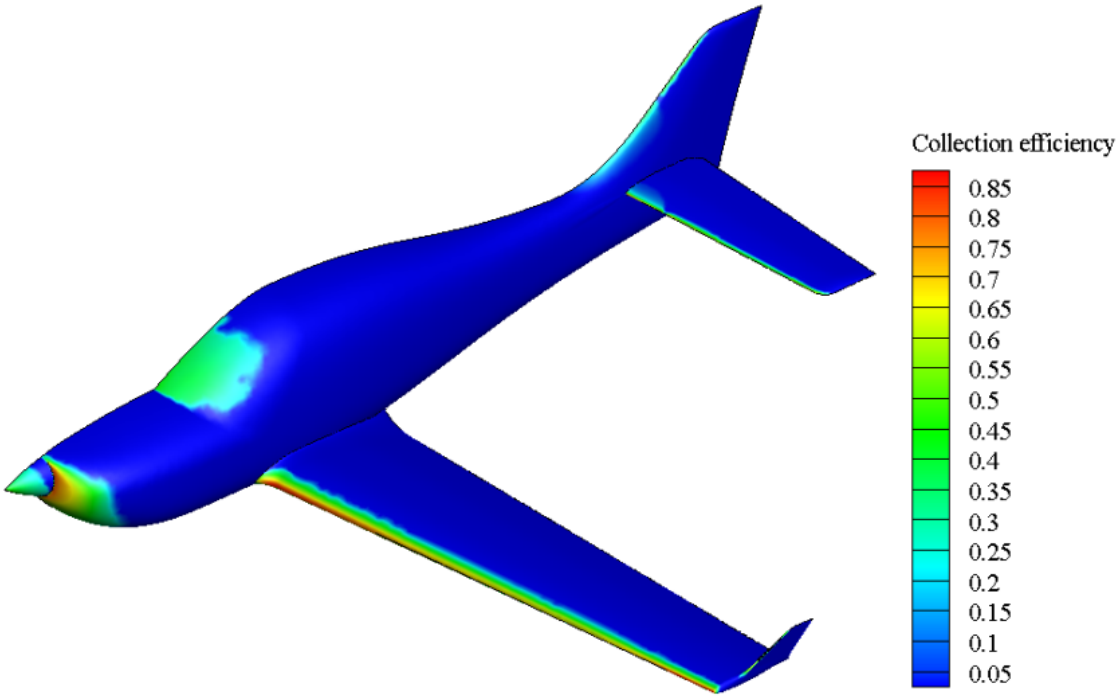

Figure 7-15 SLD icing condition collection efficiency around KC-100 aircraft

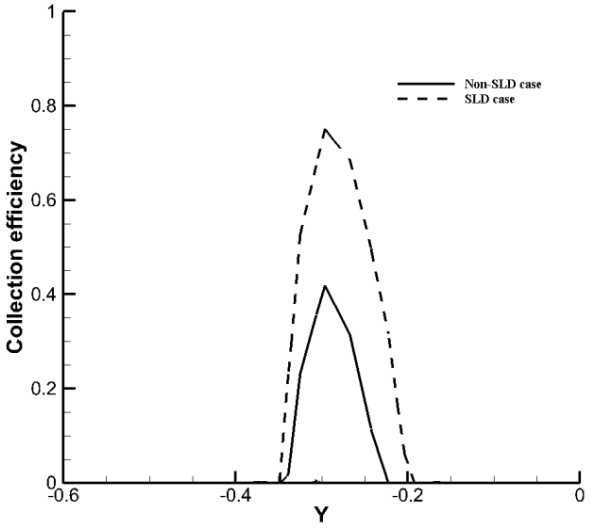

Figure 7-16 Collection efficiency at a section on the wing of KC-100 aircraft

7.2.2 Ice accretion

The simulated ice accretion on the KC-100 aircraft under conventional icing condition is shown in Figure 7-17. As expected, the ice accumulated at the leading edge of the wing, empennage, and the nose of the aircraft. As this KC-100 aircraft has its ice protection system, the accumulated ice on the surface for an exposure time of 30 minutes is possibly under control.

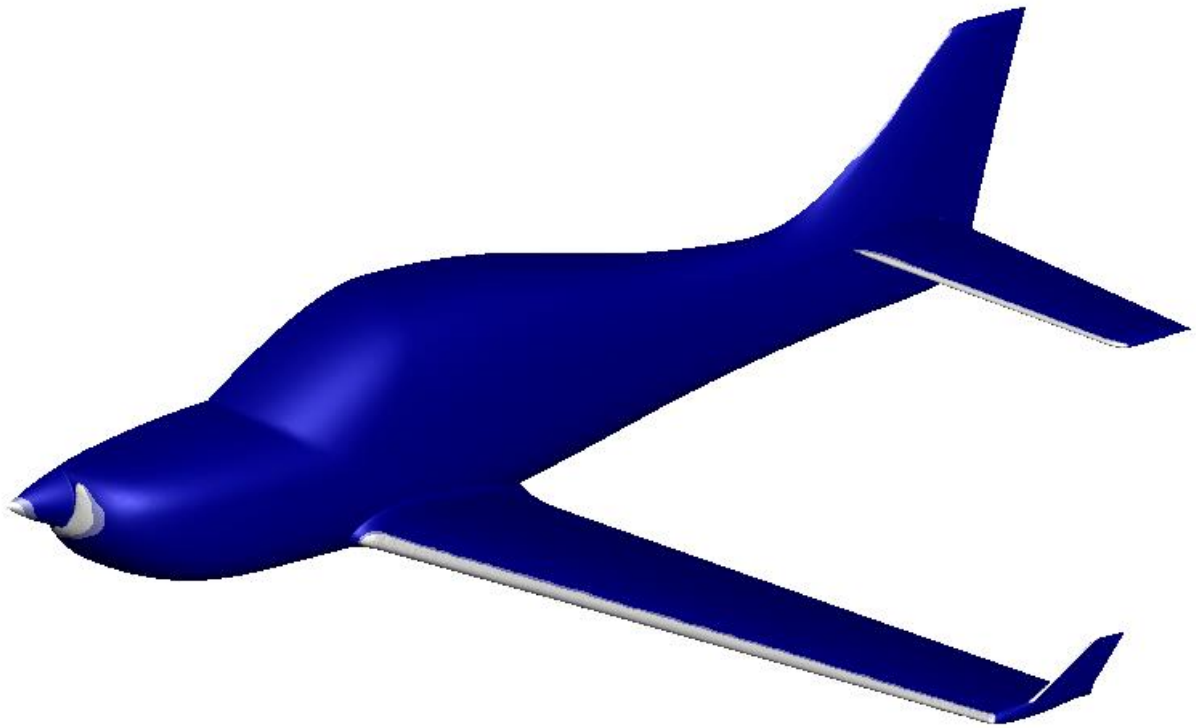

Figure 7-17 conventional ice accretion on the KC-100 aircraft

Next to the conventional metrological condition, the aircraft is simulated with SLD icing condition for an exposure time of 30 minutes. The ice accumulated surface of KC-100 aircraft is shown in Figure 7-18, in which the difference of SLD icing is easily noticeable. For the same exposure time, the ice formation is drastically increased and even on the ice accumulated on the windshield of the aircraft. The ice accumulation area is changed and significantly increased in the SLD ice accretion case. For a better understanding, Figure 7-19

compares the accumulated ice over KC-100 aircraft under both SLD and conventional icing condition.

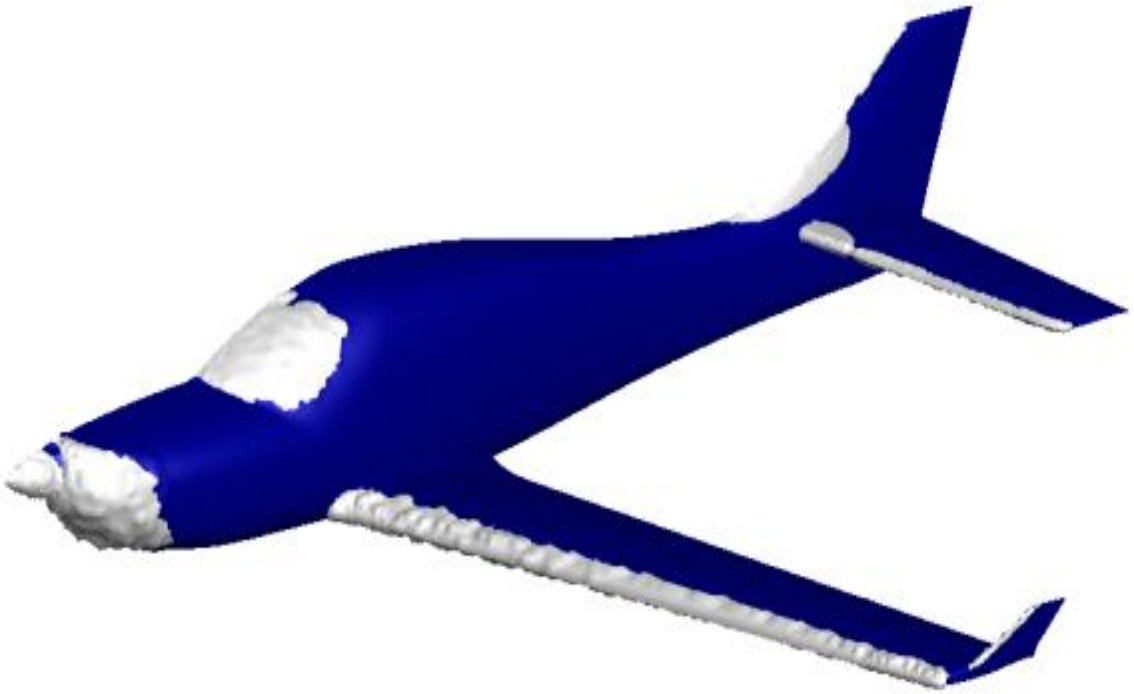

Figure 7-18 SLD ice accretion on the KC-100 aircraft

Figure 7-19 Conventional and SLD ice accretion comparison

7.3 Ice accretion study on rotorcraft intake

Ice accretion on the surface around an engine air intake during all-weather operations can deteriorate the safety of aircraft due to the engine performance degradation [6]. A careful design of ice protection system (IPS) is necessary. An experimental work was done aimed to investigate the range and amount of ice formation under various surface temperatures.

Furthermore, the heat-on and heat-off modes are investigated for a better understanding of the ice accumulation.

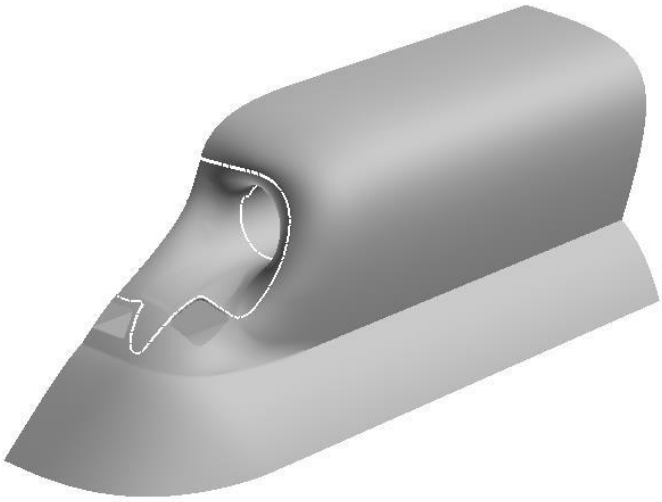

Figure 7-20 Engine air intake model configuration

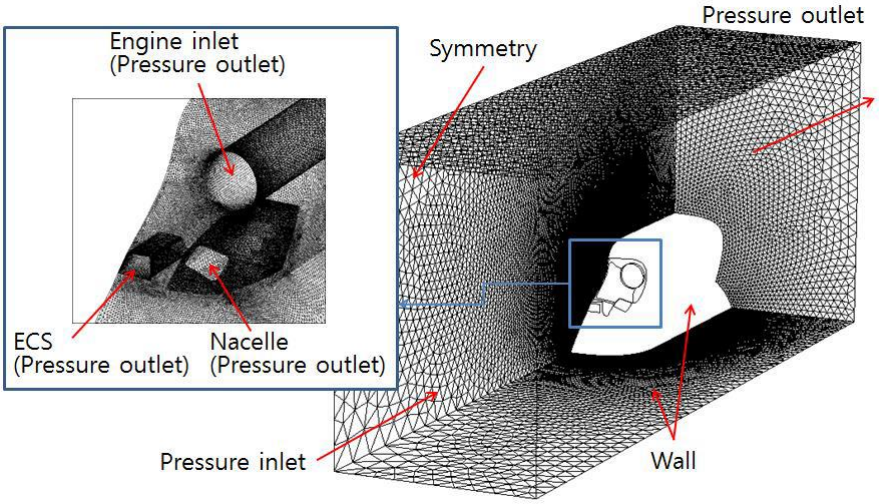

Figure 7-21 Grid distribution around the rotorcraft engine intake

The experimental test was conducted in Centro Italiano Ricerche Aerospaziali (CIRA) icing wind tunnel (IWT). The CIRA IWT [102, 103] is one of the advanced icing wind tunnels in the world with a lot of facilities such as control on altitude, velocity, temperature, and cloud conditions. For this experimental study [6], a full-scale rotorcraft engine intake was manufactured. The engine intake was experimentally included in the ice accretion study by using a unique suction mechanism built for the current engine intake model. In this chapter, the computer simulation of ice accretion on rotorcraft engine intake was conducted. The

geometry model of the rotorcraft engine intake model configuration and the computational mesh around the engine intake are shown in Figure 7-20 and Figure 7-21, respectively. For the current simulations, the metrological conditions used are illustrated in Table 7-3.

	Velocity (m/s)	Pressure (Pa)	Temperature (K)	LWC (g/m^3)	MVD (μm)
Case 1	72	101,325	263.0	0.6	20,30,40
Case 2	72	84,555	253.0	0.3	20
Case 3	65	84,555	263.0	0.6	20
Case 4	52.0	98,420	262.0	1.5	160

Table 7-3 Metrological condition for rotorcraft intake

7.3.1 Collection efficiency

Before starting the investigation of the droplet impingement on the engine inlet, the air solution is obtained for all the cases. The pressure distribution around the engine inlet at case and case 2 metrological conditions is shown in Figure 7-22.

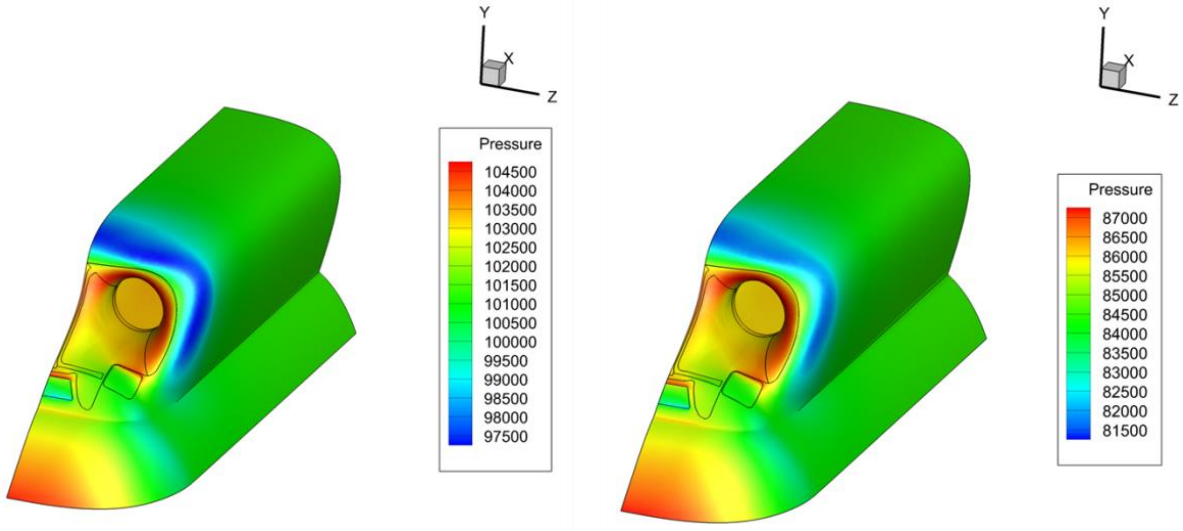

Figure 7-22 Pressure distribution around the engine intake for case 1(left) and case 2 (right)

The droplet solution predicted by the present 3D droplet solver is shown in Figure 7-23, and the present simulation results are compared with the FENSAP results revealing a fair agreement. Consequently, this model was also conducted in ice accretion case.

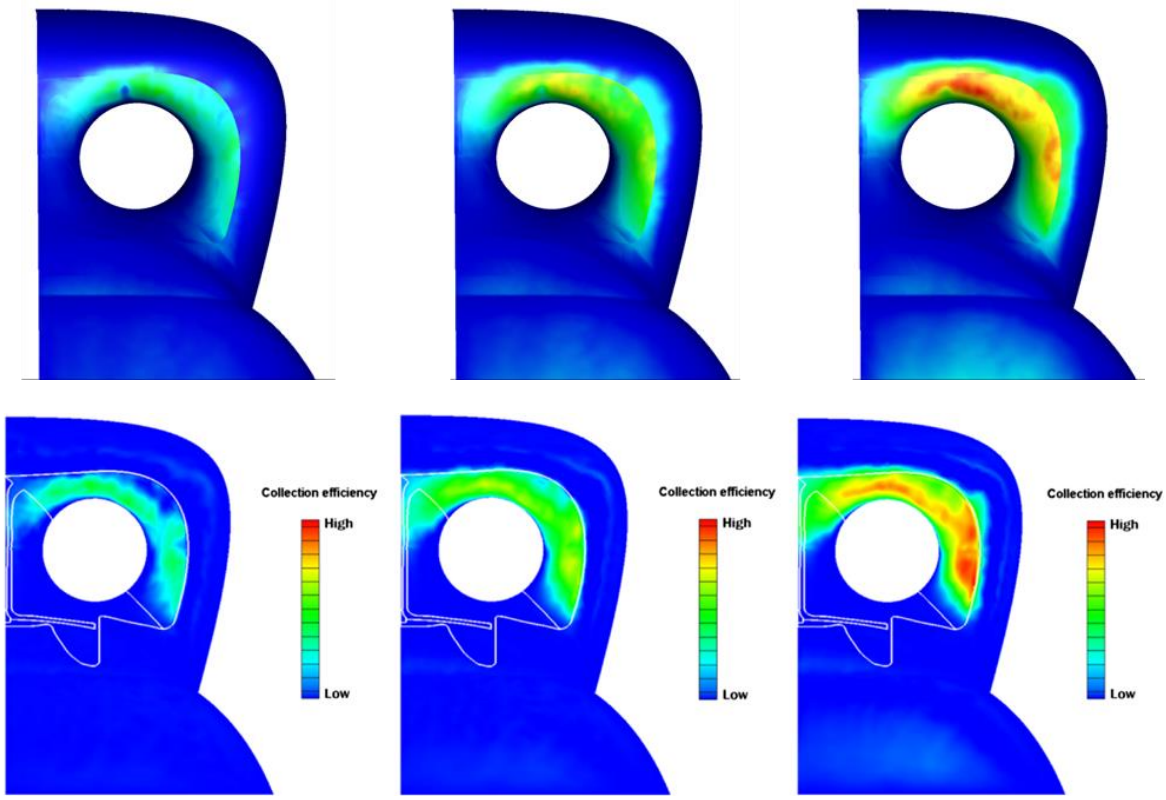

Figure 7-23 Collection efficiency around the engine air intake for MVD = 20 (left), 30 (middle), 40 (right) μm under case 1

7.3.2 Ice accretion

Next to the simulation of droplet impingement, the case 3 metrological conditions are used to simulate the ice accretion over the rotorcraft engine intake. In Figure 7-24, the ice accretion results provided by a wind tunnel, FENSAP, and current methods are shown. The ice thickness contour clearly shows that the predicted ice shape qualitatively agreed with the experimental and FENSAP results. Nonetheless, the ice thickness predicted by the present method is not properly matching with the experimental at the mid-section of the intake. Furthermore, some over predictions occurred on the upper side of the intake which might be due to the micro ice physics such as surface roughness. A further investigation of surface

roughness and heat transfer is needed for proper prediction of ice shapes on rotorcraft engine inlet.

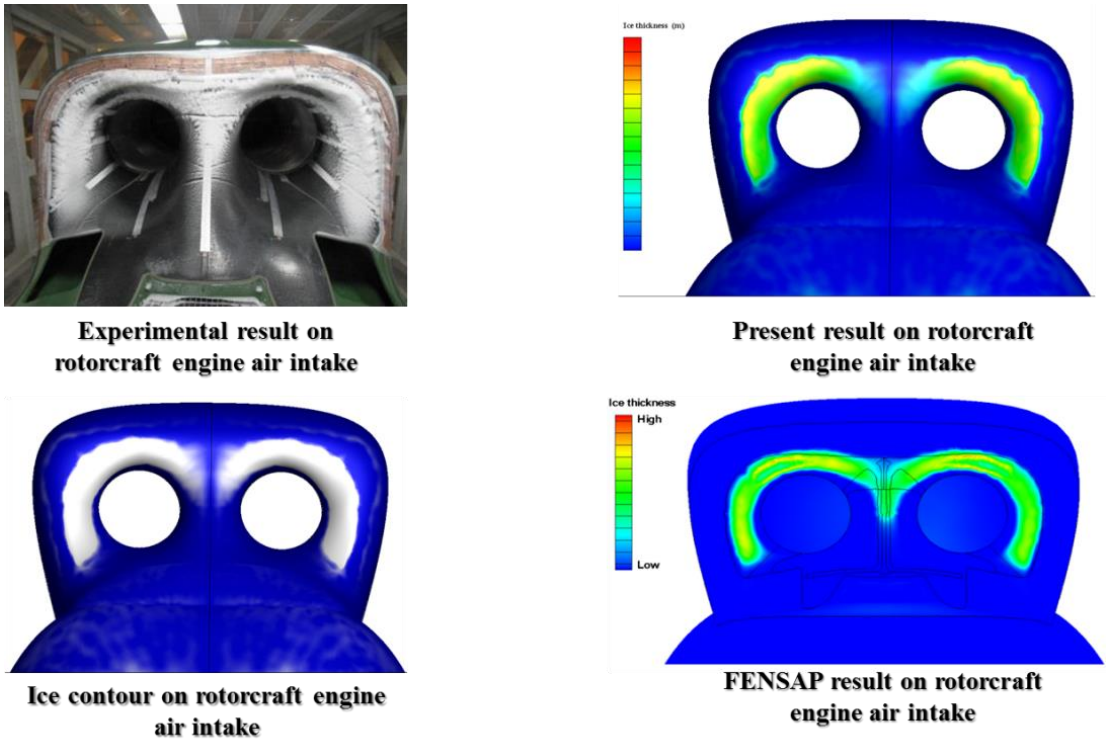

Figure 7-24 Ice accretion around the engine air intake at case 3 metrological condition for 15 minutes exposure time

7.3.3 SLD ice accretion on rotorcraft engine intake

After confirmation of the applicability of currently developed solver for various problems, SLD simulations were conducted on the rotorcraft engine intake. The metrological conditions used for these simulations are specified as case 4 in Table 7-3. The droplet diameter is increased to 160 μm along with a higher LWC value of 1.5 g/m^3. The collection efficiency and ice thickness under the metrological conditions in case 4 are shown in Figure 7-25. The collection efficiency increased dramatically and the impingement limit also increased eventually due to the bigger droplet diameter. Unlike the other three cases, the potential of ice accretion region is bigger for this case due to the droplet diameter. As

expected, the ice accreted all over the front part of rotorcraft engine intake as shown in Figure 7-25. As the thickness increases, there is no doubt that ice can affect the inflow air and the performance of the engine.

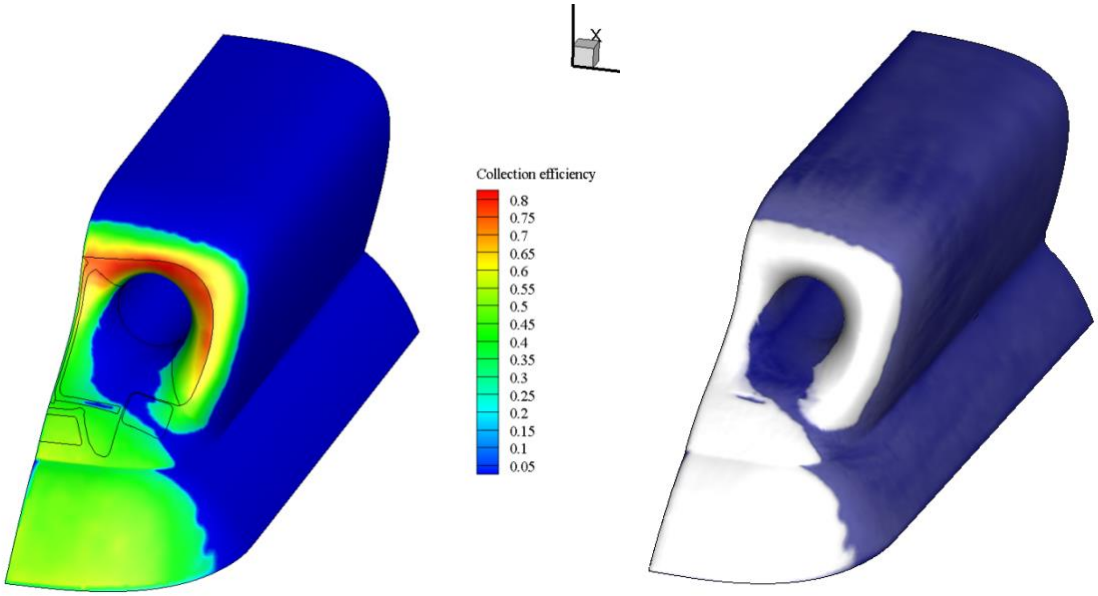

Figure 7-25 Collection efficiency (left) and ice accretion (right) around the engine air intake at case 4 metrological ice condition for 15 minutes exposure time

Chapter 8. Ice Protection System Modeling

Ice protection systems (IPS) are employed to ensure aircraft flight safety and can be implemented in wind turbines to avoid loss of performance [15, 80]. Anti-icing and de-icing systems are the two basic ice protection systems. The former prevents the ice formation while the latter removes the accreted ice layer before it causes significant degradation of performance. Several ice protection systems are used in the industry today:

- Bleed air heating system
- Electro-thermal heating system
- Ice breaking systems
- Chemical systems

IPS is designed for de-icing or anti-icing in an aircraft. The de-icing system is designed to remove ice that has accumulated, commonly on the wings and stabilizer leading edges. On the other hand, anti-icing system is turned on before entering icing condition that is designed to prevent the formation of ice on any surface by keeping it dry, by heating to a temperature that evaporates water upon impingement, or by heating the surface enough to prevent freezing. In an airplane, various ice protection systems are used depending on the requirement. For instance, leading edge of a wing may be protected by de-icing or anti-icing systems such as bleed air heating, electro-thermal heating, chemical, and ice breaking (de-icing). However, de-icing systems are not feasible to use for a pitot-static air data sensor. Hence, anti-icing system such as electro-thermal can be applicable for such case. Some of the IPS can be used as both de-icing and anti-icing systems, while some can be used as only anti-icing or de-icing system. IPS can be classified depending on their de-icing and anti-icing behaviours as shown in Figure 8-1.

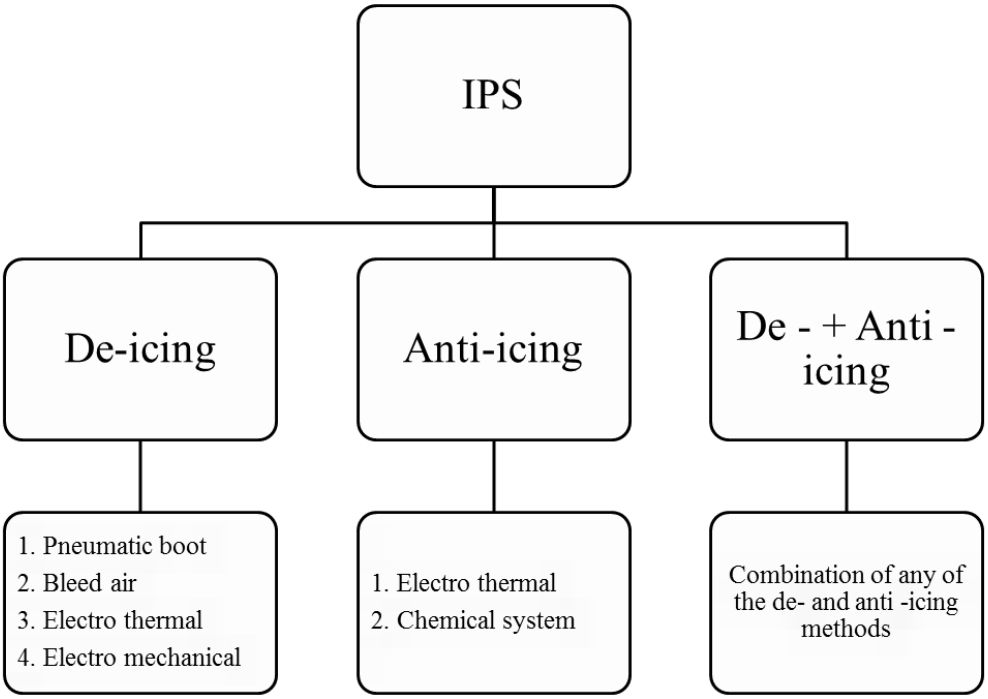

Figure 8-1 Classification of ice protection systems (IPS)

8.1 Bleed air heating system

Bleed air heating systems [104-106] can be used as an anti-icing or de-icing system to remove or prevent ice on aircraft, particularly on the wings, leading edge slats, horizontal and vertical stabilizers, engine inlets, and more. Generally, these systems use heated air that is routed spanwise along the inside of the surface need to be protected, and the source for this heated air can be the power plant of an aircraft. In business jet and large transport aircraft, hot air bled from the engine compressors can provide a satisfactory source of anti-icing heat. Figure 8-2 illustrates the typical bleed air heating system of a business jet. Generally, hot air from the compressor is routed to the wings through an ejector located at the inboard area of the wing. The ejector discharges to the piccolo tubes which distribute the hot air along the leading edge of the wing.

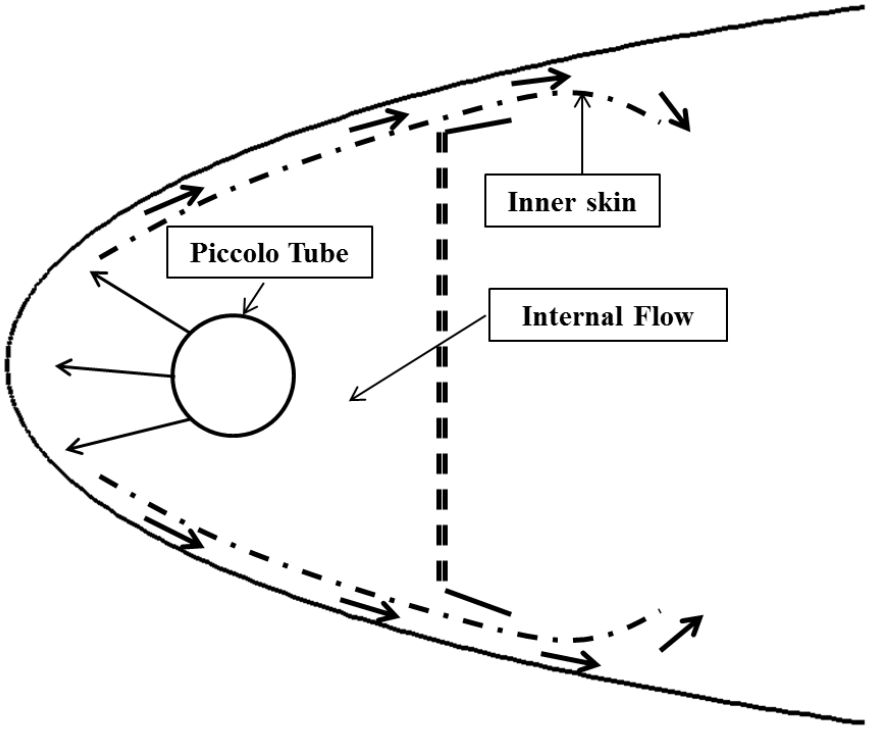

Figure 8-2 Schematic of bleed air heating system

The applicability and maintenance of the current IPS are reasonable in aircraft, but in wind turbines, it is not feasible owing to the requirement of bleed air. In order to implement bleed air heating system in a wind turbine, it should be equipped with some sources for bleed air. Moreover, operating cost and maintenance of the current IPS is reasonable in aircraft, but it would be high in wind turbines.

8.2 Pneumatic boot de-icing system

In the aircraft industry, pneumatic boot de-icing system is not new but is an often used IPS to break off formed ice on the leading edges of the aerodynamic surfaces [107-109]. The pneumatic boot is usually made of layers of rubber, with one or more air chambers between the layers, and the chambers are typically shaped as strips aligned with the long direction of the boot if multiple. The schematic diagram of a pneumatic boot de-icing system is shown in Figure 8-3 and placed on the leading edge of the wings and the stabilizers of an aircraft. The chambers are rapidly inflated and deflated, either simultaneously, or in a pattern of specific

chambers designed to break the adhesive force between the ice and the rubber, and allow the ice to be carried away by the relative wind flowing past the aircraft. However, the ice must be completely carried away from the trailing portions of the surface to avoid re-freezing behind the protected area [110]. Ice bridging phenomenon occurs in certain older designs of the pneumatic boot where the ice did not accumulate to a sufficient thickness and fragility, hence malleable ice could be pushed into a shape out of reach from of the inflatable sections of the boot. Modern designs of pneumatic boot address this dilemma by increasing the speed of inflation/deflation action, and by alternating the timing of inflating/deflating adjacent chambers.

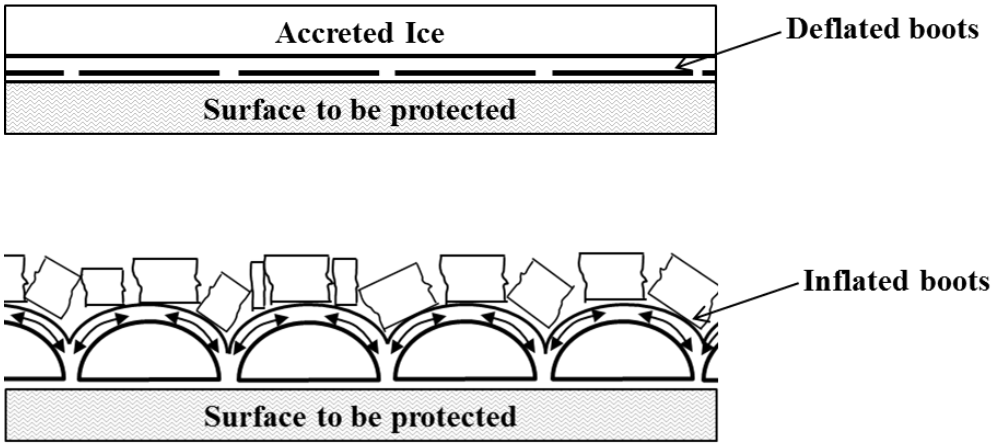

Figure 8-3 Schematic of pneumatic boot de-icing system

For the pneumatic boot de-icing systems, the source of operating air varies with the type of power plant installed on the aircraft. For a reciprocating engine aircraft, a dedicated engine-driven air pump mounted on the accessory drive gearbox of the engine is used. On the other hand, bleed air from the engine compressor can be a source for de-icing boot system in a turbine engine. A relatively low volume of air is enough for the operation of a pneumatic boot de-icing system which may have little effect on engine power. Nonetheless, the use of bleed air is more efficient than adding a separate engine-driven air pump.

Pneumatic boot de-icing is one of the successful, cheap, lightweight, and low power required systems serving in the aircraft industry for decades. However, this method is not feasible for wind turbines owing to the compressed air used for inflation of the boots. Furthermore, the pneumatic boot systems need suction pumps to maintain the deflation of the boots when it is not in use. Overall, the power requirement would be out of the budget of a wind turbine and a separate system would be necessary to generate compressed air to inflate the boots.

8.3 Chemical anti-icing

Chemical anti-icing [111] is used in some aircraft to prevent ice formation on the leading edges of the wing, stabilizers, windshields, and propellers. The wing and stabilizer systems which are often called weeping wing systems and are known by their trade name of TKS systems have their chemical anti-icing system based upon the freezing point depressant concept. An antifreeze solution is pumped from a reservoir through a mesh screen embedded in the leading edges of the wings and stabilizers which are activated by a switch in the cockpit. The liquid then flows over the wing and tail surfaces, preventing the formation of ice as it flows by mixing with supercooled water in the cloud, depressing its freezing point, and allowing the mixture to flow off on of the aircraft without freezing. Although the system is designed to anti-ice, it is also capable of de-icing an aircraft. When ice has accumulated on the leading edges, the anti-freeze solution chemically breaks down the bond between the ice and the airframe which allows aerodynamic forces to carry the ice away, hence clearing the airframe of accumulated ice before transitioning to anti-ice protection.

The TKS weeping wing system contains formed titanium panels that are laser-drilled with over 800 tiny holes (.0025inch diameter) per square inch, mated with nonperforated stainless steel rear panels and bonded to wing and stabilizer leading edges. As fluid is delivered from a central reservoir and pump, it seeps through the holes and aerodynamic

forces cause the fluid to coat the upper and lower surfaces of the airfoil. The fluid is glycol based which prevents ice from adhering to the aircraft structure. Some aircraft with weeping wing systems are certified to fly into known icing conditions although others use it as a hedge against unexpected ice encountered in flight since the systems are basically the same. Reservoir capacity permits 1- 2 hours of operation. TKS weeping wings are used primarily on reciprocating aircraft that lack a supply of warm bleed air for the installation of a thermal anti-ice system. Since the system is simple and effective, it can also be used on some turbine powered corporate aircraft.

These chemical anti-icing systems require a reservoir to store the weeping fluid, a pump to discharge the weeping fluid and other necessary system setups. The cost of weeping fluid, maintenance cost, and power requirement to operate chemical anti-icing system would be very high. Hence, chemical anti-icing systems are also not feasible for a wind turbine blade.

8.4 Electro-thermal system

Electric current is used as a source of to heat to prevent ice formation on various components on an aircraft, mostly on air data probes such as pitot tubes, static airports, total air temperature and angle of attack probes, ice detectors, and engine sensors, which may also include water lines, waste water drains, and some turboprop inlet cowls [112-114]. On the other hand, transport category and high-performance aircraft use thermal electric anti-icing in windshields. In devices that employ thermal electric anti-ice, various schemes such as an internal coil wire, externally wrapped blankets or tapes, as well as conductive films and heated gaskets are used where the current flows through an integral conductive element that produces heat, a temperature that is elevated above the freezing point of water so ice cannot form.

In recent years, the Boeing 787 Dreamliner is an example of a commercial airframe that uses electro-thermal ice protection where the resistive heating circuit is embedded inside the

glass and carbon composite wing structure. In this system, half the energy of traditional bleed-air systems (as provided by the engines) is being utilized, and that drag and noise are also reduced as claimed by Boeing. This electro-thermal IPS is easy to operate and it is possible to use this system as an anti-icing system using a low power supply. Unlike other IPS, it is easy to adopt for any shape and size depend on the requirement. Hence, the electro-thermal de-icing system can be an option to implement on a wind turbine blade [115]. The challenge is to minimize power consumption while avoiding ridges on the upper surface of the wing and wind turbine blades. In this study, the analysis of electro-thermal ice protection system is conducted for NACA0012 airfoil using a state-of-the-art CFD code to validate the current computational model. The same validated computational model is applied to a wind turbine blade DU21. The detailed design of electro-thermal IPS is explained in the coming sections.

8.5 Numerical simulation of electro-thermal ice protection system

The simulation of electro-thermal ice protection system starts with the air flow computation around the airfoil [116-118]. The compressible Navier-Stokes code based on the finite volume method and the Roe's approximate Riemann solver, FLUENT, are used. A simple Spalart-Allmaras turbulence model is employed to compute turbulence effects in dry air. A Riemann invariant is implemented for far-field boundary condition along with no slip boundary for solid surfaces.

Droplet impingement and ice accretion are simulated by DROP3D and ICE3D modules of the icing code FENSAP-ICE [30, 119]. The DROP3D [28] module solves liquid water content and droplet velocities in a Eulerian framework and predicts the amount of water collected by the exposed surface. The ICE3D [120] module determines the ice accretion and water runback in conjunction with the CHT3D module, the conjugate heat transfer module of FENSAP-ICE, based on the coupled heat convection and conduction equations.

The droplet impingement solver DROP3D is based on the finite element method and Newton's method is used to linearize the non-linear governing equations. The continuity and momentum equations of Eulerian droplet motion used by DROP3D can be written as,

$$\frac{\partial \alpha}{\partial t} + \nabla \cdot (\alpha \mathbf{u}_d) = 0, \tag{8.1}$$

$$\frac{D\mathbf{u}_d}{Dt} = \frac{C_D \,\mathrm{Re}_d}{24K}(\mathbf{u}_a - \mathbf{u}_d) + \left(1 - \frac{\rho_a}{\rho_w}\right)\frac{1}{Fr^2}\mathbf{g} + \frac{\rho_a}{\rho_w}\frac{D_a\mathbf{u}_a}{Dt}. \tag{8.2}$$

where variables α and $\mathbf{u}_d$ are the mean values of non-dimensional water volume fraction and droplet velocity over a small fluid element around the location x at time t. The terms, $C_D \,\mathrm{Re}_d(\mathbf{u}_a - \mathbf{u}_d)/24K$ represent drag force on the droplets, $(1-\rho_a/\rho_w)(\mathbf{g}/\mathrm{Fr}^2)$ represent the buoyancy force from gravity and $(\rho_a/\rho_w)(\mathrm{D_a}\mathbf{u}_a/\mathrm{Dt})$ represent the forces exerted on an air particle that would have occupied the volume of the droplet. In most cases, the last term $(\rho_a/\rho_w)(\mathrm{D_a}\mathbf{u}_a/\mathrm{Dt})$ is negligible due to the low ratio of air to water densities.

The non-dimensional air velocity, $\mathbf{u_a}$, is obtained from the solution of the Navier-Stokes equations. Due to the low liquid water concentration, the effect of the droplets on the airflow is neglected. Water volume fraction and droplet velocity vector in the whole domain can be evaluated by solving equation (8.1) and (8.2). Now, the collection efficiency (β) can be easily determined by the following relation:

$$\beta = -\alpha \boldsymbol{u}_d . \boldsymbol{n}. \tag{8.3}$$

The computation domain and grid distribution along with boundary conditions are shown in Figure 8-4. A well- known grid generation tool is used to generate the grid.

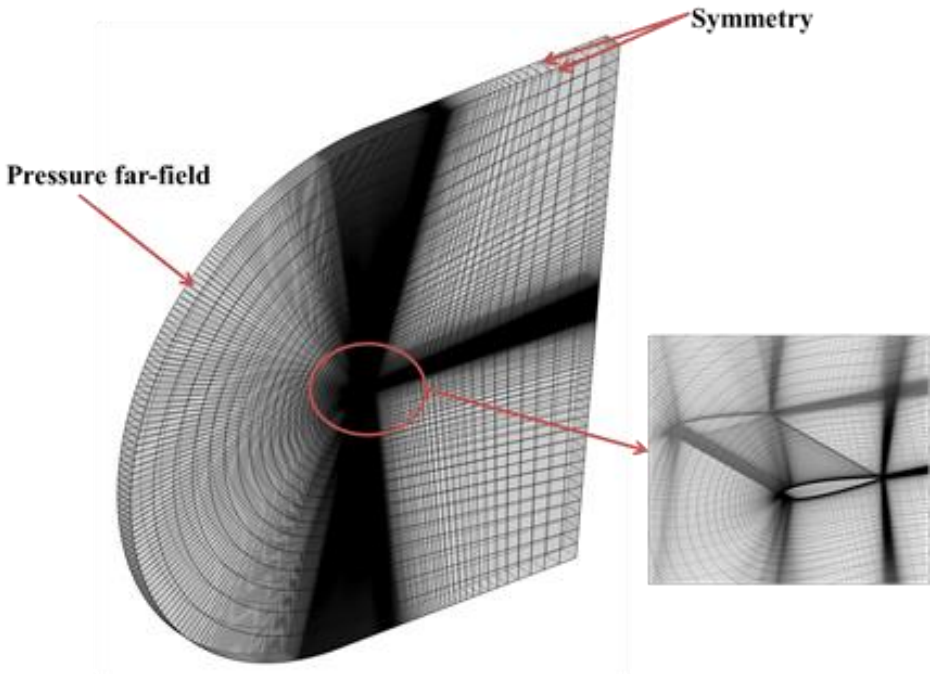

Figure 8-4 Computational domain and spatial discretisation

The ICE3D solver of FENSAP-ICE is used for ice accretion prediction. This is a 3D partial differential equation based solver employed with Messinger model. This module is capable of predicting water runback on the surface. Now, the mass and energy conservation equation can be written as follows,

$$\rho_w \left[\frac{\partial h_f}{\partial t} + div\ \left(\bar{\mathbf{u}}_f h_f \right) \right] = U_\infty LWC\beta - \dot{m}_{evap} - \dot{m}_{ice}, \tag{8.4}$$

$$\begin{aligned} &\rho_w \left[\frac{\partial h_f C_w T}{\partial t} + div\left(\bar{\mathbf{u}}_f h_f C_w T \right) \right] = \left[C_w T_{d,\infty} + \frac{\left\| \mathbf{u}_d \right\|^2}{2} \right] \times \\ &U_\infty LWC\beta - 0.5\left(L_{evap} + L_{subl} \right)\dot{m}_{evap} + \left(L_{fusion} - C_{ice} T \right)\dot{m}_{ice} + \\ &\sigma\left((T_\infty + 273.15)^4 - (T + 273.15)^4 \right) + \dot{Q}_h. \end{aligned} \tag{8.5}$$

A Finite Volume method is used to discretise these equations and cell centered scheme is employed. Finally, the melting process in the ice layer and the heat conduction through the solid layers are evaluated by 3D heat conduction module C3D. The nonlinear, unsteady heat conduction equation for each material is,

$$\frac{\partial H_M(T)}{\partial t} = \nabla.\left(k_M(T)\nabla T\right) + S_M(t). \qquad (8.6)$$

where $H_M(T)$ and $k_M(T)$ are the enthalpy and the conductivity of material *M*, respectively. Enthalpy and conductivity depend on temperature *T*, which varies in the domain continuously. In order to model electric heaters, volumetric heat source term, $S_M(t)$ has been introduced in the equations. The user can change the heater power through control sequence or by using a thermostat to confine the temperature within certain limits. Canonical Galerkin Finite Element discretisation is used to solve this equation and the implicit backward Euler scheme is used for time integration.

Unsteady conjugate heat transfer module (CHT3D) is used for de-icing simulations [121]. This module requires the time-accurate solution of mass, momentum and energy balance between air and water flows, water film, and the ice layer. The air solution computed by Navier-Stokes is the initial solution and with water mass collected on the exposed surfaces, the CHT3D module can be initiated. In the CHT3D loop, at each time step, Newton iterations are performed until the heat fluxes are conserved. Then, according to the net mass growth from the film and shrinkage due to melting, the ice shape can be computed. The flow chart of unsteady CHT3D is shown in Figure 8-5.

Electro-thermal ice protection systems are typically built with multi-layer and multi-material skin assemblies divided into separate heating strips. The simulations of these arrangements usually involve a single-fluid domain. Initial solutions are required for droplet and surface liquid water film. These solutions should be set up with a specified wall temperature on the interface, so that the initial non-zero wall heat fluxes can ensure good convergence.

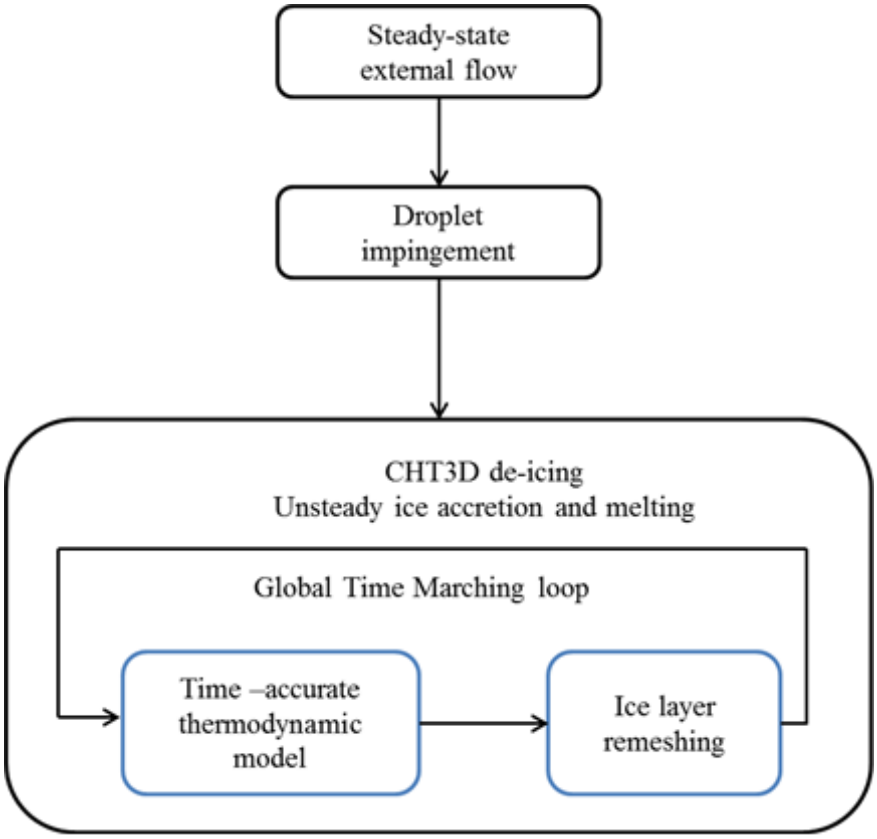

Figure 8-5 Flowchart of unsteady conjugate heat transfer

8.6 Calculation of heater properties

In a de-icing analysis of a wind turbine blade, heater parameters such as heater length, heater area and power requirement for de-icing have to be calculated prior to the modeling of the blade. Generally, ice accumulates along the leading edge of the blade; therefore the heater should be large enough that at the very minimum, the leading edge is covered. For the current analysis, the heater area is chosen based on a representative geometry of a cylinder at the leading edge with a diameter equal to a quarter of the blade thickness, followed by a section that is one-quarter the length of the chord as illustrated in Figure 8-6.

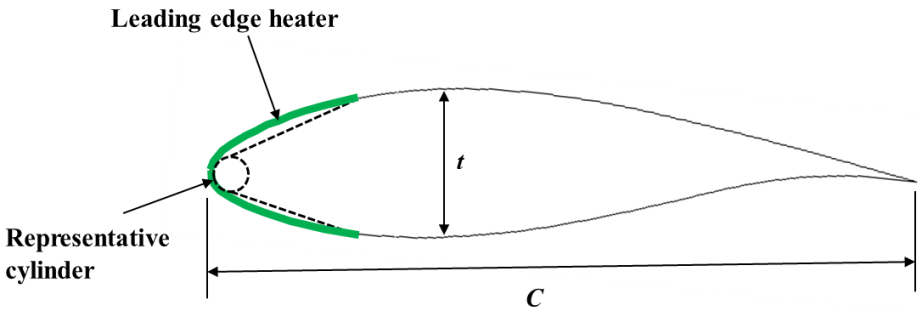

Figure 8-6 Airfoil with heating element

The length of the heater from the leading edge is calculated [122] as:

$$L_h = \frac{\pi}{16} t + \frac{1}{4} C. \tag{8.7}$$

Where t is the chord thickness and C is the chord length. In order to reduce the complexity, it is assumed that the heater length is equal on both the bottom and on the top. The total area A is calculated by multiplying the total length of the heater by the span width. At different angles of attack, the ice accumulation area will change depending on the droplet impingement. Higher angles of attack will result in a wider accumulation of ice on the pressure side of the airfoil. On the contrary, negative angles of attack will result in more ice accumulation on the suction side of the airfoil. Moreover, the trailing edge of the airfoil may also be protected in the event of run-back icing. The power of the heating elements used on the airfoil's surface is expressed in the equation and depends on the convective heat transfer coefficient (h_c), the ambient, target, and surface temperatures $T_\infty, T_{target}, T_{surf}$, and the heating area A:

$$P(t) = h_c * A * \left(T_\infty - T_{target}\right) + h_c * A * \left(T_{target} - T_{surf}\right). \tag{8.8}$$

The first right-hand-side term represents an approximation of the power needed for the de-icing and the second one represents the correction, considering the gap between the target and surface temperatures. The "heating coefficient" h_c is approximated with the convective heat transfer coefficient, evaluated using a flat plate hypothesis given by equation (8.9) .

$$h_c = \rho_{air}.Cp_{air} * V_\infty * St, \tag{8.9}$$

here the Stanton number is,

$$St = \frac{1}{2} C_f, \tag{8.10}$$

the friction coefficient C_f is evaluated for a turbulent flow because heating elements are located in the turbulent zone of the airfoil:

$$C_f = \frac{0.058}{\mathrm{Re}^{0.2}}. \tag{8.11}$$

The wind turbine blade selected for current analysis is DU21 and it is one of the airfoil sections of NREL 5MW wind turbine[123, 124]. The target temperature for the current study is assumed to be 288K and all heater parameters are as shown in Table 8-1. Calculated heater geometrical parameters (heater length and area) are used to model the heater and calculated heater power requirement is used in FENSAP for the current computational model.

Ambient temperature (K)	263.15
Surface temperature (K)	273.15
Length of heater (m)	1.0199
Heating power (W/m^2)	4313.7

Table 8-1 Heater parameters for DU21 airfoil

8.7 Results and discussion

Wright.et.al [41] from NASA Lewis Research Centre conducted experiments on thermal ice protection system for NACA0012 airfoil with a chord of 0.9144 m and span of 1.8288 m. The model was fabricated into two pieces: a leading edge section (0.224 m) of the chord, and a wooden after-body (0.6604 m). This model has seven leading edge heating zones as shown

in Figure 8-7. The leading edge material composition and thickness information are given in Figure 8-8.

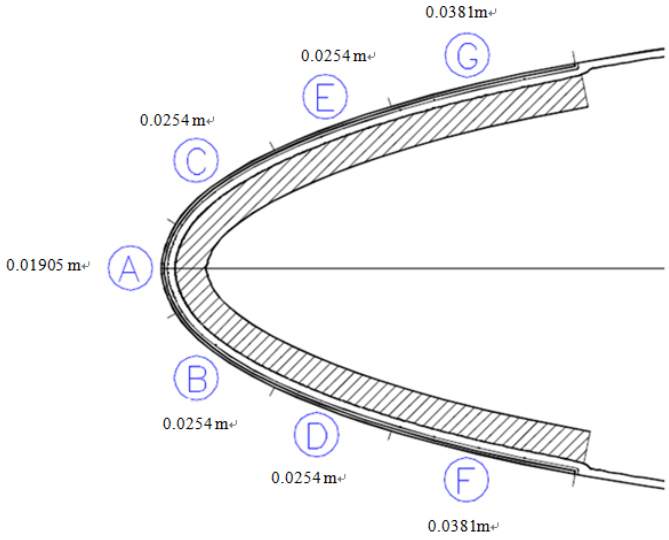

Figure 8-7 Cross-Section of the airfoil leading edge and heating zones : Where A to G are different heating regions

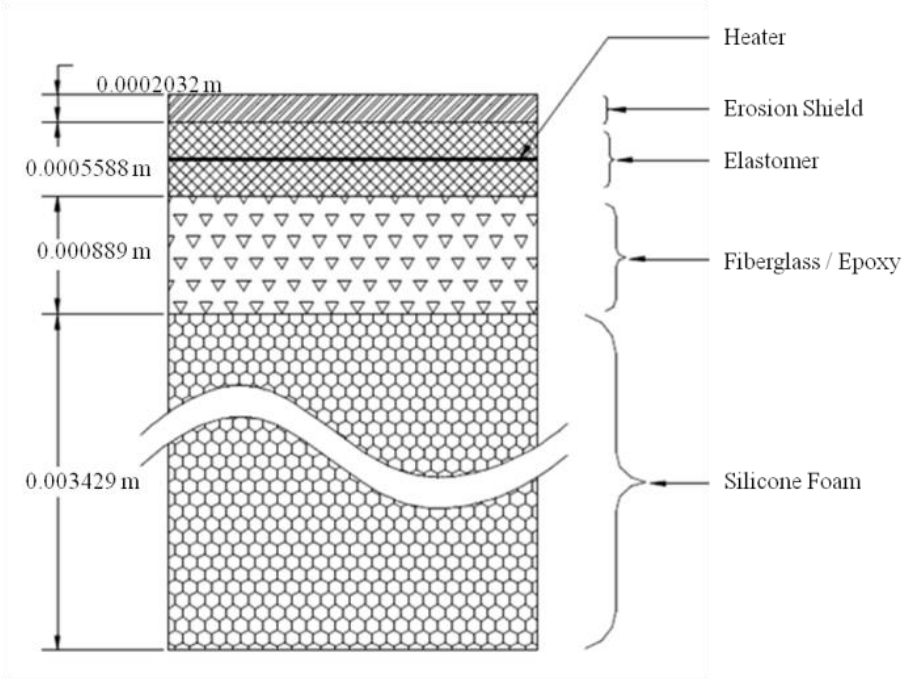

Figure 8-8 Flowchart of unsteady conjugate heat transfer

The material property of each layer is illustrated in Table 8-2. The computation domain of leading edge heater section with external flow domain is shown in Figure 8-9. The boundary conditions applied for the current study is shown in Table 8-3.

Material Name	Density (Kg/m^3)	Conductivity (W/m·k)	Enthalpy (J/kg)
Erosion shield	8025.3	16.250	137,235
Elastomer	1383.9	0.2561	343,087
Fiberglass / epoxy	1794.0	0.2940	428,859
Silicone Foam	648.75	0.1210	308,779

Table 8-2 Leading edge material properties

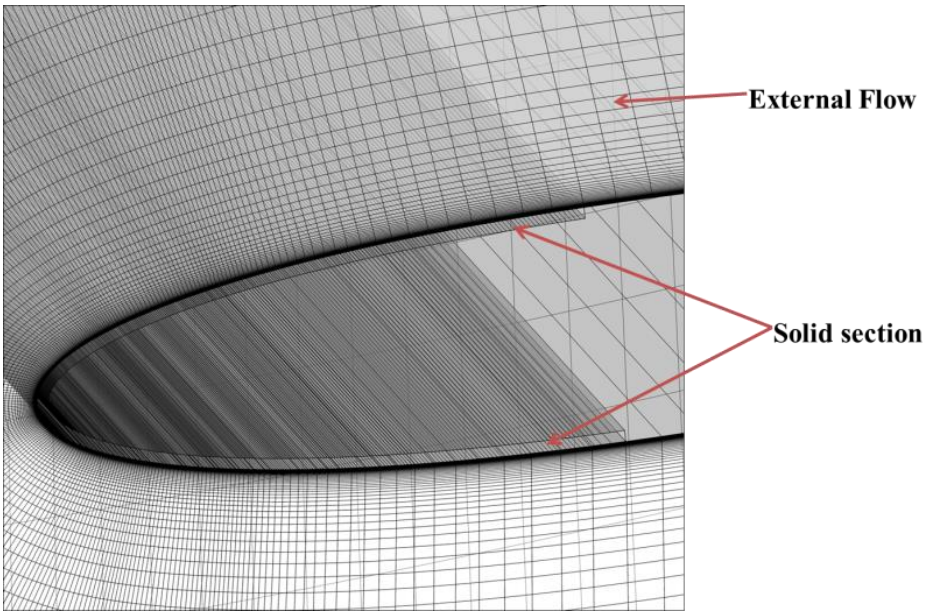

Figure 8-9 Computational domain with solid section

The accurate airflow solution around the NACA0012 airfoil is predicted by the finite volume Navier-Stokes code. The collection efficiency results are shown in Figure 8-10 and turn out to be in good agreement with the experimental data. The collection efficiency shows the potential of ice formation on the exposed surface. The computed collection efficiency results are in good agreement with the experimental.

	NACA0012	DU21
Velocity (m/s)	44	66.48
Temperature (K)	266.48	263.15
LWC (g/m^3)	0.78	0.38
Heater A (W/m^2)	7750.05	4313.68
Heater B,C (W/m^2)	10850	4313.68
Heater D-G (W/m^2)	10850	4313.68

Table 8-3 Metrological conditions used for NACA0012 and DU21 aerofoil

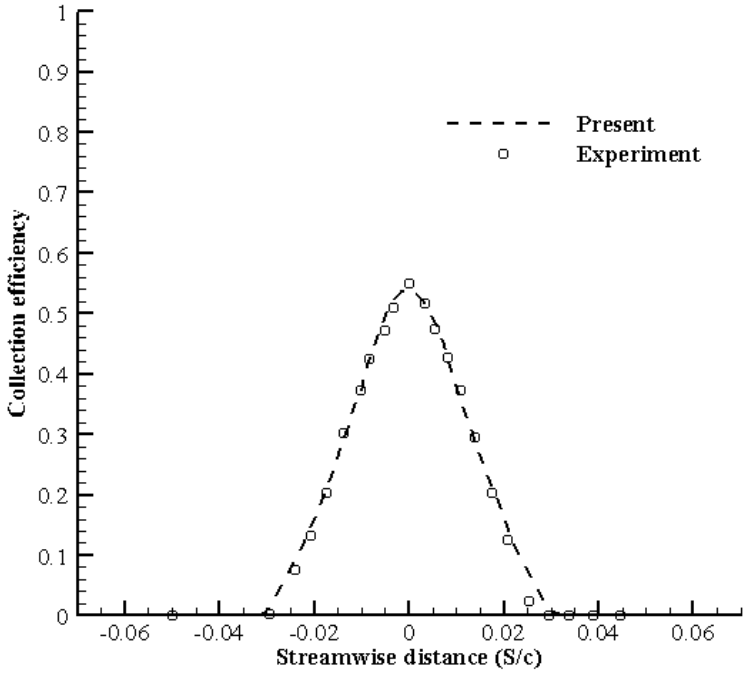

Figure 8-10 Collection efficiency comparison on NACA0012 airfoil

Seven heating elements operated in a sequence for 600 seconds are used for validating the de-icing computational model. The seven heaters were named as A-G and the heater sequences, as well as sequence of heater activation, were chosen to be same as an experiment [41]. The comparison of heater temperature is shown in Figure 8-11.

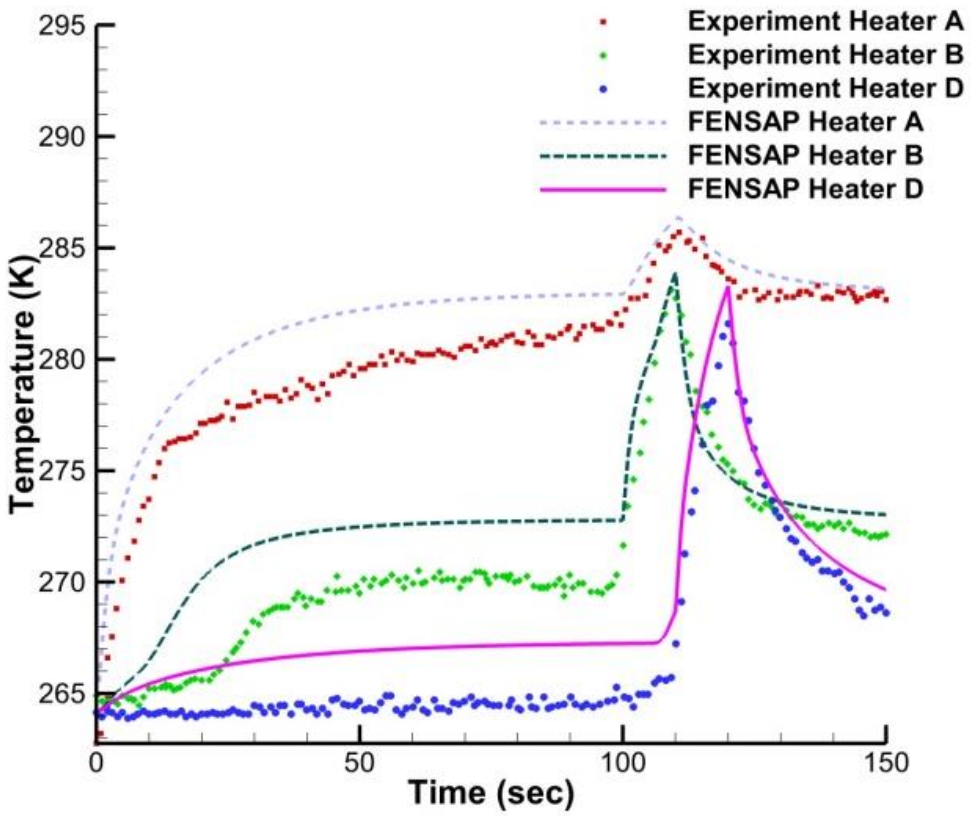

Figure 8-11 Comparison of first heater cycle temperature for NACA0012

The results compare reasonably well to the experimental data, which explicitly shows the correct implementation of heating elements and this computational model can be applied for other flow conditions. On the other hand, the cooling cycle of heater B did not match properly with the experimental data. This result may be related to limitations of thermal and runback water models of FENSAP.

The DU21 airfoil was applied with the same computational model as NACA0012 and different boundary conditions as shown in Table 8-3. Figure 8-12 illustrates the shapes of ice accretion on DU21 airfoil for various icing exposure times with a maximum exposure time of 1200 seconds.

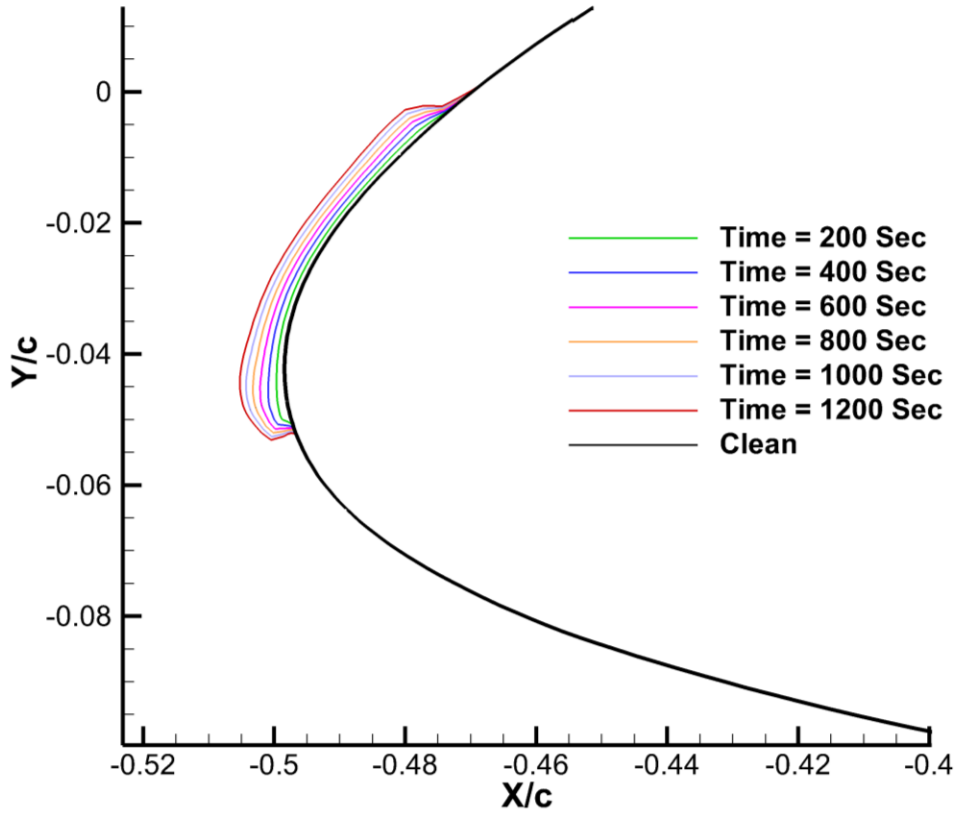

Figure 8-12 Ice accretion at various time intervals on DU21 airfoil without IPS

It is apparent that the ice formed on the surface of the airfoil disturbs the flow and changes the flow field which may affect the performance of wind turbine. IPS can be an option to avoid the performance degradation under this flow conditions. Heater parameters calculated in section 3 is used to model the heater and the heater power input in FENSAP. The material property and composition of the leading edge for the current model are chosen to be same as NACA0012. As the angle of attack and airfoil is different, heater cycle and heater sequence are changed for the current simulation. The seven heaters named as A-G and in the first cycle heater A and B are activated for 80 seconds. The heater A, B, and C are then activated in the second cycle for 20 seconds. Followed by this, heater A, D, E, F, and G are activated in the third cycle for 10 seconds. The sequences of the operation of heaters are illustrated in detail in Figure 8-13.

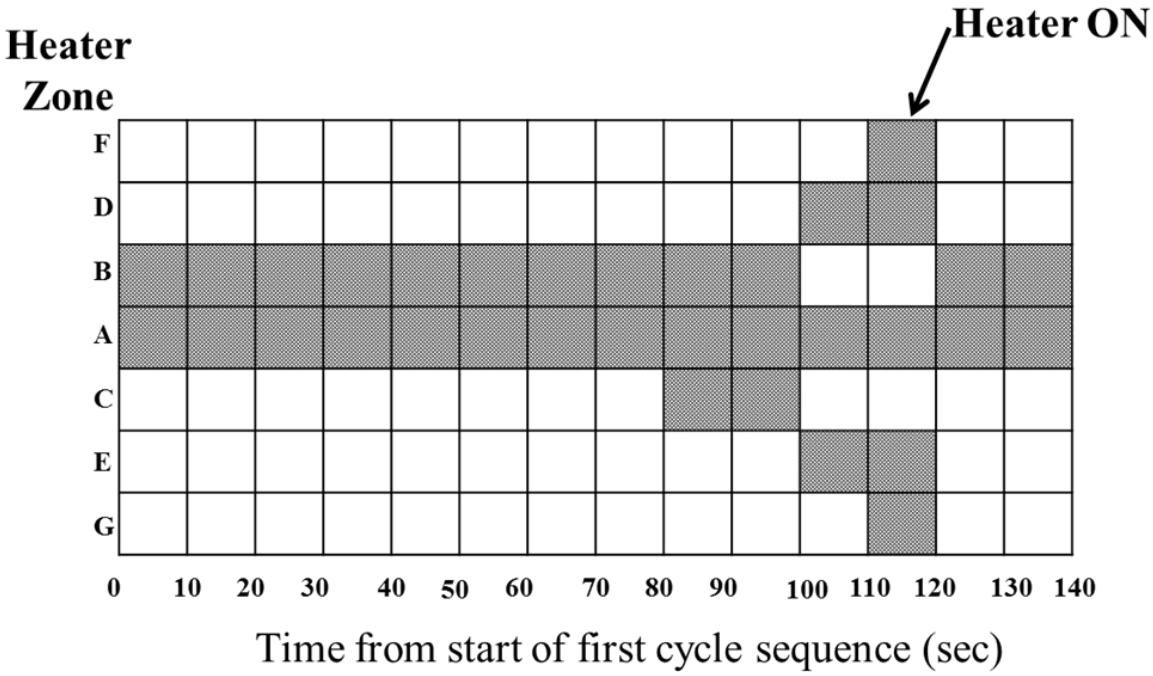

Figure 8-13 Typical heater cycle sequence for DU21 airfoil

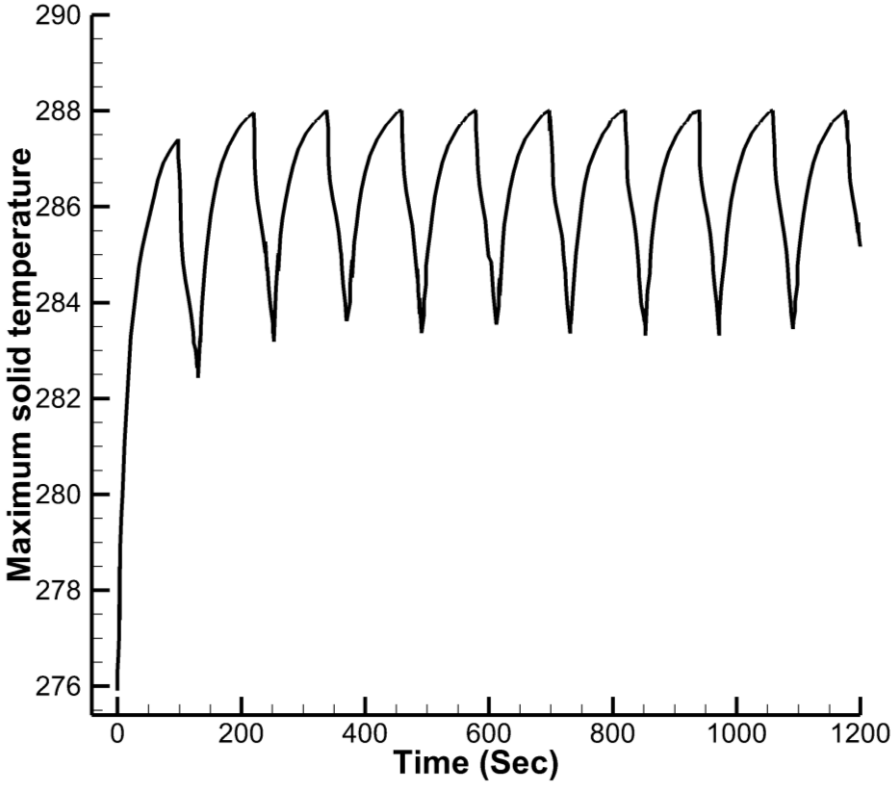

Figure 8-14 Solid surface temperature on DU21 airfoil

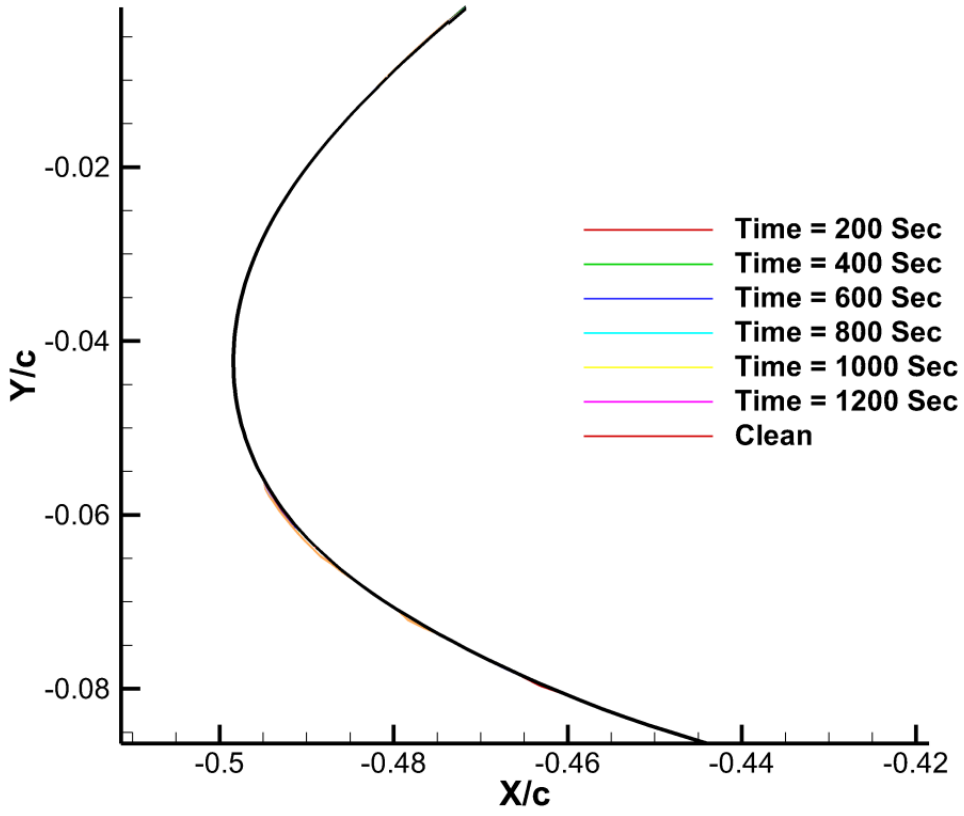

Figure 8-15 Ice accretion at various time intervals with IPS for DU21 airfoil

The maximum solid surface temperature on the airfoil is shown in Figure 8-14. The trend followed by the DU21 surface temperature is same as NACA0012 heater temperature. The maximum temperature on the surface of airfoil did not exceed much above 288K. This shows that the heater parameter calculations in section 8.6 are acceptable. The ice accretion results at various time steps with IPS are shown in Figure 8-15. Shedding of ice and dramatic reduction of ice accretion can be easily observed.

The contours of temperature in the solid structure at various time intervals for DU21 airfoil are shown in Figure 8-15. The propagation of heat during time steps is explicitly shown in this figure. The results of a DU21 airfoil with IPS are acceptable and the same methodology is applicable for other airfoil sections of NREL 5MW or any other wind turbines.

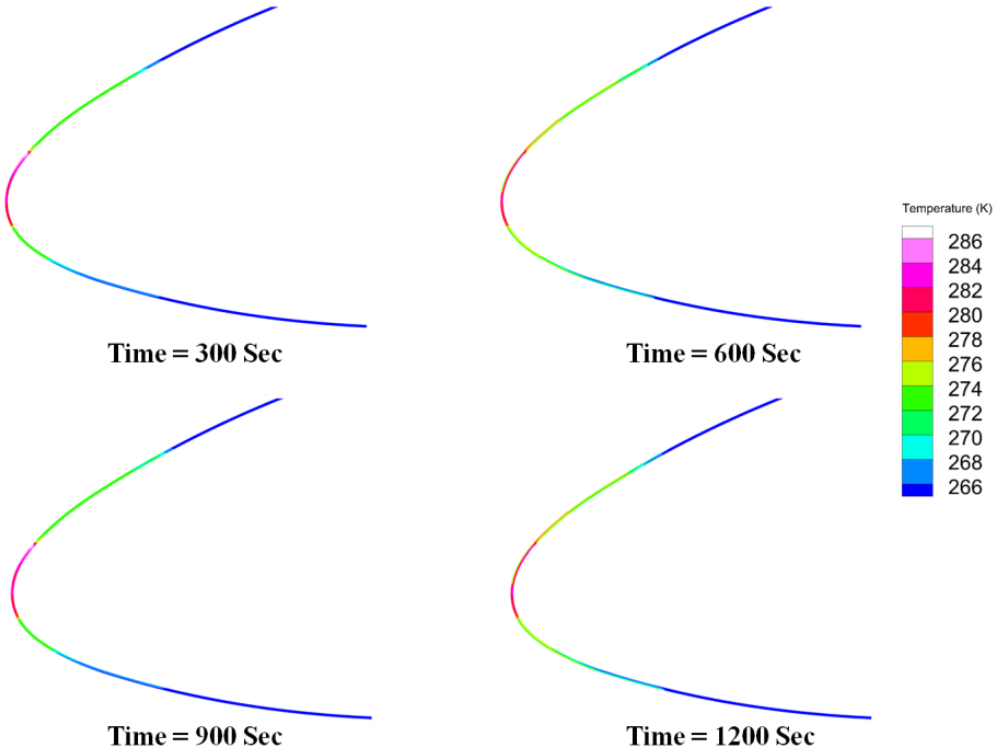

Figure 8-16 Temperature contour of solid section at various time intervals for DU21 airfoil

Chapter 9. Parallelization

One of the challenging issues in the icing simulations is the higher computational cost due to a large number of cells used to maintain the desired Y-plus value for the accurate evaluation of shear stress and heat flux. In growing computational world, parallel computing would be a better option to overcome the higher computational cost to reduce computation time. In this chapter, the methodology used for the parallelization of air solution solver and droplet solver is discussed along with their performance under the parallel framework.

9.1 Explicit FVM solver parallelization

The local nature of discretization renders the cell centered finite volume method to be compact and highly parallelizable. Since the solution is approximated independently in each element of which the inter-element data sharing is only needed among the face neighbour elements or the elements sharing a common face to calculate numerical fluxes, the inter-process communication is only required between the corresponding neighbouring processes for the computation at partition boundary faces or faces having their left and right elements with different processes.

The present FVM code was parallelized by a single program multiple data (SPMD) parallel model [125-127]. The air solver and droplet solver were parallelized by using a message-passing-interface (MPI) library [128] and Coarray FORTRAN (opencoarrays library), respectively [129]. Both MPI and opencoarrays guarantees the maximal flexibility of the parallel programming, portability, and scalability of the distributed memory parallel architectures. As seen in Figure 9-1, all the parallel processing steps were unified using a shell program.

For all the floating point operations, the software setup including a high-performance and widely portable implementation of the parallel library and 64-bit compilers with double

accuracy was used. Furthermore, with the use of Intel Xenon processors, a Linux cluster sharable among multiple users was established which is equipped with eighty cores interconnected by dual port Gigabit Ethernet.

Parallelization of the FVM solver for air flow includes the following steps: 1) domain decomposition (mesh partitioning); 2) communication process; 3) merging of sub-domains, and 4) parallel performance measurements. The description of these steps is in the following sub-sections.

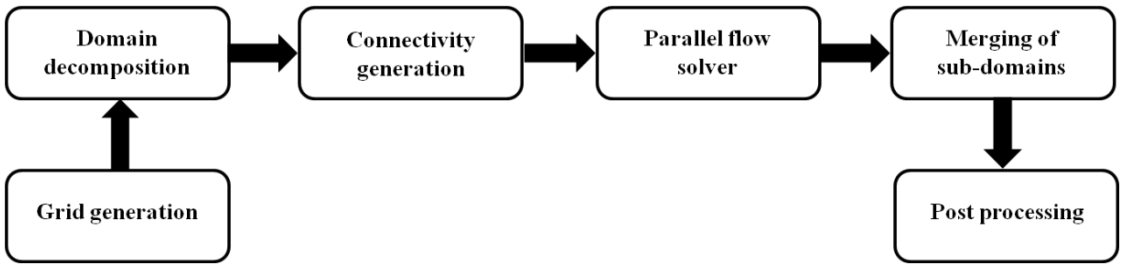

Figure 9-1 The flow of unified shell program for parallel processes

9.1.1 Domain decomposition

As the first step in the parallel programming, the computational domain is decomposed into several sub-domains and then each sub-domain is assigned to each processor using open source software, ParMETIS [130], which is an MPI-based parallel library that implements a variety of algorithms to compute fill-reducing orderings of sparse matrices, and to partition the unstructured graphs, decomposing the given mesh so that each processor has approximately the same number of elements to balance the load for the processors and minimize the number of links cut by the decomposition. The partitioned results and the including node and element connectivity information after the decomposition of the domain are assigned to the processors. For the case of flows around a cylinder and an airfoil with approximately 25,000 elements, the sub-domains generated by ParMETIS are illustrated in Figure 9-2.

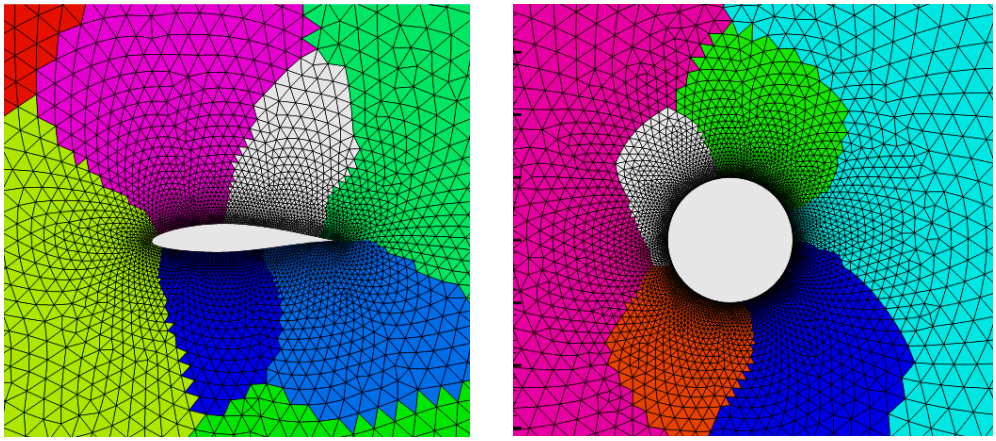

Figure 9-2 The mesh partition by ParMETIS. Different colors represent sub-domains owned by different processors

9.1.2 Communication process

The present parallel solver for both air and droplet is based on a single program multiple data (SPMD) programming model, which executes the same program in all processors with different data and can manage the processors to conditionally execute only certain parts of the program so that some of the processors may not necessarily need to execute the entire program.

MPI library and opencoarray library were used for parallelization in air solver and droplet, respectively. Both libraries have the point-to-point communication and collective communication modules which can be utilized for the present work. Communication process in a parallel solver is the engine of parallelization, which should be smooth and faster for a better performance. The delay in communication may lead to the performance loss of the parallel solver. Both parallel libraries having a variety of communication modules which can be applied for the parallelization of present air and droplet solvers. Hence, the selection of communication module is very critical and tricky to avoid unnecessary performance penalties.

General, the communication is conducted between two adjacent cells which belong to different processors and share the same face. Figure 9-3 illustrates the point-to-point data communication on the face of the cells.

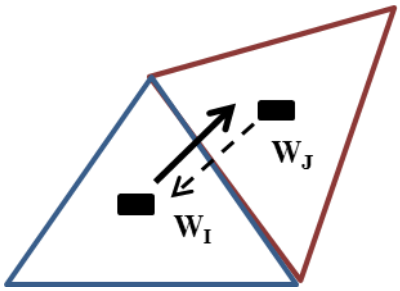

Figure 9-3 Point-to-point communication

9.1.3 Merging of sub-domains

All the partitioned sub-domains execute the same solver with respective data inputs and solve the flow fields in their local domain during the parallel computations. Individual processor plots its solution after the solution converges for post-processing purposes. However, the results were not visually smooth at the boundaries of the sub-domains due to biased interpolation of the solution and of not considering all vertex neighbourhoods for interpolations. Hence, a merging subroutine was devised for better post-processing of the solutions of parallel computations where all subdomain results were exported into a unified single domain for better visualization. All the solutions are needed to be interpolated to the node for post-processing software such as Tecplot although each element contains its own solution so that the biased interpolation that considers all the neighbours of the node could not result in very poor visualization. Merging of sub-domains was performed to avoid such limitation for post-processing after terminating parallel processing, where the results are irrespective of the number of processors as the solution in each element is calculated locally and located at the cell centre.

9.2 MPI based parallel air solver

The present air flow field solver is parallelized by using MPI library. The parallelization in the present study was achieved without compromising the serial algorithm for a higher parallel performance and allows MPI communications to completely overlap with the

computations. As summarized in Figure 9-4, this type of algorithm is easier to achieve in explicit time marching schemes which are usually referred to as hiding communication behind computation. The point-to-point communication methodology of MPI of which the message passing operation may only occur between two different processors was used in such a way that while one processor is performing a send operation, the other processor performs a matching receive operation.

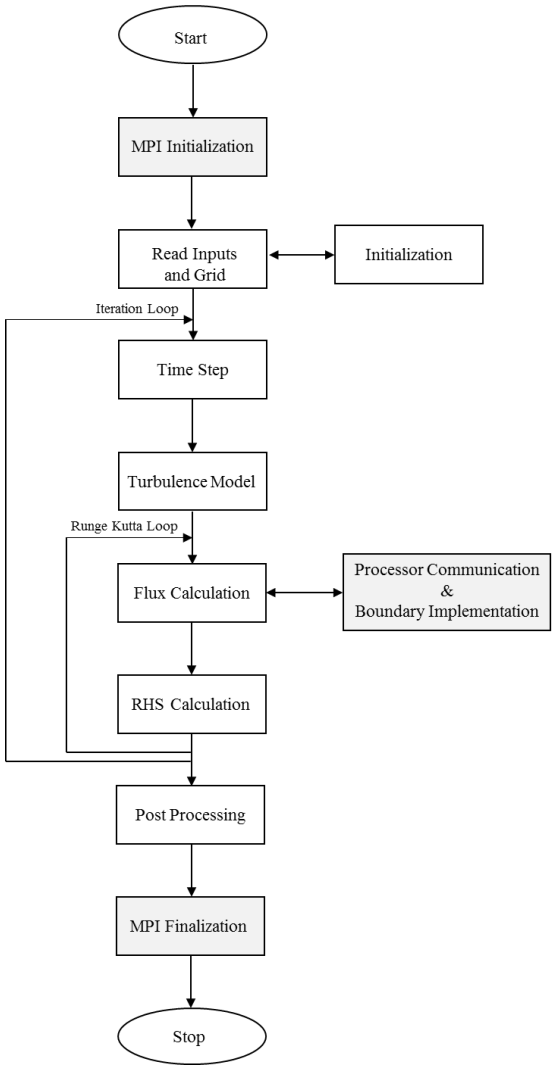

Figure 9-4 Flow chart of explicit air flow solver

Several types of send and receive routines are available in MPI point-to-point communication including the blocking and the non-blocking routines which are either often used in the SPMD model due to their flexibility and for the sake of implementation. Both methods used a buffer to avoid data loss and confusion during the transmission of data such

that the data will be copied to the buffer before the partner processor receives it. During the communication process, the data can be temporarily stored in a buffer which is a region of memory storage. In the blocking send and receive routines, the send routine will only return (block) after the completion of communication such that the computations cannot be done by the respective processors involved in communication until the process is completed while the non-blocking communication functions return immediately (do not block) even if the communication is not finished, hence care should be taken particularly to use the proper wait comment, to see whether the communication has finished or not. The latter communications are primarily used to overlap computation with communication and exploit possible performance gains.

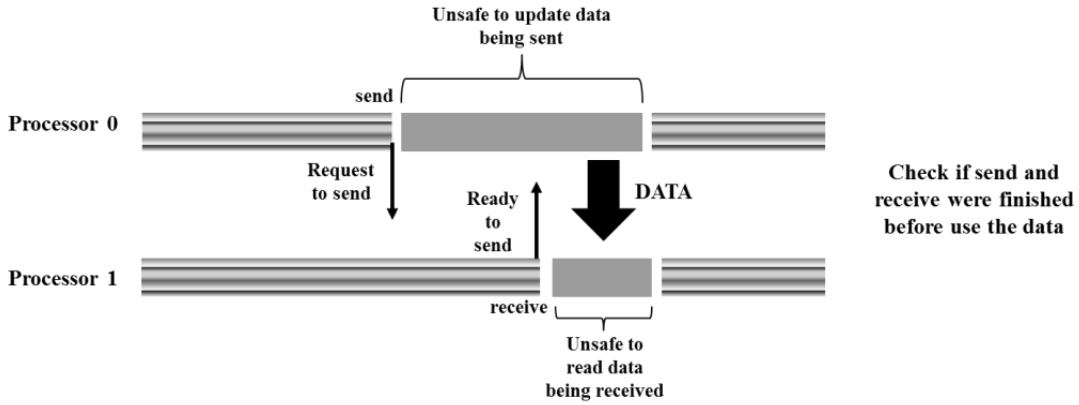

Figure 9-5 Non-blocking communication pattern (Isend and Irecv block diagram)

Initially, the communication module of the FVM solver works by sending data adjacent to partition boundaries to neighbor partitions then by receiving data from a corresponding neighbor which should be repeated for each of the element boundaries at each time steps. To save processor waiting time and avoid deadlock, non-blocking sending and receiving were used in the parallelization via application of MPI_CHECK and MPI_WAIT which is essential in confirming the completion of communication without data loss as started by calling standard MPI routines, MPI_SEND and MPI_IRECV in addition to the MPI_WAITALL routine which was used to ensure that the communication process is completed. Figure 9-5

illustrates the block diagram of the communication algorithm. The data received from the neighbouring processors once communication is completed were used for further computations.

9.3 Coarray based parallel droplet solver

In recent years, Partitioned Global Address Space model (PGAS) [131] is taking over the HPC systems and was first introduced in C language such as Unified Parallel C (UPC). The basic principle of PGAS is incorporating the parallelism in the existing programming languages by adding few additional instructions. The same method is implemented in Fortran and termed as Coarray Fortran (CAF) [132-134]. Both CAF and UPC support a global address space model for single-program-multiple-data (SPMD) parallel programming. Communication in these languages is simpler than MPI: one simply reads and writes shared variables. With communication and synchronization as part of the language, these languages are more amenable to compiler-directed communication optimization than MPI programs. Though many CAF libraries are available for CFD applications, very few are not dependent on operating system and hardware. One of the portable and easily applicable CAF libraries is Opencoarray which is used in the parallelization of droplet solver. Since the number of literature on CAF implementation on CFD is very few, more explanations are given regarding CAF. Furthermore, few CAF commands are compared with MPI comments for better explanations.

9.3.1 Basics of coarray fortran

Generally, CAF is based on SPMD programming model and the user can select the number of parallel sections (program replications) through command line instructions. In CAF, each replication of the program is called as image and has its own variable set and is executable that runs asynchronously. The intrinsic function `num_images()` is used to

determine the available number of images. Each image has its own image index which is numbered from 1 to **num_images(),** the index of an image can be readily available by using an intrinsic function **image_index().**

Unlike MPI, the objects in CAF program to be shared should be declared as a coarray variable then it can be accessed from the own image as well as from other images. For example,

```
integer:: x(5)          // Normal declaration of variable 'x'
integer:: y(5)[*]       // coarray declaration of variable 'y'
```

Here, the variables **x, y** are available in all images, but only **y** can be accessible by all images and the variable **x** is a local variable which can be accessed by only its own image. We can access y variable of other images as follows,

```
x(5) = y(5)[4]
```

The number 4 indicates the image number; hence the values in **y** are copied from the image number 4 to the variable **x** of the current image.

9.3.2 Some basic operation in CAF

Whenever a new programming model is used for application, it is important to determine its efficient commands. In parallelization of any program, few commands are highly essential such as synchronization, point-to-point communication, broadcasting, and collective operations.

9.3.2.1 Synchronization

In parallel execution, all the processes execute their own image and it is necessary to ensure that all the processors are reached at the same point before doing some communication, or collective operations. In CAF, the synchronization is done by a simple command, **sync_all** and generally, before and after collective operations synchronization is used.

9.3.2.2 Broadcasting of data

Broadcasting is an important and necessary feature of any parallel model which can be used to send the same data to all processors. For various inputs, constants for operation of the solver are read by a single processor (mostly by the master) and sent out to all processors. In case of MPI, **mpi_bcast** function is used and it can be operated as follows,

```
if (master) then
      drop_property(1)  = MVD
      ……
      drop_property(6)  = LWC
      call    mpi_bcast(drop_property,    6,    real_type,    &    masterid,
      MPI_comm_world, ierror)
else
      call    mpi_bcast(drop_property,    6,    real_type,    &    masterid,
      MPI_comm_world, ierror)
      MVD = drop_property(1)
      .......
      LWC = drop_property(6)
      endif
```

On the other hand, the coarray version of the same piece of broadcasting can be written as follows,

```
      sync_all
      MVD = drop_property [masterid]
      .......
      LWC = drop_property [mastered]
```

It is easy to understand that the local variable does not need the index and it is directly accessed from the master. The synchronization in the coarray version ensures that an image does not acquire data from the master before it is available. However, in the case of MPI version, it has an implicit synchronization within mpi_bcast.

9.3.2.3 Collective operations

Next to broadcasting, collective operations are essential to set quantities across all processors. For example, in the case of global time marching, the minimum time step over all the cells in the whole domain has to be used. Hence, it is necessary to calculate and determine the minimum time step over the whole domain. For MPI based parallel codes, **MPI_Allreduce** function is used and similar function is also available in coarray. The functions such as **co_min, co_max, co_sum**, and **co_reduce** are easily applicable functions.

In short, the implementation of coarray is easy and the number of lines of the program is also effectively reduced without any drastic performance loss. Moreover, the coarray implementation does not need any special syntax and call functions. Hence, the program is, readable, and easy to understand, maintain or extend. In the present work, Opencoarrays library, an open-source software project which produces an interface used by the GNU Compiler Collection (GCC) Fortran front end to build parallel executable programs is used to implement CAF. Opencoarrays library is easy to install and is used in Linux and macOS. It is reliable since it has been tested in several worlds' fastest supercomputers and various operating systems.

9.3.3 Implementation of coarray for droplet solver

The droplet solver also follows the basic steps and processes as mentioned in Figure 9-1 but uses droplet solver and opencoarrays library instead of flow solver and MPI library, respectively. The flow chart of the parallel droplet solver is shown in Figure 9-6. Coarrays are identified by the compiler during the compile time from the declaration of variables. Hence, initialisation commands are not necessary to initiate coarray execution. There are two options available to copy data from one image to other, "push" and 'pull". In "push' mode, local data is stored into remote image and "pull" mode copy data from remote to the local image. For example,

```
LWC [remote] = drop_property(1)      / Push mode

drop_property(1) = LWC [remote]      / Pull mode
```

Previous researches [135] notified that the "pull" mode is efficient than the "push" mode of data transfer. Therefore, "pull" mode of data transfer is used in the present code. Furthermore, it is possible to combine both MPI and coarray libraries in a single program, which may improve the parallel performance.

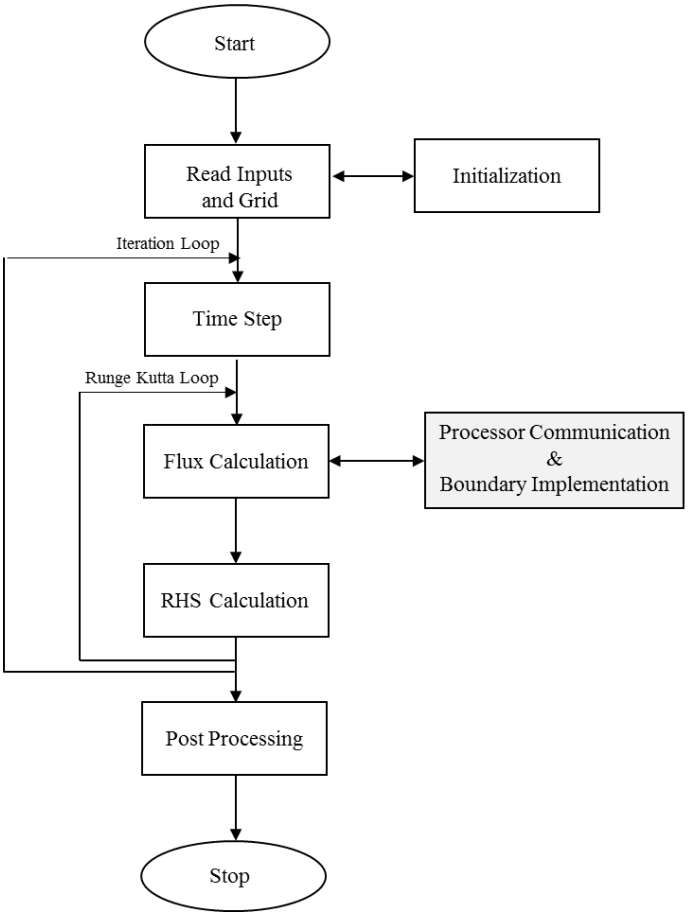

Figure 9-6 Flow chart of parallel droplet solver

9.4 Parallel performance of developed solvers

Assessment of efficiency and applicability of the parallel solver could be attained via measurement of parallel computation which generally involved a measure of relative speed-up, relative efficiency or scalability. The definition of speed-up (*Sp*) was established by Amdahl's law [136] which is a metric for the relative improvement in performance when executing a task but can be used more generally to show the effect of any performance enhancement. The relative speed-up is given by

$$S_p = \frac{t_s}{t_p}, \tag{9.1}$$

where S_p is speed-up, t_s and t_p are the elapsed time taken by a *single* processor and p processors, respectively. The speed-up of air and droplet solvers are shown in Figure 9-8.

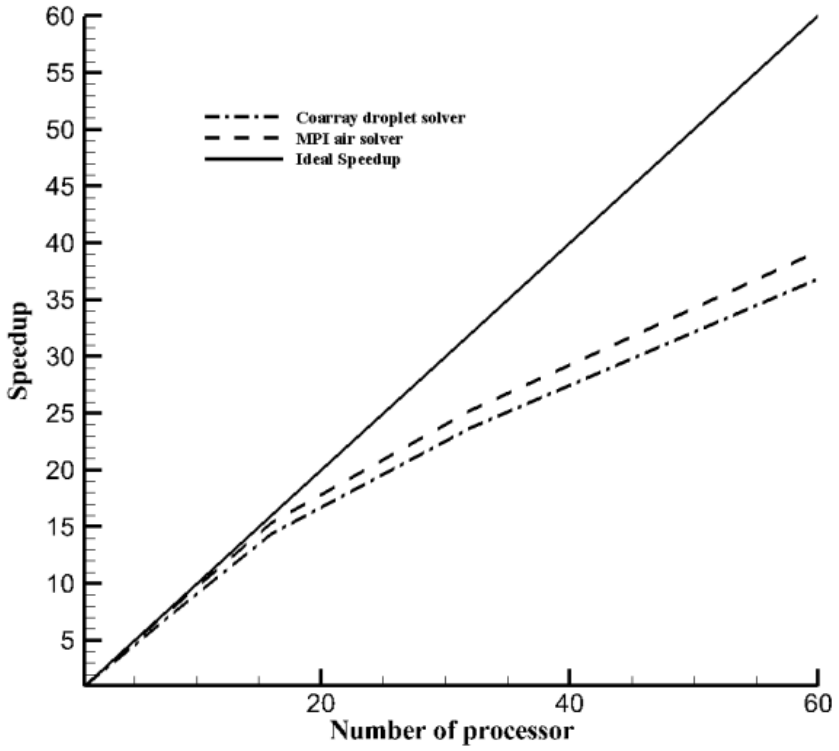

Figure 9-7 Relative speedup of air and droplet solver

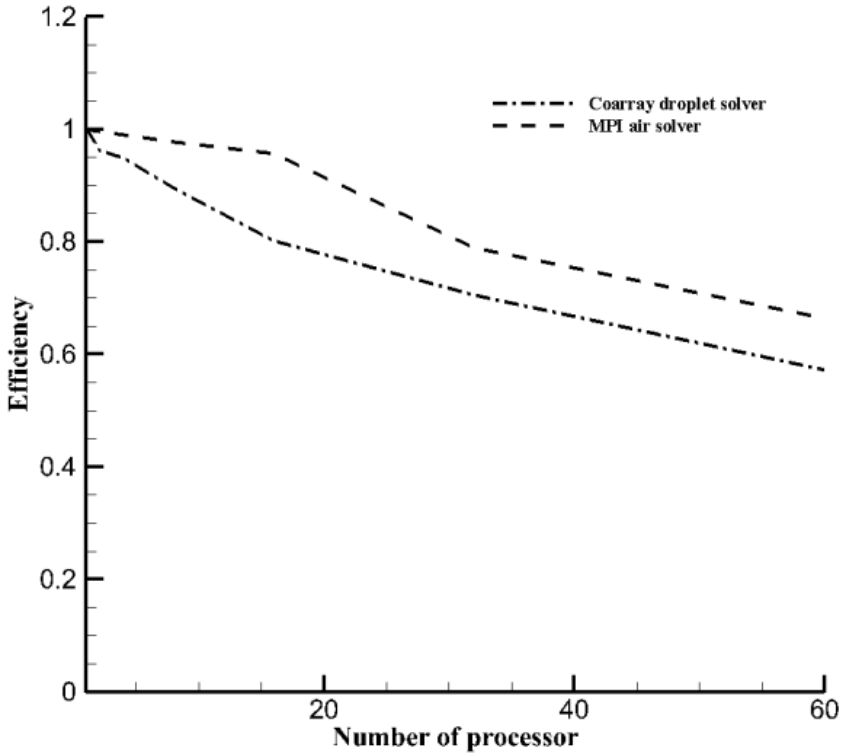

Figure 9-8 Efficiency of air and droplet solver

A metric of the utilization of the resources of the improved parallelized system is the relative efficiency (E) which is read as

$$E = \frac{S_p}{p}. \tag{9.2}$$

Analysis of performance indicates the level of speed up and efficiency of the parallel solver and for a fixed problem size, speed-up of code varies with the increase in the number of processors. Linear speed-up usually remains less than p while efficiency lies between 0 and 1. Ideally, the elapsed time, relative speed-up, and relative efficiency taken by p processors is equal to $t_p = t_1/p$, $S_p = p$, and E =1, respectively. As seen in the plot Figure 9-7, the speedup of CAF also follows the same trend as the MPI. Furthermore, the efficiency is shown in Figure 9-8 which follows the same trend as the speedup. Overall, the developed parallel solvers are performing well under given conditions, which can be used to solve various engineering problems.

Chapter 10. Conclusion and Future Works

10.1 Outlook

A Eulerian-based droplet impingement solver which provides the droplet flow field around 3D model is developed. A Finite Volume Method (FVM) is used to solve the compressible Navier-Stokes equation and shallow water based droplet equations. The large droplet effects such as splashing, rebound, and deformation drag are modeled using semi-empirical formulations. The large droplet effects are implemented in the present computational model without altering the governing equations. Further, a PDE-based ice accretion solver is developed to predict the ice shapes on the clean geometry under icing ambient conditions. The developed solver is capable of solving all regime of ice in the same framework under the given metrological conditions. The current ice accretion solver is based on FVM that can acquire inputs from aforementioned air and droplet solvers. Hence, a unified icing package is developed along with automatic grid regeneration. The grid regeneration automation is developed using script programming which can be used in commercial grid generation software.

As a part of the current study, several parameters involved in the ice accretion are investigated. The significance of ice density, heat flux, surface roughness, turbulence model, evaporation model, and multi-shot approach are investigated using the current computational models. The investigation revealed the strong influence of heat flux in ice shape and type of ice accretion. Furthermore, the deactivation of evaporation model results in excess runback ice which shows that more attention is necessary for evaporation mass flux calculations. The numerical results predicted by the current computation models are validated against experimental and other numerical results. The validation started with a 2D airfoil and extended to a 3D engine intake under various metrological conditions. The results indicated

that the present air, droplet, and ice accretion solvers are in close agreement with the experimental results. The effects of SLD are investigated in both two and three-dimensional surfaces. After a rigorous validation study of each solver, various engineering problems are studied using the developed atmospheric icing package solver.

The developed solvers are used for the ice accretion study on multi-element airfoil under various metrological conditions. The angle of attack varied from 0 to 16^0, and the MVD varied from 20 to 154 μm. The effect of angle of attack is investigated under each selected MVD, which reveals that the impingement limit has changed rapidly along with the angle of attack. Moreover, the droplet diameter effects are investigated under various angles of attacks, which showed that the main element leading edge is prone to more ice thickness at lower MVDs. On the contrary, the bigger droplets impingement limit is much far from leading edge that leads to less ice thickness at the leading edge of the main element. However, the icing scenario in slat and flap is totally different from the main element due to their position. In all metrological conditions, the ice accretion in slat is much higher which decreases its performance considerably. Nonetheless, the overall performance is not much affected by slat owing to its very less contribution on the lift when comparing to main and flap elements.

Next to iced multi-element performance analysis, a 3D propeller airplane KC-100 is considered for the investigation. The investigation starts with conventional metrological conditions which reveal that the leading edges of wing, empennages, and nose are prone to ice accretion. Next to a conventional metrological condition, an SLD condition is used for the investigation of KC-100 aircraft. The droplet impingement solution itself shows a severe potential of ice accumulation at leading edges and other components such as windshield. The impingement limit is also increased along with the maximum range of collection efficiency. Finally, the thickness and amount of ice are extremely high for an SLD metrological

simulation. Further investigations are necessary under various droplet diameters on the KC-100 aircraft.

A rotorcraft engine intake is investigated using the developed ice solver package and the results are compared with experimental results. The computed droplet and ice accretion results qualitatively agreed with the experimental results. The effect of droplet diameter on the droplet impingement is investigated and the results are compared with FENSAP results. Furthermore, an SLD metrological condition is used to investigate the rotorcraft engine intake under SLD condition. The results revealed that the SLD metrological conditional modified the impingement location and area on the engine intake. The impingement area also increased followed by increased ice thickness under SLD conditions.

Next to the ice accretion study on various engineering problems, a study is conducted on electro-thermal de-icing on an NREL 5MW wind turbine blade. The computational model is developed using commercial software FENSAP and validated with experimental results. For the current analysis, the DU21 airfoil is selected and simulations are conducted with and without ice protection system. The length of the heater and the power required for the operation of the heater are evaluated using appropriate equations. A proper heater cycle sequence is selected by trial and error method. The results reveal that the heater power is enough to remove the accumulated ice under the given metrological conditions. Moreover, the computed surface temperature never raised beyond the target surface temperature which indicated that the predicted required power is correct.

Finally, the air and droplet solvers are parallelized using appropriate parallel models such as MPI and Fortran Coarray programming. The SPMD programming technique is used for the current parallelization. The speedup and efficiency of the developed parallel solvers are investigated which shows a significant parallel performance.

10.2 Future works

After the development of Eulerian-based SLD droplet and PDE-based ice accretion solvers, the following topics may be considered for future works.

10.2.1 Additional large droplet effects

Although the first order SLD effects are implemented in this work, there are some discrepancies in the simulated result especially in the prediction of impingement limit. Author strongly believed that the discrepancies are due to the absence of other large droplet effects in the current model. The implementation of other SLD effects such as droplet breakup, droplet re-impingement, etc. can be explored as the upcoming research topics.

10.2.2 Ice crystals

Ice crystals are safety hazards for gas turbine engines while operating at very low ambient temperatures. Ice Crystal Icing (ICI) hazard does not usually result in complete engine failure (although there have been such instances) but more than one engine may be affected simultaneously. High altitude ice crystals will not adhere to the external airframe or protrusions, even though these are considerably warmer than the ambient temperature due to kinetic heating, hence will not activate conventional ice detectors. For an instance, a Boeing 747 aircraft encountered high dense ice crystal that resulted in failure of three engines instantly. The compressor blades of those engines are damaged severely that led to an accident. Hence, investigations on ice crystal including its proper detection would be a helpful tool for the prevention of accidents, particularly in commercial aircraft.

10.2.3 Microphysics of ice formation

Ice accretion on a surface involves different physics, starting with the property of ambient air, water droplets, surface roughness, etc. Hence, the mixture of all these properties brings a complex physics which affect the ice shape and amount of ice accretion. In the same

way, microphysics of ice formation involved in the ice accretion have significant effects in the ice accretion which include surface roughness of iced surface, ice shedding, runback ice, and certain droplet behaviors - all need to be explored. Hence, the study of this fundamental microphysics of ice formation can be a good candidate for as a next step of the current research.

10.2.4 Grid deformation

In the present study, automatic grid regenerator was developed used for solving problems involved in multi-shot ice accretion. However, the current method of grid regeneration is difficult to implement for an arbitrary and complex geometry due to the concern of grid quality and limitations in an automation script. Moreover, grid regeneration is feasible and easy to adapt for 2D solvers but difficult and is more time-consuming for 3D geometries. One of the feasible solutions to overcome these issues is the grid deformation solver. Grid deformation solvers are set of mathematical or analytical equations used to find the location of grid points after deformation. Generally, grid deformation solvers are built with strong algorithms with efficient solvers to determine the deformed grid node locations.

10.2.5 Ice protection system

Overall, the ultimate goal of all these ice accretion studies is to design a proper ice protection system (IPS) for the known icing conditions. Furthermore, it is possible to model IPS numerically and eventually, it can aid in the design of an effective IPS for real aircraft. Generally, hot bleed air IPS involves a cold surface to be protected and the hot air from the engine compressor. Hence, these can be modeled using conjugate heat transfer. Similarly, the electro-thermal IPS involves a heating element (source for heat) and other few conductors which is in contact with the surface to be protected. Implementation of IPS would be easy with the use of simple surface conduction equation and readily available ice accretion solver. Hence, development of IPS can be an important topic in the line of current research.

Appendix A. System of Solutions for Ice Solver

The conservative form of system of equation can be written as,

Mass equation $$\frac{\partial h_f}{\partial t}+\frac{R_{ij}^{M}}{vol}=\frac{S_M}{\rho_w} \tag{A.1}$$

Energy Equation $$\frac{\partial h_f T_{equi}}{\partial t}+\frac{R_{i\,j}^{M}}{vol}=\frac{S_E}{\rho_w C_{p,w}}+\frac{T_c S_M}{\rho_w} \tag{A.2}$$

Here**,**

$$S_M=\dot{m}_{drop}-\dot{m}_{evap}-\dot{m}_{ice}^{"}$$

$$S_E=S_{drop}-S_{ice}-S_{evap}-S_{conv}-S_{rad}$$

Regime I: Rime ice

Compatibility relation: $h_f^{n+1}=0,\dot{m}_{ice}\geq 0,T_{equi}\geq T_c$

Mass equation can be expanded as,

$$\frac{h^{n+1}-h^{n}}{\Delta t}+\frac{\dot{m}_{ice}^{n+1}}{\rho_w}-\left(\frac{U_\infty Lwc\beta}{\rho_w}-\frac{\dot{m}_{evap}}{\rho_w}\right)+\frac{R_{i\,j}^{M}}{vol}=0 \tag{A.3}$$

$$\dot{m}_{ice}^{n+1}=\rho_w\left(\frac{h^{n}}{\Delta t}+\frac{U_\infty Lwc\beta}{\rho_w}-\frac{\dot{m}_{evap}}{\rho_w}-\frac{R_{i\,j}^{M}}{vol}\right) \tag{A.4}$$

Energy balance can be derived as,

$$\frac{\partial h_f T_{equi}}{\partial t}+\vec{\nabla}\left(\frac{h^2 T_{equi}}{2\mu_w}\vec{\tau}_{wall}\right)=\frac{S_E}{\rho_w C_{p,w}}+\frac{T_c S_M}{\rho_w} \tag{A.5}$$

Here,

$$\frac{S_E}{\rho_w C_{p,w}}=\frac{(S_{drop}-S_{ice}-S_{evap}-S_{conv}-S_{rad})}{\rho_w C_{p,w}} \tag{A.6}$$

$$\frac{T_c S_M}{\rho_w} = T_c \left[\frac{U_\infty Lwc\beta}{\rho_w} - \frac{\dot{m}_{evap}}{\rho_w} - \frac{\dot{m}_{ice}}{\rho_w} \right] \tag{A.7}$$

Now,

$$S_{drop} = \frac{\dot{m}_{drop} \left(C_{p,w} \left(T_{d,\infty} - T_{equi}^{n+1} \right) + \frac{\|u_d\|^2}{2} \right)}{\rho_w C_{p,w}} \tag{A.8}$$

$$S_{ice} = \frac{\left[L_{fus} - C_{p,ice} \left(T_{equi}^{n+1} - T_c \right) \right] \dot{m}_{ice}^{n+1}}{\rho_w C_{p,w}} \tag{A.9}$$

$$S_{evap} = \frac{L_{evap} \dot{m}_{evap}}{\rho_w C_{p,w}} \tag{A.10}$$

$$S_{conv} = \frac{h_c \left(T_{equi}^{n+1} - T_\infty \right)}{\rho_w C_{p,w}} \tag{A.11}$$

$$S_{rad} = \sigma \varepsilon \frac{\left(T_{equi}^4 - T_\infty^4 \right)}{\rho_w C_{p,w}} \tag{A.12}$$

By using equations (A.6) to (A.12) in (A.5),

$$\frac{h^{n+1} T^{n+1} - h^n T^n}{\Delta t} - (S_{drop} - S_{ice} - S_{evap} - S_{conv} - S_{rad}) - T_c \left[\frac{U_\infty Lwc\beta}{\rho_w} - \frac{\dot{m}_{evap}}{\rho_w} - \frac{\dot{m}_{ice}^{n+1}}{\rho_w} \right] + \frac{R_{ij}^E}{V_i} = 0 \tag{A.13}$$

$$-(S_{drop} - S_{ice} - S_{evap} - S_{conv} - S_{rad}) = -\left[\frac{-h^n T^n}{\Delta t} \right] - T_c \left[\frac{U_\infty Lwc\beta}{\rho_w} - \frac{\dot{m}_{evap}}{\rho_w} - \frac{\dot{m}_{iu}^{n+1}}{\rho_w} \right] + \frac{R_{ij}^E}{V_i} \tag{A.14}$$

$$-(S_{drop}-S_{ice}-S_{evap}-S_{conv}-S_{rad})=-\left[\frac{-h^{n}T^{n}}{\Delta t}\right] -T_{c}\left[\frac{U_{\infty}Lwc\beta}{\rho_{w}}-\frac{\dot{m}_{evap}}{\rho_{w}}-\frac{\dot{m}_{iu}^{n+1}}{\rho_{w}}\right]+\frac{R_{ij}^{E}}{V_{i}} \tag{A.15}$$

$$-\left(-\frac{\dot{m}_{drop}C_{p,w}\left(T_{equi}^{n+1}\right)}{\rho_{w}C_{p,w}}\right)+\frac{\dot{m}_{drop}\left(C_{p,w}\left(T_{d,\infty}\right)+\frac{u_{d}^{2}}{2}\right)}{\rho_{w}C_{p,w}}+\frac{\left[L_{fus}+C_{p,ice}.T_{c}\right]\dot{m}_{ice}^{n+1}}{\rho_{w}C_{p,w}} -\frac{C_{p,ice}.T_{equi}^{n+1}.\dot{m}_{ice}^{n+1}}{\rho_{w}C_{p,w}}-\frac{h_{c}T_{equi}^{n+1}}{\rho_{w}C_{p,w}}+\frac{h_{c}T_{\infty}}{\rho_{w}C_{p,w}}-\frac{L_{evap}\dot{m}_{evap}}{\rho_{w}C_{p,w}} -\sigma\varepsilon\frac{\left(T_{equi}^{4}-T_{\infty}^{4}\right)}{\rho_{w}C_{p,w}}=source1 \tag{A.16}$$

$$-\left(-\frac{\dot{m}_{drop}C_{p,w}\left(T_{equi}^{n+1}\right)}{\rho_{w}C_{p,w}}\right)+\frac{\dot{m}_{drop}\left(C_{p,w}\left(T_{d,\infty}\right)+\frac{u_{d}^{2}}{2}\right)}{\rho_{w}C_{p,w}}+\frac{\left[L_{fus}+C_{p,ice}.T_{c}\right]\dot{m}_{ice}^{n+1}}{\rho_{w}C_{p,w}} -\frac{C_{p,ice}.T_{equi}^{n+1}.\dot{m}_{ice}^{n+1}}{\rho_{w}C_{p,w}}-\frac{h_{c}T_{equi}^{n+1}}{\rho_{w}C_{p,w}}+\frac{h_{c}T_{\infty}}{\rho_{w}C_{p,w}}-\frac{L_{evap}\dot{m}_{evap}}{\rho_{w}C_{p,w}} -\sigma\varepsilon\frac{\left(T_{equi}^{4}-T_{\infty}^{4}\right)}{\rho_{w}C_{p,w}}=source1 \tag{A.17}$$

$$\left(\frac{1}{\rho_{w}C_{p,w}}\right)\left[\left(\frac{\dot{m}_{drop}C_{p,w}\left(T_{equi}^{n+1}\right)}{\rho_{w}C_{p,w}}\right)+C_{p,ice}.T_{equi}^{n+1}+h_{c}T_{equi}^{n+1}\right]= \left(\frac{1}{\rho_{w}C_{p,w}}\right)\left[\left(\dot{m}_{drop}\left(C_{p,w}\left(T_{d,\infty}\right)+\frac{\|u_{d}\|^{2}}{2}\right)\right)+\left[L_{fus}+C_{p,ice}.T_{c}\right]\dot{m}_{ice}^{n+1} +h_{c}T-L_{evap}\dot{m}_{evap}-\sigma\varepsilon(T_{equi}^{4}-T_{\infty}^{4})\right]+source1 \tag{A.18}$$

Now, the equation a can be simplified as,

$$\left(\frac{T^{n+1}}{\rho_w C_{p,w}}\right).\left[\dot{m}_{drop}C_{p,w}+C_{p,ice}.\dot{m}_{ice}^{n+1}+h_c\right]=\left(\frac{source2}{\rho_w C_{p,w}}+source1\right) \tag{A.19}$$

$$\left(\frac{T^{n+1}}{\rho_w C_{p,w}}\right)=\frac{\rho_w C_{p,w}}{\left[\dot{m}_{drop}C_{p,w}+C_{p,ice}.\dot{m}_{ice}^{n+1}+h_c\right]}\left(\frac{source2}{\rho_w C_{p,w}}+source1\right) \tag{A.20}$$

Finally the equilibrium temperature can be given as,

$$T^{n+1}=\frac{source2+\rho_w C_{p,w}.source1}{\left[\dot{m}_{drop}C_{p,w}+C_{p,ice}.\dot{m}_{ice}^{n+1}+h_c\right]} \tag{A.21}$$

Here,

$$source1=\frac{T_c}{\rho}(U_\infty Lwc\beta-\dot{m}_{evap}-\dot{m}_{iu}^{n+1})+\frac{h^n T^n}{\Delta t}-\frac{R_{ij}^E}{V_i}$$

$$source2=\left(\dot{m}_{drop}\left(C_{p,w}\left(T_{d,\infty}\right)+\frac{\|u_d\|^2}{2}\right)\right)+\left[L_{fus}+C_{p,ice}.T_c\right]\dot{m}_{ice}^{n+1}+h_c T_\infty$$
$$-L_{evap}\,\dot{m}_{evap}-\sigma\varepsilon\left(T_{equi}^4-T_\infty^4\right)$$

Regime II: Glaze ice

Compatibility relation: $h_f^{n+1}\geq 0$, $\dot{m}_{ice}\geq 0, T_{equi}=T_c$

Mass equation can be derived as,

$$\frac{h^{n+1}-h^n}{\Delta t}+\frac{\dot{m}_{ice}^{n+1}}{\rho_w}-\left(\frac{U_\infty Lwc\beta}{\rho_w}-\frac{\dot{m}_{evap}}{\rho_w}\right)+\frac{R_{ij}^M}{vol}=0 \tag{A.22}$$

$$\frac{h^{n+1}}{\Delta t}-\frac{h^n}{\Delta t}+\frac{\dot{m}_{ice}^{n+1}}{\rho_w}-\left(\frac{U_\infty Lwc\beta}{\rho_w}-\frac{\dot{m}_{evap}}{\rho_w}\right)+\frac{R_{ij}^M}{vol}=0 \tag{A.23}$$

$$\frac{h^{n+1}}{\Delta t}+\frac{\dot{m}_{ice}^{n+1}}{\rho_w}=\frac{h^n}{\Delta t}+\left(\frac{U_\infty Lwc\beta}{\rho_w}-\frac{\dot{m}_{evap}}{\rho_w}\right)-\frac{R_{ij}^M}{vol} \tag{A.24}$$

Energy conservation equation can be written as,

$$\frac{\partial h_f T_{equi}}{\partial t} + \vec{\nabla}\left(\frac{h^2 T_{equi}}{2\mu_w}\vec{\tau}_{wall}\right) = \frac{S_E}{\rho_w C_{p,w}} + \frac{T_c S_M}{\rho_w} \tag{A.25}$$

$$\frac{S_E}{\rho_w C_{p,w}} = \frac{(S_{drop} - S_{ice} - S_{evap} - S_{conv} - S_{rad})}{\rho_w C_{p,w}} \tag{A.26}$$

$$\frac{T_c S_M}{\rho_w} = T_c\left[\frac{U_\infty Lwc\beta}{\rho_w} - \frac{\dot{m}_{evap}}{\rho_w} - \frac{\dot{m}_{ice}}{\rho_w}\right] \tag{A.27}$$

$$\frac{\partial h_f T_{equi}}{\partial t} + \vec{\nabla}\left(\frac{h^2 T_{equi}}{2\mu_w}\vec{\tau}_{wall}\right) = \frac{S_E}{\rho_w C_{p,w}} + \frac{T_c S_M}{\rho_w} \tag{A.28}$$

$$S_{drop} = \frac{\dot{m}_{drop}\left(C_{p,w}\left(T_{d,\infty} - T_{equi}^{n+1}\right) + \frac{\|u_d\|^2}{2}\right)}{\rho_w C_{p,w}} \tag{A.29}$$

$$S_{evap} = \frac{L_{evap}\,\dot{m}_{evap}}{\rho_w C_{p,w}} \tag{A.30}$$

$$S_{ice} = \frac{\left[L_{fus} - C_{p,ice}\left(T_{equi}^{n+1} - T_c\right)\right]\dot{m}_{ice}^{n+1}}{\rho_w C_{p,w}} \tag{A.31}$$

$$S_{conv} = \frac{h_c\left(T_{equi}^{n+1} - T_\infty\right)}{\rho_w C_{p,w}} \tag{A.32}$$

$$S_{rad} = \sigma\varepsilon\frac{\left(T_{equi}^4 - T_\infty^4\right)}{\rho_w C_{p,w}} \tag{A.33}$$

By using the above equations in (A.25), we get,

$$\begin{aligned}\frac{h^{n+1}T^{n+1} - h^n T^n}{\Delta t} - (S_{drop} - S_{ice} - S_{evap} - S_{conv} - S_{rad}) \\ - T_c\left[\frac{U_\infty Lwc\beta}{\rho_w} - \frac{\dot{m}_{evap}}{\rho_w} - \frac{\dot{m}_{iu}^{n+1}}{\rho_w}\right] + \frac{R_{ij}^E}{V_i} = 0\end{aligned} \tag{A.34}$$

$$\frac{h^{n+1}.T_c}{\Delta t}-\frac{\dot{m}_{ice}^{n+1}}{\rho_{wC_{p,w}}}\left(L_{fus}\ -0\right)+\frac{\dot{m}_{ice}^{n+1}.T_c}{\rho_w}=source1 \tag{A.35}$$

$$\frac{h^{n+1}.T_c}{\Delta t}-\frac{\dot{m}_{ice}^{n+1}}{\rho_w}\left[\frac{L_{fus}}{C_{p,w}}-T_c\right]=source1 \tag{A.36}$$

Since equations (A.24) and (A.36) has two unknowns, the equations are solved as follows,

$$AX=B\Rightarrow X=A^{-1}B \tag{A.37}$$

Here,

$$A=\begin{bmatrix}a_{11} & a_{12}\\ a_{21} & a_{22}\end{bmatrix};\quad X=\begin{bmatrix}h_f^{n+1}\\ \dot{m}_{ice}^{n+1}\end{bmatrix};\quad B=\begin{bmatrix}b_1\\ b_2\end{bmatrix} \tag{A.38}$$

$$A^{-1}=\frac{1}{a_{11}a_{12}-a_{12}a_{22}}\begin{bmatrix}a_{22} & -a_{12}\\ a_{21} & a_{11}\end{bmatrix};\ a_{11}=\frac{1}{\Delta t};a_{12}=\frac{1}{\rho};a_{21}=\frac{T_c}{\Delta t}. \tag{A.39}$$

$$a_{22}=\frac{1}{\rho_w}\left[T_c-\frac{L_{fus}}{C_{p,w}}\right];\ b_1=\frac{h^n}{\Delta t}+\left(\frac{U_\infty Lwc\beta}{\rho_w}-\frac{\dot{m}_{evap}}{\rho_w}\right)-\frac{R_{i\,j}^E}{vol} \tag{A.40}$$

$$b_2=source1 \tag{A.41}$$

Here,

$$\begin{aligned}source1=\frac{h^n\,T^n}{\Delta t}&+(S_{drop}-S_{ice}-S_{evap}-S_{conv}^{n+1}-S_{rad})\\ &+T_c\left[\frac{U_\infty Lwc\beta}{\rho_w}-\frac{\dot{m}_{evap}}{\rho_w}\right]-\frac{R_{i\,j}^E}{V_i}\end{aligned} \tag{A.42}$$

Regime III: No ice

Compatibility relation: $h_f^{n+1} \geq 0$, $\dot{m}_{ice} = 0, T_{equi} \geq T_c$

Mass equation can be given as,

$$\frac{h^{n+1} - h^n}{\Delta t} + \frac{\dot{m}_{ice}^{n+1}}{\rho_w} - \left(\frac{U_\infty Lwc\beta}{\rho_w} - \frac{\dot{m}_{evap}}{\rho_w} \right) + \frac{R_{ij}^M}{vol} = 0 \tag{A.43}$$

$$\frac{h^{n+1}}{\Delta t} - \frac{h^n}{\Delta t} = \left(\frac{U_\infty Lwc\beta}{\rho_w} - \frac{\dot{m}_{evap}}{\rho_w} \right) - \frac{R_{ij}^M}{vol} \tag{A.44}$$

$$\frac{h^{n+1}}{\Delta t} = h^n + \Delta t \left(\frac{U_\infty Lwc\beta}{\rho_w} - \frac{\dot{m}_{evap}}{\rho_w} \right) - \frac{R_{ij}^M}{vol} \tag{A.45}$$

Now the energy conservation equation can be as follows,

$$\frac{\partial h_f T_{equi}}{\partial t} + \vec{\nabla} \left(\frac{h^2 T_{equi}}{2\mu w} \vec{\tau}_{wall} \right) = \frac{S_E}{\rho_w C_{p,W}} + \frac{T_c S_M}{\rho_w} \tag{A.46}$$

By using the equations (A.7) to (A.12) in (A.46), we can write,

$$\begin{aligned} &\frac{h^{n+1} T^{n+1} - h^n T^n}{\Delta t} - (S_{drop} - S_{ice} - S_{evap} - S_{conv} - S_{rad}) \\ &\qquad - T_c \left[\frac{U_\infty Lwc\beta}{\rho_w} - \frac{\dot{m}_{evap}}{\rho_w} - \frac{\dot{m}_{iu}^{n+1}}{\rho_w} \right] + \frac{R_{ij}^E}{V_i} = 0 \end{aligned} \tag{A.47}$$

$$\begin{aligned} &\frac{h^{n+1} T^{n+1}}{\Delta t} - (S_{drop} - S_{ice} - S_{evap} - S_{conv} - S_{rad}) = \\ &\qquad - \left[- \frac{h^n T^n}{\Delta t} T_c \left[\frac{U_\infty Lwc\beta}{\rho_w} - \frac{\dot{m}_{evap}}{\rho_w} - \frac{\dot{m}_{iu}^{n+1}}{\rho_w} \right] + \frac{R_{ij}^E}{V_i} \right] \end{aligned} \tag{A.48}$$

$$\frac{h^{n+1}T^{n+1}}{\Delta t}-\frac{\left[-(\dot{m}_{drop}C_{p,w}\left(T_{equi}^{n+1}\right)\right]+\dot{m}_{drop}C_{p,w}\left(T_{d,\infty}\right)+\frac{\left\|u_d\right\|^2}{2})}{\rho_w C_{p,w}}$$
$$-\frac{h_c\left(T_{equi}^{n+1}\right)}{\rho_w C_{p,w}}+\frac{h_c\left(T_\infty\right)}{\rho_w C_{p,w}}-\frac{0.5\left[L_{evap}+L_{sub}\right]\dot{m}_{evap}}{\rho_w C_{p,w}} \quad \text{(A.49)}$$
$$-\sigma\varepsilon\frac{\left(T_{equi}^4-T_\infty^4\right)}{\rho_w C_{p,w}}=Source\ 1$$

$$\frac{h^{n+1}T^{n+1}}{\Delta t}-\frac{\left[-(\dot{m}_{drop}C_{p,w}\left(T_{equi}^{n+1}\right)\right]-h_c\left(T_{equi}^{n+1}\right)}{\rho_w C_{p,w}}=$$
$$\frac{1}{\rho_w C_{p,w}}\left[\left(\dot{m}_{drop}C_{p,w}\left(T_{d,\infty}\right)+\frac{\left\|u_d\right\|^2}{2}\right)+h_c\left(T_\infty\right)\right. \quad \text{(A.50)}$$
$$\left.-0.5\left[L_{evap}+L_{sub}\right]\dot{m}_{evap}-\sigma\varepsilon\left(T_{equi}^4-T_\infty^4\right)\right]+Source\ 1$$

$$T^{n+1}=\frac{\rho_w C_{p,w}}{\left(\frac{h^{n+1}\rho_w C_{p,w}}{\Delta t}+\dot{m}_{drop}C_{p,w}+h_c\right)}\left(\frac{Source\ 2}{\rho_w C_{p,w}}+Source\ 1\right) \quad \text{(A.51)}$$

Here the source terms can be given as,

$$Source\ 1=\frac{T_c}{\rho_w}\left(U_\infty Lwc\beta-\dot{m}_{evap}\right)+\frac{h^n T^n}{\Delta t}-\frac{R_{ij}^E}{V_i}$$

$$Source\ 2=\left(\dot{m}_{drop}C_{p,w}\left(T_{d,\infty}\right)+\frac{\left\|u_d\right\|^2}{2}\right)+h_c\left(T_\infty\right)$$
$$-0.5\left[L_{evap}+L_{sub}\right]\dot{m}_{evap}-\sigma\varepsilon\left(T_{equi}^4-T_\infty^4\right)$$

Appendix B. Multi-shot Ice Accretion Implementation

In multi-shot ice accretion model, a sequence of analysis procedure is required to air flow, droplet impingement, and ice accretion around a given model. The objective is to improve the accuracy and implementing the natural behaviour of the flow as close as possible numerically. In addition, the accurate air flow field is updated at each time step (no. of shot) for the updated geometry. The flow chart in Figure B-1 shows the sequence of procedures involved in the multi-shot ice accretion solver. Procedures inside the black box are performed iteratively along with the node displacement, and each section of the flow chart is explained in the following sections.

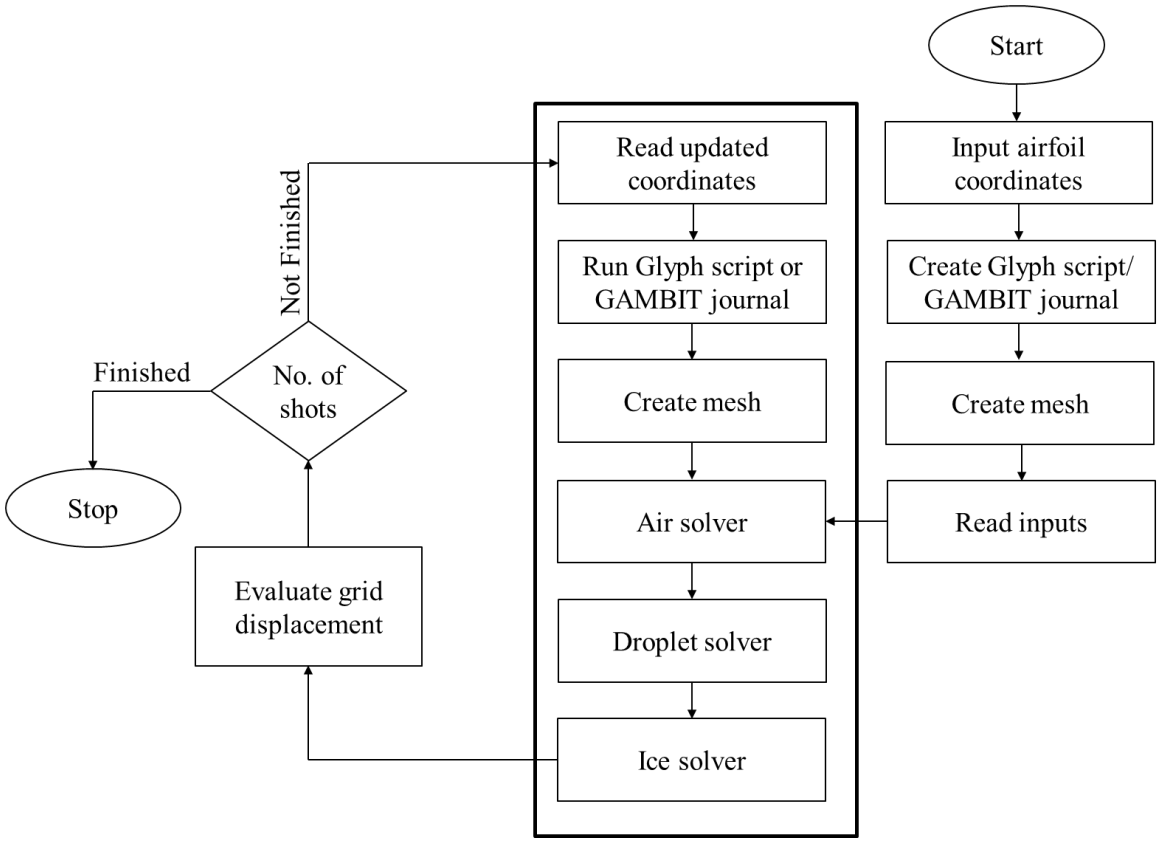

Figure B-1 Multi-shot icing package automation process flow

Appendix B.1 Pointwise Glyph and GAMBIT journal file generator

There are two mesh generators that are used for the current simulations. The user can choose which mesh generator needs to be run during the start of the process. For GAMBIT mesh generator, a journal file is generated by a FORTRAN code which needs to be changed depending on the number of coordinates. Since the geometry changes due to ice accretion, the journal file must also change per iteration. The processes of GAMBIT file generator is shown in Figure B-2.

Figure B-2 GAMBIT journal file generator process flow

On the other hand, Pointwise Glyph script can be reused without modifications. The glyph is a Tcl-based scripting language used in pointwise for the automation of meshing process. For this current study, we started with GAMBIT journal file method but we shifted to Glyph script due to its ease of adaptability and flexibility in implementation.

Appendix B.2 Mesh generation (create mesh)

After automation script (Glyph or journal file) is ready, the next step is the mesh generation using the created script. Following the predefined commands in the script, the mesh generator (GAMBIT or Pointwise) generates the mesh automatically without GUI controls. The data points are used to create a 2D airfoil face with triangle mesh. The mesh parameters should be sufficient to resolve shear stress and heat flux near the wall. Figure B-3 shows the data process for the mesh generation operation.

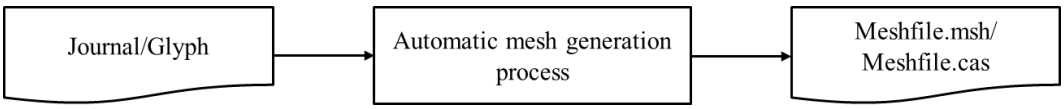

Figure B-3 Mesh generation automation process flow

Appendix B.3 Automation of solvers

Air, droplet and ice solvers must be run in a sequence, which can be controlled by the FORTRAN program. The air solver takes the flow information and mesh file as the input to solve the airflow field around a given model. The schematic process of flow of air solver automation is shown in Figure B-4. The completion of air flow solver would be the starting point of droplet solver which takes the flow information, grid, and airflow field as input to solve the droplet impingement. The schematic process flow of droplet solver automation is shown in Figure B-5. Finally, the ice accretion solver starts after the completion of droplet solver which takes the flow information, surface grid, air solution, and droplet solution as input to determine the ice accumulation on the given surface. The process flow chart of ice accretion solver is shown in Figure B-6.

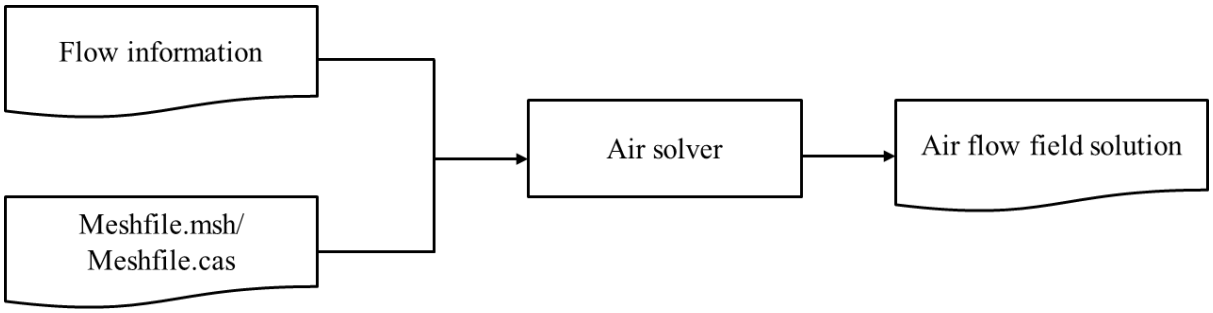

Figure B-4 Automated air solver process flow

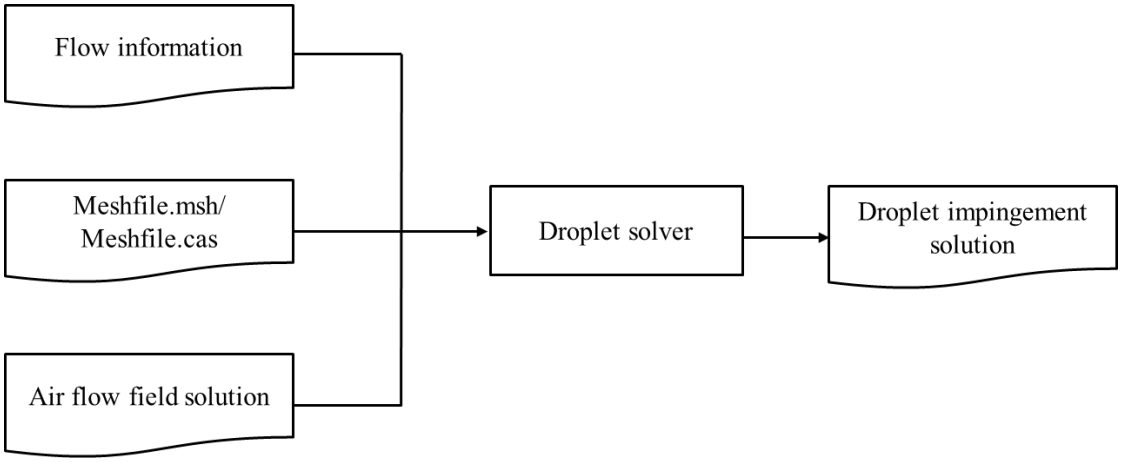

Figure B-5 Automated droplet solver process flow

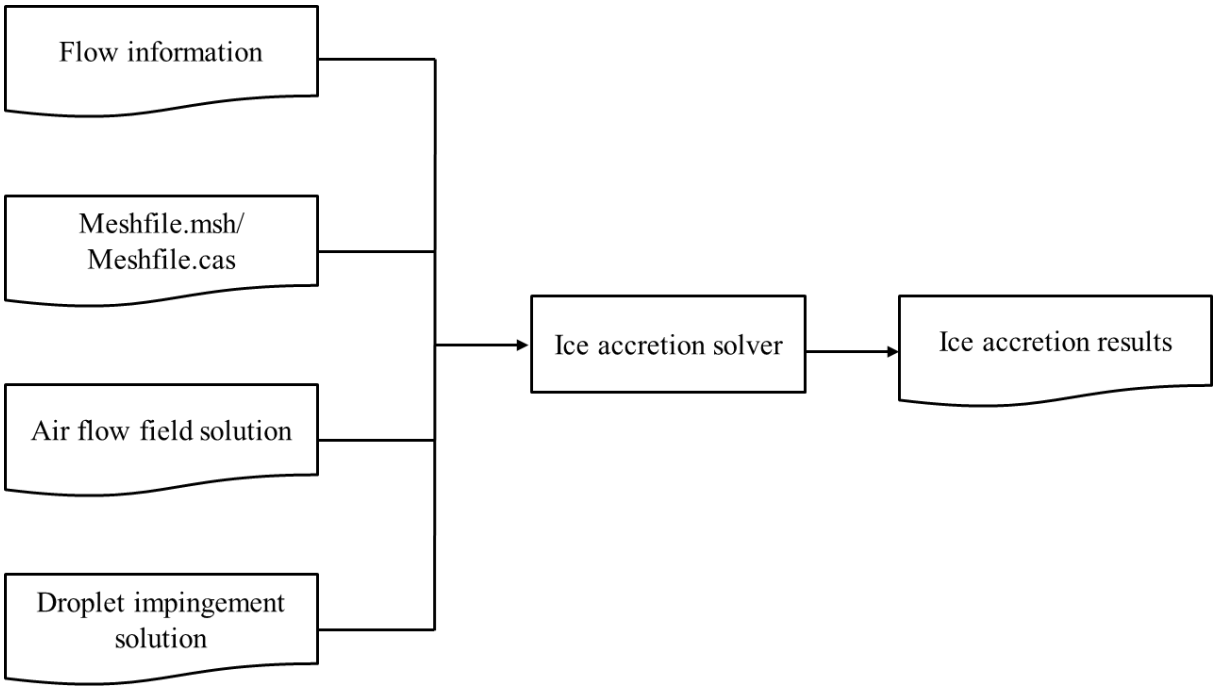

Figure B-6 Automated ice accretion solver process flow

The ice accretion results are used to calculate the nodal displacement. The displaced new coordinates are used as the input for the mesh generator to continue the cycle until the final time step is reached.

Bibliography

1. Durst, F., D. Miloievic, and B. Schönung, Eulerian and Lagrangian predictions of particulate two-phase flows: a numerical study. *Applied Mathematical Modelling*, 1984. **8**(2): pp. 101-115.
2. Tokareva, S. and E.F. Toro, HLLC-type Riemann solver for the Baer–Nunziato equations of compressible two-phase flow. *Journal of Computational Physics*, 2010. **229**(10): pp. 3573-3604.
3. Tian, B., E. Toro, and C. Castro, A path-conservative method for a five-equation model of two-phase flow with an HLLC-type Riemann solver. *Computers & Fluids*, 2011. **46**(1): pp. 122-132.
4. Bragg, M. Aircraft aerodynamic effects due to large droplet ice accretions. in *34th AIAA Aerospace Science Meeting and Exhibit*. 1996.
5. Brahimi, M., P. Tran, D. Chocron, F. Tezok, and I. Paraschivoiu, Effect of supercooled large droplets on ice accretion characteristics. *AIAA Paper*, 1997: pp. 97-0306.
6. Ahn, G., K. Jung, R.S. Myong, H. Shin, and W. Habashi, Numerical and Experimental Investigation of Ice Accretion on Rotorcraft Engine Air Intake. *Journal of Aircraft*, 2015. **52**(3): pp. 903-909.
7. Nathman, J.K. and D.A. Dietrich, Thermal analysis of engine inlet anti-icing systems. *Journal of Propulsion and Power*, 1990. **6**(5): pp. 628-634.
8. Landsberg, B., Safety Advisor: Aircraft Icing. 2008, AOPA Air Safety Foundation.
9. Lynch, F.T. and A. Khodadoust, Effects of ice accretions on aircraft aerodynamics. *Progress in Aerospace Sciences*, 2001. **37**(8): pp. 669-767.
10. Papadakis, M., H.-W. Yeong, I.G. Suares, and J. Jacob. Experimental and Computational Investigation of Ice Shedding from Aircraft Surfaces. in *44th AIAA Aerospace Sciences Meeting and Exhibit, American Institute of Aeronautics and Astronautics*. 2006.
11. Bragg, M.B., T. Hutchinson, J. Merret, R. Oltman, and D. Pokhariyal. Effect of ice accretion on aircraft flight dynamics. in *38th Aerospace Sciences Meeting and Exhibit*. 2000.
12. AI-Khalil, K.M. Ice accretion and performance degradation calculations with LEWICE/NS. in *31st Aerospace Sciences Meeting and Exhibit*. 1993.

13. Gent, R.W., N.P. Dart, and J.T. Cansdale, Aircraft icing. *Philosophical Transactions of the Royal Society of London A: Mathematical, Physical and Engineering Sciences*, 2000. **358**(1776): pp. 2873-2911.
14. Cober, S.G., G.A. Isaac, and J.W. Strapp, Characterizations of aircraft icing environments that include supercooled large drops. *Journal of Applied Meteorology*, 2001. **40**(11): pp. 1984-2002.
15. Cebeci, T. and F. Kafyeke, Aircraft icing. *Annual Review of Fluid Mechanics*, 2003. **35**(1): pp. 11-21.
16. Scavuzzo, R., M. Chu, and V. Ananthaswamy, Influence of aerodynamic forces in ice shedding. *Journal of Aircraft*, 1994. **31**(3): pp. 526-530.
17. Kind, R., M. Potapczuk, A. Feo, C. Golia, and A. Shah, Experimental and computational simulation of in-flight icing phenomena. *Progress in Aerospace Sciences*, 1998. **34**(5): pp. 257-345.
18. Tran, P., M. Brahimi, I. Paraschivoiu, A. Pueyo, and F. Tezok, Ice accretion on aircraft wings with thermodynamic effects. *Journal of Aircraft*, 1995. **32**(2): pp. 444-445.
19. FAA, A., Engine Certification Requirements in Supercooled Large Drop, Mixed Phase, and Ice Crystal Icing Conditions. *Federal Register*, 2010. **75**(124): pp. 37311-37339.
20. Jeck, R.K., Icing Design Envelopes (14 CFR Parts 25 and 29, Appendix C) Converted to a Distance-Based. 2002, Federal Aviation Administration (FAA).
21. Jeck, R.K., A new data base of supercooled cloud variables for altitudes up to 10,000 feet AGL and the implications for low altitude aircraft icing. 1983, Federal Aviation Administration Technical Center.
22. Jeck, R. A new characterization of the icing environment below 10,000 feet AGL from 7,000 miles of measurements in supercooled clouds. in *NASA Conference Publication*. 1985.
23. Regulations, F.A., Part 29-Airworthiness Standards: Transport Category Rotorcraft. *DOT, FAA, Washington, DC*, 1990.
24. Wright, W.B., User Manual for the NASA Glenn Ice Accretion Code LEWICE. Version 2.2. 2. 2002, NASA Glenn Research Center.
25. Ruff, G.A. and B.M. Berkowitz, Users manual for the NASA Lewis ice accretion prediction code (LEWICE). 1990, NASA Glenn Research Center.

26. Hedde, T. and D. Guffond, ONERA three-dimensional icing model. *AIAA Journal*, 1995. **33**(6): pp. 1038-1045.
27. Hedde, T. and D. Guffond. Improvement of the ONERA 3D icing code, comparison with 3D experimental shapes. in *31st Aerospace Sciences Meeting*. 1993.
28. Bourgault, Y., Z. Boutanios, and W.G. Habashi, Three-dimensional Eulerian approach to droplet impingement simulation using FENSAP-ICE, Part 1: Model, algorithm, and validation. *Journal of Aircraft*, 2000. **37**(1): pp. 95-103.
29. Bourgault, Y., H. Beaugendre, and W. Habashi, Development of a shallow-water icing model in FENSAP-ICE. *Journal of Aircraft*, 2000. **37**(4): pp. 640-646.
30. Aliaga, C.N., M.S. Aubé, G.S. Baruzzi, and W.G. Habashi, FENSAP-ICE-Unsteady: unified in-flight icing simulation methodology for aircraft, rotorcraft, and jet engines. *Journal of Aircraft*, 2011. **48**(1): pp. 119.
31. Moser, R. and R. Gent, Experience from Application of a 3D Ice Accretion Code. 2003, SAE Technical Paper.
32. Dima, C. and V. Brandi, Prediction of ice accretion on airfoils using CIRA multi-ice code. 2016, Centro Italiano Ricerche Aerospaziali.
33. Saeed, F., S. Gouttebroze, and I. Paraschivoiu. Modified canice for improved prediction of airfoil ice accretion. in *8th Aerodynamic Symposium of 48th CASI Conference, Toronto, Canada, Apr*. 2001.
34. Bidwell, C.S., D. Pinella, and P. Garrison, Ice accretion calculations for a commercial transport using the LEWICE3D, ICEGRID3D and CMARC programs. 1999, National Aeronautics and Space Administration, Lewis Research Center.
35. Cebeci, T. and E. Besnard. Progress Towards fhe Prediction of the Aerodynamic Performance Degradation of an Aircraft in Natural Icing Conditions. in *Proceedings of the First Bombardier International Workshop*. 1994.
36. Von Doenhoff, A.E. and E.A. Horton, A low-speed experimental investigation of the effect of a sandpaper type of roughness on boundary-layer transition. 1958, National Advisory Committee for Aeronautics.
37. White, F.M., *Viscous Fluid Flow*. 3 ed. 2011: Tata Mcgraw Hill.
38. Hobbs, P.V., *Ice Physics*. 2010: Oxford University Press.
39. Messinger, B.L., Equilibrium temperature of an unheated icing surface as a function of air speed. *Journal of the Aeronautical Sciences*, 2012.

40. Morency, F., H. Beaugendre, G. Baruzzi, and W. Habashi. FENSAP-ICE-A comprehensive 3D simulation system for in-flight icing. in *15th AIAA Computational Fluid Dynamics Conference*. 2001.
41. Wright, W.B., B. Park, O.K. Al-Khalil, and D. Miller. Validation of NASA Thermal Ice Protection Computer Codes Part 2-LEWICE/Thermal. in *35th Aerospace Sciences Meeting and Exhibit*. 1997.
42. Villedieu, P., P. Trontin, D. Guffond, and D. Bobo, SLD Lagrangian modeling and capability assessment in the frame of ONERA 3D icing suite. *AIAA paper*, 2012. **3132**: pp. 2012.
43. Jung, S. and R.S. Myong, A second-order positivity-preserving finite volume upwind scheme for air-mixed droplet flow in atmospheric icing. *Computers & Fluids*, 2013. **86**: pp. 459-469.
44. Bourgault, Y., W.G. Habashi, J. Dompierre, and G.S. Baruzzi, A finite element method study of Eulerian droplets impingement models. *International Journal for Numerical Methods in Fluids*, 1999. **29**(4): pp. 429-449.
45. Jung, S., R.S. Myong, and T.-H. Cho, Development of Eulerian droplets impingement model using HLLC Riemann solver and POD-based reduced order method. *AIAA Paper*, 2011. **3907**: pp. 2011.
46. Lapple, C., *Fluid and Particle Mechanics*. 2007: Vincent Press.
47. Toro, E.F., *Shock-Capturing Methods for Free-Surface Shallow Flows*. 2001: Wiley.
48. Balsara, D.S., A two-dimensional HLLC Riemann solver for conservation laws: Application to Euler and magnetohydrodynamic flows. *Journal of Computational Physics*, 2012. **231**(22): pp. 7476-7503.
49. Blazek, J., *Computational Fluid Dynamics: Principles and Applications:* 2005: Elsevier.
50. Barth, T.J. and D.C. Jespersen, The design and application of upwind schemes on unstructured meshes, in 27th Aerospace Sciences Meeting. 1989.
51. Venkatakrishnan, V., Convergence to steady state solutions of the Euler equations on unstructured grids with limiters. *Journal of Computational Physics*, 1995. **118**(1): pp. 120-130.
52. Jameson, A., W. Schmidt, and E. Turkel, Numerical solutions of the Euler equations by finite volume methods using Runge-Kutta time-stepping schemes. *AIAA paper*, 1981. **1259**.

53. Cao, Y., Q. Zhang, and J. Sheridan, Numerical simulation of rime ice accretions on an aerofoil using an Eulerian method. *The Aeronautical Journal*, 2008. **112**(1131): pp. 243-249.
54. Norde, E., J.M. Hospers, E. Weide, and H.W. Hoeijmakers. Aircraft Icing in Flight: Effects of Impact of Supercooled Large Droplets. in *29th Congress of the International Council of the Aeronautical Sciences*. 2014.
55. Spalart, P. and S. Allmaras. A one-equation turbulence model for aerodynamic flows. in *30th aerospace sciences meeting and exhibit*. 1992.
56. Roe, P.L., Approximate Riemann solvers, parameter vectors, and difference schemes. *Journal of Computational Physics*, 1981. **43**(2): pp. 357-372.
57. Tan, J., M. Papadakis, and M. Sampath, Computational study of large droplet breakup in the vicinity of an airfoil. 2005, US Department of Transportation, Federal Aviation Administration, Office of Aviation Research.
58. Jung, S. and R.S. Myong. Numerical Modeling for Eulerian Droplet Impingement in Supercooled Large Droplet Conditions. in *51st AIAA Aerospace Sciences Meeting including the New Horizons Forum and Aerospace Exposition*. 2013.
59. Miller, D., T. Ratvasky, B. Bernstein, F. McDonough, and J.W. Strapp, NASA/FAA/NCAR Supercooled Large Droplet Icing Flight Research: Summary of Winter 1996-1997 Flight Operations. 1998, NASA Lewis Research Center.
60. Cliff, R., J. Grace, and M. Weber, Bubbles, Drops and Particles. 1978, Academic Press Inc., New York.
61. Honsek, R., W.G. Habashi, and M.S. Aubé, Eulerian modeling of in-flight icing due to supercooled large droplets. *Journal of Aircraft*, 2008. **45**(4): pp. 1290-1296.
62. Iuliano, E., G. Mingione, F. Petrosino, and F. Hervy, Eulerian modeling of large droplet physics toward realistic aircraft icing simulation. *Journal of Aircraft*, 2011. **48**(5): pp. 1621-1632.
63. Sabri, F., O. Trifu, and I. Paraschivoiu. In-flight ice accretion simulation in SLD conditions. in *25th AIAA Applied Aerodynamics Conference*. 2007.
64. Rendall, T.C.S. and C.B. Allen, Finite-volume droplet trajectories for icing simulation. *International Journal of Multiphase Flow*, 2014. **58**(0): pp. 185-194.
65. Karl, A. and A. Frohn, Experimental investigation of interaction processes between droplets and hot walls. *Physics of Fluids*, 2000. **12**(4): pp. 785-796.
66. Cossali, G., A. Coghe, and M. Marengo, The impact of a single drop on a wetted solid surface. *Experiments in Fluids*, 1997. **22**(6): pp. 463-472.

67. Yarin, A. and D. Weiss, Impact of drops on solid surfaces: self-similar capillary waves, and splashing as a new type of kinematic discontinuity. *Journal of Fluid Mechanics*, 1995. **283**: pp. 141-173.
68. Trujillo, M., W. Mathews, C. Lee, and J. Peters, Modelling and experiment of impingement and atomization of a liquid spray on a wall. *International Journal of Engine Research*, 2000. **1**(1): pp. 87-105.
69. Stow, C. and M. Hadfield. An experimental investigation of fluid flow resulting from the impact of a water drop with an unyielding dry surface. in *Proceedings of the Royal Society of London A: Mathematical, Physical and Engineering Sciences*. 1981. The Royal Society.
70. Mundo, C., M. Sommerfeld, and C. Tropea, Droplet-wall collisions: Experimental studies of the deformation and breakup process. *International Journal of Multiphase Flow*, 1995. **21**(2): pp. 151-173.
71. Stow, C. and R. Stainer, The physical products of a splashing water drop. *Journal of the Meteorological Society of Japan. Ser. II*, 1977. **55**(5): pp. 518-532.
72. Bai, C. and A. Gosman, Development of methodology for spray impingement simulation. 1995, SAE Technical Paper.
73. Luxford, G., Experimental and modelling investigation of the deformation, drag and break-up of drizzle droplets subjected to strong aerodynamics forces in relation to SLD aircraft icing. 2005, Cranfield University.
74. Vargas, M. and A. Feo. Experimental Observations on the Deformation of Water Droplets Near the Leading Edge of an Airfoil. in *AIAA Atmospheric and Space Environments Conference*. 2011.
75. Kollár, L.E., M. Farzaneh, and A.R. Karev, Modeling droplet collision and coalescence in an icing wind tunnel and the influence of these processes on droplet size distribution. *International Journal of Multiphase Flow*, 2005. **31**(1): pp. 69-92.
76. Luxford, G., D. Hammond, and P. Ivey. Role of droplet distortion and break-up in large droplet aircraft icing. in *AIAA 42nd Aerospace Sciences Meeting and Exhibition, Reno NV, USA: AIAA-2004-0411*. 2004.
77. Pilch, M. and C. Erdman, Use of breakup time data and velocity history data to predict the maximum size of stable fragments for acceleration-induced breakup of a liquid drop. *International Journal of Multiphase Flow*, 1987. **13**(6): pp. 741-757.
78. O'Rourke, P.J. and A.A. Amsden, The TAB method for numerical calculation of spray droplet breakup. 1987, Los Alamos National Lab., NM (USA).

79. Wright, W. and M. Potapczuk. Semi-Empirical Modelling of SLD Physics. in *42nd AIAA Aerospace Sciences Meeting and Exhibit*. 2004.
80. Morency, F., F. Tezok, and I. Paraschivoiu, Anti-icing system simulation using CANICE. *Journal of Aircraft*, 1999. **36**(6): pp. 999-1006.
81. Fortin, G. and J. Perron. Wind turbine icing and de-icing. in *47th AIAA Aerospace Sciences Meeting including The New Horizons Forum and Aerospace Exposition*. 2009.
82. Makkonen, L. and J. Stallabrass, Experiments on the cloud droplet collision efficiency of cylinders. *Journal of Climate and Applied Meteorology*, 1987. **26**(10): pp. 1406-1411.
83. Jones, K.F., The density of natural ice accretions related to nondimensional icing parameters. *Quarterly Journal of the Royal Meteorological Society*, 1990. **116**(492): pp. 477-496.
84. Macklin, W., The density and structure of ice formed by accretion. *Quarterly Journal of the Royal Meteorological Society*, 1962. **88**(375): pp. 30-50.
85. Kreeger, R.E. and W.B. Wright, The influence of viscous effects on ice accretion prediction and airfoil performance predictions. *AIAA Paper*, 2005. **1373**.
86. Poinsatte, P.E., Heat transfer measurements from a NACA 0012 airfoil in flight and in the NASA Lewis icing research tunnel. 1990, Lewis Research Center.
87. Chilton, T.H. and A.P. Colburn, Mass transfer (absorption) coefficients prediction from data on heat transfer and fluid friction. *Industrial & Engineering Chemistry*, 1934. **26**(11): pp. 1183-1187.
88. Papadakis, M., Experimental investigation of water droplet impingement on airfoils, finite wings, and an S-duct engine inlet. 2002, National Aeronautics and Space Administration, Glenn Research Center.
89. Papadakis, M., A. Rachman, S.-C. Wong, H.-W. Yeong, K. Hung, and C. Bidwell. Water impingement experiments on a NACA 23012 airfoil with simulated glaze ice shapes. in *42nd AIAA Aerospace Sciences Meeting and Exhibit*. 2004.
90. Papadakis, M., K.E. Hung, G.T. Vu, H.W. Yeong, C.S. Bidwell, M.D. Breer, and T.J. Bencic, Experimental investigation of water droplet impingement on airfoils, finite wings, and an S-duct engine inlet. 2002, NASA Glenn Research Center.
91. Bidwell, C.S., Collection efficiency and ice accretion calculations for a Boeing 737-300 inlet. 1997, NASA Glenn Research Center.

92. Bidwell, C. and y.R. Mohler, Jr, Stanley. Collection efficiency and ice accretion calculations for a sphere, a swept MS (1)-317 wing, a swept NACA-0012 wing tip, an axisymmetric inlet, and a Boeing 737-300 inlet. in *33rd Aerospace Sciences Meeting and Exhibit*. 1995.
93. Wright, W.B., Validation Results for LEWICE 3.0. 2005, NASA Glenn Research Center.
94. Papadakis, M., H.-W. Yeong, S.-C. Wong, M. Vargas, and M. Potapczuk, Experimental investigation of ice accretion effects on a swept wing. 2005, NASA Glenn Research Center.
95. Potapczuk, M. and C. Bidwell. Numerical simulation of ice growth on a MS-317 swept wing geometry. in *29th Aerospace Sciences Meeting*. 1991.
96. Tan, S. and M. Papadakis, Simulation of SLD impingement on a high-lift airfoil. *AIAA Paper*, 2006. **463**: pp. 2006.
97. Petrosino, F., G. Mingione, A. Carozza, T. Gilardoni, and G. D'Agostini, Ice accretion model on multi-element airfoil. *Journal of Aircraft*, 2011. **48**(6): pp. 1913-1920.
98. Bidwell, C., Icing calculations for a 3D, high-lift wing configuration. *AIAA*, 2005. **1244**: pp. 2005.
99. Zhang, C., F. Wang, W. Kong, and H. Liu. The Characteristics of SLD icing accretions and aerodynamic effects on high-lift configurations. in *33rd AIAA Applied Aerodynamics Conference*. 2015.
100. Aerospace-Technology. https://en.wikipedia.org/wiki/KAI_KC-100_Naraon.
101. Jung, S.K., S.M. Shin, R.S. Myong, T.H. Cho, H.H. Jeong, and J. Jung. Ice accretion effect on the aerodynamic characteristics of KC-100 aircraft. in *48th AIAA Aerospace Sciences Meeting Including the New Horizons Forum and Aerospace Exposition*. 2010.
102. Ragni, A., B. Esposito, M. Marrazzo, M. Bellucci, and L. Vecchione. Calibration of the CIRA IWT in the High Speed Configuration. in *43rd AIAA Aerospace Sciences Meeting and Exhibit*. 2005.
103. Esposito, B.M., A. Ragni, F. Ferrigno, and L. Vecchione, Cloud calibration update of the CIRA Icing Wind tunnel. 2003, SAE Technical Paper.
104. Papadakis, M. and S. Wong, Parametric investigation of a bleed air ice protection system. *AIAA paper*, 2006. **1013**: pp. 2006.

105. Lee, J., D. Rigby, W. Wright, and Y. Choo. Analysis of Thermal Ice Protection System (TIPS) with Piccolo Tube Using State-of-the-Art Software. in *44th AIAA Aerospace Sciences Meeting and Exhibit*. 2006.
106. Papadakis, M., S.-H. Wong, H.-W. Yeong, S.-C. Wong, and G.T. Vu, Icing tests of a wing model with a hot-air ice protection system. *AIAA Paper*, 2010. **7833**: pp. 2010.
107. Albright, A., D. Kohlman, W. Schweikhard, and P. Evanich, Evaluation of a pneumatic boot deicing system on a general aviation wing model. 1981, NASA Lewis Research Center.
108. Thomas, S.K., R.P. Cassoni, and C.D. MacArthur, Aircraft anti-icing and de-icing techniques and modeling. *Journal of Aircraft*, 1996. **33**(5): pp. 841-854.
109. Blaha, B.J. and P.L. Evanich, Pneumatic boot for helicopter rotor deicing. 1981, Lewis Research Center.
110. Bowden, D.T., Effect of Pneumatic De-icers and Ice Formations on Aerodynamic Characteristics of a Airfoil. 1956, National Advisory Committe for Aeronautics.
111. Parent, O. and A. Ilinca, Anti-icing and de-icing techniques for wind turbines: Critical review. *Cold Regions Science and Technology*, 2011. **65**(1): pp. 88-96.
112. Mayer, C., A. Ilinca, G. Fortin, and J. Perron, Wind tunnel study of electro-thermal de-icing of wind turbine blades. *International Journal of Offshore and Polar Engineering*, 2007. **17**(03).
113. Coffman, H., Helicopter rotor icing protection methods. *Journal of the American Helicopter Society*, 1987. **32**(2): pp. 34-39.
114. Mohseni, M. and A. Amirfazli, A novel electro-thermal anti-icing system for fiber-reinforced polymer composite airfoils. *Cold Regions Science and Technology*, 2013. **87**: pp. 47-58.
115. Yaslik, A.D., K.J. De Witt, T.G. Keith, and W. Boronow, Three-dimensional simulation of electrothermal deicing systems. *Journal of Aircraft*, 1992. **29**(6): pp. 1035-1042.
116. Silva, G.d., O.d.M. Silvares, and E.d.J. Zerbini, Numerical simulation of airfoil thermal anti-ice operation part 1: mathematical modeling. *Journal of Aircraft*, 2007. **44**(2): pp. 627-634.
117. Silva, G.d., Guilherme Araujo Lima, O. de Mattos Silvares, and E.J.d.G.J. Zerbini, Numerical simulation of airfoil thermal anti-ice operation. Part 2: Implementation and results. *Journal of Aircraft*, 2007. **44**(2): pp. 635-641.

118. Dillingh, J.E. and H.W. Hoeijmakers. Numerical simulation of airfoil ice accretion and thermal anti-icing systems. in *24th International Council of Aeronautical Sciences*. 2004.
119. Manual, N.S.U., Newmerical Technologies Inc. 2010.
120. Beaugendre, H., F. Morency, and W.G. Habashi, FENSAP-ICE's three-dimensional in-flight ice accretion module: ICE3D. *Journal of Aircraft*, 2003. **40**(2): pp. 239-247.
121. Croce, G., H. Beaugendre, and W. Habashi. CHT3D-FENSAP-ICE conjugate heat transfer computations with droplet impingement and runback effects. in *40th AIAA Aerospace Sciences Meeting & Exhibit*. 2002.
122. Suke, P., Analysis of heating systems to mitigate ice accretion on wind turbine blades. 2014, McMaster University.
123. Myong, R.S., Atmospheric Icing Effects on Aerodynamics of Wind Turbine Blade. *ASME IMECE2013*, 2013.
124. Jonkman, J., S. Butterfield, W. Musial, and G. Scott, Definition of a 5-MW reference wind turbine for offshore system development. 2009, National Renewable Energy Laboratory (NREL), Golden, CO.
125. Löhner, R. and J.D. Baum, Handling tens of thousands of cores with industrial/legacy codes: Approaches, implementation and timings. *Computers & Fluids*, 2013. **85**: pp. 53-62.
126. Moureau, V., P. Domingo, and L. Vervisch, Design of a massively parallel CFD code for complex geometries. *Comptes Rendus Mécanique*, 2011. **339**(2-3): pp. 141-148.
127. Marshall, J., A. Adcroft, C. Hill, L. Perelman, and C. Heisey, A finite-volume, incompressible Navier Stokes model for studies of the ocean on parallel computers. *Journal of Geophysical Research: Oceans*, 1997. **102**(C3): pp. 5753-5766.
128. Pacheco, P.S., *Parallel Programming with MPI*. 1997: Morgan Kaufmann.
129. Fanfarillo, A., T. Burnus, V. Cardellini, S. Filippone, D. Nagle, and D. Rouson. OpenCoarrays: open-source transport layers supporting coarray Fortran compilers. in *Proceedings of the 8th International Conference on Partitioned Global Address Space Programming Models*. 2014.
130. Karypis, G. and V. Kumar, A fast and high quality multilevel scheme for partitioning irregular graphs. *SIAM Journal on Scientific Computing*, 1998. **20**(1): pp. 359-392.
131. Carlson, B., T. El-Ghazawi, B. Numrich, and K. Yelick, Programming in the partitioned global address space model. *Tutorial at Supercomputing*, 2003: pp. 44.

132. Mellor-Crummey, J., L. Adhianto, W.N. Scherer III, and G. Jin. A new vision for Coarray Fortran. in *Proceedings of the Third Conference on Partitioned Global Address Space Programing Models*. 2009.
133. Numrich, R.W. and J. Reid. Co-Array Fortran for parallel programming. in *ACM Sigplan Fortran Forum*. 1998.
134. Jin, G., J. Mellor-Crummey, L. Adhianto, W.N. Scherer III, and C. Yang. Implementation and performance evaluation of the hpc challenge benchmarks in coarray fortran 2.0. in *Parallel & Distributed Processing Symposium (IPDPS), IEEE International*. 2011.
135. Ashby, J.V. and J.K. Reid. Migrating a scientific application from mpi to coarrays. in *CUG 2008 Proceedings. RAL-TR-2008-015*. 2008.
136. Amdahl, G.M. Validity of the single processor approach to achieving large scale computing capabilities. in *Proceedings of Spring Joint Computer Conference*. 1967.